Design, fabrication and characterisation of graphene electromechanical resonators

Tao Chen

A thesis submitted for the degree of Doctor of Philosophy.

The University of Edinburgh

May 22, 2014

Abstract

In this thesis, the design, fabrication and characterisation of graphene electromechanical resonators have been presented. Graphene features ultrahigh Young's modulus and large surface to volume ratio that make it ideal for radio frequency (RF) components, sensors and other micro/nano-electromechanical systems (MEMS/NEMS).

A novel batch fabrication process for graphene electromechanical resonators has been developed by using poly-Si film as sacrificial layer. Previously reported fabrication processes of graphene resonators use SiO_2 as sacrificial layer only because graphene is visible on 300nm SiO_2/Si substrate. However, the wet etching of SiO_2 involves HF, which is not compatible with metal connections or SiO_2 serving as dielectric or passivation layer in graphene NEMS devices. Moreover, the liquid surface tension during drying after wet etching could damage graphene bridges even critical point drying is used. Therefore, in this work, poly-Si is adopted as the sacrificial material. To facilitate the fabrication of graphene resonators, a poly-Si/SiO_2/Si substrate has been designed and optimised to make graphene visible under optical microscope for the first time to the author's knowledge.

Chemical vapour deposition (CVD)-grown monolayer graphene sheet has been transferred onto the optimised poly-Si/SiO_2/Si substrate and patterned into strips. Metal electrodes have been deposited by lift-off process to make electrical connections, which is prerequisite for integrating graphene resonator into practical devices. The graphene bridges have been released by etching the poly-Si layer with XeF_2 in vapour phase, which completely avoids the capillary force induced damage to the graphene bridges. De-fluorination process has been performed by hydrazine reduction to recover graphene's conductivity. This fabrication process is scalable for massive production of graphene electromechanical resonators, thus furthering their practical application.

One-source current mixing characterisation setup has been constructed to test the graphene resonators. Besides the fundamental peak, the activation and enhancement of the second mode of doubly clamped resonator by electrostatic actuation have been observed for the first time. The second mode amplitude reaches 95% of the fundamental mode, whereas only odd higher modes of small intensity have been reported before in other MEMS/NEMS resonators actuated by electrostatic force or magnetomotive force. The findings in this thesis could lead to substantial increase of the sensitivity of sensors based on the graphene resonators. Modal analysis based on Euler-Bernoulli equation has been performed to understand the mechanism behind the activation and enhancement of the second mode. Finite element analysis agrees very well with experimental results and complies with the theoretical model.

Finally, a set of novel alignment marks has been designed, which can be incorporated to process mechanically exfoliated 2D material flakes of micron size and irregular shape with conventional photolithography tools, as have been demonstrated by the successful fabrication of a graphene transistor. This optical alignment technique provides an alternative for prototype device development besides electron beam lithography to prevent electron-induced damage to fragile 2D materials.

Declaration of originality

I hereby declare that the research recorded in this thesis is my own work, produced without the prohibited assistance of third parties and without making use of aids other than those specified. The thesis has been written entirely by myself and the work presented has been conducted in the School of Engineering at the University of Edinburgh from 2010-2014 under the supervision of Prof. Rebecca Cheung. This work has not been submitted for any other degree or professional qualification.

Tao Chen

Signature

Date

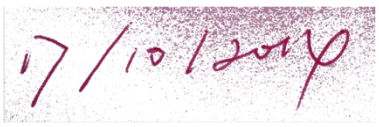

To my family

献给我的家人

“Three passions, simple but overwhelmingly strong, have governed my life: the longing for love, the search for knowledge, and unbearable pity for the suffering of mankind”. Bertrand Arthur William Russell, 3rd Earl Russell, OM, FRS

“对爱情的渴望，对知识的追求，以及对人类苦难无法忍受的怜悯，这三种简单而又强烈的感情支配着我的一生”。伯特兰·亚瑟·威廉·罗素，第三代罗素伯爵

Acknowledgement

I would like to sincerely thank my supervisor Professor Rebecca Cheung for her patient guidance and continuous support of my research toward PhD degree. Her professional and scientific spirit enlightens my way of pursuing the knowledge and truth. From Dr. Camelia Dunare, Dr. Enrico Mastropaolo, and Dr. Andrew Bunting, I learned the skills and tricks of micro-fabrication, for which I am deeply grateful. My gratitude must go to Kevin Tierney, Hugh Frizell, Ewan Macdonald, Stewart Ramsay, Richard Blair, Brian Neilson, and Professor Tom Stevenson who trained me to operate those complex and delicate tools or helped me setting up equipment. Their kindness and humour has been a great relief of fatigue in the clean room. Thanks must go to MEMSSTAR stuff, Tony O'Hara, Graeme Pringle, and Daniel Drysdale for helping me with their advanced XeF_2 and HF release system, as well as Dr. Andrei Gromov and Dr. Oleg Nerushev for helping me with Raman and AFM measurements. I would also like to thank my colleagues Ilka, Giuseppe, Yifan, Jeremy, Andres, Alexander, Howard, and Ewen. It has been a great pleasure to work and hang out with these talented and interesting people. I especially want to express my gratitude to Jennifer, Sidney, and other members of the Hantons, with whom I stayed for the first year in Edinburgh. They have encouraged me, taken care of me, and shown me a completely new culture that I blend into quickly with their help. I am not able to list all the names of friends and whoever lent their hands to me in the four years of life and study in Edinburgh, but I deeply appreciate their warm heart.

I am deeply thankful to my wife who has always been there for me with her tenderness, patience and grace. My parents in law have strongly supported me not only with my studies, but also endowed me the courage to welcome the birth of my first baby and assume the responsibility of a father, for which I am sincerely grateful. I would also like to thank my cousins and relatives who supported me with my study. I should not just say thanks to my mother, father and brother. They share my pain and joy, success and defeat, glory and shame.

Contents

List of figures

List of Tables

Acronyms and nomenclature

Acronyms	
AC	Alternating current
AM	Amplitude modulation
AFM	Atomic force microscope
BN	Boron Nitride
CAGR	Compound average growth rate
CNT	Carbon nanotube
CVD	Chemical vapour deposition
DFT	Density functional theory
DC	Direct current
FEA	Finite element analysis
FFT	Fast Fourier transform
FM	Frequency modulation
FWHM	Full width at half maximum
HF	Hydrogen fluoride
HOPG	Highly ordered pyrolytic graphite
IC	Integrated circuit
ICP	Inductor coupled plasma
MD	Molecular dynamics
MEMS/NEMS	Micro/nano-electromechanical system
MoS_2	Molybdenum disulphide
RIE	Reactive ion etching
SEM	Scanning electron microscope
XeF_2	Xenon di-fluoride

Nomenclature	
$\mathcal{E}$, U	Energy
$\mathcal{H}$	Hamiltonian

k	Wavenumber
$\psi,\ \varphi$	Wave function
$n,\ p$	Electron and hole concentration
$\mu_n,\ \mu_p$	Electron and hole mobility
e	Elementary charge
$\hbar$	Planck's constant
$\boldsymbol{k_B}$	Boltzmann constant
T	Temperature
$\mathcal{N}$	Atomic scale number
r	Position vector
a_{cc}	Length of carbon-carbon bond in graphene
$\mathbb{E}$	Electric field
$\mathbb{H}$	Magnetic field
$V,\ I,\ R,\ G$	Voltage, current, resistance, conductance
ε	Permittivity
C_{Gr}	Graphene gate capacitance
E	Young's modulus
E_{2D}	2D in-plane stiffness
ν	Poisson ratio
Θ	Third order moduli
ϵ	Strain
δ	Displacement
σ	Stress
M	Bending moment
F	Force
Q	Quality factor
T	Tension
λ	Wavelength
ρ	Mass density
v_F	Electron Fermi velocity
f	Frequency
n	Damping coefficient
$\boldsymbol{\psi}$	Spatial mode

w	Deflection

Chapter 1

Introduction

In this chapter, the background of micro/nano-electromechanical system (MEMS/NEMS) and its future development trend will be reviewed first. The concept of graphene will be introduced and its potential applications will be briefly discussed. Most importantly, the motivation and research goals of this thesis will be presented. The layout of the thesis is at the end of this chapter.

1.1 Introduction to Micro/Nano-electromechanical system

1.1.1 MEMS technology

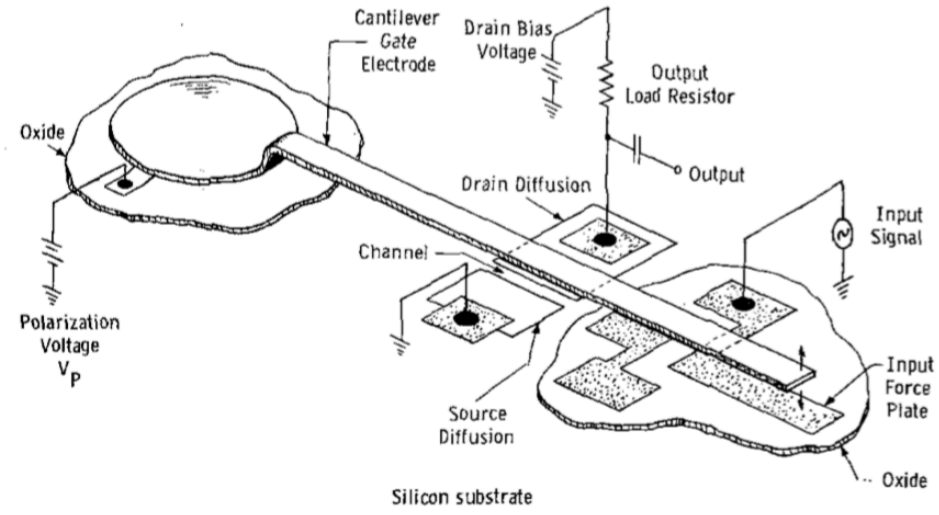

Figure 1.1: Resonant gate transistor, the first MEMS device [1]

In the past half-century or so, MEMS has played a crucial role in reshaping the industry, society, and our lives. As its name indicates, MEMS devices are usually miniature-sized, yet comprise a complete system of specially designed mechanical and electrical components, all integrated in one single chip to perform various tasks. The MEMS technology has evolved from the integrated circuit (IC) technology. The first MEMS device, a resonant gate transistor that can be used as frequency selector (Figure 1.1) [1], appeared in 1967, right along the emergence of IC technology. Since

then, the development of MEMS technology accompanies and interweaves with IC technology. They share most of the fabrication equipment and processes. Yet, MEMS should not be viewed as an IC adding one or two mechanical components. It has its own features in many aspects. Unlike the endless pursuit of integration rate in IC, MEMS technology pays more attention to the diversity and integrity of its functionalities. It has been exploring innovative application of materials with novel processing techniques to realize more and more functions, so that the research in MEMS becomes more and more interdisciplinary. For instance, the combination of MEMS technology and biomedical science has resulted in marvellous devices such as micro-needles, micro-arrays, and micro-fluidic device [2]. These devices either speed up the diagnostic of diseases or facilitate biology and medicine research.

The development of a new MEMS device is more complicated than a new IC. As mechanical components are often constituents of MEMS devices, MEMS relies on the bulk process and surface process techniques such as the wet etching or inductor coupled plasma etching (ICP) for fabricating mechanical structures including cantilevers [3], diaphragms [4][5], and cavities [6]. In the fabrication procedure of mechanical component, compatibility of process steps needs to be taken into account from the very beginning. The design of a MEMS device also largely differs from that of an IC. Because the ICs are based on similar transistors, the only difference being their dimensions, thus the processes can be standardized. To the contrary, the MEMS Law, “one MEMS, one process, one package”, has been validated since the very beginning. The point in this generalized rule is that there is hardly any generic platform for MEMS devices. The obstacle towards a standardized MEMS process lies with the diversified requirements of the mechanical structures. And the materials of these mechanical components also vary from one device to the other. There have been attempts to offer a quasi-standard process that makes the design of MEMS easier, however, not much has been achieved.

MEMS technology has benefited from the advance of IC technology. The matured material and process equipment lowers the production cost of MEMS. But advances in MEMS technology also facilitate the evolvement of IC technology. For example, bulk process technique has mainly been used in the scope of MEMS device. As it is getting harder and harder to scale down the size of transistors to increase integration

rate, multiple IC dies have been stacked together to keep the chip area while increasing the number of transistors. The stacking of chips requires 3D interconnects, which is realized by the though silicon via (TSV) technology which relies on the typical bulk processing technique developed in MEMS technology.

1.1.2 MEMS application and trend

Figure 1.2: MEMS market forecast from 2012 to 2018 in US dollars. The device types are marked by different colours [7]

Since its appearance, the MEMS technology has found its way into consumer electronics, medical care, and aerospace industries. Typical MEMS devices in application include pressure sensor [8][9], accelerometer/inertial sensor [10], micro-pumps [2][11][12], ink-jet, gas sensors, and so on. Although the functioning of MEMS devices is intangible sometimes, they do benefit the human society in different ways. For example, MEMS pressure sensor features low power consumption and small dimension, thus can be installed in tyres to monitor pressure condition and provide earlier warning against fatal tyre explosion [9], greatly

boosting traffic security. MEMS technology has accelerated the replacement of traditional sensors and actuators with miniature and intelligent devices that are less power and volume demanding. According to market analysis report (see Figure 1.2), the MEMS market value has surpassed 10 billion US dollars in 2012. In the following years up until 2018, the MEMS sector is predicted to see a compound average growth rate (CAGR) of 13%, which means the market value will double in next five years. In Figure 1.2, different types of MEMS devices are distinguished by different colours. Pressure sensor, microfluidics, and gyroscopes are the three dominating types of device in terms of market value. This trend will continue in the future.

MEMS technology will keep developing. First, the dimensions of MEMS devices will scale down to further reduce the cost per die. The scaling down of MEMS device lead to the concept of nano-electromechanical system (NEMS), which comprises core functioning components in the nanometre scale. A typical example is the graphene electromechanical resonators that contain graphene sheet less than a nanometre thick. On the other hand, as stated above, MEMS/NEMS relies on new materials to realize new functions or improve the performance of existing devices. Therefore, incorporating new materials in MEMS/NEMS devices has always been research highlight in this area, and also the propelling force of this PhD project.

1.2 Graphene introduction

1.2.1 The concept of graphene

Graphite academic communities have been aware of the concept of graphene since 1960s, when chemist Hanns-Peter Boehm coined the terminology “graphene” from “graphite” and the suffix “ene”. In specific and strict senses, “graphene” only refers to an individual layer of graphite’s planar honeycomb lattice. However, “graphene” has also been adopted for up to ten layers of graphite by convention. The bifurcation of graphite and graphene originates from their distinctive electrical properties [13]. Unlike bulk graphite, monolayer graphene’s valence band and conduction band touch upon each other at Dirac point, thus, in undoped graphene, Fermi level coincides with Dirac point. The electron energy $\mathcal{E}$ and wavenumber k follow a linear

relationship around Dirac point, therefore, the electrons and holes behave like massless particles. Such massless particles transport at a velocity comparable to light, rendering extremely high carrier mobility [14][15][16][17]. When graphene layer increases, the band structure will become more and more like bulk graphite [13]. Although the concept of graphene has been known to scientists for decades, it is only after Andrei Geim and Konstantin Novoselov first isolated monolayer graphene and reported its electric field effect and superb electrical transportation that a surge occur in the research of graphene [14][18].

In contrast to the transition of electrical properties, the mechanical properties of graphene resemble those of bulk graphite [19]. The honeycomb 2D lattice of graphene formed by sp^2 carbon-carbon bonds leads to extremely high in-plane stiffness, which has been one of the most significant properties graphene possesses. The phenomenal mechanical strength of graphene/graphite lattice structure has already found widespread applications long before the discovery of monolayer graphene. For instance, carbon fibre, which contains graphene flakes of a few microns large, has been widely used in aerospace industry and military section for its ultra-strength and lightweight. As the large volume growth and process of graphene mature, it is rapidly emerging as a novel material for future MEMS/NEMS devices due to its exceptional properties. Inspired by the discovery of monolayer graphene by mechanical exfoliation, other monolayer materials have been produced and found in the same way. These materials include molybdenum disulphide (MoS_2) [20], boron nitride (BN) [21], just to name a few. Therefore, graphene has opened a new era of material research and applications.

1.2.2 Graphene preparation

The first graphene flakes prepared for research have all come from mechanical exfoliation of graphite [22]. Since the interaction between graphene layers in graphite is the weak Van de Walls force, thus it is easy to thin graphite by repeatedly peeling off a few layers of graphite using the "Scotch tape". Although exfoliation offers a fast solution for research purpose in laboratory, the industrialization cannot rely on it since it cannot be scaled up for mass production. Lots of efforts have been poured to large area growth of graphene. Large area growth of monolayer graphene

has been realized in two ways, the sublimation of SiC and the surface growth on catalyst by chemical vapour deposition (CVD) techniques [23][24]. The sublimation of SiC involves ultrahigh temperature to vaporize the silicon atoms on the SiC surface, leaving carbon atoms to bond in a hexagonal lattice. The advantage of this technology is that the graphene is readily located on top of an almost insulating material. However, it could also be a barrier against transferring graphene to other substrates. The most promising and flexible method for mass production of large area monolayer graphene could be the CVD growth, which has already been available commercially. Roll-to-roll CVD growth of graphene is a streamline production that can potentially reduce the cost substantially [25]. That is the reason why CVD-grown graphene sheet has been used to fabricate graphene resonators in chapter 5. The technology of obtaining graphene, if not monolayer, is not limited to the aforementioned two techniques. For example, graphite flakes can be exfoliated by ultrasonic power, and the resulted graphene flakes are dispersed in solutions [26], or the graphene can be obtained from reducing graphene oxide flakes [27]. These two techniques are suitable for producing graphene to be used in electrodes.

1.2.3 Graphene application

The promising future of graphene resides in its wonderful properties in various aspects. These superior properties can be applied in many future products. As mentioned above, electrons transport in graphene at a velocity comparable to light [28][29], leading to high conductivity. Therefore, there have been expectations that graphene will be the material to replace silicon in logic devices. The well-known Moore's Law states that the number of transistors in integrated circuit doubles in every two years. As the integration rate increases, the size of the transistors scales down. In a decade or so, the integration rate cannot be increased any more by conventional scaling down of transistor feature size, since the channel length and insulator thickness will reach the quantum limit. The solutions for keeping pace to the ever-escalating demand of computing performance include 3D interconnection to enable stacking of multi-chip vertically to increase the integration rate while remaining the die area, or to develop faster transistors than silicon-based ones. That's why graphene has drawn so much attention since its field effect and unparalleled

conductivity has been reported. Reports have shown the feature frequency of graphene transistors have been pushed forward to up to 300GHz [30][31], which could replace traditional GaAs devices that have been widely used in radio frequency (RF) circuits. Besides, the graphene could allow large current to flow through, and the graphene has good thermal conductivity. Therefore graphene transistor also could find application in microwave technologies and defence sector. However, there is no bandgap in intrinsic graphene, which prevents the graphene channel from shutting down and causes large leakage current. Although the ultra-thin thickness of graphene could prevent the short channel effect in conventional silicon transistors, the leakage current looms upon graphene's potential application in logic devices. Various methods have been explored to open a bandgap in graphene. However, there is always a trade-off between the bandgap and the charge mobility in graphene.

Although the potential of replacing silicon by graphene remains controversial, its applications in electrodes are bound to come into market in near future. As an ultra-thin material, graphene only absorbs up to 2.3% of visible light due to its unique band structure [32]. Hence, graphene is an ideal material for transparent electrodes [33][34]. Sukang Bae et al has reported transparent electrodes made from CVD-grown graphene [25]. Multilayer graphene has been stacked to increase the conductivity of the electrode film. A transparency of approximately 90% can be obtained with a sheet resistance as low as 30Ω/square, outperforming traditional indium tin oxides (ITO) transparent electrode. The transparent graphene can be incorporated into touch-screen panel device, as well as flexible and wearable electronics. Due to graphene's 2D nature, its surface to volume ratio is unprecedentedly high, making it ideal for electrodes in batteries or supercapacitors. Such high surface to volume ratio also means that the graphene sheet can absorb substance effectively, which is favourable for sensors based on graphene. The graphene also features high Young's modulus (~1TPa) [35], leading to large resonance frequency in graphene resonators and high sensitivity for sensor applications as will be discussed in detail in chapter 2, inspiring us into the research topic of graphene resonators.

1.3 Objectives of this project

1.3.1 Issue with fabrication of suspended graphene bridges

The techniques of fabricating suspended graphene structures are quite diversified. The mechanically exfoliated graphene are normally put down onto a 300nm SiO_2 surface [14]. These graphene flakes have irregular shape. Using electron beam lithography (EBL), the graphene can be patterned into strips and contacted by lift-off metal electrodes [36]. The SiO_2 can be etched away in wet etchant such as buffered HF solution (BHF) and dried by critical point drying technique to achieve freestanding graphene [36]. An alternative route is to pattern trenches into the SiO_2 layer and put down exfoliated graphene on the SiO_2 surface [19], there is a chance that some graphene flakes may straddle over the trenches. However, these two techniques are hardly scalable for batch fabrication. A. Zande et al reported fabricating large arrays of graphene resonator using CVD-grown graphene [37], and the procedure for suspension of graphene is the same as for exfoliated graphene flakes. But their resonators have no proper electrical connection, which means the graphene resonators cannot be integrated in circuits. Moreover, the wet etching process with BHF is erosive to many metals used in MEMSs such as aluminium.

1.3.2 Proposed solution to batch fabrication

Conventional ways of fabricating freestanding graphene sheet is not compatible with MEMS/NEMS fabrication process because of the erosive BHF. The fundamental aim of this project is to study the batch fabrication of freestanding graphene bridges integrated with metal electrodes. Poly-Si is proposed to be employed as a sacrificial layer, the first time for fabricating freestanding graphene. Poly-Si is very commonly used in MEMS resonators' fabrication, because it is very easily etched away. Poly-Si can also be etched in gaseous phase by xenon di-fluoride (XeF_2), which completely avoids the capillary force during drying step after wet etching. XeF_2 does not attack metal or other commonly used material in IC technology at all. Under XeF_2 atmosphere, the fluorine atoms dissociate and adsorb to the surface of graphene. Moreover, the fluorine atoms will form chemical bonds with graphene, thus changing the properties of graphene, and bring opportunities for diversified applications. In

this project, the influence of fluorination and de-fluorination on the properties of graphene will be studied and discussed in chapter 5.

1.3.3 Electrical characterisation of graphene resonators

There have been two techniques to characterize the resonance of graphene resonators, which will be discussed in detail in chapter 3. One is the optical method, which uses one laser beam to thermally actuate the graphene sheet, and detect the deflection of graphene by sensing the reflection of another laser beam. This technique is more lab-oriented due to its complicated setup, and it is almost impossible to be integrated in MEMS/NEMS. Therefore, for more general application, one needs to turn to another technique, which detects the frequency of graphene electrically. As the novel fabrication process offers modification to graphene, its new physical properties will be explored taking advantage of its metal electrodes. Therefore, electrical characterisation technique will be studied in chapter 3, the fabrication of the graphene resonators with metal electrodes will be discussed in chapter 5, and the test of the performance of graphene resonators electrically will be presented in chapter 6. The expected achievements would lay foundation not only for application of MEMS/NEMS resonators in sensor, but also for studying novel physical phenomenon of nano-scale.

1.4 Thesis arrangement

The structure of this thesis is illustrated in Figure 1.3. The narrow arrows indicate the dependency of chapters, while the workflow is indicated by the wide arrows. Naturally, the downstream chapters also depend on their upstream chapters. The wide arrows on the right side denote the main streamline of this PhD project, which is the design, fabrication and characterisation of graphene resonators. On the left part, the chapter 7 is parallel to chapter 5, which is an enabling technique intended for processing exfoliated 2D material flakes with conventional photolithography tools. Chapter 2 and chapter 3 are the common foundation of chapter 4, 5, 6, and 7. The main topics in all the chapters are elaborated below.

Chapter 2 will be devoted to the introduction of graphene's electrical and mechanical properties. The unique electron energy band structure of graphene is derived from the

hexagonal lattice structure, which explains the conductivity and optical transparency of graphene. The band structure of different layers of graphene also lead to different Raman spectrum features, which is important for distinguishing monolayer graphene from multilayer graphene. The mechanical properties of graphene will also be discussed, based on density functional theory (DFT) calculation and molecular dynamics (MD) simulations.

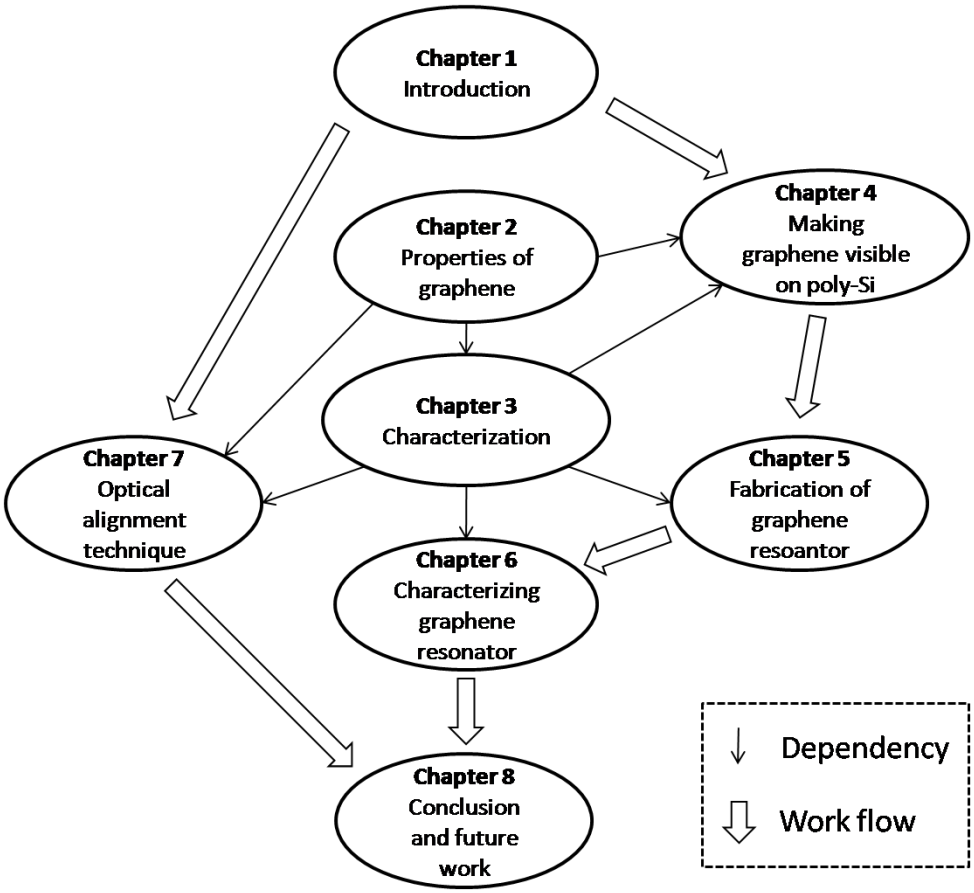

Figure 1.3: Structure of the thesis

Chapter 3 will discuss the characterisation techniques of graphene and graphene resonators. Raman spectroscopy is a common denominator in graphene, because it is capable of characterizing the quality and number of layers of graphene non-destructively. Therefore, a lot of pages have been devoted to elaborate the relationship between Raman features and the lattice structure of graphene. The last part of this chapter focus on the electrical characterisation of the resonance frequency of graphene sheet using the current mixing technique.

Chapter 4 will talk about the optimization of graphene's visibility on poly-Si layer. As graphene sheet will be transferred on poly-Si layer first in this project, making graphene visible under optical microscope will facilitate the inspection and manipulation of graphene. The origin of the contrast of graphene will be theoretically discussed. Based on the theory, the thicknesses of poly-Si and underlying SiO_2 are optimised to improve the visibility. The influence of the doping level in poly-Si on the conductivity of graphene will also be studied by simulation.

Chapter 5 will present the fabrication of suspended graphene sheet using poly-Si as a sacrificial layer. The vapour phase etching of poly-Si by XeF_2 and the reduction of fluorinated graphene by hydrazine will be introduced. The influence of the XeF_2 on the electrical and mechanical properties of graphene will be discussed according to experimental and simulation results. The determinant factors of the overall yield of conductive graphene bridges will be discussed in detail.

Chapter 6 is devoted to the characterisation of graphene resonators. The model of graphene resonators will be discussed, and the measured results of graphene resonators will be presented. The frequency and quality factors of graphene resonators will be compared to its counter parts. The model analysis will be performed to explain the observed high order harmonics in graphene resonators. To further explore the mechanism behind the enhanced higher harmonic, finite element analysis will be performed to obtain the response of the graphene resonant to different electrostatic actuation voltage distribution.

Chapter 7 will present an alignment technique for fabricating devices from irregular exfoliated flakes 2D material. This alignment technique can be incorporated into photo masks that can be exposed by conventional photo lithography tools and avoid the use of electron beam lithography. The application of this technique will be demonstrated by the fabrication of a simple graphene field effect transistor.

In chapter 8, the major findings in the previous chapters will be recalled, as well as the shortcomings that need improvement. Possible future application of the graphene resonators developed in this thesis will also be briefly discussed.

Chapter 2

Properties of graphene

2.1 Introduction

In this chapter, graphene's electrical and mechanical properties will be reviewed. Monolayer graphene features extremely larger carrier mobility and Young's modulus [16][38], surmounting almost all the other counterpart materials. The excellent electrical and mechanical properties of pristine graphene are intrinsically determined by its unique lattice structure and electron energy band structure. Therefore, the lattice configuration of graphene will be discussed, and the electron band diagram of pristine graphene sheet will be deduced. The electron transport mechanism in graphene will be touched as well. The introduction of mechanical properties will follow the electrical property part. A continuum elastic model will be introduced, with which the important metric parameters of the mechanical properties will be presented. The theoretical and experimental results of these parameters will be reviewed and discussed.

Graphene's physical properties are affected by many factors. First, the dimension plays an important role in graphene's band structure. Band structures of monolayer graphene, double-layer graphene, and bulk graphite are different from each other [13]. Their distinctive electron band structure will lead to different Raman spectrum characteristics, so the Raman spectroscopy can be used to determine the number of graphene layers as will be discussed in chapter 3. The lateral size also influences graphene's electrical properties. The lateral confinement turns graphene to quasi-1D graphene nano-ribbon (GNR) and induces bandgap in graphene [39][40][41][42]. The size of graphene sheet is well beyond the regime where quantum effect plays important role in this thesis. Therefore, the discussion mainly stays within diffusive transport range. Due to graphene's 2D nature, the surface to volume ratio is extremely high that makes graphene very susceptible to the influence of its surrounding environment. For instance, the phonon scattering of SiO_2 substrate limits the electron velocity in graphene [16][43]. Graphene is also easily doped by

substance attached to it [44]. Such influences may lead to control of graphene's properties [44]. There have been various techniques to dope the graphene and tune the conductivity including various functionalisation methods such as hydrogenation [45], oxidation [46], and halogenations [47], which add radicals to either the graphene basal plane or dangling bonds at the edges, modifying graphene's chemical and physical attributes. The functionalisation of graphene will be left to chapter 5 when the fabrication of graphene resonator is discussed.

The mechanical properties determine the performance of graphene resonators and sensors based on them, which is the major subject of this thesis. Due to the 2D nature of monolayer graphene, graphene resonators are extremely sensitive to physical quantity change, which is highly favourable for sensor applications. However, graphene resonators also suffer low quality factor at room temperature. The quality factor is very much related to the test environment, thus, this topic will be left to chapter 6 when the measurement results of the graphene resonators are presented. In the last part of this chapter, the topics will be extended to the dynamic range and sensitivity of graphene resonators.

2.2 Band structure of graphene

2.2.1 Lattice structure

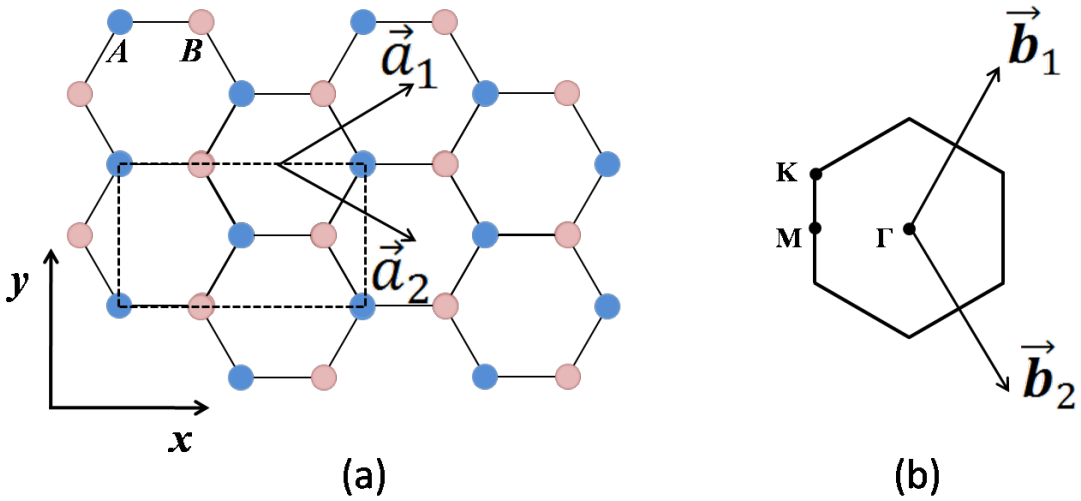

Figure 2.1: Lattice structure of graphene (a) and first Brillouin zone in reciprocal space

The carbon atoms in graphene are arranged in a 2D honeycomb lattice as shown in Figure 2.1(a). The primitive cell of graphene contains two inequivalent carbon atoms as marked by blue and orange colour respectively. For convenience of discussion, the blue atoms are denoted by *A*, and orange atoms by *B*. The inequivalence originates from the angle of adjacent bonds of the two atoms. Therefore, the graphene lattice can be viewed as two interweaved rhombic 2D lattices. The carbon-carbon bond length a_{cc} is about 1.42Å [48]. The coordinate basis of the lattice comprises two vectors $(\vec{a}_1, \vec{a}_2)$ which form an acute angle of 60°. The reciprocal basis vectors are determined by $\vec{a}_i \cdot \vec{b}_j = 2\pi\delta_{ij}$. The Brillouin zone, together with the high symmetry points is shown in Figure 2.1(b). Each isolated carbon atom possesses four valance electrons (*2s, 2p$_x$, 2p$_y$, 2p$_z$*) [28]. When the carbon atoms are bonded in the hexagonal lattice, the *2s*, *2p$_x$* and *2p$_y$* orbitals are hybridized to form co-planar σ and σ* bonds, while the remaining *2p$_z$* orbital creates the delocalized π bond (bonding) and π* bond (anti-bonding), which is perpendicular to the graphene plane. The planar σ bonds between neighbouring carbon atoms are responsible for high in-plane stiffness of graphene [41].

Graphene serves as the basic building block for many carbon allotropes. It can be wrapped up to form a spherical 0D fullerene with a few pentagon defects [49], or rolled along an axis to form carbon nanotubes. And most commonly, in graphite, the graphene layers are stacked in either hexagonal lattice (alpha graphite) or rhombohedra lattice (beta graphite) [13]. The interlayer interaction between graphene layers in graphite is Van der Waals force, which is weak and facilitates mechanical exfoliation and the facile sliding of the layers, an intriguing property that makes graphene suitable for self-lubricating electrodes in electric motors. The spacing between graphene layers is about 3.34Å, though weak, it causes the split of anti-symmetric π bonds and distinguishes the band structure of multilayer graphene from monolayer graphene. Since graphene lattice can be viewed as flattened carbon nano-tubes (CNT) cut along its longitudinal direction, graphene's chirality corresponds to CNTs'. As shown in Figure 2.1(a), the *x* direction corresponds to zigzag CNT, while the *y* direction to armchair CNT. The correspondence is counter-intuitive due to the convention of nomenclature for CNT.

2.2.2 Tight binding description

P. R. Wallace has studied the band structure of graphite first in 1946 [28]. Although the terminology graphene has not yet been proposed at that time, the concept of monolayer graphite, has been conceived and the band structure of bulk graphite has been deduced from it [50]. Since the bonding and anti-bonding σ bands are quite separated and far away from the Fermi level as will be seen in next section, their contribution to conductivity of graphene can be neglected. Therefore, applying tight-binding approximation, one can treat the carbon atoms in graphene as possessing only one conduction electron from $2p_z$ state of carbon atom that can be described with a simple tight-binding Hamiltonian [28]. Suppose φ is the normalized $2p_z$ orbit wave function for isolated carbon atoms, the wave function of graphene system ψ can be written as the sum of the wave function from *A* atom φ_A and *B* atom φ_B

$$\psi = \varphi_A + \boldsymbol{\lambda}\varphi_B \tag{2.1}$$

Where $\boldsymbol{\lambda}$ is any constant and

$$\varphi_A = \sum\nolimits_A e^{2\pi i k \cdot r_A} \varphi(r - r_A) \tag{2.2}$$

$$\varphi_B = \sum\nolimits_B e^{2\pi i k \cdot r_B} \varphi(r - r_B) \tag{2.3}$$

by Bloch theorem. Here, k represents the wavenumber. The summations are taken over all *A* atoms in the graphene lattice and *B* atoms as well. r_A and r_B represent the position vectors of *A* and *B* type carbon atoms respectively. Putting the wave function into Schrödinger's equation and after basic mathematical treatment, we have

$$\mathcal{H}_{AA} + \boldsymbol{\lambda}\mathcal{H}_{AB} = \mathcal{E}\mathcal{S} \tag{2.4}$$

$$\mathcal{H}_{BA} + \boldsymbol{\lambda}\mathcal{H}_{BB} = \lambda\mathcal{E}\mathcal{S} \tag{2.5}$$

Where

$$\mathcal{H}_{ij} = \langle \varphi_i | \mathcal{H} | \varphi_j \rangle \ \ (i, j = A, B) \tag{2.6}$$

And $\mathcal{H}$ is the Hamiltonian of the system. Let

$$\mathcal{S} = \langle \varphi_A | \varphi_A \rangle = \langle \varphi_B | \varphi_B \rangle = \mathcal{N}_p \tag{2.7}$$

Where $\mathcal{N}_p$ is the number of primitive cells in the graphene sheet. To simplify the solution of the energy, it should be assumed that the wave function of A and B atoms are not overlapped, that is to say

$$\langle \varphi_A | \varphi_B \rangle = \langle \varphi_B | \varphi_A \rangle = 0 \tag{2.8}$$

Since λ exists, we can get the secular equation from equation 2.4 and 2.5

$$\begin{vmatrix} \mathcal{H}_{AA} - \mathcal{E}\mathcal{S} & \mathcal{H}_{AB} \\ \mathcal{H}_{BA} & \mathcal{H}_{BB} - \mathcal{E}\mathcal{S} \end{vmatrix} = 0 \tag{2.9}$$

By solving the above equation and considering the symmetry of graphene lattice [28], we readily get

$$\begin{aligned} \mathcal{E} = \frac{1}{\mathcal{N}} (\mathcal{H}_{AA} \pm \mathcal{H}_{AA}) = \mathcal{E}_0 + 3\gamma_0{}' \pm \sqrt{3}\pi\gamma_0 |k - k_c| a_{cc} \\ -3\pi^2 \gamma_0{}' |(k - k_c)|^2 {a_{cc}}^2 \end{aligned} \tag{2.10}$$

Where γ_0 and $\gamma_0{}'$ represent the nearest-neighbour and next-nearest-neighbour hopping amplitudes, which take the approximate values of 2.5eV and 0.1eV respectively [51]. k_c represents the corner of the Brillouin zone. If the relatively smaller $\gamma_0{}'$ is neglected, then the energy measured from the corners of Brillouin zone *K* where $\mathcal{E} = \mathcal{E}_0$ can be written as

$$|\mathcal{E} - \mathcal{E}_0| \approx \sqrt{3}\pi\gamma_0 |k - k_c| a_{cc} \tag{2.11}$$

From the above equation, it can be seen that the top of valence band touches the bottom of the conduction band at the corners of Brillouin zone (Figure 2.2). The point where the two bands meet is called Dirac point. So graphene can be viewed as a semimetal or a zero bandgap semiconductor. The energy-momentum dispersion, as described by the above equation, does not follow the common quadratic relationship, but instead, a linear curve. As a result, the electronic group velocity is $v_F = \sqrt{3}\pi\gamma_0 a/2\hbar$, about 8.5×10^5m/s. Here $\hbar$ is Planck's constant. The charge carriers near the corners of Brillouin zone mimic massless relativistic particles travelling at a velocity comparable to the speed of light.

2.2.3 *Ab initio* calculation

The above deduction provides an analytical solution to band structure and facilitates calculation of carrier density. A more comprehensive study on the bands structure

can be performed by the first principle method, also called *ab initio* method. The first principle method is based on quantum mechanics and does not require empirical data but only constitutive elements' locations in the periodic table. Instead of solving Schrödinger's equation, practical implementation of first principle calculation is made possible by applying the density functional theory (DFT) [52]. DFT states that wave functions and observants of a physical system are functionals of the density of electrons. In contrast to solving many-body Schrödinger's equations based on the wave functions of individual atoms, which has $3\mathcal{N}_a$ variables, DFT considers the density of electron with just three variables of coordinates. Here, $\mathcal{N}_a$ is the number of atoms. Therefore, DFT requires much less computation resource, and has been proven to be a successful and economic tool of investigating various physical properties of atomic and molecular systems.

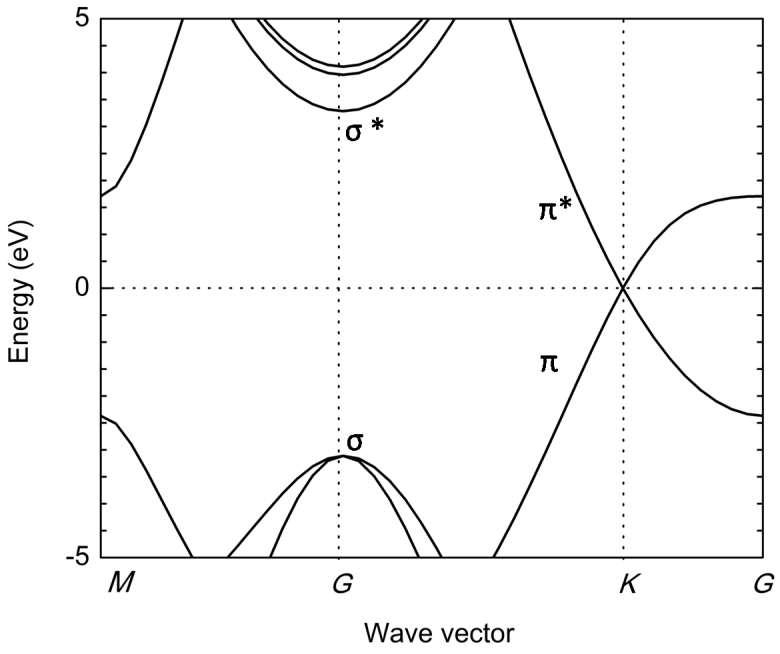

Figure 2.2: Band structure of monolayer graphene calculated with CASTEP

The DFT calculation requires the lattice to be periodical in all three directions. To rule out the mutual interaction of graphene layers, the inter-layer spacing, or the period perpendicular to the *xy* plane in Figure 2.1(a) should be much larger than graphite's inter-layer spacing. The graphene lattice has been modelled in computer with Materials Studio 4.0, which incorporates a first principle programme CASTEP [53], and the interlayer spacing has been set to 20Å. The geometry of the graphene

lattice has first been optimised using the Broyden-Fletcher-Goldfarb-Shanno (BFGS) algorithm [54], which iterates calculating the energy of a system and adjusting the lattice configuration until the minimum total energy is found. The corresponding lattice configuration will be the optimised lattice configuration. The energy band structure at the high symmetry points in reciprocal lattice has been plotted in Figure 2.2 [55]. The bonding π and touches anti-bonding π* bonding at *K* points which is consistent with the tight binding model. The σ bands are indeed far away from the Fermi level, confirming the assumption of the tight binding model. It has been reported that the electron band structure calculated by tight binding model is considerably close to that calculated with *ab initio* method near *K* point. But the discrepancy broadens for energy bands away from Fermi energy [56].

2.2.4 Band structure of multilayer graphene

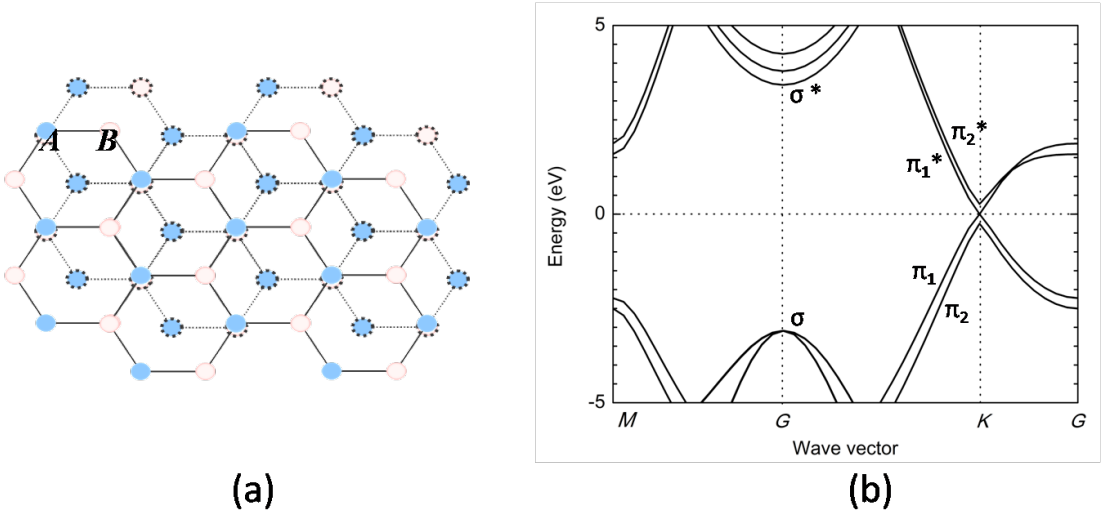

Figure 2.3: AB stacking of double layer graphene (a) and its band structure (b)

The monolayer graphene sheets can be stacked up to form bilayer graphite, trilayer graphene, and up to bulk graphite. The most common stacking order is AB or Bernal stacking, as shown in Figure 2.3(a). The dashed lines denote atoms and bonds at the bottom layer, which has been shifted by a bond length with respect to the top graphene layer. Due to the interaction between the π bonds of neighbouring layers, the π and π* band in double layer graphene split into π_1, π_2 and π_1^*, π_2^* bands around *K* point in reciprocal space as shown in Figure 2.3(b). For even more layers of graphene, their conduction band and valence band become overlapped more and

more with increasing layers [13]. From 11 layers on, the overlapping will be around 41 meV and changes not much for even thicker graphite (less than 10%). A tuneable bandgap could be induced in double layer graphene by applying different electrostatic potential to the two layers [57], which could be advantageous as to minimize the leak current of graphene transistors and increase the on-off current ratio in graphene field effect transistors. Nevertheless, such band opening achievement costs the carrier mobility. The energy-momentum dispersion in double layer graphene is more of parabolic shape rather than a linear one as in monolayer graphene, thus the electron velocity will be reduced.

2.3 Electrical transport in graphene

2.3.1 Carrier density

In semiconductors, the carrier density and mobility are two of the determinant factors of their conductivity. When the Fermi level is located precisely at the Dirac point, also called charge neutral point (CNP), no free charge carrier exists at absolute zero temperature. Nevertheless, the ideal case can never be realized, and the transport of graphene is either electron-like or hole-like. Due to the extremely large electron and hole velocity in graphene, approaching 200,000cm^2/Vs in suspended clean graphene [16], the carriers can transport hundreds of nanometres without being scattered, leading to peculiar quantum transport behaviours [16][58]. For our graphene transistor and graphene bridges of a length much longer than the electron's free range, the transport mechanism is much more of conventional diffusive transport, where the conductivity $\boldsymbol{\sigma_c}$ can be expressed as

$$\boldsymbol{\sigma_c} = \boldsymbol{e}(n\mu_n + p\mu_p) \tag{2.12}$$

n and p are the concentration of electrons and holes. μ_n and μ_p represents the electron and hole mobility. The carrier mobility depends on velocity of electron as well as the average time between scatterings. The common scattering mechanisms in semiconductors include defect scattering, phonon scattering, and so on [59][60]. Here, we only look at the charge carrier density in pristine graphene where no external doping exists. According to the above deduction of energy dispersion curve, the electronic density of states (DOS) per unit area can be derived as

$$\mathcal{N}(\mathcal{E}) = 2\int \frac{dk}{|grad_k \mathcal{E}|} = \frac{4(\mathcal{E}-\mathcal{E}_D)}{3\pi {\gamma_0}^2 {a_{cc}}^2} \tag{2.13}$$

The electrons obey Fermi-Dirac distribution function $\mathcal{F}(\mathcal{E})$, therefore, the 2D electron density in graphene can be expressed as

$$\begin{aligned}\int_0^\infty \mathcal{N}(\mathcal{E})\,\mathcal{F}(\mathcal{E})d\mathcal{E} &= \int_0^\infty \frac{4(\mathcal{E}-\mathcal{E}_D)}{3\pi {\gamma_0}^2 {a_{cc}}^2}\frac{1}{1+\exp\left(\frac{\mathcal{E}-\mathcal{E}_D}{\boldsymbol{k_B}\mathcal{T}}\right)}d\mathcal{E} \\ &= \frac{4\boldsymbol{k_B}^2\mathcal{T}^2}{3\pi {\gamma_0}^2 {a_{cc}}^2}\mathcal{F}_1\left(\frac{(\mathcal{E}-\mathcal{E}_D)}{\boldsymbol{k_B}\mathcal{T}}\right) = 4\left(\frac{\boldsymbol{k_B}\mathcal{T}}{\hbar \upsilon_F}\right)^2 \mathcal{F}_1\left(\frac{(\mathcal{E}-\mathcal{E}_D)}{\boldsymbol{k_B}\mathcal{T}}\right)\end{aligned} \tag{2.14}$$

Where $\mathcal{F}_1$ represents the first order Fermi-Dirac integration, and $\boldsymbol{k_B}$ is the Boltzmann constant. Equation 2.14 will be important for the calculation of the modulation doping level in graphene in section 4.4 of chapter 4.

2.3.2 Ambipolar diffusive transport

2.3.2.1 Field effect measurement

The carrier density of graphene can be modulated by electrostatic voltage as most semiconductor materials do. One of the major findings of Novoselov and Geim in 2004 is the gate-effect of graphene [14], which is key to realize transistors. When a gate structure is integrated with the graphene channel, the gate voltage can be applied to induce electrostatic charges and tune the resistivity of graphene [14]. Normally, graphene transistors are fabricated from exfoliated graphene on 300nm SiO_2/Si substrate, and the substrates are used as back gate. Due to the thickness of SiO_2 and trapped charge scattering, the gate effect of this type device is not prominent. Double-gate graphene transistors have been introduced with a thin top gate insulator thus enhancing the gate control [31][61]. Depending on the charge type induced, the Fermi level is either lifted up (electron doping) or lowered down (hole doping). The electrostatic charge density can be deduced easily from the model of parallel plate capacitor. Assuming that the graphene is pristine without any doping effect induced by impurities or contaminations, the Fermi level coincides with the Dirac point and the concentration of charge carrier is minimized, if not reduced to zero at $\mathcal{T} = 0$. In practice, the graphene sheets fabricated are doped by either molecular doping or modulation doping, then there will be net charge carriers in the graphene piece even

without gate voltage, the Fermi level will not be at the Dirac point. In this case gate voltage will be needed to balance the graphene to neutrality point. The relationship between n and voltage V_g will become

$$n = C_{ox}(V_g - V_0)/e \tag{2.15}$$

Where C_{ox} is the gate capacitance, and V_0 is the applied voltage that can deplete all the existing charge carriers in the graphene, namely, moving the Fermi level back to the Dirac point. V_0 is normally non-zero as graphene can easily be doped by impurities.

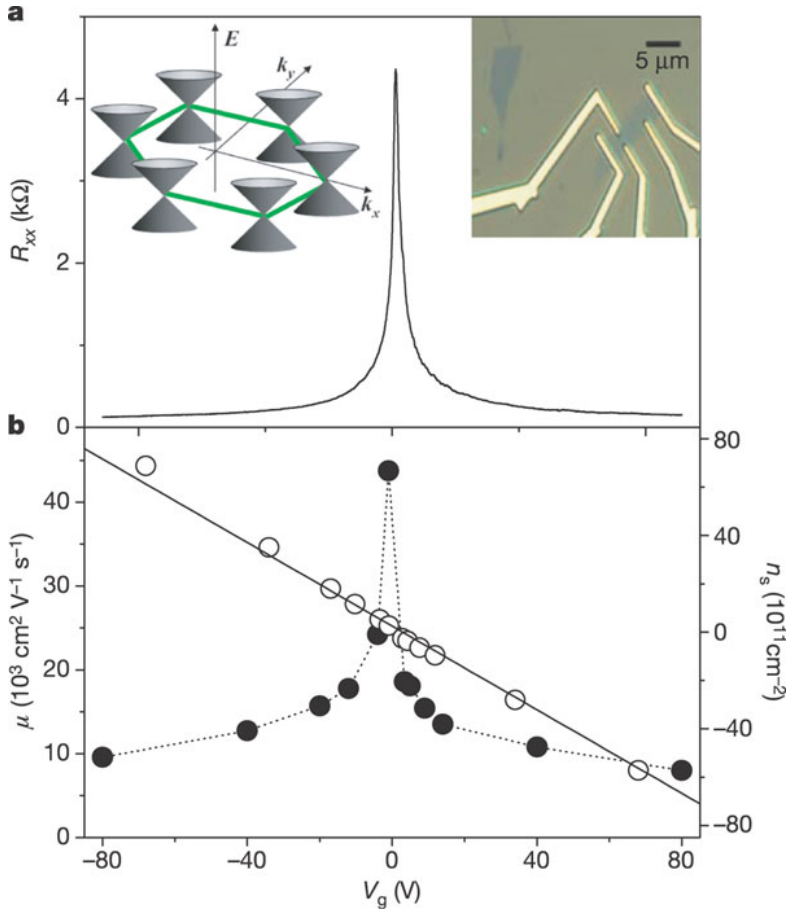

Figure 2.4: Resistance (a), mobility and electron concentration (b) against gate voltage [18]

The gate effect plays a very important role in characterizing the transport of graphene. Figure 2.4(a) shows the resistance of a graphene field effect transistor measured against the back gate voltage [18]. The inset shows the optical image of the graphene device. The graphene sheet has been exfoliated from HOPG and deposited with Au/Cr for electrical contact. The resistance has a very sharp peak, indicating the

depletion of charge carriers, which agrees well with the theory that when the Fermi level lies at the Dirac point, the carrier concentration is minimized. However, there is a finite maximum resistance, indicating that the conductance can never go to zero. This is believed to be due to inhomogeneous puddles of electrons and holes unevenly distributed in graphene sheet [62]. Figure 2.4(b) plots the charge density and mobility against the gate voltage. The charge concentration and the resistivity in (a) are both symmetric, indicating the mobility of electrons and holes equal to each other in this device. The carrier mobility surges from 10,000cm^2/Vs to about 40,000 cm^2/Vs with decreasing carrier concentration.

2.3.2.2 Scattering mechanisms

Other reported carrier mobility in graphene varies from device to device due to different measurement condition and the fabrication processes [16][29][43]. The scattering sources in graphene come internally from its own phonon and lattice defects [63], or externally from coulomb force of charge impurities and substrate phonon modes [62][60]. Initially the ionized impurities in SiO_2 layer have been believed to be the major scattering source. E. H. Hwang et al proposed a transport theory for graphene which explains the carrier density dependence of conductance in graphene [51]. They assumed that the ionized impurities in the SiO_2 substrate is the dominant scattering source and their model fits the experiment data very well [62]. Unexpectedly, although experiments do confirm that in suspended graphene sheet, the carrier mobility increases by certain amount, it is after the annealing that the electron mobility reaches a remarkable value of 200,000cm^2/Vs [29]. The experiment results indicate that suspension alone does not increase the mobility to maximum value. By annealing, the impurities adhered to the graphene can be removed. Therefore, the adsorbents on graphene contribute the most to the scattering source. In clean suspended graphene, even the absorbents and coulomb scattering are minimized, the electrons are still subject to phonon scattering and defects scattering. Characterisation of suspended graphene sheet at room temperature reveals that the mobility can be reduced to a few thousand cm^2/Vs by flexural phonon scattering at room temperature [64], roughly the scale of mobility on SiO_2 substrate. For CVD-grown graphene, the carrier mobility is further limited by grain boundary to about 1100cm^2/Vs [65], which is enough for transparent electrode applications. A

typical sheet resistance of monolayer CVD-grown graphene is around 125Ohm/square [66].

2.4 Mechanical properties of graphene

In this section, a simple continuum elastic model and key parameters for describing graphene's mechanical behaviour will be introduced. The most important parameter is the Young's modulus of graphene. The theoretical calculation and experimental measurements of Young's modulus will be reviewed. Graphene's exceptionally large Young's modulus is crucial to graphene resonator's dynamic range and sensitivity of sensors based on graphene resonators. The ideal strength of graphene is another important quantity that measures how durable graphene is to withstand the external force, which is vital for the robustness of sensors based on graphene sheet as thin as 3.34Å.

2.4.1 Continuum elastic model

For studying the static or dynamic behaviour of a many-body ensemble such as graphene lattice shown in Figure 2.1, the system's energy provides a convenient, and sometimes inevitable, viewpoint. To describe the interaction potential energy of carbon atoms, a valence force field model can be adapted from the model of bulk crystal structure. The sp^2 potential energy U_{sp^2} of carbon-carbon bonds in grapene can be expressed in the atomic scale as [67][68]:

$$U_{sp^2} = \frac{1}{2}\sum_{i=1}^{\mathcal{N}_{at}}\sum_{j}\frac{\boldsymbol{\alpha}}{4a_{cc}^2}\left(\bar{r}_{ij}\cdot\bar{r}_{ij}-a_{cc}^2\right)^2 + \sum_{i=1}^{\mathcal{N}_{at}}\sum_{j<k}\frac{\boldsymbol{\beta}}{a_{cc}^2}\left(\bar{r}_{ij}\cdot\bar{r}_{jk}+\frac{a_{cc}^2}{2}\right)^2 + \sum_{i=1}^{\mathcal{N}_{at}}\sum_{j<k}\boldsymbol{\gamma}\bar{D}_i\cdot\bar{D}_i \tag{2.16}$$

Here, i indexes individual carbon atom whose nearest atoms are indexed by j and k. $\mathcal{N}_{at}$ denotes the number of atoms in the graphene sheet under consideration. $\bar{r}_{ij}$ represents the bond vectors pointing from one atom towards its nearest atoms. $\bar{D}_i$ is the dangling bond vector perpendicular to the local tangential plane. $\boldsymbol{\alpha}$, $\boldsymbol{\beta}$, and $\boldsymbol{\gamma}$ are constants here. For graphene, their values are 155.9J/m^2, 25.5J/m^2, and 7.4J/m^2 respectively [69]. The first term on the right-hand side of the equation is the

deformation energy caused by uniaxial length change of the bonds, while second term denotes energy associated with the in-plane angle change between adjacent bonds. The last term represents the out-of-plane deformation energy of graphene. As the coefficient γ is rather small compared with α and β, the bending deformation energy can be neglected in most cases, which is one of the reasons why the graphene can be treated as 2D material with no bending stiffness when modelling the graphene resonator in chapter 6.

The calculation based on the above equation would be impossible due to the countless number of atoms. Therefore, in practice, a continuum isotropic shell has been used to model the elastic behaviour of graphene. In linear deformation range, the strain energy U can be expressed as functions of local in-plane strain ϵ_x,ϵ_y, ϵ_{xy} and curvature κ_x, κ_y, κ_{xy} [70]. For simplicity, higher moduli are omitted

$$U = \frac{1}{2}\iint \left\{ \frac{E_{2D}}{(1-\upsilon^2)}\left[(\epsilon_x+\epsilon_y)^2 - 2(1-\upsilon)(\epsilon_x\epsilon_y - \epsilon_{xy}^2)\right] + D_{2D}\left[(\kappa_x+\kappa_y)^2 - 2(1-\nu)(\kappa_x\kappa_y - \kappa_{xy}^2)\right]\right\} dS \tag{2.17}$$

where E_{2D}, ν, and D_{2D} are the in-plane stiffness, Poisson ratio, and flexural rigidity for the shell. These three parameters are most important for describing the mechanical properties of graphene and to be discussed in detail from both theoretical and experimental perspectives. Due to graphene's 2D nature, the in-plane stiffness E_{2D} has the dimensionality of surface tension N/m. The flexural rigidity D_{2D} originates from the third term in equation 2.21, so its value is also very small and can be neglected as well. The terms in the integral as a whole represent the deformation energy density. There are two conditions on the validity of the equation. First, the length scale of the deformation should be much larger than the lattice constant [69], and second, the three parameters must be isotropic in graphene's 2D plane. As will be seen, the assumed 2D isotropy of the model can be justified by the graphene's hexagonal symmetry and the appropinquity of calculated Young's modulus in armchair and zigzag directions in small deformation range. E_{2D} and ν can be treated as constant only when the deformation remains in linear regime. For applications such as modeling graphene resonators, the linear deformation condition is normally fulfilled. The bulk Young's modulus E is related to the 2D stiffness

E_{2D} by $E = E_{2D}/t_g$. t_g is the thickness of graphene, normally taking the value of 3.34Å, which is the inter-layer spacing in graphite.

2.4.2 Nonlinearity of in-plane stiffness and ideal strength

In the above equation 2.17, the second order elastic modulus E_{2D} has been assumed to be linear, which does not taken into account the softening of stiffness under high tension. If strain of graphene continues to increase, the stress will reach a maximum where the graphene starts to fracture. This stiffness softening is common to almost every material. To account for the nonlinearity of stiffness, another parameter should also be considered, so again, if the isotropy is presumed, the stress should be expressed as

$$\sigma = E\epsilon + \Theta\epsilon^2 \tag{2.18}$$

where σ is the symmetric second stress, ϵ is the uniaxial Lagrangian strain, and Θ is the third-order elastic modulus.

The value of Θ is normally negative, leading to decreasing of stiffness at high tensile strains. The maximum stress σ_I achievable in a material with perfect lattice structure is called ideal strength [71][72], beyond which the material will be torn apart. The ideal strength characterizes the physical properties of bonds in lattice structures. Nonetheless, materials usually break far below the ideal strength due to stress concentration around defects, thus it has been difficult to measure the ideal strength of a materials due to universally existing lattice defect. However, a graphene sheet exfoliated from Highly Ordered Pyrolytic Graphite (HOPG) or Kish graphite can be defect-free up to a millimetre, thus enabling direct characterisation of ideal strength, which will be discussed later. The deformation energy can even be expressed as even high order elastic modulus [73], however, it will not be discussed in this chapter as it is not relevant.

2.4.3 Calculation of Young's modulus

2.4.3.1 DFT calculation

The mechanical properties of graphene sheet can be investigated by first principle methods as well. The dotted rectangle in Figure 2.1(a) encloses a super-cell of

graphene. The super-cell of such a rectangular shape allows independent investigation of stress-strain relationship along armchair and zigzag directions, which are the two most representative directions. To obtain the deformation energy, a geometry optimization can be performed on the unstrained graphene super-cell to find the lattice structure of minimum energy as described in section 2.2.3. Then a lattice constant of the super-cell, in x direction for example, can be increased to achieve a target strain and fixed so that the non-boundary atoms are allowed to relax to a configuration with which the system energy is minimized again. The potential energy discrepancy between the strained structure and original graphene lattice is the total strain energy U. Such a calculation process mimics the procedure of stretching a shell to acquire the strain-stress curve. The only difference is that the stress is not a direct readout, but deducted from the energy-strain relationship. As mentioned above, since the x and y directions are orthogonal to each other, the stiffness and Poisson ratio in each direction can be calculated separately. For instance, if a homogenous strain is applied to the super-cell in x direction, the strain energy density U_D becomes

$$U_D = \frac{U}{S} = \frac{1}{2} E_{2Dx} \epsilon_x^2 \tag{2.19}$$

Here, S represents the area of graphene super-cell under consideration. The second order differentiation of the above equation gives the E_{2Dx}, the 2D stiffness along armchair direction. The lattice constant of the super-cell along y direction should see a contraction strain ϵ_y when a tensile strain along x direction is applied. So the Poisson ratio is obtained as $\nu = |\epsilon_y/\epsilon_x|$.

Figure 2.5 shows stresses and Poisson ratios against strain of graphene in both armchair and zigzag directions calculated by the *ab initio* methods [74]. The equivalent stress in vertical axis refers to the bulk stress, which has been derived from 2D super-cell stress σ_{2D} using $\sigma = \sigma_{2D}/t_g$. It can be observed from the curve that, in small strain range, the equivalent bulk Young's modulus is approximately a constant of 1050Gpa for bother armchair and zigzag direction. The Poisson ratio of armchair graphene at 5% strain is about 0.18, a little bit larger than zigzag graphene's 0.15 at the same strain. The Poisson ratio scales inversely as the strain. If the two Poisson ratio curves are reversely extrapolated to near zero strain, they will

intersect near zero strain, which means that, under small strain condition, the Poisson ratios along both armchair and zigzag direction are almost equal. The maximum stress points, as coloured in red for uniaxial tension in x direction (zigzag direction), is 110GPa when $\epsilon_x = 0.194$, while for graphene tensioned in y direction (armchair direction), the maximum stress is 121GPa at $\epsilon_y = 0.266$. The stress in x direction reaches its maximum in a smaller strain, indicating that the absolute value of third-order modulus Θ in x direction is larger than that in y direction, leading to faster softening in x direction. The deduced third order modulus along zigzag direction is -946.9 N/m, while that along armchair direction is -759.7 N/m. These calculated values are in consistent with other DFT calculations [75].

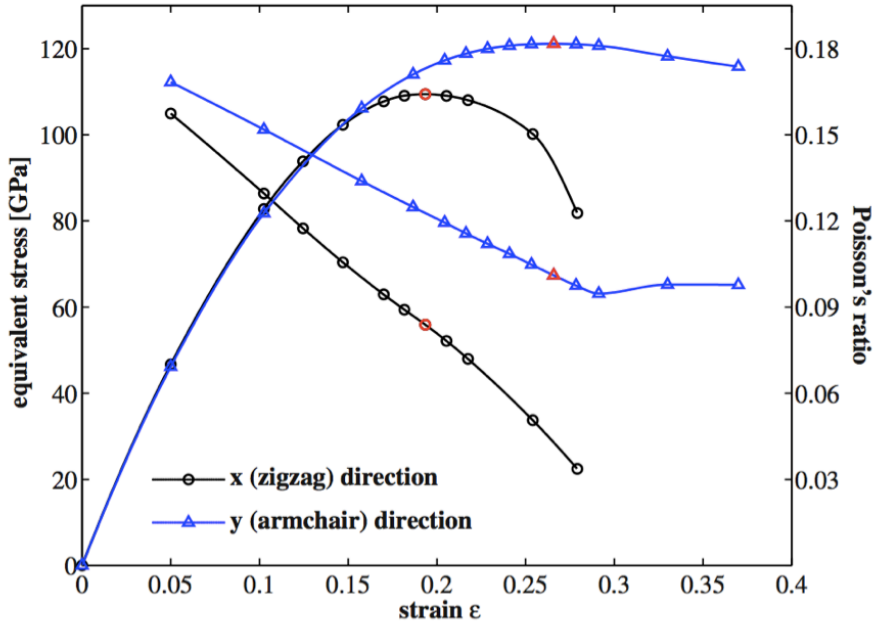

Figure 2.5: DFT calculation of stresses and Poisson ratios along both zigzag (circle) and armchair direction (triangle) against strain [74]

2.4.3.2 Molecular dynamic simulation

As opposed to first principle method, MD simulation utilized empirical potential function of atoms to evaluate the interaction forces among atoms under tension. Using Newton's law, the location and trajectory of atoms can also be obtained at each simulation step [76]. The molecular dynamic simulation is a transient simulation from which information can be extracted. To acquire the stress-stain relationship of graphene, a strain can be applied to edges of graphene sheets either in

the armchair or zigzag direction, and the stress can be retrieved directly. The capability of MD simulation depends on the potential function it uses, for example, the adaptive-intermolecular-reactive-bond-order-potential allows for covalent bond breaking and creation with associated changes in hybridization of atomic orbitals within a classical potential [77][78], enabling the simulation of ideal strength.

Figure 2.6 shows the stress-strain curve obtained from MD simulation [79]. The Young's modulus along armchair direction is 0.89TPa, and the stress reaches maximum at about 105GPa. The Young's modulus along zigzag direction is about 0.83TPa, and the stress reaches maximum at 137Gpa. The Young's moduli along different directions at small strain are just slightly different from each other. The softening of stiffness is also quicker in zigzag direction than in armchair direction as predicted by first principle calculation. The stress drops sharply after reaching the maximum strain, indicating fracture of graphene. The values obtained from MD simulation are considerably close to *ab initio* calculations.

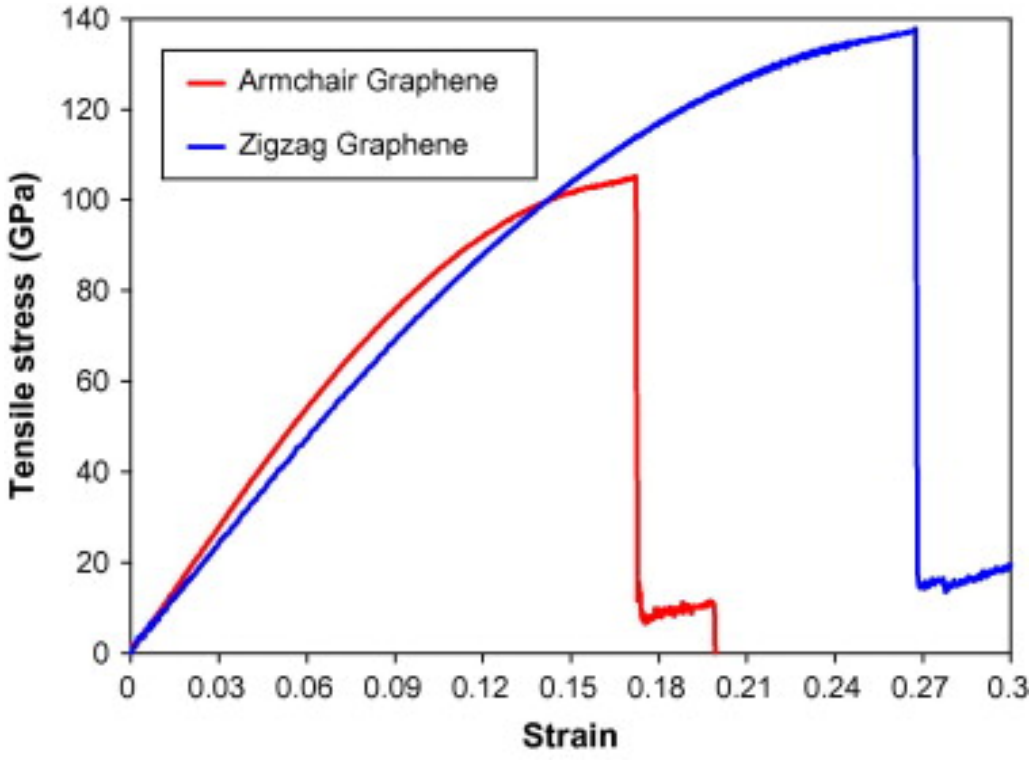

Figure 2.6: Stress-strain relationship of graphene from MD simulation [79]

Table 2.1: Lists of mechanical parameters of graphene calculated by DFT or MD simulation

Source method	Material	E_{2D} (N/m)	υ	σ_I (N/m)	D (N/m)
K.N. Kudin DFT [70]	Gr	345	0.149	-	-
X. Wei DFT [71]	Gr	348	0.169	39.5	-
F. Liu DFT [74]	Gr	350.7	0.186	36.74(zz*) 40.4(ar**)	-946.9(zz) -759.7(ar)
Q. X. Pei MD [79]	Gr	287.24	-	45.8(zz) 35.7(ac)	-
G. Kalosakas DFT & MD [78]	Gr	320.6	0.22	33±1(zz) 42±3(ar)	700(zz, DFT) -670(zz, MD) -670(ar, DFT) -560(ar, MD)

*zz, zigzag; **ar, armchair

To summarize the calculated mechanical parameters of graphene, some of the values from different sources are listed in Table 2.1 for comparison. It can be seen from the table that the in-plane stiffness of graphene is very well concentrated at around 350N/m. The stiffness along zigzag and armchair direction does not differ from each other very much, which justifies that the assumed isotropy of the continuum elastic model discussed previously. The ideal strengths are also very close to each other. The common phenomenon observed is that the ideal strength along armchair direction is larger than zigzag direction and indicates the third order modulus is higher along armchair direction. There is no surprise that the Young's modulus almost equals to that of carbon nanotubes (CNT) since CNT are just rolled-up graphene sheet [80][81].

2.4.4 Experimental results

2.4.4.1 Nano-indentation by tips of atomic force microscope

Nano-indentation has been a well-established technique for characterising materials' stiffness and other elastic parameters of either bulk material or suspended thin films [82][83]. For characterising suspended thin films, the tips of atomic force microscope (AFM) are popularly used as indenters due to their accurate positioning and precise application of force [84]. The nano-sized AFM tip radius ensures that the load can be modelled as point-load, which simplifies interpretation of the measured results. By applying a pre-set force on the tip whilst contacting film surface, AFM system

retrieves the deflection of the cantilever where the tip is located as well as the vertical displacement of the tip holder, so as to acquire a force-displacement relationship for mechanical properties calculation.

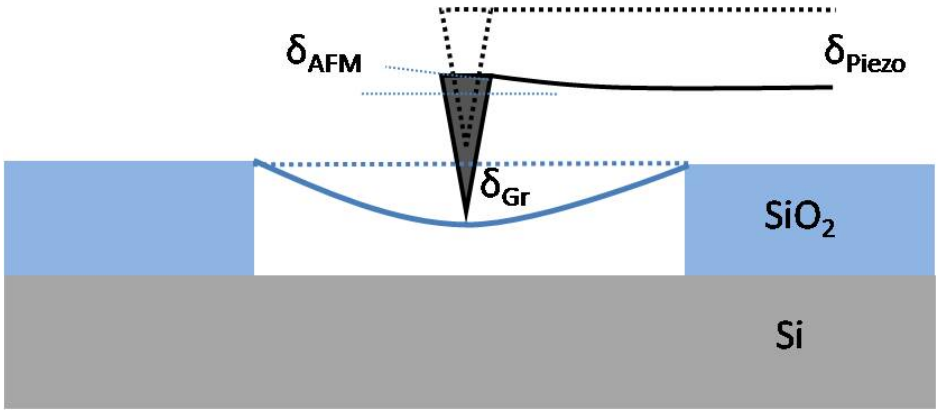

Figure 2.7: Illustration of nano-indentation with AFM tip

To perform the nano-indentation, the graphene sheet can be suspended in two forms, either doubly clamped bridge or round membrane clamped at its circumference [38] [35]. Figure 2.7 shows the schematic of AFM tip tapping on a suspended graphene sheet at its centre, when the force between tip and sample increases as the tip is moving downwards, both AFM tip cantilever and graphene bridge will deflect. One can easily obtain the relationship of the displacements as

$$\delta_{Gr} = \delta_{Piezo} - \delta_{AFM} \tag{2.20}$$

Where δ_{Gr} is the displacement of graphene sheet, δ_{Piezo} is the movement of AFM tip holder, and δ_{AFM} is the deflection of AFM tip cantilever. δ_{Piezo} and δ_{AFM} can be read from the AFM system to obtain the force with calibrated AFM cantilever size and Young's modulus, so as to deduce the relationship between graphene's deflection δ_{Gr} and the exerted force F.

C. Lee et al fabricated suspended graphene membrane by exfoliating and transferring graphene sheets onto pre-patterned holes and performed AFM tip nano-indentation [35]. Finite element analysis indicates that the force-displacement curve is insensitive to the radius of AFM tip when the tip radius r_{AFM} is much smaller than the radius of graphene disk r_{Gr}. The simulation also suggests that, as long as the tip is positioned within one tenth of graphene radius from the membrane centre, the force-displacement behaviour does not vary much. Such insensitity of indenting

graphene disk proves to be a notable advantage over indenting graphene bridge because it allows more operational margin. The relationship between the applied force and displacement of a suspended graphene disk can be approximated as

$$F = \sigma_0(\pi r_{Gr})\left(\frac{\delta_{Gr}}{r_{Gr}}\right) + E_{2D}(\boldsymbol{q}^3 r_{Gr})(\frac{\delta}{r_{Gr}})^3 \tag{2.21}$$

Where σ_0 is the build-in stress in graphene, and $\boldsymbol{q} = 1/(1.05 - 0.15\nu - 0.16\nu^2)$ is a dimensionless constant. If the Poisson ratio ν takes 0.165 of bulk graphite, $\boldsymbol{q}$ is about 1.02. Figure 2.8 show the force-displacement acquired from a graphene disk [35]. Using the equation 2.21 to fitting the acquired force-displacement curve. The 2D stiffness is approximated 342N/m, remarkably consistent with first principle calculations.

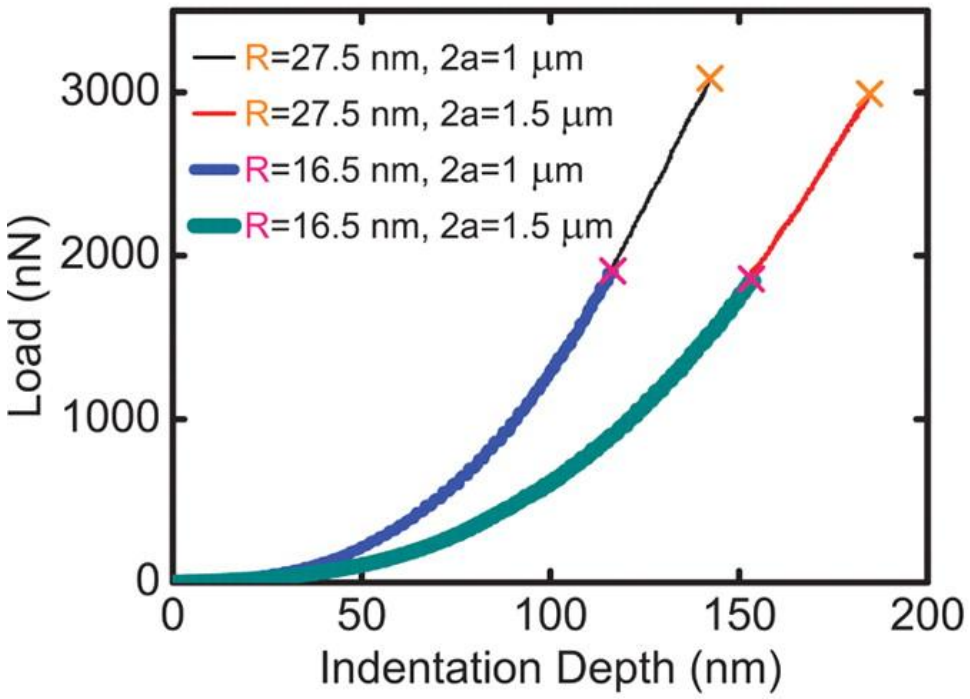

Figure 2.8: Indentation force against depth [35]. R and a in the figure denote r_{AFM} and r_{Gr}

The force-displacement curve of fracture test has also been conducted on those graphene disks. The break points are marked by crosses. As observed from the curve, the breaking stress only depends on diameter of AFM tip, but not the radius of graphene membrane. For a graphene disk clamped at its circumference, the maximum stress σ_m induced by a spherical tip pressing at the centre is a function of the applied point-load F.

$$\sigma_m = \left(\frac{FE_{2D}}{4\pi r_{AFM}}\right)^{\frac{1}{2}} \tag{2.22}$$

This is consistent with the observed inverse dependency of tip radius and breaking force in Figure 2.8. The breaking point occurs when $\sigma - \epsilon$ curve flattens, where $d\sigma/d\epsilon = E + 2\Theta\epsilon = 0$. Therefore, the maximum strain will be $\sigma_m = -E/2\Theta$ and maximum stress equals to $-E^2/2\Theta - E/2 = 55\ \mathrm{N/m}$ based on the experimental data in Figure 2.8. The solved value of the third-order elasticity Θ is about -690N/m，this value is remarkably consistent with *ab initio* calculations.

Similar indentation has been performed on suspended few layer graphene bridges fabricated in the same way but put across pre-patterned trenches [38]. E is derived to be about 0.5Tpa, lower than the above theoretical and experimental values, which are about 1TPa. The Young's modulus measured on suspended bridges tends to be inaccurate inherently, because the shape of the graphene bridge is not well defined. Moreover, the force-displacement curve is much more sensitive to the tip location on the suspended bridges [38].

2.4.4.2 Extracting information from graphene resonator

The implementation of graphene resonators does not only lead to various applications, but also provide another route to study the mechanical properties of graphene. The fundamental frequency of harmonic resonators follows the general rule of $f_0 \propto \sqrt{E/\rho}$, where f_0 is the fundamental frequency, and ρ is the mass density. With known ρ, detecting the fundamental resonance frequency allows deduction of Young's modulus. Graphene resonators can be actuated and sensed in several ways. Commonly applied techniques include thermal actuation by laser and optical detection [19], electrostatic actuation and electrical detection [36], or electrostatic actuation and optical detection [19], as shall be discussed in chapter 3. The inset of Figure 2.9(a) shows the optical image of a graphene resonator fabricated by mechanical exfoliation [19]. The graphene sheet has been put over a pre-patterned trench in SiO_2 layer. With the silicon substrate being used as back gate, the graphene sheet can be actuated electrostatically. For a doubly clamped graphene bridge under tension T_0, its fundamental frequency can be expressed as [85]

$$f_0 = \left\{ \left[A \left(\frac{E}{\rho} \right)^{\frac{1}{2}} \frac{t_g}{L^2} \right]^2 + \frac{A^2 0.57 T_0}{\rho L^2 W t_g} \right\}^{\frac{1}{2}} \tag{2.23}$$

Where ρ can use the value of graphite (2200kg/m^3), and A is a constant. For doubly clamped bridge, A takes the value of 1.03. The tension T_0 comes from various aspects including the fabrication process, the van der Waals force between graphene and substrates, and so on.

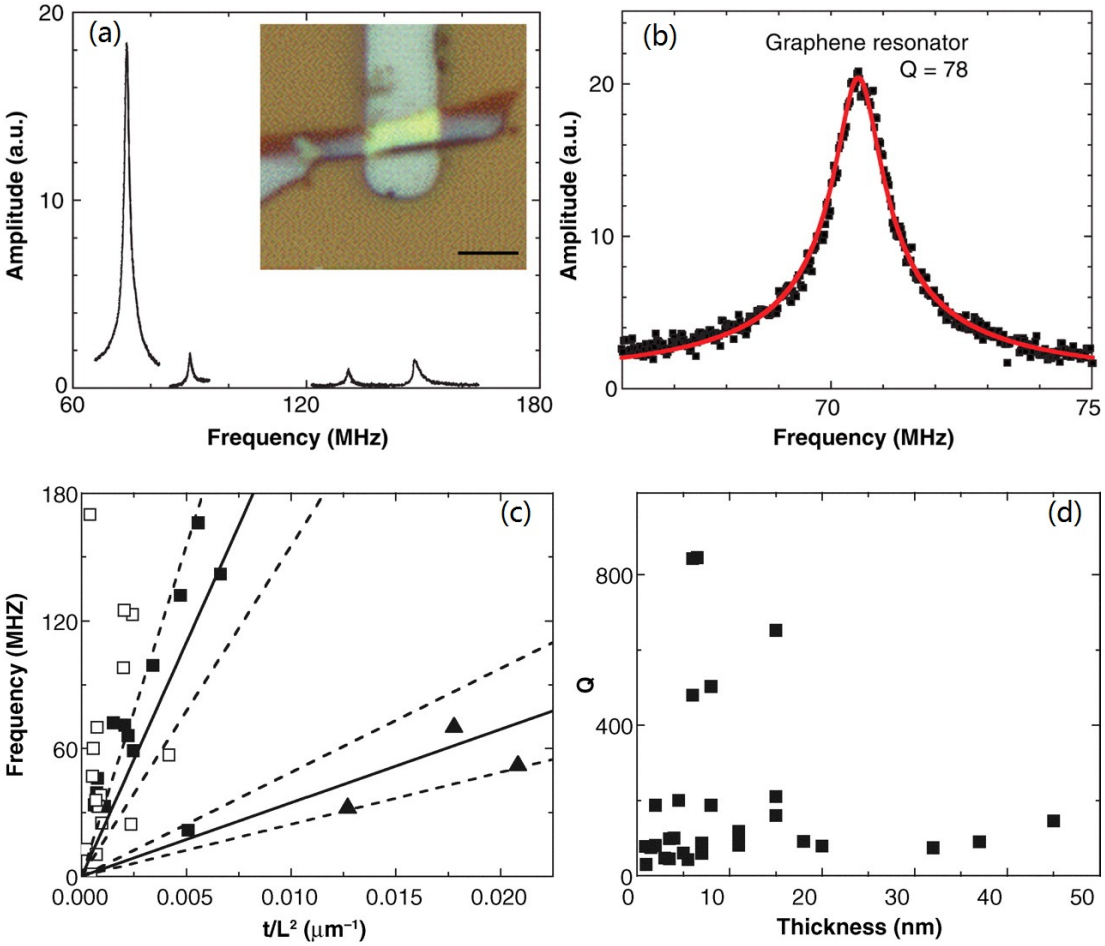

Figure 2.9: Measurement results of graphene resonators, adapted from [19]

Figure 2.9(a) shows the frequencies of a resonator actuated and detected optically [19]. Several peaks have been observed from the measured data. The lowest frequency peak at 75MHz is the fundamental frequency, and the corresponding quality factor is 210. A Lorentz peak fits experimental peaks very well, as can be seen from the fundamental frequency of a monolayer graphene resonator (see Figure

2.9(b)). The higher mode frequencies depend strongly on the geometry of the resonators. Due to the irregular shape of exfoliated graphene bridge, the higher mode frequencies are hard to interpret, in contrast to the measurement results as shall be discussed in chapter 6.

Figure 2.9(c) plots the measured fundamental frequencies of 33 resonators against t/L^2 [19]. The triangles represent cantilevers, which are out of concern of this chapter. The hollow squares represent double-clamped bridge resonators with $t <$ 7nm, while the solid squares represent resonators with $t >$ 7nm. The two dashed lines represent theoretical frequency calculation using equation 2.23, with the build-in tension assumed to be zero. The upper dashed line and lower dashed line enclosing the squares are calculated with Young's modulus of 0.5TPa and 1Tpa respectively. The solid line represents the calculated frequency for Young's modulus of bulk graphite (1Tpa), which fits the experimental the best. Thus it is plausible to conclude the Young's modulus of graphene is close to that of bulk graphite. As mentioned in the above section, measuring irregularly shaped graphene bridge is not very accurate.

2.5 Dynamic range and sensitivity

Dynamic range refers to the scope in which the vibration magnitude of a resonator responds linearly to the stimulus, which has been commonly used to characterise the performance of amplifiers and sensors [86][87]. Higher dynamic range is preferable for most applications such as mass sensors or RF devices. When the actuation intensity increases, the amplitude of resonance increases linearly up to a certain point and starts to cross over. Nonlinearity in resonator originates from different internal and external factors [88][89]. As pointed out in the previous section, the Hooke's Law only holds in small deformation range, otherwise the stiffness of the material softens under high stress, thus introducing nonlinearity. Moreover, for resonators actuated electrostatically, the electrostatic force induce between graphene and the substrate are normally assumed to be proportional to voltage difference, but in fact, the graphene will bend under the electrostatic force, thus the capacitance is variable, introducing another nonlinear term in the driving force. All the nonlinear terms will add to the driving and resilient force of the vibrating beam. Other sources for

nonlinearity include nonlinear damping, geometry, and so on. In general, the nonlinear motion of a resonator under a sinusoidal force can be described by the Duffing-equation [90]

$$M_{eff}w''(t) + \alpha w'(t) + M_{eff}\omega_0^2 w(t) + \beta w^2(t) + \gamma w^2(t)w'(t) = Fcos(\omega t) \tag{2.24}$$

Here $w(t)$ is the displacement, M_{eff} is the effective mass, α represents the damping coefficient, β is the cubit spring constant, and γ is the nonlinear dampling coefficient. $M_{eff} \approx 0.73M_{total}$ for the first mode. The onset of nonlinearity w_c is by convention defined at the 1dB compression point [91]. An analytical expression for w_c may be solved from the above equation by considering only leading order terms. For a rectangular resonator like suspended graphene bridge [87]

$$w_c = \omega_0 \frac{L^2}{\pi^2}\sqrt{\frac{\rho\sqrt{3}}{EQ}} \tag{2.25}$$

Which determines the upper bound of graphene resonator's linear response range [87]. Here, Q is the quality factor. The intrinsic lower bound of graphene resonator's response range is set by the thermal noise floor if the noise from other sources are omitted. Thermal noise refers to the thermal oscillation of a resonator without external excitation. The power density of thermal noise is expected to have the form

$$\boldsymbol{S}_x(\omega) = \frac{4\boldsymbol{k_B}\mathcal{T}Q}{M_{eff}\omega_0^3} \tag{2.26}$$

Following ref [87]. The DR is defined as

$$DR = 20\,log\frac{0.745w_c}{\sqrt{2\boldsymbol{S}_x\Delta f}} = 20\,log\left[0.367\frac{L^2(\omega_0)^{5/2}}{\pi^2 Q}\sqrt{\frac{\rho M_{eff}}{\boldsymbol{k_B}\mathcal{T}\Delta f E}}\right] \tag{2.27}$$

Here, Δf is the measurement bandwidth. Since $\omega_0 \propto \sqrt{E/\rho}\,/L^2$, the dynamic range is actually proportional $\sqrt{\omega_0^3}$. The dynamic range for the resonator in ref[19] is around 60dB, lower than NEMS resonators made from bulk material [87], mainly due to the small M_{eff} for ultimately thin graphene sheet. The extremely high surface area of graphene makes graphene resonators ideal for mass sensing.

Assuming that the absorbed substance does not couple strongly with the mechanical properties of graphene, the frequency shift caused by effective mass change of the graphene resonator can be expressed as [91]

$$d\omega = \frac{\partial \omega_0}{\partial M_{eff}} dm \approx \frac{\omega_0}{2M_{eff}} \delta m \tag{2.28}$$

So the mass sensitivity is

$$\frac{d\omega}{dm} \approx \frac{\omega_0}{2M_{eff}} \tag{2.29}$$

Based on this simple equation, one could expect ultra-sensitive mass sensors based on NEMS resonator due to their small dimension and low effective mass. The CNT resonator has even shown a remarkable 1yg (yg=10^{-24}g) sensitivity [92], ravelling the best sensitivity of 1zg (zg=10^{-21}g) in NEMS resonators [93], due to CNT's large Young's modulus and 1D nature. This sensitivity is inversely proportional to M_{eff}, while the dynamic range increases with M_{eff}. Thus, there is a trade-off between dynamic range and mass sensitivity. As a result, although smaller dimension leads to better sensitivity, the dynamic range is also compromised. In chapter 6, a possible way to overcome such constraint will be discussed, which is to look at higher order harmonics that has higher frequency for the same dimension.

2.6 Conclusion

In this chapter, the electrical and mechanical properties of graphene have been discussed. The most outstanding attributes graphene possesses are its large carrier mobility and ultrahigh Young's modulus. The experimentally obtained highest mobility in annealed freestanding graphene is as high as 200,000cm^2/Vs at room temperature, although an even higher mobility is predicted theoretically. These exceptional properties have their root in graphene's unique truly two-dimensional hexagonal lattice structure and electron band structure.

The conduction band and valence band of monolayer graphene at the K points at the corners of Brillouin zone touches each other. So, there is no bandgap in monolayer graphene and the Fermi level is located either in the conduction band or the valence band, therefore, monolayer graphene has been viewed as a semimetal. The point where the two bands engage is called Dirac point. When the Fermi level is tuned to

the Dirac point, the conductance of graphene is minimized. However, the conductance can never go to zero due to some quantum effect such as the puddles of electrons and holes unevenly distributed in graphene sheet. The energy dispersion near the K point is exactly linear, leading to massless electrons and holes travelling at a speed comparable to light speed. In real graphene devices, the electron mobility are limited by defects scattering, internal and external phonon scattering, as well as scattering by absorbents. Once the layer of graphene is increased to two or more, the conduction and valence band will split to two sub-bands and overlap for an amount proportional to the number of layers. This sharp change would lead to distinctive Raman feature in monolayer graphene and multilayer graphene, which is especially useful to confirm the monolayer graphene as will be seen throughout this thesis.

The Young's modulus of graphene has been theoretically studied with *ab initio* method and molecular simulations by various groups, which is found to be around 1TPa, similar to bulk graphite and carbon nanotubes. The experimental measurements comply remarkably well with the theoretical values. The large Young's modulus leads to higher frequency graphene resonators that could find applications in RF component and sensor. The true 2D nature of graphene makes the surface to volume ratio ultimately large, a very favourable properties for sensors. And also, the graphene sheet has low mass density, which, combined with large Young's modulus, could give the graphene resonators large dynamic range and sensitivity.

Chapter 3

Characterisation methodology

3.1 Introduction

In this chapter, the principles of Raman scattering will be introduced first, followed by the phonon properties of graphene. The phonon properties of graphene and its interaction with graphene's electron band structure as well as photons will be reviewed, so as to understand the origin of graphene's Raman peaks. The relationship between number of graphene layers and its Raman peaks will be established. The remainder of this chapter is allocated to the characterisation of graphene resonators, which is the focal point of this research. The two most popular techniques for the resonance measurement include optical method and electrical method, whose principles will be introduced. The advantages and disadvanges of both techniques will be elaborated. The technical implementation of electrical method will be analysed in depth, as it will be used to test the graphene resonators.

The characterisation of graphene involves many aspects ranging from the lattice structure determination, bandgap analysis, profiling, and optical imaging to the performance measurement of graphene devices. Novel characterisation methods are not only important for routine experiments but also sometimes lead to new discoveries, which is especially true for graphene. After all, it is the sophisticated design of a 300nm SiO_2/Si substrate that first enabled the swift examination of graphene under optical microscope [94], which triggered the development of graphene science. In this chapter, the characterisations are classified into two categories, the material characterisation and device characterisation. The material characterisation is apt to focus on the basic physical properties of graphene, such as lattice parameters, while device characterisation is more concentrated on the performance and behaviour of graphene devices, such as sensitivity. Yet, there has been no clear boundary of these two categories.

Various tools of specific function have been employed in the characterisation of graphene's physical properties. For lattice structural analysis, the x-ray diffraction

spectroscopy (XRD) is capable of resolving the lattice arrangement [95][96] by obtaining the image of diffracted x-ray beam, which corresponds to the reciprocal lattice of graphene and can be used to derive the lattice parameters [97]. In comparison, the transmission electron microscopy (TEM) appears to be more versatile, which can image either the real graphene lattice with a resolution of sub-nanometer [17][36] or acquire the reciprocal lattice image by adjusting the focus of electron beam. Both techniques can be used to decipher the lattice configuration in graphene. The scanning electron microscopy (SEM), on the other hand, provides a nanometer-scale examination of the shape of graphene and structural relationship to, if any, substrates [46][98]. The SEM image offers an effective route to observe the morphology of graphene when optical image cannot be obtained because of low contrast or resolution limit. The advantage of SEM is its large area of field and depth of field. Atomic force microscopy (AFM) is another tool for morphology measurement, which has a sub-nanometer spatial resolution, thus it has been commonly used to profile graphene devices and confirm the observation of other techniques [18]. To investigate the band structure or binding energy between carbon atom and other elements, the equipment involving photon-electron interaction should be employed. The x-ray photoemission spectroscopy (XPS) can be used to resolve the electron binding energy of atoms and radicals. Thus it is useful to analyse the functionalized graphene in terms of determining element types and relative quantity [99][100]. The angle resolved photoemission spectroscopy (ARPES) probes deep into the energy band structure of electrons in graphene, which could help to study the energy band of various forms of graphene [57]. The most straightforward yet most important optical characterisation technique will be introduced in chapter 5 where the experiments on making graphene visible on poly-Si film is presented.

In the research project of this dissertation, the Raman spectroscopy has been used extensively to identify the number of graphene layers and assess how integral the lattice is during fabrication processes. The Raman spectrum features are related to the graphene's defects, doping level, number of layers, stacking order, and so on [101][102], thus it provides a common denominator for monitoring the graphene's physical status non-destructively. Therefore, the first part of this chapter is devoted to the Raman features of graphene.

3.2 Principle of Raman spectroscopy

Raman spectroscopy is based on the inelastic scattering of light by crystal lattices or molecules [103]. The photons exchange energy with crystal or molecule vibration modes, accomplished with electrons being the medium. When light beam aims at substances, the electromagnetic wave of the light beam induces an electric dipole moment $\mathbb{P} = \mathbb{a}\mathbb{E}$ in the material. Here $\mathbb{a}$ is the polarizability of the material and $\mathbb{E}$ is the electric field of the light wave. The electric dipole moment will then exert electrostatic force on ionic core of atoms in the substance and exchange energy with vibration modes. The amount of energy the phonon can accept or release is quantized due to the quantization of phonon energy as shown in Figure 3.1.

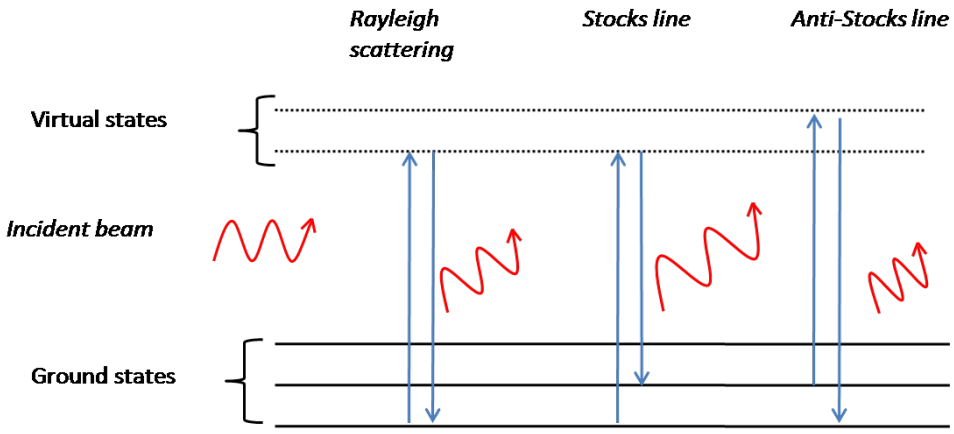

Figure 3.1: Interaction of phonon states and photon in Raman spectroscopy

The electric field of frequency ω excites the lower energy phonons to a higher virtual energy level. When the phonons relax back to a ground state, it will release the surplus energy by means of emitting light indirectly. Depending on the relative position of original and final state, the light emitted by the material comprises three parts as illustrated in Figure 3.1. If the phonon relaxes to exactly the same ground state that it has been actuated from, the scattered light has the same wavelength of the incident light (left part of Figure 3.1). Such process is called Rayleigh scattering, which is elastic and the photon gain or lose no energy. On the other hand, the phonon can either relax back to a higher (middle part) or lower (right part) energy level than the original one, absorbing or releasing an amount of energy $\Delta\mathcal{E}_p$, and the scattered light frequency will shift by $\Delta\mathcal{E}_p/\boldsymbol{h}$, where $\boldsymbol{h}$ is the Planck's constant. The lower

frequency component is called Stokes line, while the higher frequency one anti-Stokes line. The Stokes lines are usually more intensive than anti-Stokes line as it is more likely that the low energy phonons are excited to higher states. This inelastic scattering of light is called Raman effect which is named after the Indian scientist Raman for his discovery of such scattering mechanism. The frequency shifts of the scattered light exactly correspond to the vibrational energy states of the material under test. Thus, the Raman spectroscopy can be used to examine the vibrational properties of materials. In the earlier stage of Raman spectroscopy, the light source is filtered fluorescent beam or sunlight whose wavelength is far from monochromatic, thus limiting the resolution. Modern Raman systems incorporate one or more lasers as light source to achieve high resolution.

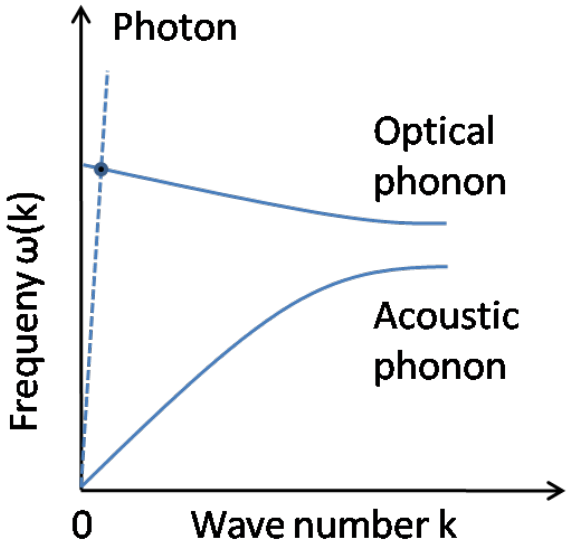

Figure 3.2: Schematic drawing of phonon and photon dispersion curve

The phonon modes that can interact with the laser excitation should comply with Raman selection rule complementary to infrared absorption selection rule. Only those vibrational modes that change polarizability α under vibration are Raman active [104]. When one considers the scattering of photon by lattice waves or phonons, their interaction should also satisfy both energy and momentum conservation laws. Figure 3.2 shows the schematic view of phonon and photon dispersion curve. Only the phonon at the intersecting point (round dot), where the phonon and photon have the same momentum and energy, can be detected by Raman spectroscopy.

3.3 Raman features of graphene

3.3.1 Phonon dispersion of graphene

The unique lattice structure of graphene does not only lead to its exceptional electronic properties but also other fascinating attributes. Due to the combination of strong C-C bonds and light mass of carbon atoms, the acoustic phonon velocity or sound velocity in graphene is extremely fast, which is responsible for the record high thermal conductivity of graphene [105][106][107]. Such thermal conductivity, together with graphene's electric properties, accredits graphene the potential to solve the thermal dissipation problems faced by current IC technology. The optical phonons, on the other hand, are hallmarks of graphene in Raman spectroscopy. Since the phonon modes highly depend on the lattices structure, any defects or disorder will manifest themselves through phonon modes, which are detectable by Raman spectroscopy.

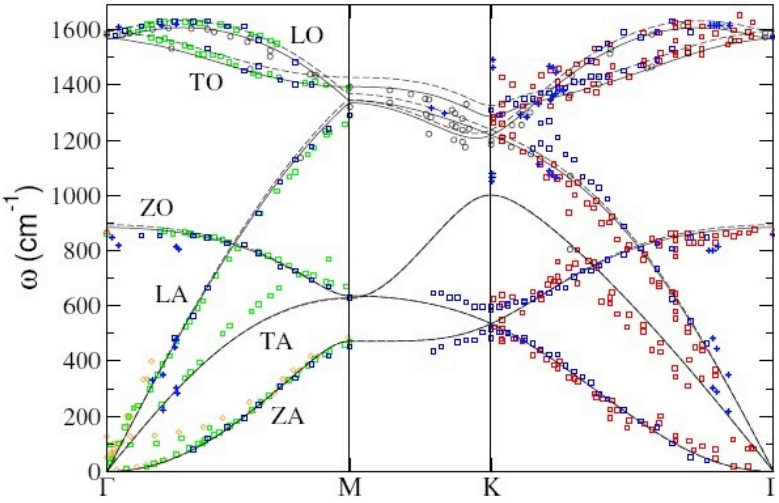

Figure 3.3: Phonon dispersion curve of graphene, adapted from [108]

To understand the Raman spectrum of graphene sheets, it is a prerequisite to solve the phonon dispersion curve. Figure 3.3 shows the *ab initio* calculation of the phonon dispersion curve of graphene as well as data points obtained by different experimental methods including x-ray scattering [109], neutron scattering [110], infrared absorption [111], Raman spectroscopy [112], and electron energy loss spectroscopy (EELS) [108][113][114]. Graphene lattice vibration modes contain six

branches. The phonon dispersion curves include in-plane optical branches (O) and acoustic branches (A). According to the vibrations parallel with or perpendicular to the C-C bond directions, the phonon branches are conventionally classified as longitudinal (L) and transverse (T) phonon modes. Moreover, the transverse vibration modes can also be out-of-plane (Z). Therefore, there are totally six phonon branches labelled as TO, LO, ZO, TA, LA, and ZA in Figure 3.3. As stated in the above section, only the degenerated LO and TO phonon at the Brillouin zone centre Γ is Raman-active in principle as required by the momentum and energy conservation. Nevertheless, more delicate and complex coupling mechanism may come into play and lead to the phonon near K point being detected, as will be discussed in the following section. A better explanation as to which phonon should be Raman-active could be justified by the group theory [99][112].

3.3.2 Raman spectrum of monolayer graphene

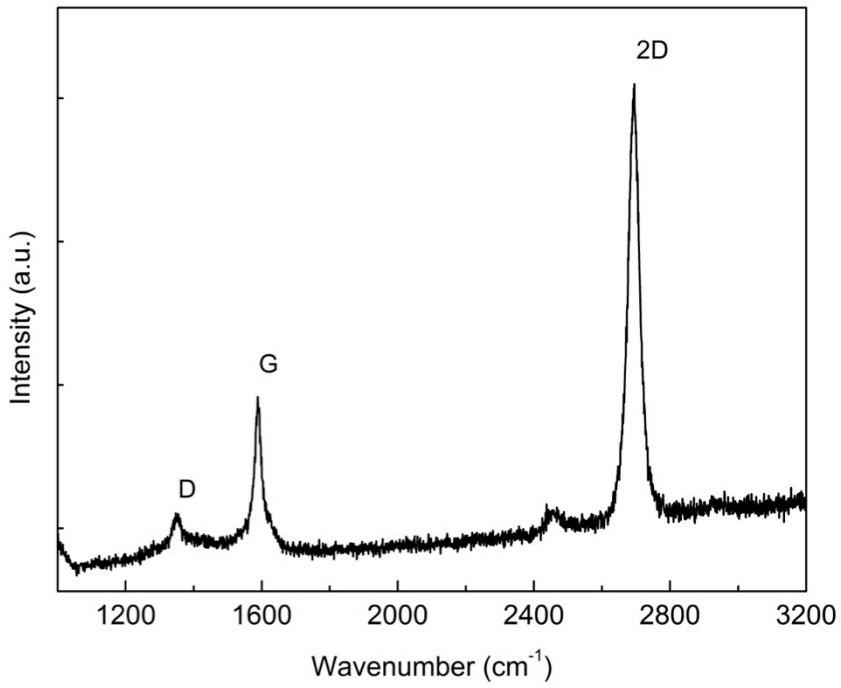

Figure 3.4: Typical Raman spectrum from one of the exfoliated graphene samples

Without further clarification, all Raman spectrum discussed in this dissertation have been taken with the Renishaw inVia Reflex Raman system with 514nm wavelength. Figure 3.4 shows the Raman spectrum taken on a graphene flake exfoliated from kish

graphite (Grade 300, Graphene Laboratories, Inc) and patterned into strips with methods to be discussed in chapter 7. Not surprisingly, Raman spectrum contains two characteristic bands, the G band and 2D band, which lie at ~1580 and ~2710 cm^{-1} respectively with 514 nm laser illumination, consistent with Raman spectrum of pristine graphene [115]. When there are defects in graphene, a D band will turn up at around 1350 cm^{-1}. The assignments of these bands have undergone a long debate. From molecular viewpoint, the G band is attributed to the stretching of sp^2 bonds, corresponding to the degenerated TO and LO phonon branches near Γ point in Brillouin zone, while D band is believed to come from the breathing modes of the hexagonal ring of carbon atoms near K point [101][116][117]. The ground for such assignment is the fact that the two bands are also observed in all poly-aromatic hydrocarbons [117][118]. However, such process violates the aforementioned Raman selection rule and the 2D band has a Raman shift almost double the D band, blurring the interpretation of these two bands.

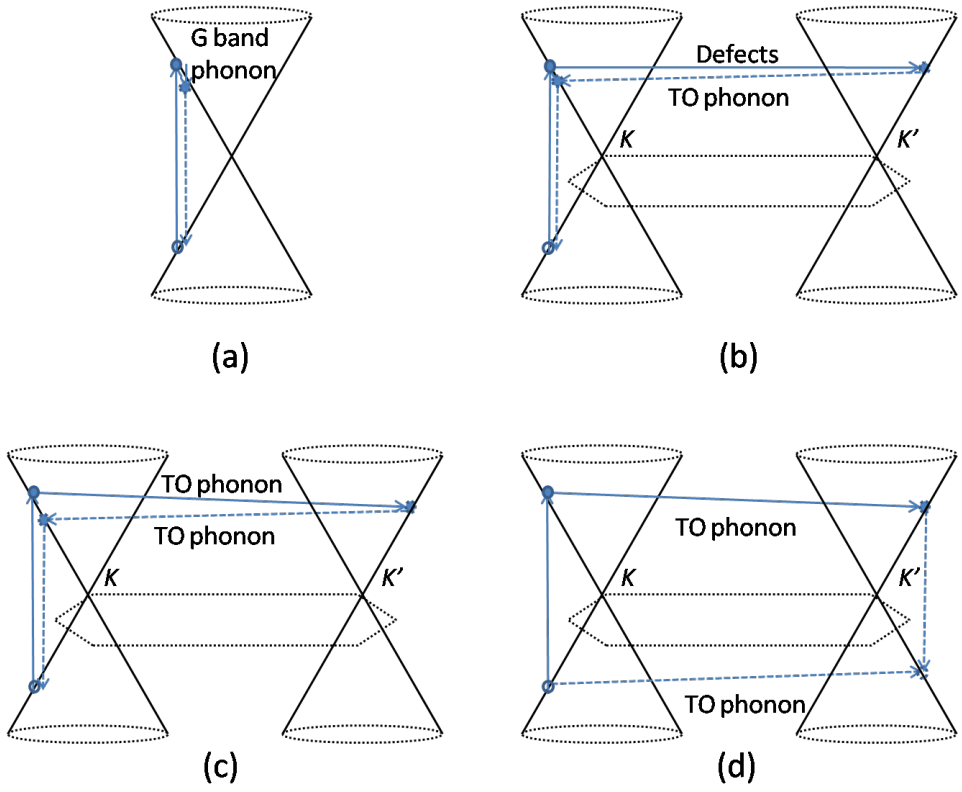

Figure 3.5: Illustration of double resonance process

Therefore, another explanation has been proposed that the appearance of D and 2D bands involves second-order process that allows usually Raman-inactive phonons

around K points to be detected [119]. Figure 3.5 shows the photon scattering mechanisms of G band (a), D band (b), and 2D band (c, d) in graphene. G band is the only ordinary first order process where an electron is excited to conduction band by the photon, losing some energy to the degenerated LO or TO phonon, then relax back to the valence band. The rest of the two bands, D and 2D, are associated with double resonant process where Graphene's unique cone shape band structure plays an important role in their activation and manifestation. The D band process is associated with one defect and one phonon. An excited electron near K point may be elastically scattered to the adjacent K' point in the Brillouin zone by a defect, and then it is scattered back by a phonon with energy exchange, and finally recombine with a hole and release the energy by means of light emission. This mechanism agrees with the experimental phenomenon that D band only turns up in graphene with defects, or on graphene edge where the periodical lattice terminates.

The 2D band involves two phonons (Figure 3.5(c)). The excited electron around K point is scattered forth to and back from around the K' point both by two TO phonons, unlike a defect playing a role in the D band process. In such Raman process, only electrons are scattered between adjacent conduction bands. Nevertheless, the holes can also be scattered by phonons, which causes the triple resonance Raman process as shown in Figure 3.5(d) [120]. The hole initially created by the laser photon can also be scattered to the valence band around K' point, and the electron can recombine with it after being scattered to around K' point. The triple resonance process also contributes to the 2D band of graphene's Raman spectrum. The amounts of energy exchanged in both approaches are the same, which equal to two TO phonons' energy. That is why the 2D band always exists even without defects, and the wavelength of 2D band always double that of the D band, consistent with observed Raman spectrum. It would appear that all the phonon branches could be activated in the double resonance or triple resonance process, in contrary to only D band is observable, however, this is not the case. The in-depth physics is out of the scope of the thesis. More detailed discussion can be found in [121].

Due to the strong association of second order processes with graphene's cone shape electron band structure, the Raman shifts of D and 2D band would depend on the laser energy. With larger laser photon energy, the valence band electron will be

excited to a higher conduction band, with larger momentum. Therefore, to scatter such electron between adjacent K point and K' point, a larger phonon momentum is required. From Figure 3.3, it is shown that the TO phonon around K point is symmetric and the energy measured from the K point is linearly dependent on its momentum. It has been experimentally confirmed that both D band and 2D band frequencies upshift linearly with increasing laser energy. The slope of $\partial k_{2D}/\partial \mathcal{E}_{laser} = 50$ cm^{-1}/eV [102], and for 2D band $\partial k_{2D}/\partial \mathcal{E}_{laser} \approx 100$ cm^{-1}/eV [122][122][123].

Besides the peak existence and location, the intensity ratio of D band and G band $I(D)/I(G)$ provides information about the quality of the graphene. When studying the Raman spectrum of graphite, Tuinstra and Koening first established and relationship between the average grain size L_a and the intensity ratio as follows [116].

$$\frac{I(D)}{I(G)} = \frac{C(\lambda)}{L_a} \tag{3.1}$$

where $C(488nm) \approx 4.4nm$. Using XRD data as reference and integrated areas ratio instead of the above peak intensity ratio, Cançado et al empirically obtained a general equation for $C(\lambda)$ [124], which states

$$C(\lambda) = 2.4\times10^{-10}\lambda^4 \tag{3.2}$$

3.3.3 Raman spectrum of multiple layer graphene

Just as the dependence of graphene's band structure on its thickness, the Raman peaks also evolve with increasing number of graphene layers because of the involvement of electron band structure in double resonance process. As stated in chapter 2, the band structure of double layer graphene differs from that of monolayer graphene, the valence and conduction orbits split into four orbits, usually labelled as π_1^*, π_2^* and π_1, π_2 respectively. The electron-hole pair can be excited between $\pi_1^* \rightleftharpoons \pi_1$ or $\pi_2^* \rightleftharpoons \pi_2$. By interacting with phonons, the conduction band electrons will be knocked to π_1^* or π_2^* band around the adjacent K' point. With the double resonance mechanism in mind, it is fair to postulate that the double resonance process takes four routes.

Figure 3.6 schematically shows the four possible excitation of electrons and their interaction with phonon. The four processes are labelled as P_{11}, P_{12}, P_{21}, and P_{22} respectively. Thus, the 2D band contains four closely located peaks. Figure 3.7 (b) shows the Raman 2D band of a double layer graphene sheet. The 2D band is clearly asymmetric and could be fitted by four Lorentz peaks (green lines) plotted below the 2D band, while the 2D band of a monolayer graphene could be fitted very well by a single Lorentz peak (Figure 3.7 (a)).

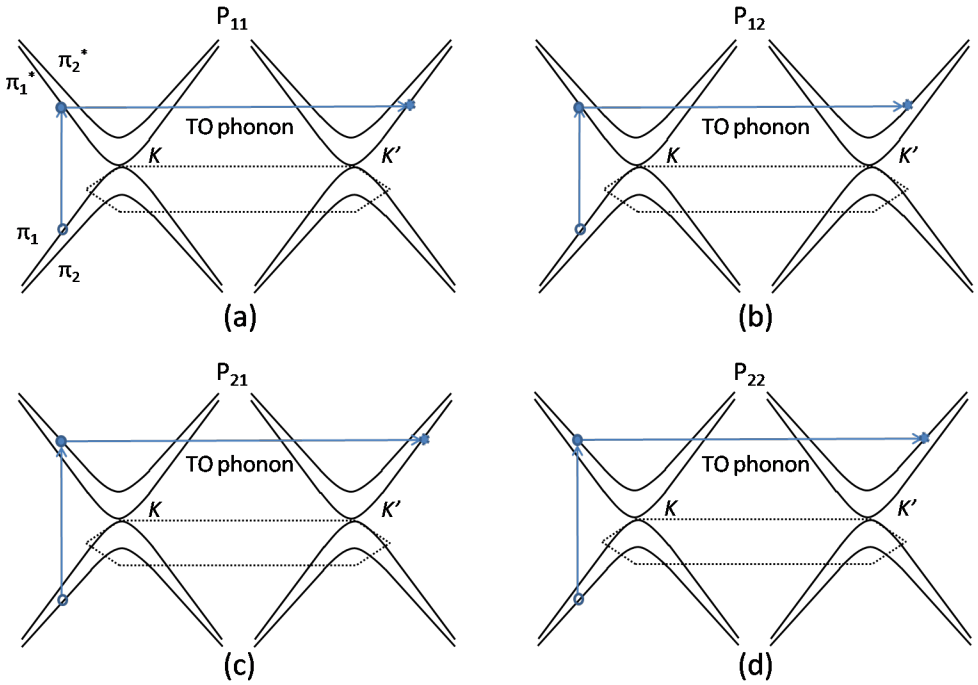

Figure 3.6: Double resonance in double layer graphene

For more than two layers of graphene, the band structure gets more complicated and more Raman peaks will be allowed. For example, in triple-layer graphene, the number of allowed Raman peaks in 2D band is 15 [102]. Comprehensive analysis of the allowed Raman peaks in multi-layer graphene can be approached from the symmetry analysis of lattice, electron and phonon. Such analysis turns out to be impractical to be verified experimentally, since four Lorentz peaks together are capable of fitting almost all shape of Raman bands and it is impossible to distinguish all the individual peaks. Figure 3.7 (a) shows the 2D band of bulk graphite, which can be fitted by just two peaks (green lines). It has been shown that the number of layers can be distinguished from the 2D band for up to 4 layers [125]. From 5-layer

on, the 2D band becomes almost indistinguishable from highly ordered paralytic graphite (HOPG). These bands provide reference for identifying the number of layers under 4. For G band, the line shape does not change much with number of layers, however, the peak of monolayer graphene shifts to higher wavenumber, because of the combination of self-doping and higher frequency of Raman active phonon due to mode splitting [102].

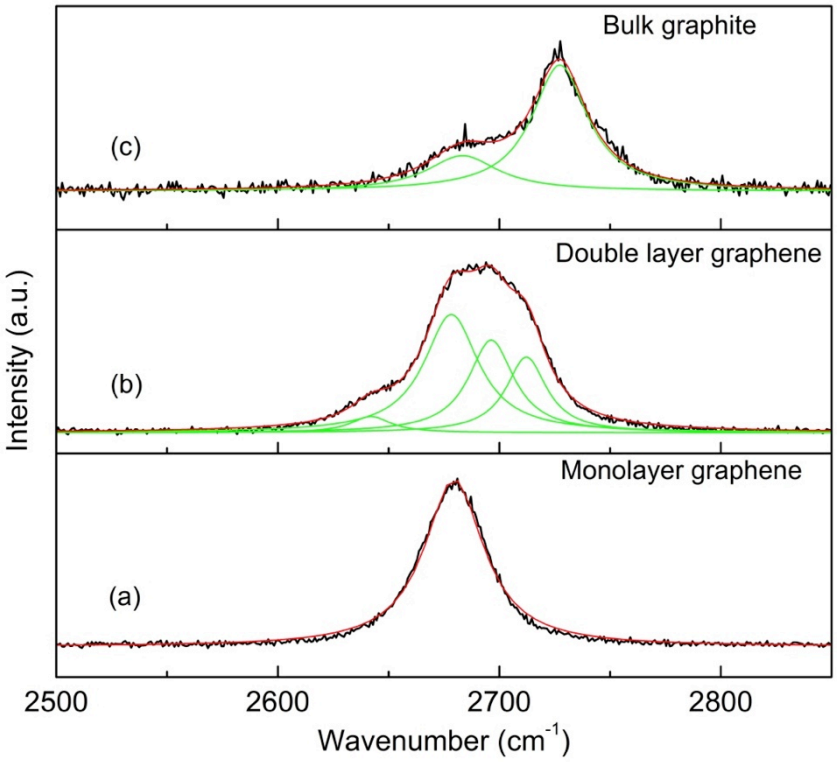

Figure 3.7: 2D band of Raman spectrum for monolayer, double layer, and bulk graphite from exfoliated graphene samples

3.4 Frequency characterisation of graphene resonators

The characterisation of graphene resonator's frequency and associated parameters have been challenging due to its unique physical properties. First, the resonant frequency of graphene is normally quite high because of its low mass density and unparalleled stiffness, surpassing the measurement scope of most ordinary measurement instruments. Moreover, the light transmission rate of graphene is as high as 97%, almost transparent, thus detecting the dim reflected light from graphene surface is very complicated. The measurement of graphene resonator can be divided

into two portions, namely the actuation and the detection. The actuation techniques include thermal actuation, electrostatic actuation, while the detection can be based on the conductance change of the graphene resonator upon resonance or the angle change of light reflection by graphene's basal plane. Any characterisation could be a combination of an actuation method and a detection method as long as they are compatible. In this section, two of the popular characterisation techniques for graphene resonator measurement will be introduced. One is optical approach that uses laser beams to realize the thermal actuation and light reflection detection, while the other route is by electrostatic force actuation and conductance change detection.

3.4.1 Optical setup for measurement

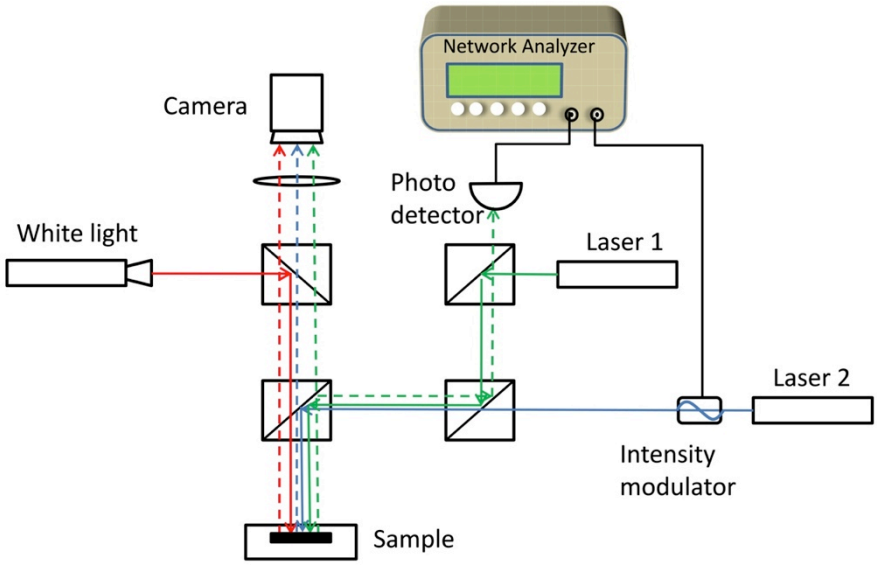

Figure 3.8: Optical characterisation setup based on thermal actuation and interference detection

Figure 3.8 shows a typical setup to detect the resonant frequency of graphene resonators. Both actuation and detection utilize laser beams, but in different ways. The actuation laser beam passes an intensity modulator, through which the beam intensity can be adjusted, so as to modulate the actuation signal onto the laser beam. The laser beam heats up the graphene sheet, thus inducing thermal stress and stimulating the graphene sheet into resonance. Another laser beam is equipped to detect the resonance. The detection beam from the laser is coupled through prisms to focus on the graphene sheet. The reflected light is collected and detected by a photodiode. When the graphene is vibrating, the reflected light changes its direction,

as well as the output of photodiode. The intensity modulation and the monitoring of photodiode output are both accomplished by a network analyser.

The advantage of this measurement setup is that the measured results are easier to interpret, as there are no spurious peaks from electronic components. The frequency range that can be measured with the optical setup reaches at least 200MHz [19]. And also, the optical measurement is less demanding as no electrical connection is required. The drawback of this set up is as obvious as its advantages. All the optical tools have no way to be integrated in chip scale, as the diffraction effect hinders the scaling down of the feature sizes of optical components. Hence the electrical measurement technique has been developed.

3.4.2 Electrical characterisation of graphene resonators

To enable electrical measurement, the graphene resonator requires its two ends to be electrically connected, as well as a gate electrode so as to apply the electrostatic force. Figure 3.9 schematically shows the structure and equivalent electric circuit of a graphene resonator fabricated with sacrificial layer technique to be discussed in chapter 5. The silicon substrate has been used as the back gate. C_s, C_d, and C_{Gr} represents the capacitance between the source electrode, drain electrode, graphene sheet and the silicon substrate respectively.

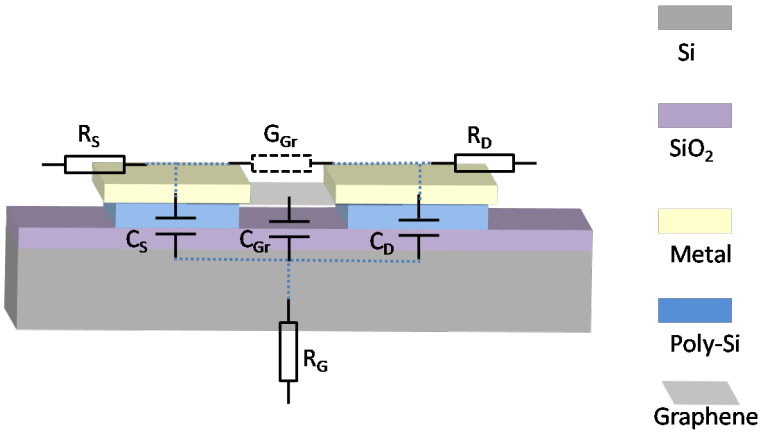

Figure 3.9: Schematic drawing of a graphene resonator with metal electrodes. The silicon substrate is used as back gate, and the two metal pads are used source and drain electrode respectively

To induce an electrostatic force on the graphene sheet, the source electrode can be grounded, and a voltage $V_a = V_{DC} + V_{AC}(\omega t)$ is applied to the gate. The DC

component V_{DC} is included to adjust the static stress in the graphene sheet so as to tune the frequency of the resonators as will be discussed in chapter 6. The AC component $V_{AC}(\omega t)$ of frequency ω is used to drive the graphene sheet into resonance. Then the electrostatic force exerted on graphene sheet can be expressed as

$$F = \frac{1}{2}C'_{Gr}(V_{DC})^2 + C'_{Gr}V_{DC}V_{AC}(\omega t) \tag{3.3}$$

Where C'_{Gr} is the differentiation of C_{Gr} with respect to the vertical distance between graphene and the substrate. When the graphene sheet vibrates, the distance between graphene and the substrate is varying, so is the capacitance

$$C_{Gr} = C_{Gr0} + C'_{Gr}dz \tag{3.4}$$

Where C_{Gr0} is the static capacitance. With higher order non-linear terms omitted in small deflection regime, C'_{Gr} can be treated as a constant approximately.

3.4.3 Current mixing and resonance detection

Although the electrostatic actuation seems straightforward, the detection of the resonance is not. Assuming a source-to-drain voltage V_{sd} is applied between the two ends of the graphene sheet, the amplitude of the current flowing through the graphene will be modulated by the resonance of the graphene sheet, because the conductance of the graphene resonator changes with vibration. The conductance change originates from two aspects, the electrostatic charge concentration change and the piezoresistive effect. The charge induced in the graphene sheet is related to the electrostatic voltage V_a as well as the capacitance C_{Gr}

$$\begin{aligned}\boldsymbol{Q}_{Gr} = V_a C_{Gr} = V_{DC}C_{Gr0} + V_{DC}C'_{Gr}dz + V_{AC}(\omega)C_{Gr0} \\ + V_{AC}C'_{Gr}dz\end{aligned} \tag{3.5}$$

Upon resonance, the charge carrier concentration change can be expressed as

$$d\boldsymbol{Q}_{Gr} = V_{DC}C'_{Gr}dz + V_{AC}(\omega)C_{Gr0} + V_{AC}C'_{Gr}dz \tag{3.6}$$

And the total conductance of the graphene sheet is

$$\begin{aligned}G_{Gr} = G_{Gr0} + \frac{dG}{d\boldsymbol{Q}_{Gr}}(V_{DC}C'_{Gr}dz + V_{AC}(\omega)C_{Gr0} \\ + V_{AC}(\omega)C'_{Gr}dz) + \frac{dG}{dz}dz\end{aligned} \tag{3.7}$$

Where, G_{Gr0} indicates the intrinsic conductance of the graphene sheet with no gate voltage induced charges. $dG/d\boldsymbol{Q}_{Gr}$ is the dependence of conductivity on the charge density, and dG/dz is the dependence of conductivity on the strain of the graphene sheet, or equivalently the piezoresistive effect. If a constant voltage is applied to the drain electrode of the graphene resonator, the current flowing throw the graphene is

$$I_{Gr} = V_{sd}G_{Gr} = V_{sd}G_{Gr0} + V_{sd}\frac{dG}{d\boldsymbol{Q}_{Gr}}V_{DC}C'_{Gr}dz + V_{sd}\frac{dG}{d\boldsymbol{Q}_{Gr}}V_{AC}(\omega t)C_{Gr0} + V_{sd}\frac{dG}{d\boldsymbol{Q}_{Gr}}V_{AC}(\omega)C'_{Gr}dz + V_{sd}\frac{dG}{dz}dz \tag{3.8}$$

There are three terms, i.e. the second, fourth and fifth term, whose amplitude is proportional to the deflection of the graphene sheet. The fourth term actually contains a DC component and a 2ω component due to multiplication of two triangular functions, whose amplitudes correspond to the deflection of the graphene sheet. Nevertheless, direct measurement of the DC component poses great challenge because of the noises from various sources. Both the second and fifth term have a relatively high frequency of ω, however, it is still impractical to detect these signals. As shown in the equivalent circuit in Figure 3.9, the parasitic capacitance together with graphene's own resistance form a low pass RC filter, dramatically limiting the bandwidth of the graphene resonator and attenuates the higher frequency signal. To make sure the small current signal is not affected by the parasitic low pass filter, one could replace the constant V_{sd} with an AC voltage at frequency $\omega + \Delta\omega$, which will then mix with the ω components in equation 3.8, so that there will be a signal of low frequency $\Delta\omega$ whose amplitude is proportional to the resonance amplitude.

$$I_{Gr}(\Delta\omega) \propto V_{sd}(\omega + \Delta\omega)\frac{dG}{dQ_{Gr}}V_{DC}C'_{Gr}dz + V_{sd}(\omega + \Delta\omega)\frac{dG}{dz}dz \tag{3.9}$$

The frequency difference $\Delta\omega$ is normally so low that it does not attenuate after passing the parasitic low pass filter. However, to extract the signal at $\Delta\omega$ from noises, a lock-in-amplifier must be used.

3.4.4 Lock-in amplifier

Lock-in amplifiers are used to detect and measure extremely weak AC signals immersed in intensive noises. It is equivalent to a band pass filter with ultra-narrow

bandwidth. To extract the signal from noises, the lock-in amplifier requires a reference wave with the same frequency of the to-be-measured AC signal. Figure 3.10 shows the block diagram of lock-in amplifier. The core of a lock-in amplifier is a phase-sensitive detector (PSD), which is just a multiplier that produces the product of the reference signal and the input signal. The output of the PSD is

$$\begin{aligned} V_{PSD} &= V_s V_r \sin(\omega_s t + \theta_s)\sin(\omega_r t + \theta_r) \\ &= \frac{1}{2} V_s V_r \cos\big((\omega_s - \omega_r)t + \theta_s - \theta_r\big) \\ &\quad - \frac{1}{2} V_s V_r \cos\big((\omega_s + \omega_r)t + \theta_s + \theta_r\big) \end{aligned} \tag{3.10}$$

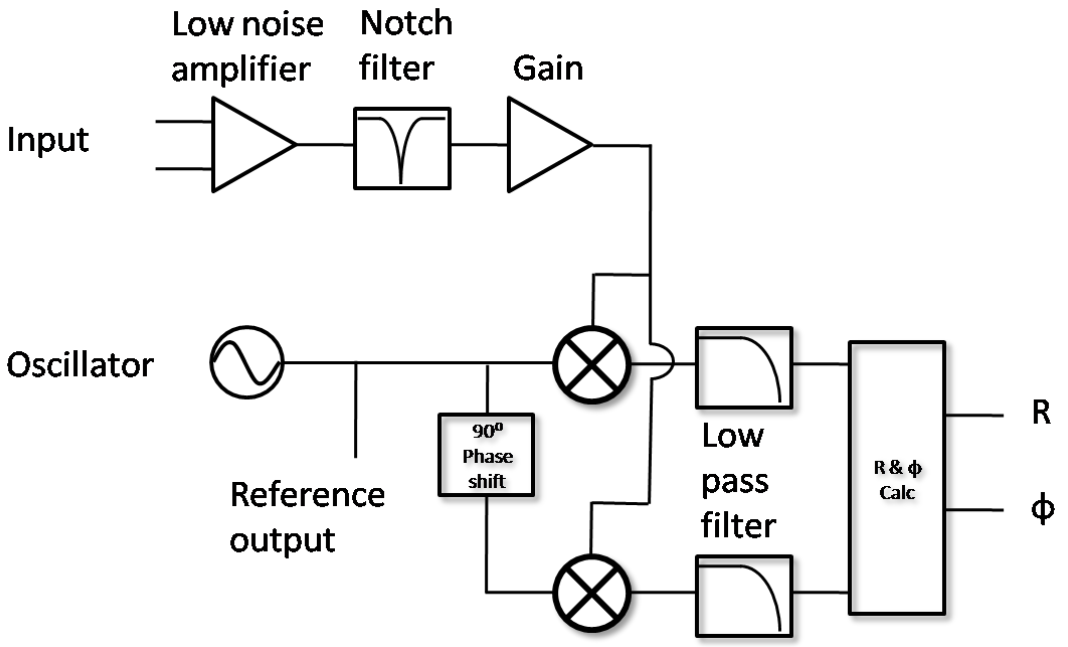

Figure 3.10: Block diagram of lock-in amplifier

The subscripts s and r represent signal and reference respectively. The output of the PSD is filtered with a low pass filter, and the AC signal will be attenuated to an extent depending on the roll-off rate and cut-off frequency of the filter. If the signal frequency equals the reference frequency, the output of the filter will be a DC signal proportional to the signal.

$$V_{PSD} = \frac{1}{2} V_s V_r \cos(\theta_s - \theta_r) \tag{3.11}$$

So, the output of the PSD is determined by the phase difference between the reference and the signal. To detect the magnitude of the signal, another PSD can be incorporated, and its reference is phase shifted by $\pi/2$, so

$$V_{PSD'} = \frac{1}{2} V_s V_r \sin(\theta_s - \theta_r) \tag{3.12}$$

Then the magnitude of the signal can be obtained as

$$V_s = 2\sqrt{{V_{PSD}}^2 + {V_{PSD'}}^2}/V_r \tag{3.13}$$

With known reference voltage, the magnitude of the signal can be obtained. The cut-off frequency of the low pass filter is determined by the time constant. The noise away from the to-be-measured frequency by a distance equal to half the cut-off frequency of the low pass filter will be attenuated extensively. So the time constant determines the equivalent noise bandwidth (ENBW). To reduce the noise and enlarge the signal to noise ratio, a larger time constant is preferred for the low pass field. However, with large time constant, the amplitude of the signal needs more time to build up at the output of the low noise amplifier. Thus, there is trade-off between data acquiring speed and signal to noise ratio.

3.4.5 Measurement configuration

As elaborated above, the measurement of the graphene resonator requires two different signals of ω and $\omega + \Delta\omega$. The $\Delta\omega$ component should also be sent to the PSD of lock-in amplifier as a reference. The implementation of the current mixing could be conducted with one-source setup or two-source setup. The one-source setup needs only one signal generator to produce the two frequencies by modulation [126]. Both frequency modulation (FM) and amplitude modulation (AM) can be used since they can both produce the frequency spectrum required (Figure 3.11(a)). The modulated signal is applied to the drain of the graphene bridge which, upon resonating, mixes the frequency components. This setup is relatively easy to be implemented. However, The amplitudes of the two frequency components are correlated and cannot be adjusted independently. The electrostatic force along the graphene is uneven due to the voltage drop across the graphene sheet. The uneven voltage will induce inhomogeneous electrostatic actuation force which results in the

activation and enhancement of second resonance mode, which is of great academic and practical value as will be discussed in chapter 6 in detail.

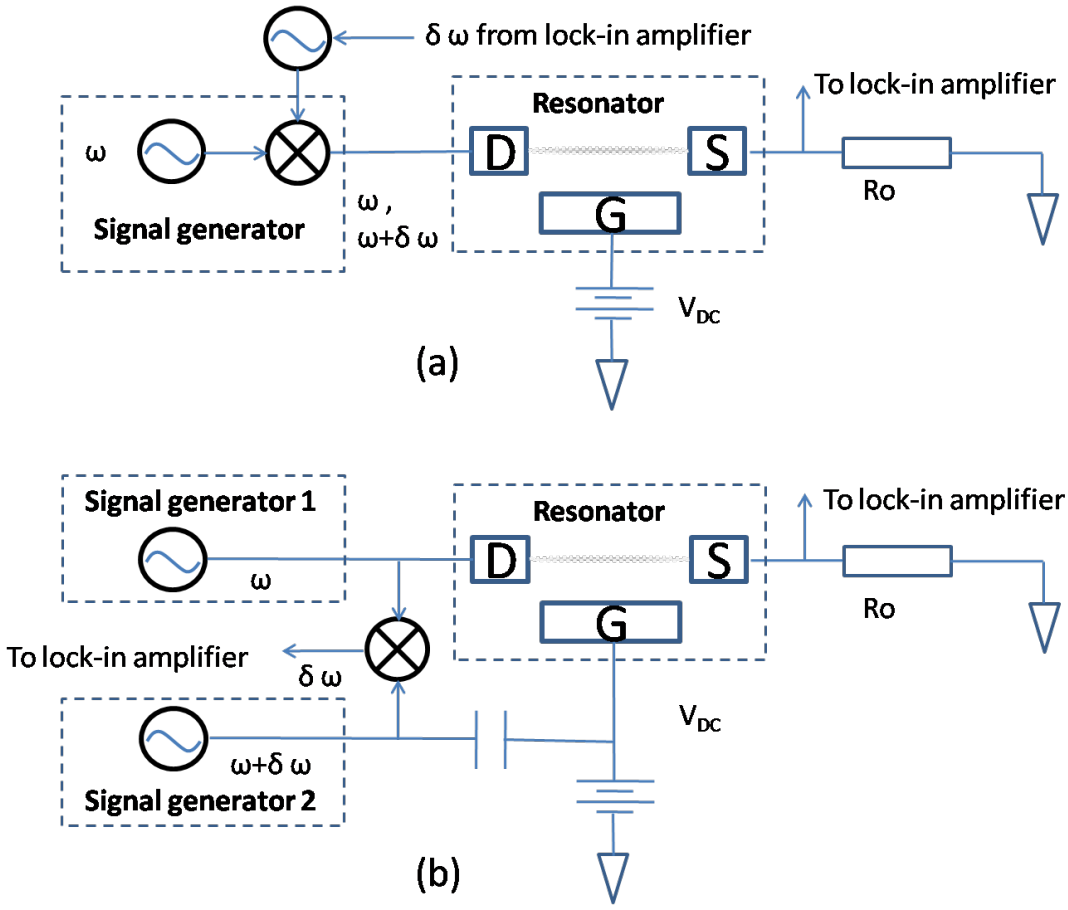

Figure 3.11: Schematic circuit diagram of one-source (a) and two-source measurement setup for electrical characterisation of graphene resonators [36][126]

In the two-source set up (Figure 3.11(b)) [36], two signal generators output ω and $\omega + \Delta\omega$ separately. One is applied on the gate to drive the resonance into resonance, while the other one is fed to the drain electrode. The two signals are also synthesized by RF mixer to generate the $\Delta\omega$ reference signal for the lock-in amplifier. The advantage of this setup is that the actuation voltage is applied uniformly on the graphene sheet, and the amplitudes of both signals can be adjusted separately. However, this setup requires adjusting the frequency of the two signal generators simultaneously. Their frequency difference $\Delta\omega$ does not keep constant but shifts all the time due to the mismatching between different equipments. Moreover, the lock-in

amplifier produces its internal reference by phase locking to the external reference. But the phase locking causes phase oscillation to the internal reference, which is equivalent to introducing a noise of frequency near the reference signal.

3.4.5.1 AM modulation

An AM modulation signal can be expressed as

$$V_{AM} = A(1 + mBsin(\omega_m t + \phi_m))sin(\omega_c t) \tag{3.14}$$

Where A and ω_c are the amplitude and frequency of the carrier wave respectively, B is the magnitude of the modulation wave of frequency ω_m and initial phase ϕ_m. m is the modulation depth.

Expanding the above formula we get

$$\begin{aligned} V_{AM} = A\big(1 + mBsin(\omega_m t + \phi_m)\big)sin(\omega_c t) \\ = Asin(\omega_c t) \\ + \frac{1}{2}mAB(cos\big((\omega_c - \omega_m)t - \phi_m\big) \\ - cos\big((\omega_c + \omega_m)t + \phi_m\big) \end{aligned} \tag{3.15}$$

Clearly, the AM signal contains ω_c, $\omega_c + \omega_m$, and $\omega_c - \omega_m$.

3.4.5.2 FM modulation

Analysis of the spectrum of FM modulation is much less straightforward then AM modulation. The expression of a FM signal is

$$V_{FM} = Asin(\omega_c t + \frac{\omega_D}{\omega_m}\sin(\omega_m t + \phi_m)) \tag{3.16}$$

The above equation can be expanded to

$$V_{FM} = A\sum_{n=-\infty}^{\infty} J_n(\frac{\omega_D}{\omega_m})\cos((\omega_c + n\omega_m)t) \tag{3.17}$$

Where J_n is the n-th order Bessel function of the first kind. Although the FM signal may seem to contain much more frequencies, the high frequency bands fade quickly away from the centre frequency ω_c. So the main harmonics in FM signal are ω_c, $\omega_c + \omega_m$, $\omega_c + 2\omega_m$, and a few more depending on ω_D/ω_m. The advantage of FM signal is that it is more resistant to the environment interference.

3.4.6 Implementation of electrical measurement

Figure 3.12 shows the single source measurement setup that has been constructed for the resonance characterisation. The whole system includes vacuum chamber, oil pump, lock-in amplifier, signal generator, and a computer equipped with data acquisition board and Labview software. The vacuum chamber has been connected to the oil pump which can pump down the pressure to 3mbar. The chamber lid has three signal feedthroughs that enable electrical connection between inside and outside of the chamber. A vacuum gauge is also attached for monitoring the pressure.

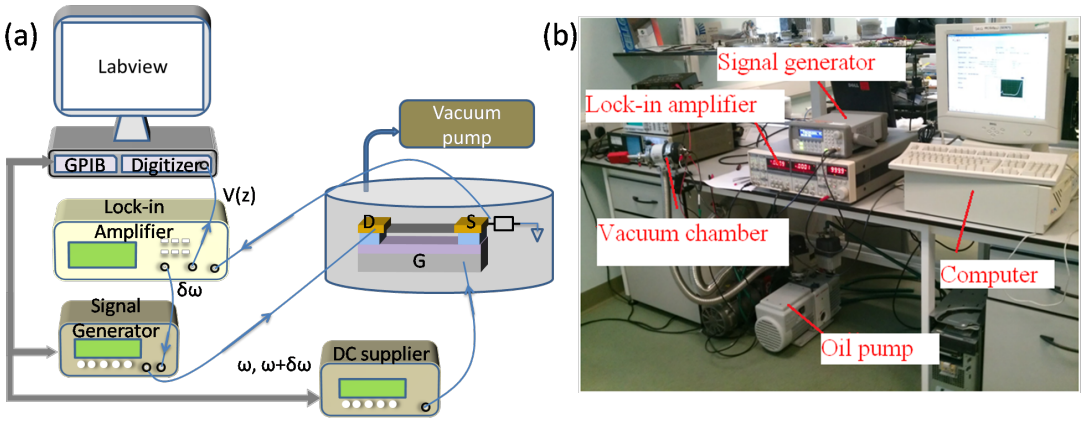

Figure 3.12 One-source setup for graphene resonator characterisation. (a) Schematic of the signal flow. (b) Image of the equipments

A 250KHz-1GHz RF signal generator ((HP E4400B) has been used to provide FM or AM signal. The RF signal contains an inner low frequency generator that produces modulation signal and can output that signal to the Lock-in amplifier (Model 830, Stanford Research Systems) as reference. Alternatively, it has sockets for acquiring the modulation signal from external source. The lock-in amplifier can also source its reference signal from its own signal generator or external equipment. Therefore there are two options for producing the modulation signal/lock-in reference. In our characterisation setup, the modulation signal of the signal generator comes from the Lock-in amplifier. This arrangement has advantages over the other way round, because the phase lock of lock-in amplifier uses a phase lock loop (PLL) to replicate the external reference. However, PLLs do not ideally follow the input wave but with a phase shift noise as mentioned above. This phase noise equals to a broadened frequency spectrum thus deteriorates the accuracy of the measurement. The mixed

current is measured indirectly by connecting a relatively small resistor R_o in series with the graphene channel to convert the current signal to voltage signal.

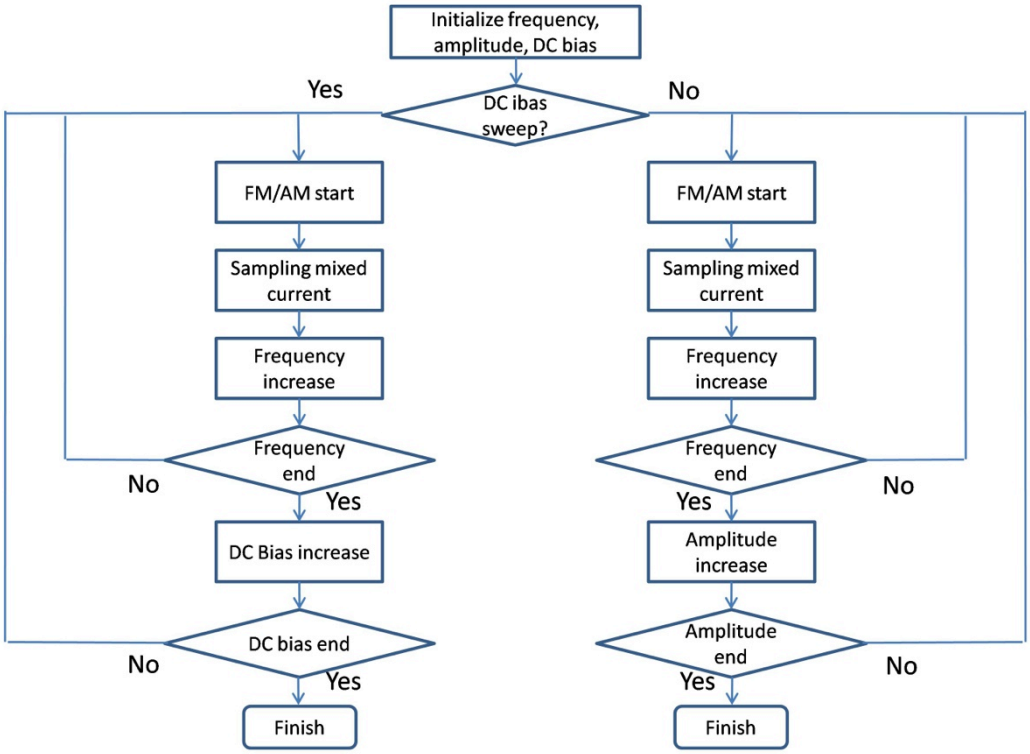

Figure 3.13: Flow chart of the electrical characterisation program

A programmable DC source (TSX5310P) has been used to provide the DC bias for gate electrode. Both the DC source and signal generator are connected to computer with general-purpose-interface-bus (GPIB). The output of the lock-in amplifier is sampled by the data acquisition board. The GPIB bus and the data acquisition board are controlled by Labview to realize automated test. The Labview program offers sweeping of frequency response nested with sweeping of DC bias or the actuation voltage. Figure 3.13 shows the flow chart of the program.

3.4.7 Signal to noise ratio optimization

The mixed current flowing through graphene is extremely weak. Although a lock-in amplifier is capable of removing the noise outside a very narrow equivalent band centring at the reference frequency efficiently, the in-band noise power may still jeopardize the measurement. So the measurement setup should maximize the signal

intensity while suppressing the noise as much as possible. The noise comes from various aspects. First, resistors have thermal noise which originates from the random uneven diffusion of charge carriers. The power density of thermal noise is proportional to temperature $\mathcal{T}$, resistance R, and the bandwidth Δf. The root mean square voltage is expressed as

$$V_{noise}(rms) = \sqrt{4\boldsymbol{k_B}\mathcal{T}R\Delta f} \tag{3.18}$$

Where $\boldsymbol{k_B}$ is the Boltzmann constant. Another typical but less strong noise is the shot noise that is proportional to the current

$$I_{noise}(rms) = \sqrt{4\boldsymbol{e}I\Delta f} \tag{3.19}$$

Here, $\boldsymbol{e}$ denotes the elementary charge and I is the current. Furthermore, the RF signal generator and the internal reference generator of lock-in amplifier also have phase noise which is limiting the measurement accuracy. The thermal noise from resistors and phase noise cannot be eliminated. However, it is possible to reduce the equivalent noise bandwidth. The bandwidth of a lock-in amplifier depends on the internal low pass filter of lock-in amplifier and the roll-off rate. At 24dB roll-off, the equivalent noise bandwidth of the lock-in amplifier is [127]

$$\Delta f = \frac{5}{64\boldsymbol{\tau}} \tag{3.20}$$

Where $\boldsymbol{\tau}$ is the time constant of the low pass filter. The associated signal build-up time for 24dB roll-off is $10\boldsymbol{\tau}$. If the time constant is set to 1s, the delay time would be 10s for acquiring one data point.

The mixed current is converted to voltage by a small resistance R_o. Assuming the resonant amplitude, thus the conductivity variation dG_{Gr} and mixed current I_{mix}, remains unaffected by the small R_o, then the voltage on the current sensing resistor R_o is

$$V_o = \frac{R_{Gr}R_o}{R_{Gr} + R_o} I_{mix} \tag{3.21}$$

Therefore, the output voltage is proportional to R_o when $R_{Gr} \gg R_o$. The graphene's resistance is effectively in parallel with the current sensing resistor, thus the noise root-mean-square (RMS) voltage at the output of lock-in amplifier is

$$V_{noise}(rms) = \sqrt{4\boldsymbol{k_B}\mathcal{T}R_o \parallel R_{Gr}\Delta f} = \sqrt{4\boldsymbol{k_B}\mathcal{T}\frac{R_{Gr}R_o}{R_{Gr}+R_o}\frac{5}{64\boldsymbol{\tau}}} \approx \sqrt{4kTR_o\frac{5}{64\boldsymbol{\tau}}} \quad (3.22)$$

The noise amplitude is proportional to the square root of R_o. Comparing equation 3.19 and 3.20, a conclusion can be drawn that the signal to noise ratio increases with R_o. To minimize the influence of R_o on the measurement, its value should be as small as possible, however, there exists a lower boundary. However, to make sure the equivalent input noise of the lock-in amplifier does not severely reduce the signal to noise ratio, it is preferable that the noise from R_o is comparable to the equivalent input noise of the lock-in amplifier. According to the user manual [127], the equivalent input noise of the lock-in amplifier is $5n\mathrm{V_{rms}}/\sqrt{\mathrm{Hz}}$. Therefore, a 1.5kΩ will produce comparable noise level. The optimised value for R_o cannot be determined at this stage as the mixed current strength cannot be estimated yet. However, this resistance value provides a good start, and it can be decided in heuristic manner during the measurement. In chapter 6, it can be seen that a 390Ω resistor is enough to produce sufficient signal to noise ratio.

3.5 Conclusion

In this chapter, the characterisation techniques involved in the research have been discussed. The quantities that need to be characterized fall into two categories, either the physical properties of the graphene material or the performance of graphene devices. For graphene's physical property characterisation, the Raman spectroscopy has been discussed in terms of its principle and also the association between Raman feature and the structure of graphene. The electrical measurement technique is the other major topic of this chapter, the technical details of implementing the one-source measurement technique has been discussed in detail.

The Raman spectrum provides a non-destructive characterisation method for detecting the number of graphene layers, as well as the lattice integrity. The pristine graphene has two Raman peaks located at 1580cm^{-1} (G band) and 2700cm^{-1} (2D band) respectively. The 2D band of monolayer graphene can be fitted well with one Lorentz peak. When the number of layers increases, the 2D band will broaden due to

double resonance and triple resonance process, which involves the interaction of phonon and electrons in graphene. For double layer graphene, its 2D band contains four sub-peaks. The 2D band can be used to distinguish up to 4 layers of graphene. For even larger number of layers, their 2D band structure will be similar to that of bulk graphite. When the graphene lattice contains defects, a D band at $1350cm^{-1}$ will appear. The intensity ratio of D band G band can be used to assess how ideal the graphene lattice is.

The electrical measurement technique for characterizing graphene resonator has been introduced. To bypass the attenuation by parasitic low pass filter formed by graphene's resistance and pad capacitance, two high frequency signal can be mixed by the graphene resonator to produce a low frequency signal whose amplitude is proportional the resonance amplitude. The one-source measurement setup is easier to be implemented, as less equipment is required. Moreover, the one-source measurement setup avoids feeding the lock-in amplifier with an external reference signal, which produces more noise by PLL and reduces the measurement accuracy. In the one-source setup, the drain electrode of graphene resonator can be fed with either FM signal or AM signal. Both modulation techniques are capable of producing the desired frequency components, but the FM signal is more resistive to environment interference. The applied electrostatic force on the graphene sheet is not uniforms but drop from the drain end to the source end, which leads to activation of even resonant mode in graphene resonators, which will be discussed in chapter 6.

Chapter 4

Making graphene visible on poly-Si film

4.1 Introduction

In the first part this chapter, the design of a poly-Si/SiO_2/Si multilayer substrate for graphene resonator fabrication will be discussed. First, the theory for origin of graphene's contrast on substrate and the contrast calculation method will be introduced. Then the thicknesses of poly-Si film and SiO_2 film will be optimised by means of parametric study. Following is the experimental verification. The discussion of poly-Si's influence on graphene's electron concentration comes the last.

Monolayer graphene sheets are highly transparent, with its absorption rate in visible range being around 2.3%. Although such attribute is extremely appreciated for transparent electrodes applications [33][128], it posts a great challenge to the fabrication and manipulation of monolayer graphene sheet. In this chapter, the design of a substrate consisting of stacked poly-Si film and SiO_2 film on Si wafer for graphene resonator fabrication will be presented. The influence of thicknesses of poly-Si and SiO_2 thin films on the visibility of graphene will be studied so as to optimise the graphene's contast to such substrate. Poly-Si has long been used as a sacrificial layer in MEMS device fabrication [129], but not yet for graphene resonator fabrication before. To take advantage of the mature poly-Si sacrificial layer technology for the fabrication of suspended graphene structure, making graphene visible on poly-Si film under optical microscope is an inevitable prerequisite. The contrast of graphene on poly-Si is not only determined by the graphene/poly-Si interface, but also interfaces underneath. Therefore, a poly-Si/SiO_2/Si structure is proposed and optimised. The contact of graphene with the poly-Si film will bring adjustments to the graphene's band structure by the so-called modulation doping mechanism [44][130], as will be discussed later, thus changing its electrical properties. Since I-V characterisation of graphene sheets on poly-Si needs to be conducted during the fabrication of graphene resonators, as will be discussed in

chapter 5, the influence of the poly-Si film on grahene's conductivity will be investigated by means of simulation of the modulation effect.

The visibility optimization facilitates agile locating and inspection of graphene sheets for device fabrication. The legendary discovery of monolayer graphene can be largely attributed to the sophisticatedly designed 300nm SiO_2/Si substrate that visualizes the ultrathin 2D material under optical microscope [14]. Most graphene structures for either graphene's physical properties study or application inherit the design of the 300nm SiO_2/Si substrate, or modify the oxide thickness of SiO_2 to 90nm which functions in a similar way [16][29][36][131]. Suppose a single layer graphene is placed on top of an ordinary substrate, mono-crystalline silicon wafer for instance, the contrast between the substrate and the graphene sheet will be too small to be distinguishable for ordinary naked eyes since its absorption rate is only 2.3% in the visible wavelength range [25][132]. Finding the monolayer graphene under other instruments such as scanning electron microscope (SEM), although viable, will be a tedious work and prohibitively time consuming. Nevertheless, to expand the exploration of graphene devices demands graphene to sit on other substrates as well. In these cases, the substrates design faces more constraints so as to enhance the visibility of graphene sheet. For instance, to take advantage of the excellent properties of graphene and gallium arsenide (GaAs) to make electronic devices, M. Friedemann et al engineered the visibility of graphene by designing a periodical structure of gallium arsenide [133].

4.2 Theory of contrast

4.2.1 Origin of high contrast

Making an atomically thin material visible is a tricky but feasible task. As reported in the [134][135], a distinctive optical contrast between graphene and substrate originates from the difference between the light reflectivity of graphene-covered area and the rest of substrate without graphene. To substantially change the reflection of a substrate with only one layer of material as thin as 3.34Å, the reflection of the substrate itself has to be sensitive to the changes of its surface conditions, as is the case for the widely used 300nm SiO_2/Si or 90nm SiO_2/Si substrate. The thicknesses

of SiO_2 on Si meet destructive interference condition (Figure 4.1(a)), that is to say, the light reflected by the air/SiO_2 interface, has the same amplitude as the light reflected by the SiO_2/Si interface, but a phase shift of 180°.

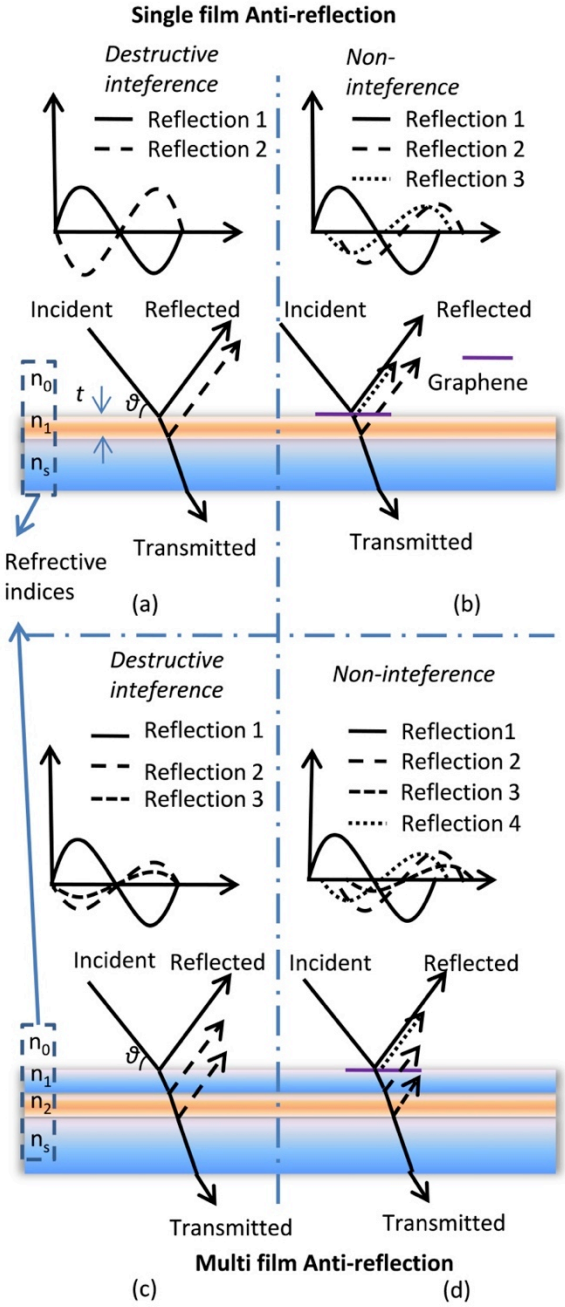

Figure 4.1: Principle of enhancing the visibility of graphene on poly-Si inspired by the 300nm SiO_2/Si substrate [134]

The destructive interference condition is easily destroyed by just a single layer of graphene (Figure 4.1(b)) as it introduces one more reflecting interface. From these

substrates, a general guidance can be extracted that all the substrate structures which allow graphene to be visible under optical microscope should be specifically designed to be an anti-reflective optical system at least in a certain wavelength range.

However, the anti-reflection cannot be realized for poly-Si layer on Silicon substrate, since the refractive index of poly-Si is almost the same as crystalline Silicon. If poly-Si film is deposited straight onto Si, their interface will not reflect light because of their equal refractive index according to Fresnel's Law. To achieve destructive interference condition for poly-Si film, it is necessary to insert between poly-Si and Si substrate a thin film with considerably different refractive index. In consideration of process convenience, a SiO_2 layer has been chosen to enable the reflected light from the three interfaces to cancel each other as much as possible as shown in Figure 4.1(c). Under this crucial condition, when a graphene is placed on top (Figure 4.1(d)), the light cancellation effect will be influenced maximally.

4.2.2 Reflectivity of multilayer system

To optimise the thickness of the proposed multi-film optical system, it is necessary to derive the relationship between the film thicknesses and the reflection rate. For multilayer optical system, it is convenient to use the transfer matrix theory to calculate the reflectivity [136]. The transfer matrix theory is capable of equalizing a multilayer optical system by a single equivalent interface. In this chapter, the light beam is assumed to be perpendicular to the substrate for simplicity. For a *m*-layer optical system such as the one shown in Figure 4.1(c), the electric and magnetic field magnitude at the interface of *0*th layer and *1*st layer can be expressed as

$$\begin{bmatrix} \mathbb{E}_0 \\ \mathbb{H}_0 \end{bmatrix} = \mathbb{M}_1 \cdots \mathbb{M}_{j+1} \cdots \mathbb{M}_m \begin{bmatrix} \mathbb{E}_m \\ \mathbb{H}_m \end{bmatrix} = \begin{bmatrix} B \\ C \end{bmatrix} \tag{4.1}$$

where, $\mathbb{E}_j$ and $\mathbb{H}_j$ are the electric and magnetic field respectively at the interface between the *j*th layer and *j+1*th layer. *T*he *m*th layer is the surface of the bottom substrate. B and C are just the two entries of the result matrix. $\mathbb{M}_j$ is the characteristic matrix of a individual film and represents the coupling of electric and magnetic field of two adjacent interfaces, namely the $j-1th/jth$ layer interface and $j/j+1$ layer interface.

$$\mathbb{M}_j = \begin{bmatrix} cos\Delta_j & \frac{i}{\eta_j} sin\Delta_j \\ i\mathbb{N}_j sin\Delta_j & cos\Delta_j \end{bmatrix} \tag{4.2}$$

Where $\mathbb{N}_j$ is refractive index of the jth layer [137]. Δ_j is the phase shift or optical path induced by the *j*th layer

$$\Delta_j = \frac{2\pi}{\lambda} \mathbb{N}_j d_j cos\theta_j \tag{4.3}$$

d_j is its thickness. The product of all the characteristic matrices

$$\mathbb{M} = \prod_{j=1}^{m} \mathbb{M}_j = \prod_{j=1}^{m} \begin{bmatrix} cos\Delta_j & \frac{i}{\eta_j} sin\Delta_j \\ i\eta_j sin\Delta_j & cos\Delta_j \end{bmatrix} \tag{4.4}$$

relates the electric and magnetic field of the top interface to the bottom interface, therefore, it is called transfer matrix. The equivalent optical conductance $\mathbb{Y}$, which also equal to the equivalent refractive index, is defined as

$$\mathbb{Y} = \frac{\mathbb{E}}{\mathbb{H}} = \frac{C}{B} \tag{4.5}$$

The reflective rate $\mathbb{R}$ is

$$\mathbb{R} = \left| \frac{\mathbb{N}_0 - \mathbb{Y}}{\mathbb{N}_0 + \mathbb{Y}} \right|^2 \tag{4.6}$$

There are different ways of defining contrast. We follow P. Blake et al to define the contrast as [134]

$$\mathbb{C} = \left| \frac{\mathbb{R}_2 - \mathbb{R}_1}{\mathbb{R}_1} \right| \tag{4.7}$$

Where $\mathbb{C}$ is the contrast, $\mathbb{R}_1$ is the reflection of substrate, and $\mathbb{R}_2$ is the reflection of the area with graphene. This contrast is actually the intensity contrast.

4.3 Results and discussions

4.3.1 Simulation

Parametric study of reflectivity as well as contrast has been conducted based on the above formulas, to achieve the highest visibility of graphene on poly-Si/SiO_2/Si

substrate. The thicknesses of poly-Si and SiO_2 film are the variables adjusted in small steps in the parametric analysis to calculate the corresponding contrast of monolayer graphene. Since the refractive indices involved are all dispersive over the visible wavelength range, the refractive index at each wavelength point is interpolated from existing discrete tables [138]. Graphene is assumed to have a similar refractive index of bulk graphite $2.6 - 1.3i$, and the thickness of monolayer graphene is estimated to be 3.34Å. Previous reports have confirmed that these parameters fit the experimental results very well [134].

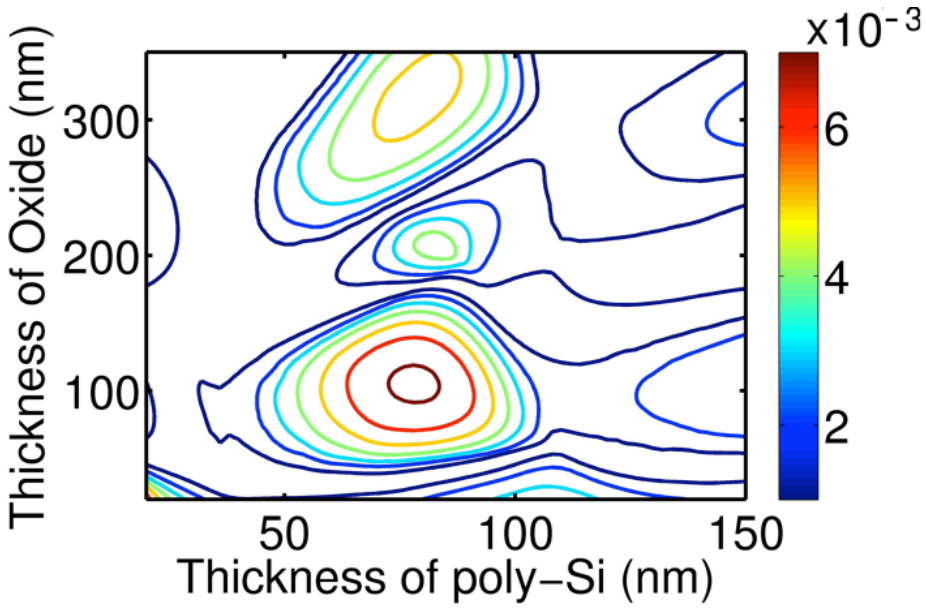

Figure 4.2: Contour plot of integral contrast against the thicknesses of poly-Si and SiO_2

Since the contrast is wavelength dependent, an integral contrast has been defined over 400-740nm wavelength range. The integral contrast is simply an integration of contrast with respect to the wavelength from 400nm to 740nm. Figure 4.2 is the contour plot of the integral contrast against the thicknesses of both poly-Si and SiO_2. The parametric calculation has been implemented in Matlab code which can be found in appendix A.1. The thickness of poly-Si increase from 20 to 150nm, while the thickness of SiO_2 increases from 20 to 350nm, both by 2nm per step. As can be seen from the plot, there are three maxima corresponding to 75nm poly-Si/100nm SiO_2, 80nm poly-Si/200nm SiO_2, and 75nm poly-Si/300nm SiO_2 respectively, while the overall maximum is located at 75nm poly-Si/100nm SiO_2.

When the thickness of the poly-Si is fixed at 75nm, the integral contrast is increasing and decreasing alternatively with increasing SiO_2 thickness, however, the intensity of peaks with thicker SiO_2 are weakened for thicker SiO_2 due to the dispersion of the reflection with wavelength. A thicker film thickness will make reflective curve more dispersive (dashed red line) as shown in Figure 4.3, because the optical path Δ_j will be more dependent on the wavenumber with larger d_j according to equation 4.3. Therefore, the integral contrast will decrease. Similarly, when the thickness of SiO_2 is fixed, the contrast also falls with thicker poly-Si, even more rapidly. Besides the dispersion of reflectivity, the absorption of poly-Si also contributes to the decrease of peak intensities. The thicker the poly-Si film is, the more the light will be attenuated.

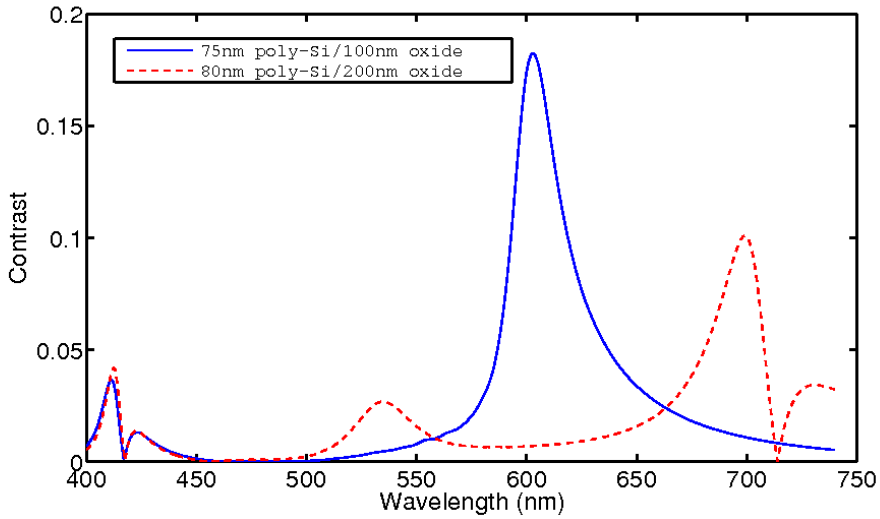

Figure 4.3: Contrast comparison of graphene on 75nm poly-Si/100nm SiO_2 and 80nm poly-Si/200nm SiO_2

It has been found in Figure 4.2 that the combination of 75nm thick poly-Si and 100 SiO_2 layer will produce maximum integral contrast. The reflectivity (Figure 4.4(a)) and contrast (Figure 4.4 (b)) against wavelength have been plotted at this point. The contrast on 75nm poly-Si substrate is more dispersive with wavelength compared with graphene on 300nm SiO_2 substrate [139]. The wavelength that has maximum contrast is found to be near the wavelength of 600nm. There is a relatively large range spanning from 590 nm to 620nm where contrast larger than 10% can be obtained. The inset of Figure 4.4 (a) zooms in at the details of the reflection curve around 600nm. The reflectivity of substrate without graphene is larger than the area

covered by monolayer graphene. The enhancement of graphene's visibility on the poly-Si/SiO_2 is slightly different from the 300nm SiO_2 substrate where the presence of graphene layer increases the reflectivity. Since the refractive index difference at the interface of air/poly-Si is larger than that at the air/graphene interface, the reflectivity of 600nm light will be higher at the air/poly-Si interface compared to the air/graphene interface, as illustrated in the inset of Figure 4.4(a). Therefore, the presence of graphene on the poly-Si will cause higher destructive interference, thus decreasing the reflectivity.

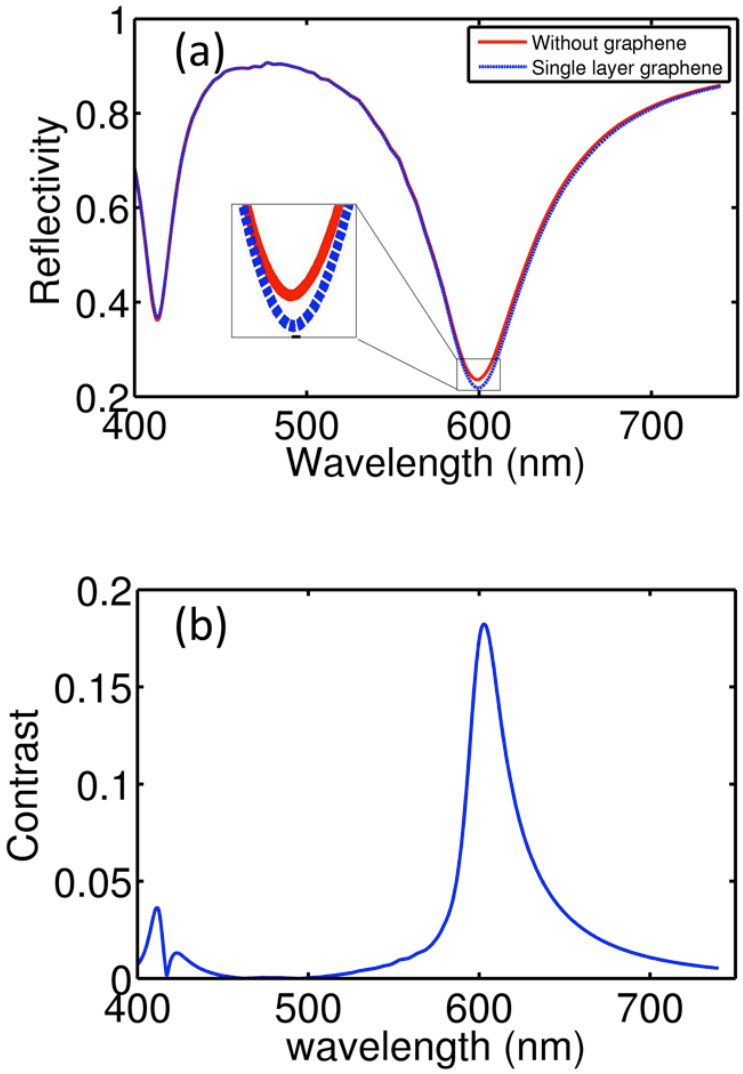

Figure 4.4: Dependence of reflectivity (a) and contrast (b) on wavelength

It is worth mentioning that it is the integral contrast that has been used as an objective function in the parametric analysis rather than contrast at a wavelength

point. If the single point contrast is used as an objective function, then a very high contrast may be achieved in a very narrow bandwidth. However, the overall contrast may still be low due to the dispersion of contrast over the wavelength as well as the thicknesses of the films. It will not leave enough margin for process errors. Moreover, the possibility of finding an existing narrow band optical filter or light source at exactly the maximum contrast wavelength will be very low.

4.3.2 Experiment

In order to compare the contrast of graphene on widely used SiO_2 substrate with the optimised 75nm poly-Si/100nm SiO_2/Si multilayer substrate (poly-Si substrate), both type of substrates have been prepared. First, 100nm SiO_2 is grown on top of a 4" silicon wafer by wet oxidation. Then 75nm poly-Si layer has been deposited on top of SiO_2 by low pressure chemical vapour deposition (LPCVD). The 285nm SiO_2 is grown on Si wafer with the same method as for the 100nm SiO_2.

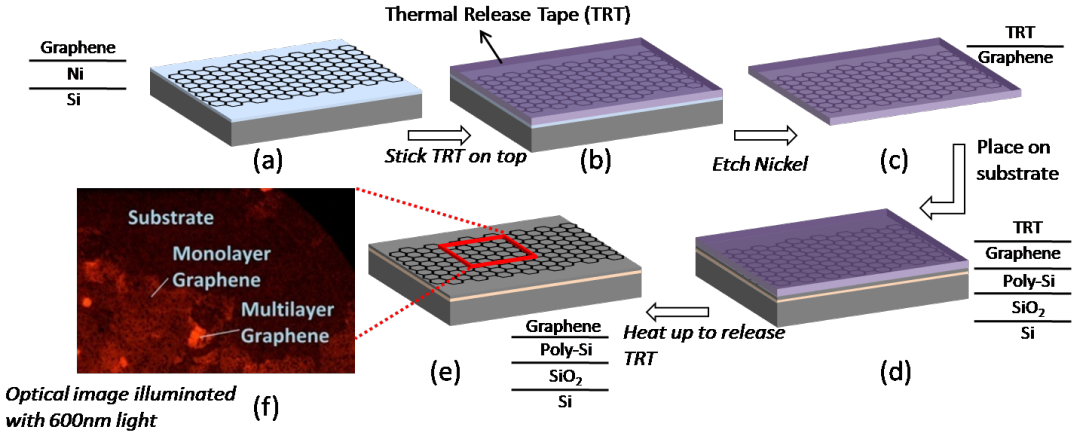

Figure 4.5: Transfer of CVD-grown graphene on Ni film onto poly-Si substrate

CVD-grown graphene on Ni catalyst has been transferred to the substrates by the process shown in Figure 4.5. First, a piece of thermal release tape (TRT) has been stuck on the graphene/Ni/Si (a-b). Then the samples are soaked in 1M aqueous $FeCl_3$ solution to dissolve all the nickel away so that graphene sheet together with the TRT will be separated from the silicon substrate (c). After being rinsed with de-ionized water for three times to clean $FeCl_3$ and dried with nitrogen gun, the graphene side of graphene/TRT sheet is placed gently on the poly-Si substrates using tweezer tip to

squeeze out the air gradually between substrate and graphene (d). Once a good contact is formed, the whole structure is placed on a hotplate at 100°C to release the tape (e). To remove the tape residue, the samples have been rinsed in isopropanol, acetone, and de-ionized water for 5min each in sequence. The resulted graphene on poly-Si/SiO_2/Si substrate are shown in (f).

4.3.3 Characterisation

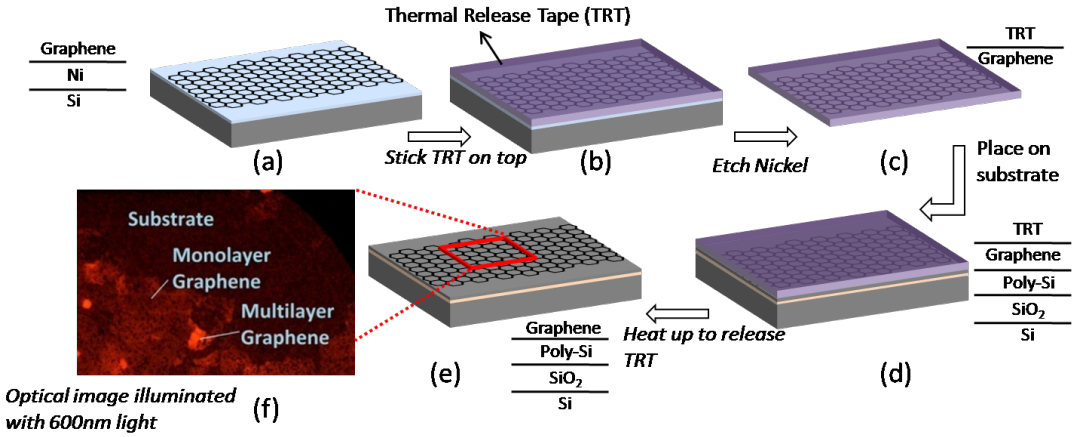

Figure 4.6: Comparison of the influences of two illumination spectrum on the visibility of graphene on both poly-Si and SiO_2 substrate

Figure 4.6(a) shows the image of graphene sheet on top of the optimised poly-Si/SiO_2/Si substrate under optical microscope with ordinary halogen lamp light, while Figure 4.6(b) is the image of the same location as (a) but a narrow band filter (Band pass Filter, 600±2nm centre, 10±2nm FWHM, Newport Spectra-physics Ltd.) has been inserted to the light path to achieve quazi-monochromatic illumination. Similarly, Figure 4.6(c) and (d) are graphene sheet transferred onto 285nm SiO_2/Si substrate under ordinary and 600nm illumination respectively. The scale bars are 10μm.

A Raman spectrum has been taken at point labelled as SLG (single layer graphene) in the optical image in Figure 5(b). To reduce the possible sample heating effect, the laser power has been kept lowest. The wavelength of the laser is 514nm. Due to the thinness of graphene, the signal to noise ratio (SNR) is very low. Multiple accumulations have been used to increase the SNR. The G band and 2D band are very strong (Figure 4.7(a)), which are located at 1580 and 2700cm^{-1} respectively.

These two bands are the signatures of graphene [115]. The defects related D band has not been observed in the spectrum. This is consistent with previous reports for good quality graphene [102].

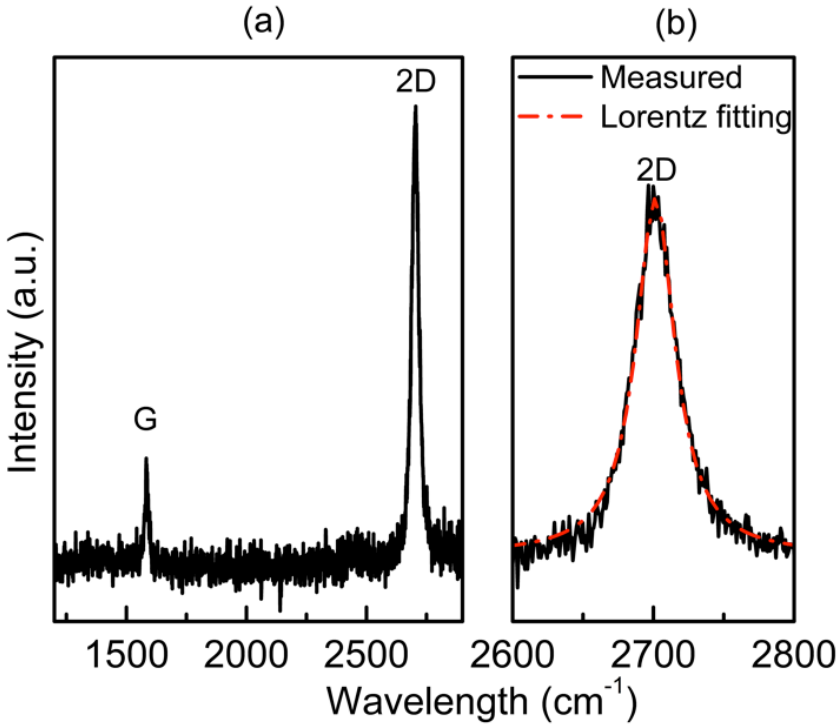

Figure 4.7: Raman spectrum taken at the place labelled as SLG in **Figure 4.6**(b)

Typically, 2D band originates from double resonance effect as elaborated in section 3.3.3 of chapter 3, consisting of 4 peaks for more than 2 layers of graphene, which is due to energy band splitting of both the conduction band and the valence band. The intensity of the four peaks and the shape of 2D band are dependent on the number of layers. In the case of monolayer graphene, only one peak in the 2D band can be resolved. Therefore, it is possible to distinguish between monolayer graphene and multilayer graphene. A closer examination of 2D band (Figure 4.7(b)) shows that the band is symmetrical and can be fitted very well with just one Lorentz peak, which confirms that the labelled area is monolayer graphene indeed.

In order to verify that the formulae used in the simulation are correct, the simulated reflection spectrum (Figure 4.6 (a)) has been converted into colour vector expressed in red (**R**), green (**G**), and blue (**B**) components by International Commission on Illumination (CIE) colour matching function [140]. The colour matching functions

use three weight curves to calculate the spectrum's contribution to **R**, **G**, and **B** components according to human cone cells' perception of light wavelength. The Matlab code for the spectrum to colour calculation can be founded in appended A.1. The calculated **RGB** values are then compared to the **RGB** value extracted from ordinary optical image of the substrate as shown in Figure 4.6(a). Ideal white light illumination has been assumed for the colour calculation. As the illumination intensity affects the absolute **RGB** values, it is the ratios among the **RGB** components that are compared. The calculated $\mathbf{R}:\mathbf{G}:\mathbf{B}$ ratio from Figure 4.4(a) by colour matching function is $0.35:0.86:1$, while the RGB ratio extracted from Figure 4.6 (a) is $41:124:154 = 0.27:0.81:1$. The extracted and the simulated $\mathbf{R}:\mathbf{G}:\mathbf{B}$ ratios agree with each other. The small difference between the ratios may come from the difference between spectrum of halogen lamp and the ideal white light spectrum, as well as the diffraction of microscope and interference light scattered in from environment. The comparison of calculated and measured colour proves the theory applied should be reliable.

In Figure 4.6(a), the whole graphene sheet is barely seen, but in Figure 4.6(b), single layer graphene, as confirmed by Raman spectroscopy, as well as randomly located multi-layer graphene patches are clearly observed. There are also holes in graphene sheet so that the poly-Si layer is exposed. The morphology is consistent with reported graphene grown on nickel [34]. The contrast between the monolayer graphene area and the poly-Si/SiO_2/Si substrate has been calculated to be 8.7% by extracting light intensities from both areas, large enough to be seen under optical microscope, indicating that the substrate does enhance the visibility of single layer graphene with illumination wavelength of 600nm. It has been the first time that monolayer graphene has been made visible above poly-Si layer with such a high contrast. Figure 4.6(c) is the image of CVD-grown graphene on 285nm SiO_2 illuminated under normal light. The contrast between graphene and the substrate is 6%, slightly increasing to 6.5% when illuminated with filtered light (Figure 4.6(d)). The enhancement of contrast on SiO_2 substrate is about 0.5%, complying with the reported contrast on SiO_2 substrate against wavelength [134].

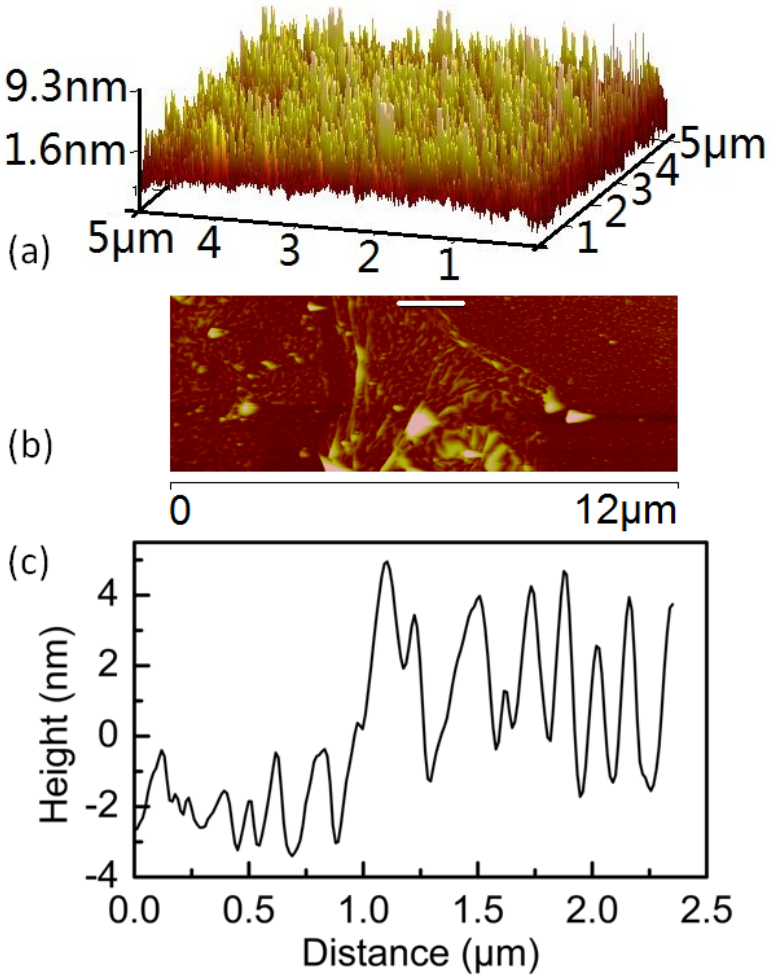

Figure 4.8: (a) Contour of the poly-Si surface scanned by AFM. (b) AFM characterisation of the area enclosed in dashed square in **Figure 4.4**(b). (c) Height profile along the line in (b)

It is important to point out that, assuming all surfaces are smooth, the reflection of graphene covered area will be weaker than the substrate according to the simulation, as the refractive index of graphene is closer to air than poly-Si, thus less reflective, while the observed result in Figure 4.6(b) is to the contrary. The uncovered poly-Si area is observed to be less reflective. One of the possible causes could be the roughness of the surface of CVD grown poly-Si, which scatters away the light, therefore, less light is collected by the objective lens of the microscope. Figure 4.8(a) shows atomic force microscope (AFM) image of poly-Si substrate, taken with VEECO Dimension 3100 AFM. The RMS average surface roughness r_{rms} of the poly-Si surface is about 2.19nm (Figure 4.8(a)), more than double of the typical value r_{rms} of polished crystalline Si wafer, which is less than 1nm. The other

possibility is that there are tape residuals on top of graphene which scatter more light into the objective lens. The later appears more likely to be true as will be seen in Figure 5.4(a) annealed graphene sheet does exhibit lower reflection than substrate. Figure 4.8(b) is the AFM image corresponding to the area enclosed in the dotted rectangular in Figure 4.6(b), while Figure 4.8(c) is the height profile along the line in Figure 4.8(b) from right to left, that is to say, from substrate to graphene. Although the height profile is quite rough, a step of about 1.752nm between graphene and the substrate is clearly identifiable, confirming the existence of graphene sheet. In summary, although probably the reflection is decreased from the predicted intensity due to surface roughness, the requirements of antireflection of the substrate have been fulfilled to allow a significant change of reflection by monolayer graphene, hence, the visibility of monolayer graphene is increased.

4.4 The influence of poly-Si on electrical property of graphene

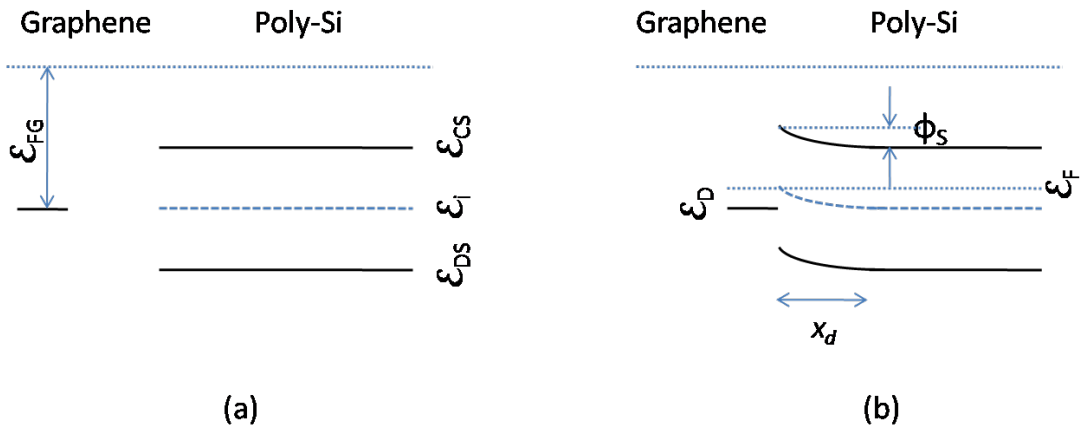

Figure 4.9: Band structure of graphene and poly-Si

Once the graphene sheets contact poly-Si film, electrons will flow from one material to the other depending on the chemical potential difference of the two materials, thus graphene is doped either with electrons or holes. Such process is called modulation doping. Figure 4.9 shows the band structure of separated graphene and undoped poly-Si film (a), along with graphene touching n-doped poly-Si film (b). Both graphene and poly-Si have a work function of around 4.6V [141][142]. For pristine graphene sheet, its Fermi level $\mathcal{E}_{FG}$ coincides with the Dirac point $\mathcal{E}_D$ as described in section 2.2 in chapter 2. When intrinsic graphene is brought into contact with

undoped poly-Si film, their band structure remains the same as separated. However, for instance, if the poly-Si film has been n-doped, then its Fermi level $\mathcal{E}_F$ will be higher than the intrinsic Fermi level, and electrons near the poly-Si surface will flow to the graphene side until the Fermi levels in two materials equal to each other. So the energy band of poly-Si will bend up towards interface. However, the band diagram of graphene will not bend because of its 2D nature. The band of graphene has been illustrated as a line for clarity in Figure 4.9(b), but actually it has no length because graphene almost has near-zero thickness. The whole Fermi level of graphene will be lifted up until equal to the Fermi level in poly-Si.

To investigate to what extent the ion doping level in poly-Si would affect the graphene's conductivity, the carrier density in graphene will be calculated as a function of the doping level in poly-Si. As derived in section 2.3.1 in chapter 2, the carrier density n_{nG} in graphene is related to its Fermi level $\mathcal{E}_{FG}$ by

$$n_{nG} = \frac{2}{\pi}\left(\frac{\boldsymbol{k_B}\mathcal{T}}{\hbar v_F}\right)^2 \mathcal{F}_1\left(\frac{\mathcal{E}_{FG} - \mathcal{E}_D}{\boldsymbol{k_B}\mathcal{T}}\right) = \mathcal{F}_{nG}(\mathcal{E}_{FG}) \tag{4.8}$$

On the poly-Si side, its band bending $\boldsymbol{\phi}_S(x)$ should satisfy the Poisson equation

$$\frac{d^2\boldsymbol{\phi}_S(x)}{dx^2} = -\frac{\rho(x)}{\boldsymbol{\epsilon}_s} = -\frac{\mathcal{N}_d(x)}{\boldsymbol{\epsilon}_s} = -\frac{d\mathbb{E}(x)}{dx} \tag{4.9}$$

Where $\boldsymbol{\phi}_S(x)$ is the band bending at depth x measured from the interface. $\rho(x)$ is the charge density, and $\boldsymbol{\epsilon}_s$ is the dielectric constant of silicon. When the donors are completely ionized, the electron density equals to the donor concentration $\mathcal{N}_d(x)$. $\mathbb{E}(x)$ is the electric field strength. Boundary conditions are $\boldsymbol{\phi}_S(0) = 0$ and $\mathbb{E}(x_d) = 0$, then an explicit expression for $\boldsymbol{\phi}_S(x)$ can be found

$$\boldsymbol{\phi}_S(x) = -\frac{e\mathcal{N}_D}{\boldsymbol{\epsilon}_s}(xx_d - \frac{x^2}{2}) \tag{4.10}$$

The maximum bending is located at the boundary of the depletion region $x = x_d$.

$$\boldsymbol{\phi}_S(x_d) = \frac{e\mathcal{N}_D x_d^2}{2\boldsymbol{\epsilon}_s} \tag{4.11}$$

Here x_d is the depth of depletion region. Electrons doped into graphene should equal the total number of electrons generated in the depleted region

$$n_{nG} = x_d \mathcal{N}_d \tag{4.12}$$

With the above equation, the electrons doped into graphene can be calculated numerically with the algorithm shown in Figure 4.10. After initialization of the doping level in poly-Si and the corresponding Fermi level, the Fermi level difference of graphene and poly-Si is compared, if they do not equal, then the Fermi level of graphene is lifted up by an amount of one hundredth of the Fermi level difference, and the number of modulation doped electrons is calculated, as well as the depletion depth, band bending in poly-Si. The above process is iterated until the Fermi level in the two material equals. Figure 4.11 plots the electron density in graphene, graphene Fermi level, depletion depth in poly-Si, and band bending in poly-Si against the iteration steps. It can be seen that the program converges well within 500 steps. The simulation code is written in Matlab and can be found in appendix A.2

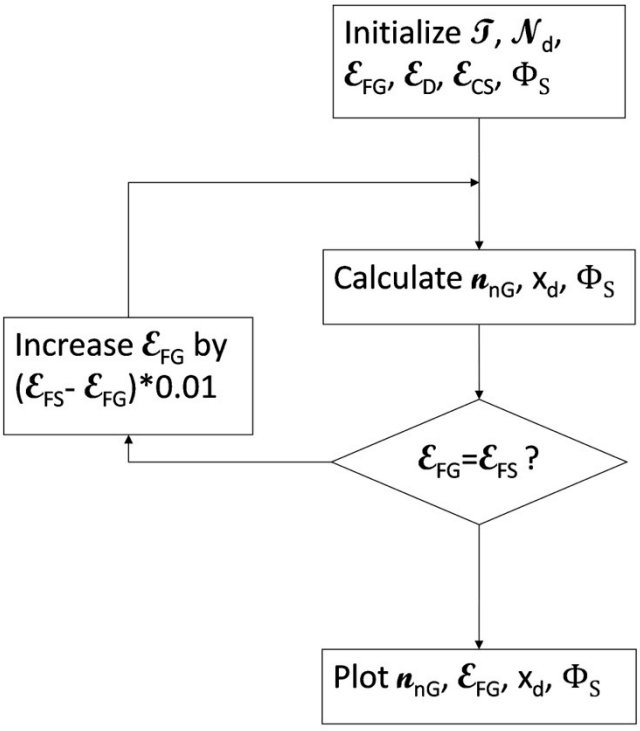

Figure 4.10: Flow chart of the algorithm for calculation the modulation doping level of graphene by poly-Si

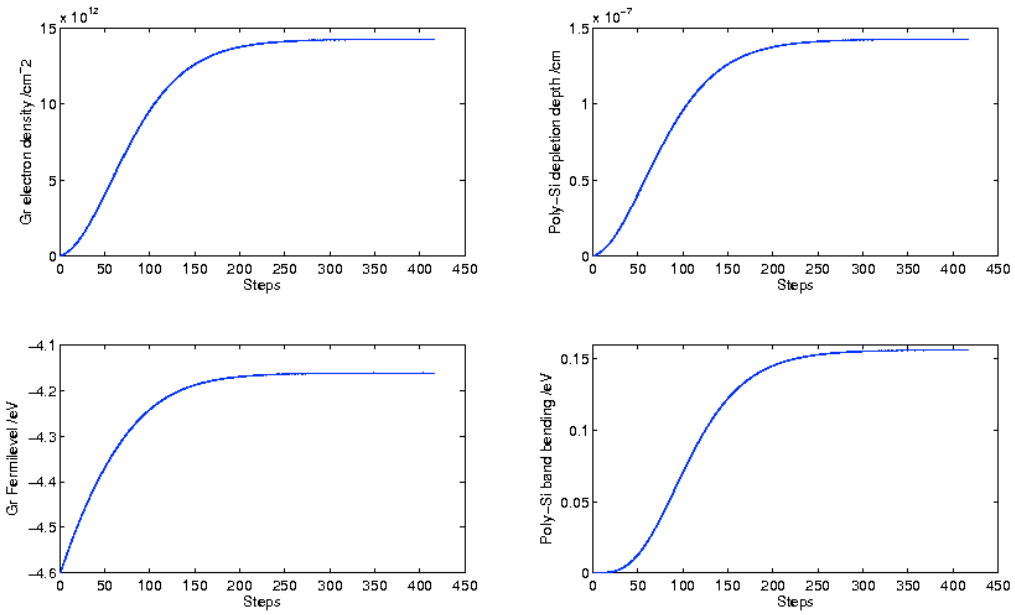

Figure 4.11: Convergence of graphene electron density, poly-Si depletion depth, graphene Fermi level, and poly-Si band bending

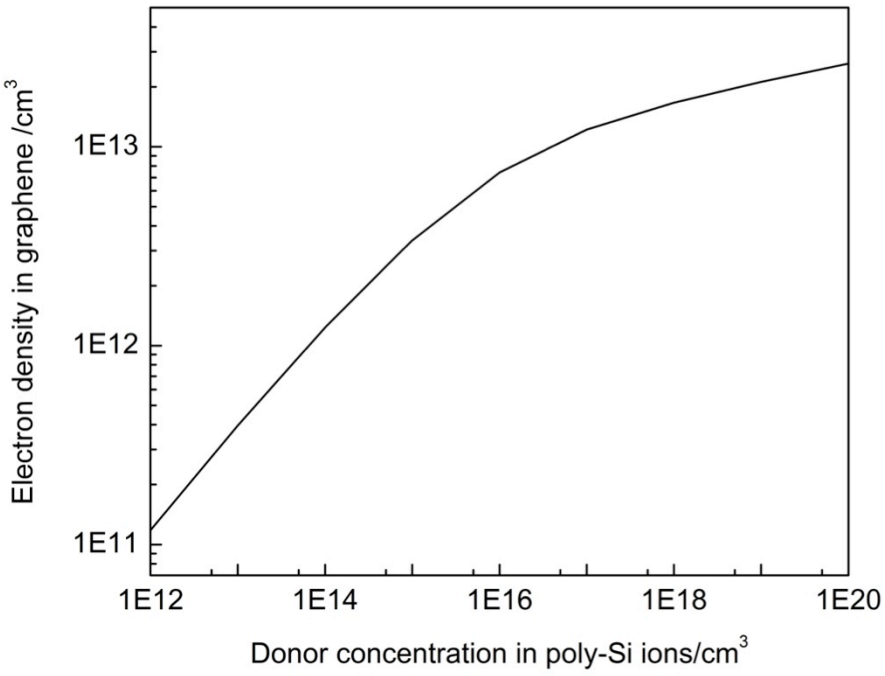

Figure 4.12: Modulation-doped electron density in graphene against donor concentration in poly-Si layer

Figure 4.12 (a) plots the electron density in graphene against the donor concentration in poly-Si, which agree very well with previous calculations [143]. The modulation

doped electron density in graphene increases linearly with increasing donor concentration in poly-Si at below 10^{15} ions/cm^3, then the increase rate softens. When the donor concentration in poly-Si is below 10^{15} ion/cm^3, the electron density in graphene is two orders of magnitude lower. This result suggests that even poly-Si is unintentionally doped during growth, its effect on the graphene's conductance is very limited, which is very important for the in-process quality monitoring during the fabrication of the graphene resonators to be discussed in chapter 5.

4.5 Conclusions

In this chapter, a poly-Si/SiO_2/Si substrate has been proposed for the fabrication of suspended graphene structure. The poly-Si layer is very suitable to be used as sacrificial layer in MEMS device fabrication. The insertion of a SiO_2 layer is intended to make it feasible to achieve an anti-reflective substrate, which is key to maximize the visibility of graphene under optical microscope. Such visibility is important as it facilitates quick inspection and monitoring of the fabrication process.

A method for optimizing the visibility of graphene on poly-Si/SiO_2/Si has been developed based on the transfer matrix theory of thin film optics. Contour plot of integral contrast against both thicknesses of poly-Si and SiO_2 has been obtained by parametric study. The optimised thicknesses of both SiO_2 and poly-Si have been found to be 75nm and 100nm respectively. The contrast is dispersive over the visible light range, and a relatively large contrast can be obtained in a wavelength range around 600nm. The poly-Si/SiO_2/Si structure and ordinary 285nm SiO_2 substrate have been fabricated. CVD grown graphene has been transferred to the substrates with the aid of thermal release tape. The samples have been examined under illumination of normal halogen lamp and the light filtered by 600±2nm narrow band optical filter. The contrast of monolayer graphene on poly-Si, as confirmed by Raman spectroscopy, has been enhanced on the 75nm poly-Si/100nm SiO_2/Si substrate from almost none to a contrast of 8.7%. In comparison, the contrast of graphene on SiO_2 does not change substantially because graphene's contrast on SiO_2 is much less dispersive.

When graphene is in contact with the poly-Si layer, the electrons will flow from one side to the other depending on the Fermi energy of these two materials, which is

called modulation doping. A calculation has been done to investigate how the donor concentration in poly-Si would affect the electron concentration in graphene. It has been found that for donor concentration below 10^{15} ions/cm^3, the electron concentration in graphene is about two orders of magnitude lower. When poly-Si is even heavily doped, the modulation doping effect will soften. The calculation suggests that when poly-Si is lightly doped, its influence on the electron concentration in graphene is limited, which is an important fact to know for the in-process characterisation of graphene' conductivity as will be discussed in chapter 5.

Chapter 5

Fabrication of suspended graphene bridges

5.1 Introduction

This chapter is devoted to the fabrication of suspended graphene bridges from CVD-grown graphene sheet. The suspension of graphene bridge is the key to realize graphene resonator and to study the mechanical properties of graphene [19][36] [37][144][145][146]. Moreover, the carrier mobility of graphene is limited by the substrate's phonon scattering [16][43], freestanding graphene enables investigation of its intrinsic electrical properties. Reports have shown that suspended graphene sheets exhibits extremely high carrier mobility that enters the ballistic transport regime [16][29]. Suspended graphene structures have been achieved in three ways. One is to put graphene down to pre-patterned trenches or holes [19][38][147]. This method is preferred for achieving suspended graphene from mechanically cleaved graphene flakes. However, the success of fabricating such a device relies on sheer luck when a desired flake happens to settle over the trenches. Therefore, this approach is not scalable for mass production. Since graphene has been grown in large area on SiC by sublimation, suspension of the graphene can be achieved by wet etching SiC underneath [145]. This method bounds the substrate to SiC, lacking flexibility for the diversified applications. The other technique that holds promise for mass production is to fabricate graphene bridges from CVD-grown graphene. The graphene can be transferred and patterned on a sacrificial layer that can be etched away to release the graphene sheet [36][37]. SiO_2 layer has been a popular sacrificial layer for graphene resonator since the graphene flakes are normally put down on 300nm SiO_2 for its visibility on such substrate. However, the etching of SiO_2 always involves HF that may also attack metal. The samples released in wet etchant need critical point drying to avoid surface tension induced damage.

To push forward application of graphene, the possibility of batch fabricating suspended graphene bridges from CVD-grown graphene sheet has been explored. The key difference from the existing technology is that poly-Si will be used as a

sacrificial layer that can be etched in vapour phase by xenon di-fluoride (XeF_2), which completely solve the issue of capillary force induced device breakage and also avoid the harsh environment of wet etchant. In this chapter, the fabrication process and the yields will be discussed. A side effect of vapour phase release is the fluorination of graphene by the gas etchant XeF_2. Fluorinated graphene possesses large bandgap that reduces the conductivity, however, the Young's modulus, although degraded, still supersedes those of Silicon and steel, which is why believe this fabrication process is believed to be suitable for making graphene resonators. To enable electronic characterisation, the conductivity of graphene needs to be recovered to some extent, therefore, the de-fluorination technique will be introduced as well.

5.2 Design of suspended graphene structure

The structure of the suspended bridges takes into account its compatibility with fabrication process and convenience for characterisation. To facilitate the electrical measurement, the graphene bridges have been arranged in a four-point probe structure.

5.2.1 Principle of four-point probe measurement

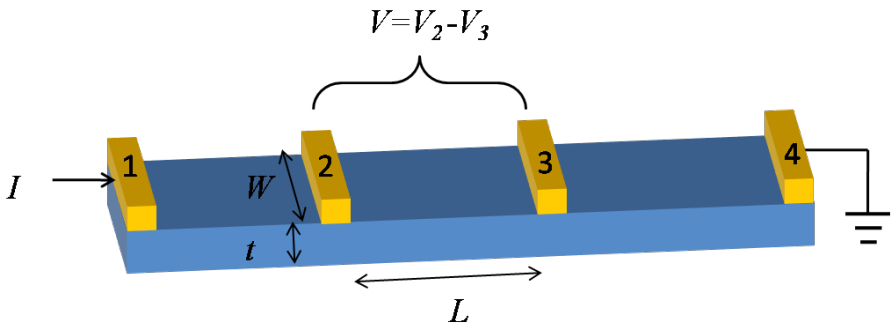

Figure 5.1: Schematic of four-point probe measurement setup

Conductance of a material characterizes how effective the charge carrier transports in it. Measurement of conductance could be an effective approach to deduct physical parameters such as charge velocities. The conductance $G = I/V$, where I is the current flowing through the material, and V is the electric potential drop caused by the current. Nevertheless, accurate measurement of the voltage drop across the

material is not always possible due to the contact resistance between the probes and the material under test. The voltage reading does not only include the voltage drop across the material, but also the voltage drop on two contact resistors formed between the probe and the material under test. For semiconductor materials, this drawback deteriorates even more due to the potential barrier at the interface of semiconductor and the probes. To overcome such problem, the four-point probe method has been a popular structure for characterizing the conductance of materials, eliminating the influence of the contact resistance. Figure 5.1 is a schematic drawing illustrating the principle of four-point probe measurement. To measure the conductance of a rectangular material (blue), four contacts (labelled as 1-4) can be made to the material. Usually, a constant current is flown from electrode 1 to electrode 4, and the voltage at electrode 2 and 3 is monitored. Since the voltage measurement takes as little current as none, the contact resistance between electrode 2, 3 and the material does not obscure the precise reading of the voltage drop. Therefore the conductance of the material is precisely $G = I_1/(V_2 - V_3)$.

5.2.2 Graphene resonator layout

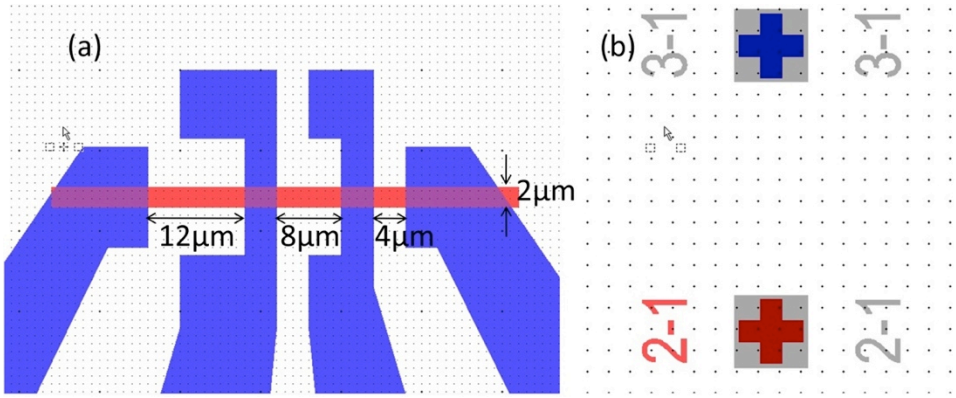

Figure 5.2: (a) Mask design of the graphene resonators. (b) Alignment marks

The mask layout of the graphene resonator is shown in Figure 5.2(a). Four metal electrodes (blue) contact a graphene strip (red) of 2μm wide, which is approaching the minimum size that can be fabricated with standard photolithography equipment. As will be shown later, narrower width shortens the time for complete release of graphene by XeF_2. The electrodes divide the graphene strip into three channels whose lengths are 4μm, 8μm, and 12μm respectively. The lengths of the graphene

bridges vary to allow transmission line measurement [148]. The electrodes have been placed in parallel so that when the graphene is released, three doubly clamped graphene bridge resonators are formed. The metal electrodes also serve as anchors to fix the suspended graphene bridges. The ends of the middle electrodes have been attached to large blocks of metal. The width of the blocks excesses the width of the graphene strips so that when graphene is completely released the metal electrodes are still supported. Otherwise, the sagging long suspended metal beam could cause the graphene to touch the substrate.

5.3 Fabrication processes

5.3.1 Four point probe structure fabrication

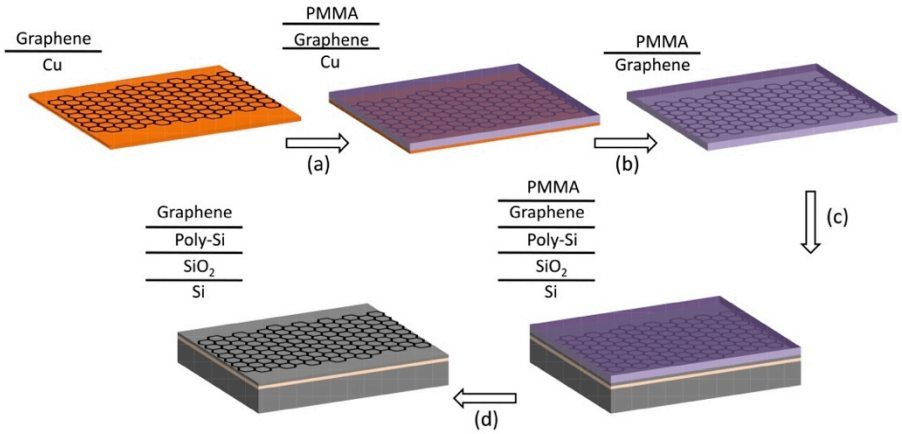

Figure 5.3: Transfer of graphene onto poly-Si/SiO_2/Si substrate. (a) Spin coating PMMA. (b) Etching backside graphene and copper. (c) Scooping graphene onto substrates. (d) Dissolving PMMA

The fabrication starts with transferring the CVD-grown graphene (Single layer graphene on copper foil, Graphene Laboratory, Inc) onto the poly-Si/SiO_2/Si substrate discussed in chapter 4. The transfer method inherits from the widely used poly(methyl methacrylate) (PMMA)-assisted transfer technique [149]. Figure 5.3 shows the schematics of the transfer technique. The monolayer graphene sheet has been grown on copper foil (purchased from Graphene Laboratories Inc.). Due to the nature of CVD process, graphene sheet covers both sides of the copper foil. To support the graphene sheet after copper foil is etched away, a thin layer of PMMA (~500nm) has to be spin coated on topside graphene (Figure 5.3(a)). To allow the spin coating, graphene/Cu sheet is fixed to a carrier wafer at four edges with tape to

adapt to the chuck of the photoresist spinner. Without baking, the PMMA/Graphene/Cu/Graphene has been taken in to reactive ion etching (RIE) system to etch the backside graphene and expose the copper layer for following copper etching procedure. Experiments show that 30s of O_2 plasma etching could effectively remove the backside graphene. Then the PMMA/graphene/Cu sheet has been put into 1M $FeCl_3$ solution to dissolve the copper foil (Figure 5.3(b)).

$$FeCl_3+Cu=>FeCl_2+CuCl \tag{5.1}$$

When placing the PMMA/graphene/Cu sheets into the $FeCl_3$ solution, care needs to be taken to make sure the PMMA-covered side is facing upward. The sheets should be floating on the surface of the $FeCl_3$ solution thanks to the surface tension. After about half hour, the copper would be removed completely and the PMMA/graphene sheet appears to be semi-transparent. Samples are then scooped up and placed onto the surface of clear DI-water to rinse $FeCl_3$. Such cleaning processes have been repeated for three times to make sure no $FeCl_3$ is left over the graphene surface. Finally, the samples are scooped up with the poly-Si/SiO_2/Si substrate. The samples are then left at room temperature for 24 hours to dry and allow graphene to form strong adhesion to the poly-Si surface (Figure 5.3(c)). The PMMA is finally removed by soaking the samples in acetone for 2 hours (Figure 5.3(d)).

Figure 5.4 shows the as transferred graphene. (a) is the image of graphene sheet on 75nm poly-Si/SiO_2/Si substrate. The illumination wavelength is about 600nm as described in chapter 4. Holes and contaminations have been observed. Limited by the contrast on poly-Si substrate, graphene sheets have also been transferred to 285nmSiO_2/Si for comparison, as shown in Figure 5.4(b). Clearly there are cracks in the sheet, which might originate from scratches or water surface tension-induced breakage during drying. Double layer patches scatter scarcely over the whole sheet accounting a small portion of the whole area as shown in the inset. There are also PMMA residues left that could lead to deterioration of the conductivity of graphene as mentioned in section 2.3.2 of chapter 2 [16]. To remove the PMMA residue as much as possible, the samples have been placed in furnace and annealed at 200°C for 2hours, which would not damage graphene [150]. Figure 5.4(c) shows the graphene sheet after annealing. Obviously, most PMMA particles have been removed.

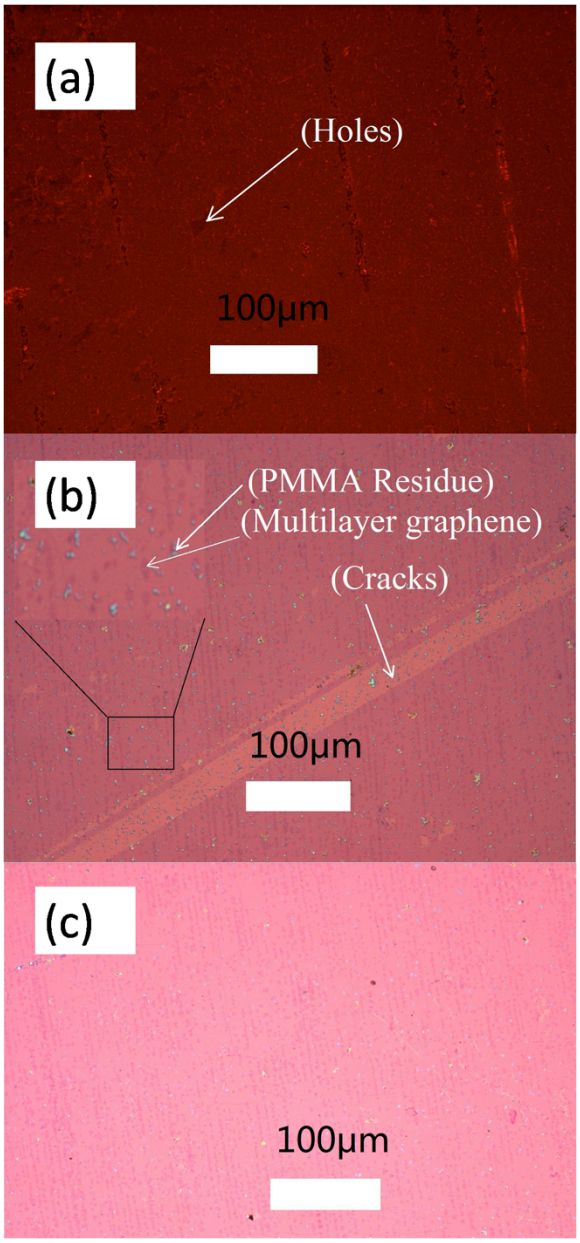

Figure 5.4: Optical image of graphene transferred to poly-Si/SiO_2/Si substrate (a), and 285nm SiO_2 substrate before (b) and after (c) annealing

After the transfer process (Figure 5.5(a)), about 1.7μm thick of AZ5214E image reversal photoresist has been spin coated on the samples and patterned with the first layer mask (grey squares in Figure 5.2(b)) so that the alignment squares area are exposed (see Figure B.1 for whole mask). Then the exposed poly-Si has been etched by argon milling to leave the alignment marks into the poly-Si layer. The reason for adding this step in is because the visibility of graphene is relatively poor, so that following photo masks cannot be effectively aligned to the graphene patterns. After

the alignment marks are patterned, another layer of positive photoresist (SPR350-1.2μm) has been spin coated on top of the graphene sheet and exposed (see Figure B.1). Such a layer of photoresist serves as protective layer for graphene etching. The unprotected part of graphene is then etched by 30s O_2 plasma and forms the graphene strip (Figure 5.5(b)). After that, a layer of AZ5214E is spin coated and exposed for metal lift-off (see Figure B.1). 1nm Cr/80nm Au, and 3nm Cr/100nm Au have been deposited by electron-evaporation for two different batches of devices respectively (Figure 5.5(c)). The samples have been soaked in acetone to remove the photoresist and lift-off the metal electrodes. The as-fabricated graphene strips are then ready for the release of graphene bridges (Figure 5.5(d)).

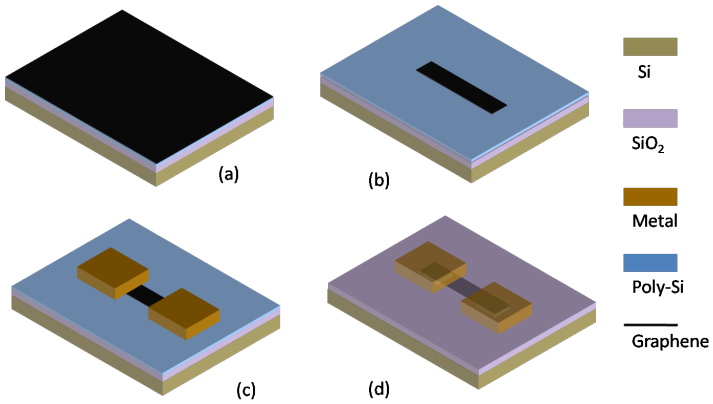

Figure 5.5: Fabrication process of suspended graphene bridges. (a) Graphene transferred on to 75nm poly-Si/100nm SiO_2/Si substrate. (b) Graphene patterned with oxygen plasma. (c) Metal lift-off. (d) Etching of poly-Si with XeF_2

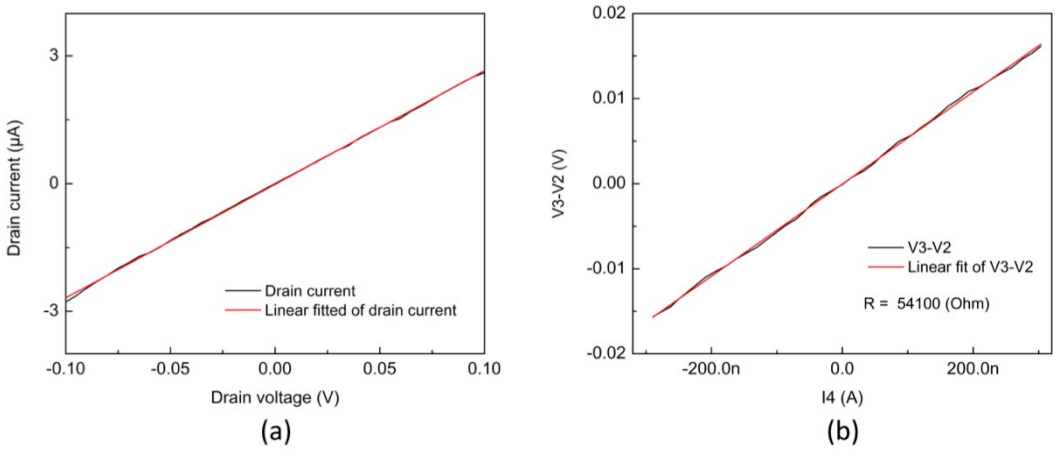

Figure 5.6: Two-probe I-V measurement (a) and four-probe I-V measurement of a graphene bridge before release

The I-V measurements have been conducted on the graphene strips at room temperature. Two adjacent electrodes have been used as source and drain respectively, and the Si substrate is used as a back gate. Figure 5.6(a) shows the measured drain current of a sample against drain voltage, with the gate voltage set to zero. As discussed in section 4.4 of chapter 4, the undoped poly-Si layer does not conduct current and will not affect the band structure of graphene. The measured 2-probe results show that a large portion of the strips does not conduct electric current. For a sample with all three channels conductive, the four-probe measurement has been performed as shown in Figure 5.6(b), the sheet resistance is about 13.5kΩ/square. For other conducting graphene strips, the 2-probe resistances are random value as plotted in Figure 5.7, which, in contrast to other report [148], does not show an obvious dependence on the length of the channel, suggesting that the random contact resistance is large and dominant. Those devices that do not conduct current at all are solid evidence to support that the poly-Si is indeed non-conductive and does not obscure the measurement of the graphene channel.

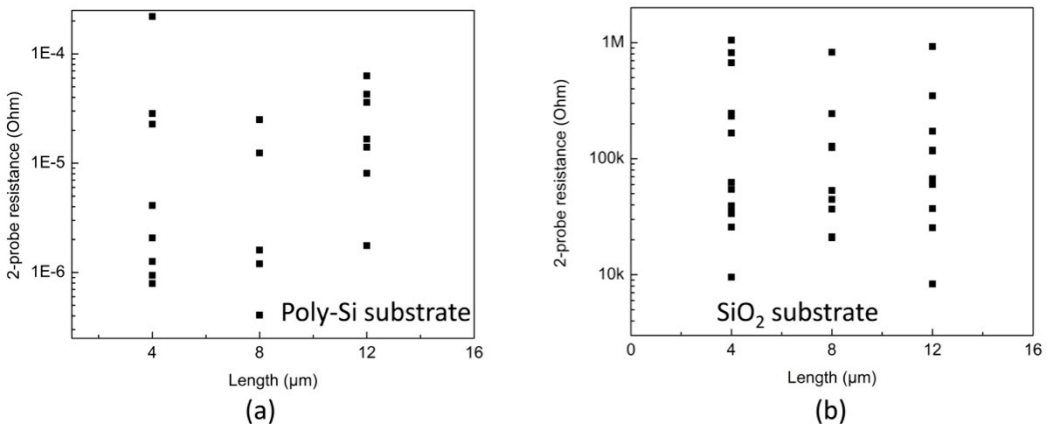

Figure 5.7: Two-probe resistance of graphene bridges on poly-Si and SiO_2 substrate

Table 5.1: List of conducting bridges/total bridges of different types of substrates and Metal thickness

Substrate / Metal	285nm SiO_2/Si	90nm SiO_2/Si	75nm poly-Si/100nm SiO_2/Si
1nm Cr/ 80nm Au	26/120	9/40	13/240
3nm Cr/ 100nm Au	5/120	23/120	7/240

Table 5.1 lists the number of conducting bridges and total number of bridges for different types of substrate and different thickness of metal. Figure 5.8(a) plots the histogram of percentages of conducting graphene channels. It can be seen that thicker metal leads to lower chance of conducting for all three types of substrate. If all the graphene channels on SiO_2 are counted together, it is observed that the graphene channels on SiO_2 has higher chance of being conducting (Figure 5.8(b)). The failure of conducting current originates from different sources. One obvious cause is the cracks formed during the transfer process as shown in Figure 5.4. On the other hand, the lower yield of graphene on poly-Si suggests something else. It has been shown that the metallization condition has crucial effect on the contact resistance because the metal atom bombarding the graphene sheet with high energy will introduce defects to graphene and greatly reduce the contact quality [151]. The surface roughness of poly-Si is worse than SiO_2 as measured in section 4.3.2 of chapter 4, therefore, the graphene sheets may not be well supported by the poly-Si surface and are more susceptible to the metal atoms.

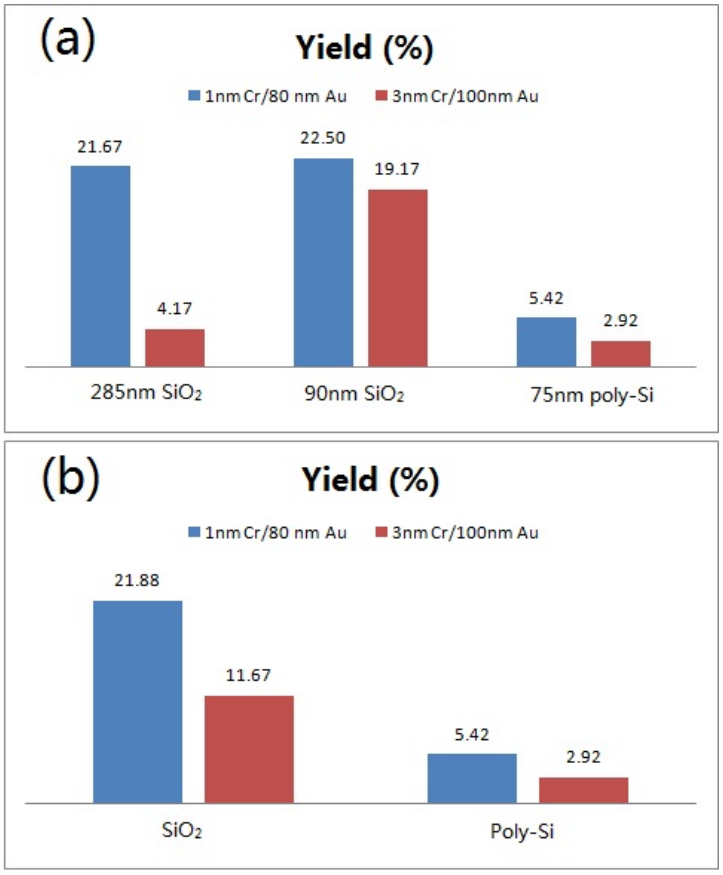

Figure 5.8: Histogram of conducting channels

5.3.2 Release of graphene bridges

Based on the as-fabricated graphene four-point probe structure, the poly-Si layer can be etched to release the graphene bridges. The etching of poly-Si can be done in liquid etchant or in vapour phase by XeF_2. The vapour phase release is of great advantage in the sense of avoiding liquid surface tension and erosion to metal electrodes.

XeF_2 is a highly reactive isotropic gaseous etchant, popularly used in the production of MEMS for etching various forms of silicon [152]. During etching, XeF_2 molecules absorb to the surface of silicon and decompose into Xenon (Xe) and fluorine (F) atoms. The fluorine, which is the main functioning radical in silicon etching, reacts with silicon. The formula describing the reaction process is

$$2XeF_2+Si=>SiF_4+2Xe \tag{5.2}$$

The reaction product SiF_4 is also in gaseous phase at room temperature, therefore, it is carried away by the gas flow to exhaust line and does not block further reaction. Thus, the etching rate of Si with XeF_2 is considerably fast. XeF_2 etches Si with extremely high selective ratio to other commonly used materials such as SiO_2 and metals [152], a favourable characteristic for fabrication.

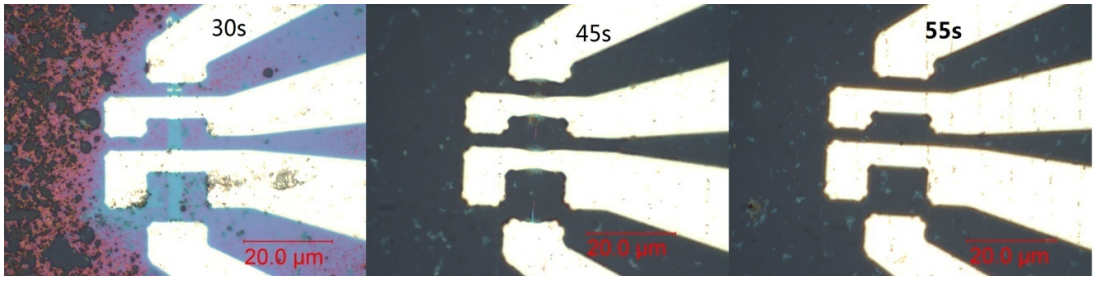

Figure 5.9: The images of graphene bridge after being etched with XeF_2 for different time

The graphene bridges have been released with the MiNi XeF_2 etch system from MEMSTAR company. The etching pressure was set at 2Torr and the flow rate 50sccm. Such a low pressure has been used to reduce the etching rate and prevent excessive undercut of the electrodes. Figure 5.9 shows the optical image of graphene bridge etched for 30, 45 and 55s respectively. The completion of release can be verified by checking the residual of poly-Si underneath graphene under optical

microscope. In the middle image, there is still a dim line of poly-Si lift under the central line of graphene, which indicates that the XeF_2 does not penetrate the graphene sheet nor the interface between graphene and poly-Si, but consuming poly-Si from two sides. The total etch time should be between 45 and 55s, equivalent to an etch rate of 18~22 nm/s. The middle figure also shows that poly-Si under the middle part of the graphene is etched faster than that under the two ends.

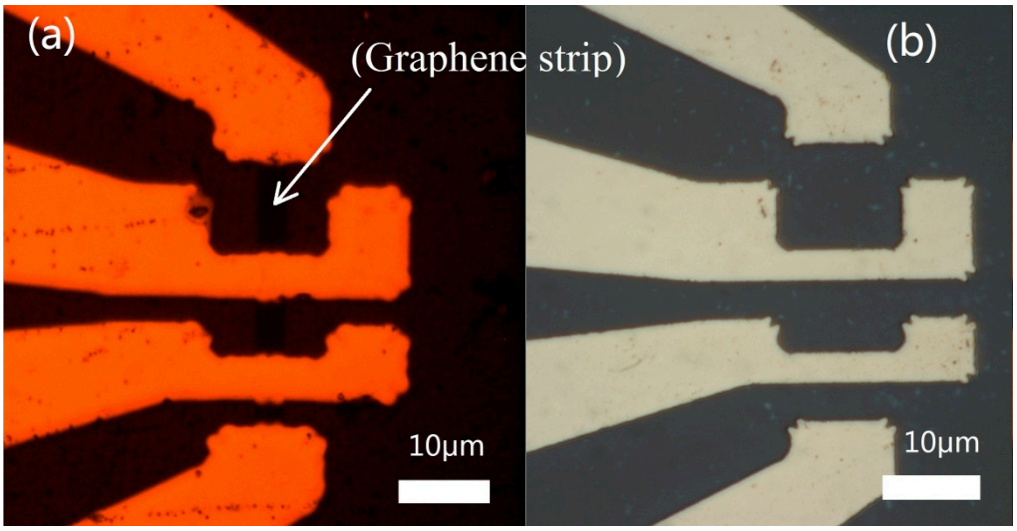

Figure 5.10: Optical image of bridges before and after XeF_2 Etching

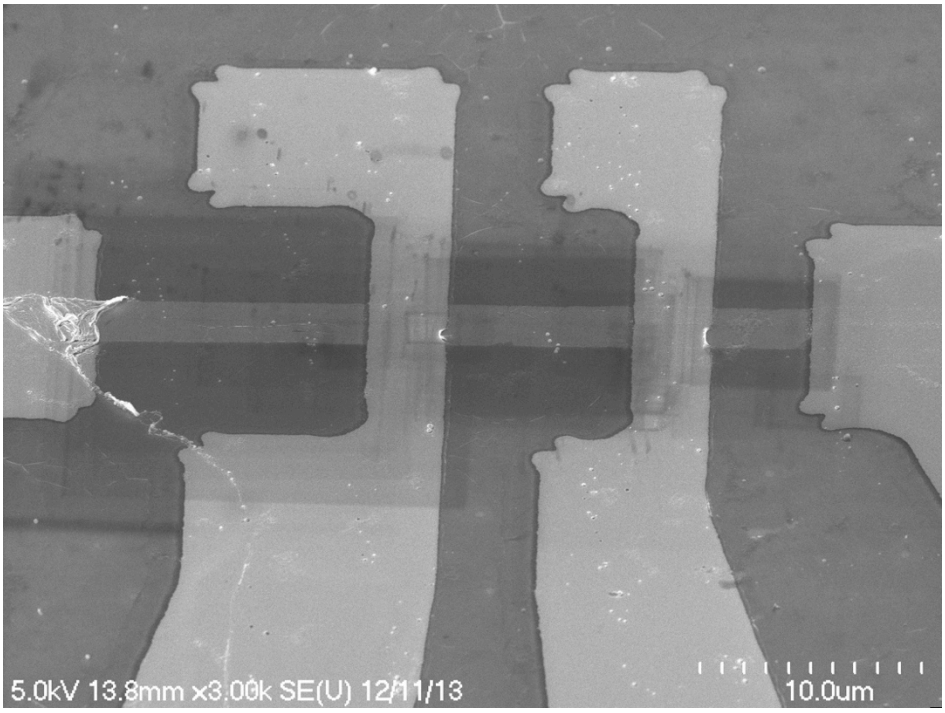

Figure 5.11: SEM image of graphene bridge after release

Figure 5.10 compares the optical image of graphene bridges before (a) and after release (b). In (a), the illumination is 600nm. The graphene strip is observed to be darker than the poly-Si substrate, complying with the theoretical analysis in chapter 4. After being etched by XeF_2, graphene becomes almost completely transparent as nothing can be observed between the electrodes in Figure 5.10(b). SEM images have been taken at this device to confirm the existence of graphene bridges as shown in Figure 5.11. Those darker areas in the background originate from the electron charging effect during imaging, as the sample is not coated with metal so as not to damage the graphene sheet. No obvious ripples can be seen in the graphene bridges, in contrast to those reported in [37].

5.3.3 Fluorination of graphene

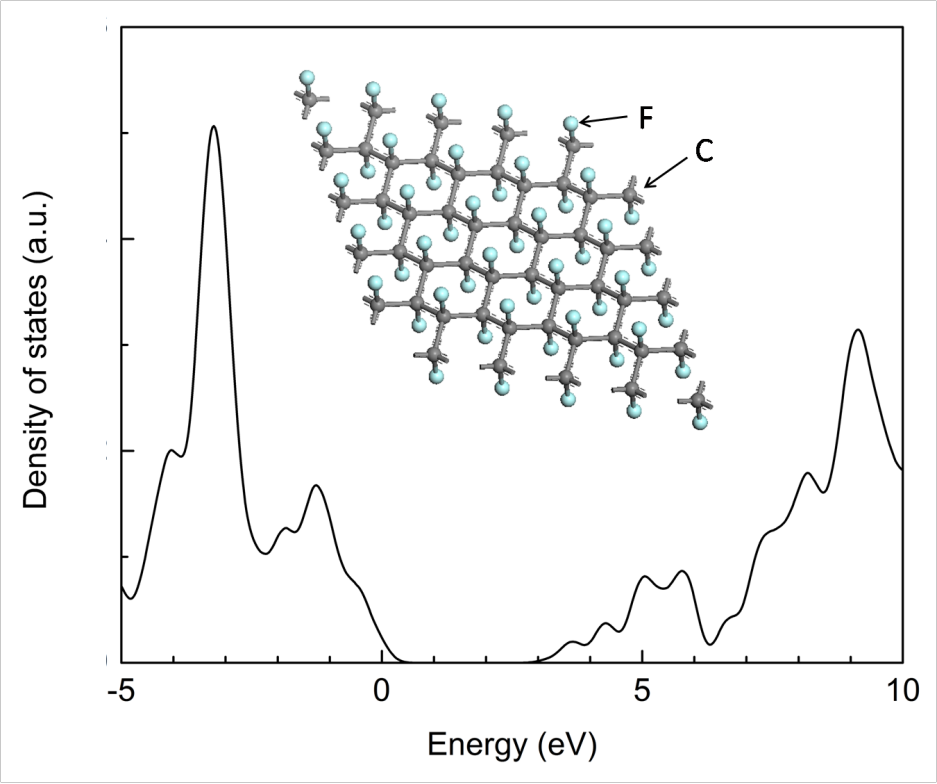

Figure 5.12: Electron density of states of CF

The XeF_2 does not etch the graphene skeleton, however, the fluorine atom will form chemical bonds to the graphene sheet thus modify the electrical properties of graphene [47], such process is called fluorination of graphene. Fluorination of graphene has been one of the functionalisation techniques of graphite-like materials

including oxidization [46], hydrogenation [79], and so on. Fluorination of carbon materials dates back more than half a century ago. Early stage of study has been focused on graphite, and then on carbon nanotube [153][154][155]. The XeF_2 has been found to be a strong fluorination agent without etching the graphene. J. T. Robinson et al performed single side fluorination of graphene/Cu and double side fluorination on graphene transferred SOI wafer by XeF_2 [99]. The double side fluorination is enabled possible by etching pinholes in the transferred graphene which lets the gas to pass to the underlying silicon. Fluorination is an effective way to tune the properties of graphene in term of opening bandgap [47][156]. Theoretical calculations shows that the bandgap width increases with larger fluorine coverage [99]. In [99], the fluorine content is found to saturate at 25% atomic concentration for single side fluorination and 50% for double side fluorination. Figure 5.12 plots the density of states of fluorinated graphene with 50% fluorine atoms, which has been calculated by CASTEP applying density functional theory as described in chapter 2. The inset shows the lattice configuration of fully fluorinated graphene [157]. It can be clearly observed that, there is a band gap of about 2.7eV, which is consistent with previous calculations [99][157]. The Fermi energy level enters the top of the valence band, suggesting that the Fluorination tends to dope graphene with holes.

5.3.4 De-fluorination of graphene

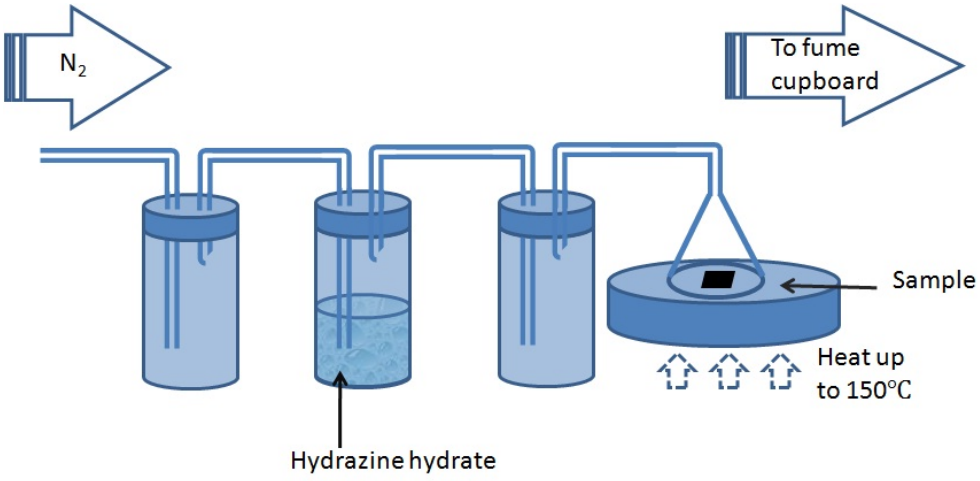

Figure 5.13: Setup for hydrazine reduction

The ideal de-fluorination process should remove all the fluorine atoms while maintaining the hexagonal skeleton of graphene. There are two types of de-fluorination techniques that have been reported. One is the thermal annealing at around 400°C. As the binding energy of C-F bond is relatively low, when the fluorine atoms acquire enough thermal energy, they break from the basal plane of graphene. The alternative way involves the reaction of reductive agent with the fluorinated graphene. H_2/Ar is a commonly used combination of gases. However, they also require a high temperature at around 400°C for about 4 hours and does not recover the conductivity of graphene [99]. A more reductive agent, hydrazine, would only require about 100°C and completely reduce the fluorinated graphene in 24 hours, although the toxicity of hydrazine is a drawback.

Figure 5.13 shows the setup designed for hydrazine vapour de-fluorination of the fluorine graphene. The hydrazine used has been in aqueous form which is much safer to handle. The hydrazine vapour is carried out of the hydrate by N_2 gas. The whole bubbling system consists of three bubbler serving different purposes. The first bubbler is a safety buffer in case the N_2 line pressure drop below the atmospheric pressure. The third bubbler serves as a condenser that removes water vapour from the gas flow and prevents liquid condensation on the samples which may break the graphene by the capillary force when the liquid evaporates again. The sample is placed on a hotplate and the temperature is set at 160°C to facilitate reaction. Such a temperature also prevents water condensation. The gas is introduced to the surface of the sample by a downward facing funnel placed over the top of the sample.

5.4 Results and discussion

5.4.1 Raman characterisation

Figure 5.14(a) shows the Raman spectrum taken at four key nodes of the fabrication process. (a) is taken after the graphene transfer. Only two bands, G (1580cm^{-1}) and 2D (2750cm^{-1}), have been observed. The symmetry of 2D band and the intensity ratio of 2D band to G band suggests that the as-transferred graphene has good quality [115], and the graphene sheet is indeed monolayer as discussed in chapter 3. After patterning the graphene with O_2 plasma (b), a D band (1350cm^{-1}) emerges and the

base line rises towards larger wavelength. The D peak is defects-related, however, the appearance of it here only implies that there are defects existing under the laser spot of the Raman system.

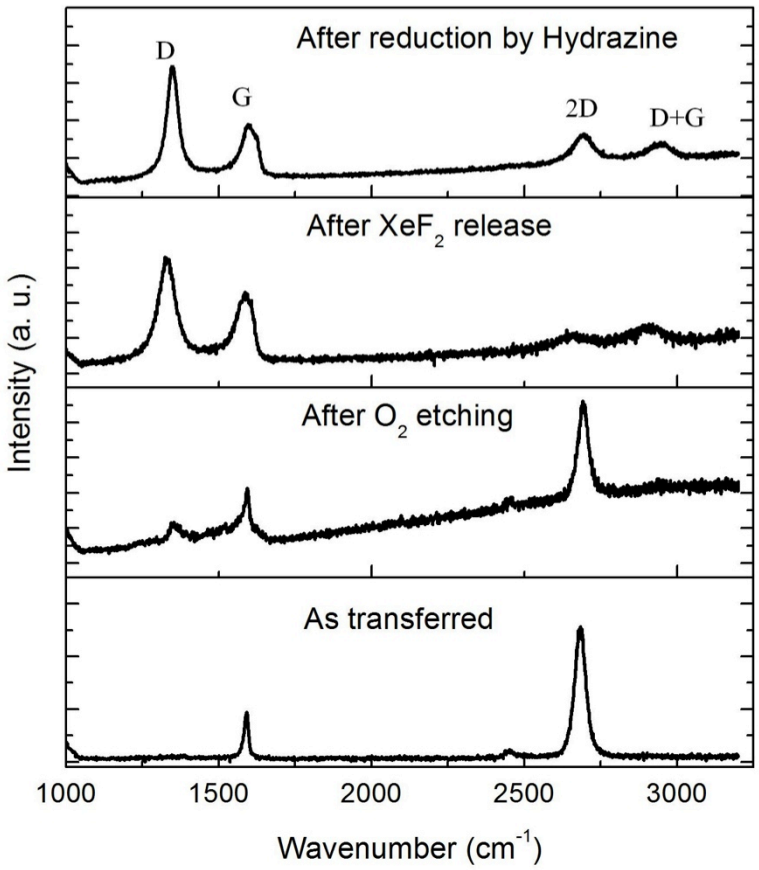

Figure 5.14: Raman spectrum of graphene bridge taken at four key nodes of the fabrication process

This D band most likely comes from the edge effect of graphene, since the intensity ratio of 2D band and G band has not changed substantially [102]. Thus, the internal graphene lattice is still intact. After exposure to XeF_2 for 55s with a flow rate of 50sccm at 2Torr, the D peak protrudes to higher than a broadened G peak (c), and the 2D peak has almost disappeared. All these features correspond to structural disorder [156]. The defects are induced by the fluorination process where the fluorine atoms bond to the carbon atoms, thus changing the sp^2 carbon-carbon bond, but do not damage the hexagonal skeleton of graphene lattice [99]. The hydrazine is a highly reductive agent that removes the fluorine atoms from the graphene sheet, which is called a de-fluorination process. The hydrazine reduction has been the most effective approach to remove fluorine atoms while keeping the graphene's unique lattice [99].

The Raman spectrum after hydrazine reduction shows the 2D band is recovered, suggesting partial recovery of the sp^2 bond lattice (d).

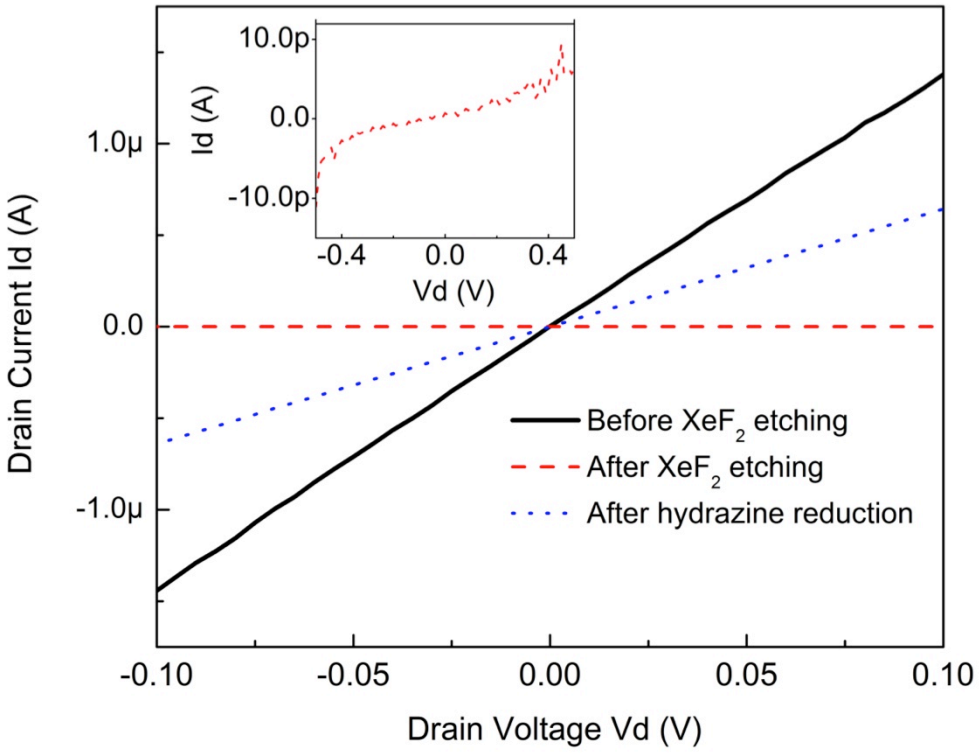

Figure 5.15: I-V characteristics before and after XeF_2 etching, as well as after hydrazine reduction

Figure 5.15 plots the two-probe I-V measurement results of the graphene bridges before (black solid line) and after the XeF_2 etching (red dashed line), as well as after hydrazine reduction (blue dash-dotted line). The conductivity severely deteriorates after fluorination due to the bandgap opening in fluorinated graphene, as rescaled for clarity in the inset. The sheet resistance has increased by approximately 15GΩ/square assuming the contact resistance has not been affected by the fluorination process. After 24 hours reduction by hydrazine, the conductivity is largely restored, in consistency with the Raman spectroscopy. The conductivity recovery may have also benefitted from unintentional doping by the N_2 gas that carries XeF_2. Other substance such as water molecular may also contribute to the doping [99]. It should be pointed out that, although hydrazine may not be able to recovered the conductance due to lattice defects caused by the fluorination and de-fluorinated process, it does not affect the Young's modulus much [47], which is crucial for retaining the anticipated performance of graphene resonators.

Figure 5.16 plots the gate effect on the drain current of a graphene bridge of 12μm long. The drain voltage is fixed at 0.1V. The conductance decreases with increasing gate voltage, which suggests that the as fabricated graphene has been doped with holes. The charge neutrality point cannot be observed when the gate voltage is in -5~5V range. A even larger magnitude of gate voltage has not been applied because the electrostatic force could pull the graphene towards the substrate and even damage it [51]. As can be seen in section 5.3.3, the fluorine atoms attached to carbon atoms in graphene tends to dope holes in graphene as the Fermi level resides in the conduction band. Moreover, other surrounding substances like water and O_2 also dope the graphene with holes.

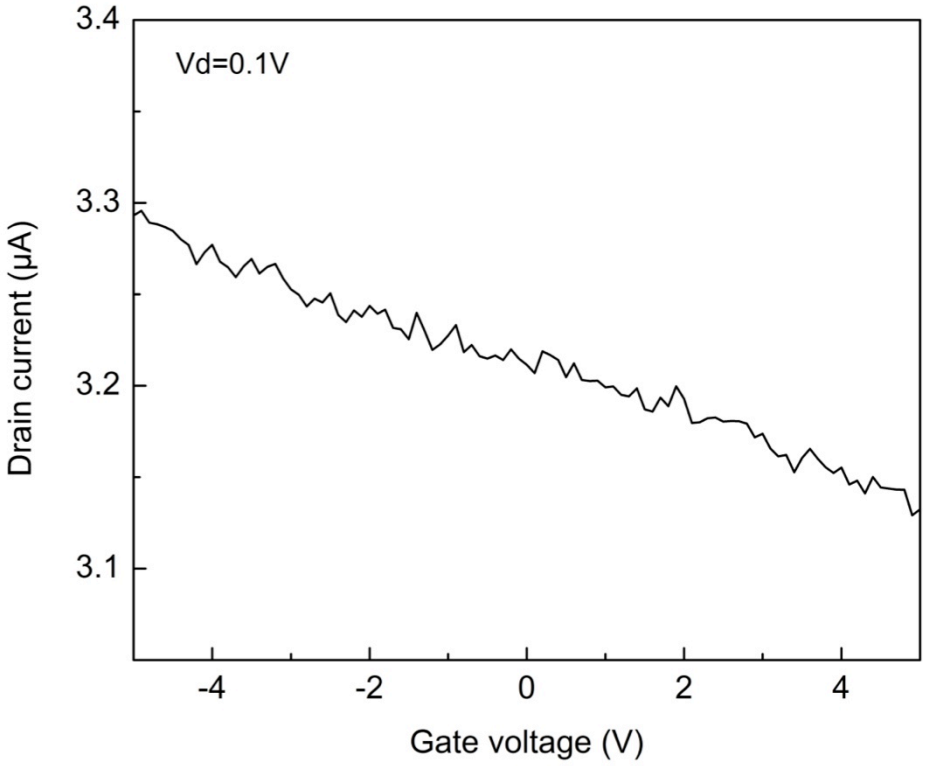

Figure 5.16: Gate effect on the free standing de-fluorinated graphene bridge

5.5 Conclusion

This chapter has described the design and fabrication of suspended graphene structures from CVD-grown graphene sheet on copper foil. The fabrication process is intended for mass production. The poly-Si film has been used as sacrificial layer and etched with XeF_2 in vapour phase. The major issue of erosive HF etching and

capillary force has been solved. No breakage of the graphene bridges has happened during the XeF_2 release process, which is key to improve the yield of graphene resonators.

The graphene bridges has been designed and arranged in the four-point probe structure, which facilitates the in-process monitoring of the quality of graphene sheet. The graphene sheet has been fluorinated by XeF_2, which opens a large bandgap in it. The bandgap width largely depends on the amount of fluorine atoms and severely deteriorates the conductance of the graphene, which hinders the electrical measurement of the graphene resonators. Reduction by hydrazine at 160°C can largely restore the conductivity of graphene sheet, enabling the electrical characterisation of resonance of the suspended graphene bridges. Although the conductivity recovery is not complete, the mechanical properties of graphene is reported to remain almost the same, thus the exceptional properties of the graphene resonators can still be anticipated.

A problem raised in the fabrication process is the low yield of conducting graphene bridges after the metallization. Evidence shows that longer metal deposition would reduce the proportion of conducting graphene channels and the total two-probe resistance is not prominently related to the length of the bridges, suggesting the contact resistance is the major contributor to the total resistance. The contact resistance is large because the graphene sheets are too thin to withstand long-term metal atom bombardment. However, this damage could be improved if a much better metal deposition rate control is available.

Chapter 6

Resonance measurement of graphene bridge resonator

6.1 Introduction

In this chapter, we discuss the electrical measurement of the resonance of the fabricated graphene bridge resonators as described in chapter 5 with the single source current mixing measurement technique described in chapter 3. The resonant frequency of graphene resonator is highly dependent on the built-in stress, which means the performance of the graphene resonators can be effectively manipulated through adjusting the electrostatically induced stress. The frequency tuning effect can be clearly observed in the graphene resonators, which offers flexibility in applications. Thanks to the electrical contacts made to the graphene bridges, its mechanical behaviour can be tested electrically. Compared to optical measurement technique [19], electrical measurement enables the graphene resonators to be integrated monolithically in a single system in the future graphene resonator-based sensors or RF components. Although the resonance of a graphene bridge resembles resonators made of other materials in many ways [158][159], it also possesses its uniqueness due to the ultra-minimum thickness. Monolayer graphene is an ideal two-dimensional material that also has no bending stiffness.

The most intriguing feature observed in the characterisation results of the graphene resonators is the large amplitude of second order harmonics. The frequency and amplitude of second mode resonance are more sensitive to both the DC bias as well as the physical properties change such as the mass density. In this chapter, It will be theoretically proved that the appearance of strong higher mode resonance has its root in the distribution of electrostatic voltage difference between graphene and substrate, thus the electrostatic force configuration. The non-uniform electrostatic force along the graphene bridge could drive the second order harmonic into resonance because the projected actuation force onto the second order mode is not zero. To probe into the actuation mechanism, finite element analysis (FEA) has been conducted to look

at the transient forced response of the graphene bridges. Based on the theory, it is proposed that the single source actuation and measurement technique could effectively actuate fundamental or second order mode resonance. Controllable actuation of higher mode resonance could lead to improvement of the sensitivity of graphene resonator-based sensors.

6.2 Modelling of graphene resonators

6.2.1 Newtonian equations

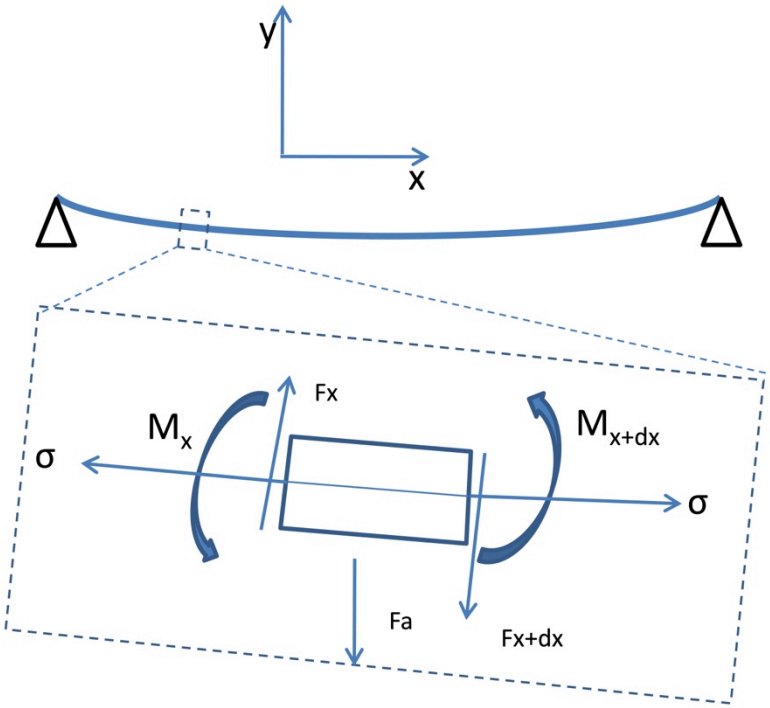

Figure 6.1: Force and moment balance on an infinitesimal section of doubly clamped graphene bridge

To understand the behaviour of graphene resonators, one should look at the dynamics of its resonance. Figure 6.1 shows the schematic drawing of a doubly clamped beam, whose width, thickness, and length are W, t_g, and L respectively. Following the analysis in [160], the y-direction of motion for an infinitesimal section of the beam is considered, the dynamic equation of the small section can be obtained according to Newton's Law. When the maximum deflection of the beam satisfies $w_{max} \ll L$, it is plausible to omit the in-plane displacement, that is to say, only the flexural

movement will be taken into consideration. Therefore, the motion of the infinitesimal section is governed by

$$F|_x - F|_{x+dx} - F_a dx - \sigma t_g W w_x|_x + \sigma t_g W w_x|_{x+dx} - \alpha w_t dx = \rho t_g W dx w_{tt} \tag{6.1}$$

Where $F|_x$ is the sheer force perpendicular to the basal plane of the graphene sheet at point x. $M|_x$ is the bending moment at point x. σ is the stress in the graphene sheet. σ includes the built-in stress as well as the deflection-induced stress. The build-in tension means that the graphene is pre-stretched [38]. The pre-stretching could possibly have arisen from the transfer process. When water recedes from the graphene/SiO_2/water interface, the graphene is pulled by capillary force. Moreover, at both ends of the graphene sheet, the Van Del Waals force between graphene and the anchoring metal electrodes also contributes to the pre-stretching of the graphene sheet. The deflection-induced stress could lead to the interaction between different modes [161]. In small deflection regime, such stress can be neglected. w_x and w_t are the first order differentiation of the vertical displacement with respect to distance and time respectively, and so forth for w_{xx} and w_{tt}. F_a represents the electrostatic force subjected by the infinitesimal section. Normally, the electrostatic voltage contains a DC component and an AC component as elaborated in chapter 3, so does the electrostatic force. The DC part is intended to adjust the stress in the graphene beam in order to tune the resonance frequency. ρ is the density of grahene. α denotes the damping coefficient. Dividing both sides of equation 6.1 by dx, it is obtained that

$$-F_x - F_a + \sigma t_g W w_{xx} - \alpha w_x = \rho t_g W w_{tt} \tag{6.2}$$

According to the balance of bending moment

$$-M|_x + M|_{x+dx} + F|_x dx + \frac{\rho dx^2}{2} = 0 \tag{6.3}$$

Dividing both sides by dx after omitting the fourth term on the left side, which is the higher order infinitesimal quantity, then

$$F|_x = -M_x \tag{6.4}$$

Replacing $F|_x$ in equation 6.2 with $-M_x$, the equation transforms to

$$M_{xx} + \sigma t_g W w_{xx} - \alpha w_x = F_a + \rho t_g W w_{tt} \tag{6.5}$$

Because

$$M_{xx} = E\boldsymbol{I} w_{xxxx} \tag{6.6}$$

Where $\boldsymbol{I}$ is the area moment of inertia, then the motion of the infinitesimal section should satisfy

$$E\mathrm{I} w_{xxxx} + \sigma t_g W w_{xx} - \alpha w_x = F_a + \rho t_g W dx w_{tt} \tag{6.7}$$

During vibration, the beam is elongated, so the stress σ is also changing. Because the strain is

$$\epsilon = \frac{\int_0^L \sqrt{1 + {w_x}^2}\, dx - L}{L} \approx \frac{\int_0^L {w_x}^2\, dx}{2L} \tag{6.8}$$

The net stress is

$$\sigma = \sigma_0 + \frac{\int_0^L {w_x}^2\, dx}{2LE} \tag{6.9}$$

Thus we have the final equation for the beam's movement

$$\begin{aligned} E\boldsymbol{I} w_{xxxx} + (\sigma_0 + \frac{\int_0^L {w_x}^2\, dx}{2LE}) t_g W w_{xx} - \alpha w_x \\ = F_a + \rho t_g W dx w_{tt} \end{aligned} \tag{6.10}$$

6.2.2 Fundamental frequency

Due to the small bending stiffness of graphene, the first term in equation 6.10 can be neglected. If the vibration amplitude is sufficiently small, the built-in tension dominates, and the second term on the right side of equation 6.9 can also be omitted. Generally speaking, the resonance of graphene resembles a string more than a solid beam. The fundamental frequency of the graphene resonator is then

$$f_0 = \frac{1}{2L}\sqrt{\frac{\sigma}{\rho}} \tag{6.11}$$

When the DC components of the electrostatic force is applied on the gate to tune the resonance, the fundamental frequency can be expressed as [36]

$$f(V_g) = \frac{1}{2L}\sqrt{\frac{\sigma_0 + \sigma(V_{DC})}{\rho}} \tag{6.12}$$

Where $\sigma(V_{DC})$ is the stress related to the electrostatic force corresponding to DC voltage. In some literature, the following equation is also widely used [19][85].

$$f_0 = \left\{\left[A\left(\frac{E}{\rho}\right)^{\frac{1}{2}}\frac{t_g}{L^2}\right]^2 + \frac{A^2 0.57T}{\rho L^2 W t_g}\right\}^{\frac{1}{2}} \tag{6.13}$$

Where A is about 1.03 for doubly clamped beam, and T represents the tension. This equation is derived for an Euler-Bernoulli beam with thickness t_g. However, for single layer graphene, the thickness is only 3.34Å, so the first term on the right side is small enough to be omitted, and equation 6.13 becomes equivalent to equation 6.11.

6.3 Electrical characterisation results

6.3.1 Characterisation conditions

The as-fabricated graphene resonators described in chapter 5 are ready to be tested using the current mixing technique elaborated in chapter 3. The single source setup has been implemented for its simplicity. The source electrode of the graphene resonator has been connected to ground through a 390Ω resistor. For frequency modulation (FM) signal actuation, the drain electrode is fed with a FM signal, and the gate is fixed at a DC voltage intended for frequency tuning $V_g = V_{DC}$. The pressure in vacuum chamber can be pumped down to about 3mbar. The samples are left at room temperature, which is approximately 290K. The frequency deviation of the FM signal is 100kHz, and its amplitude (the actuation voltage) is either swept with fixed gate voltage or kept constant for gate voltage sweeping. For gate voltage sweep, the actuation has been set to 400mV. The modulation wave from the reference output socket of the lock-in amplifier has a frequency of 616.3Hz. The time constant of the lock-in amplifier is set to 0.1s and sensitivity to 500μV. Amplitude modulation (AM) signal has also been used to actuate the graphene resonators. The

modulation frequency is the same as FM signal, and the AM modulation depth is 50%.

6.3.2 Gate voltage sweep with FM actuation

Figure 6.2 shows the measured mixed current amplitude at 616.3Hz of a graphene resonator that is 2μm wide and 12μm long for different gate voltages with a fixed actuation voltage of 400mV (peak to peak voltage of the FM carrier wave). Clearly four bands can be observed at zero gate voltage. The four bands are labelled as A, B, C, and D respectively. At zero gate voltage, band C appears to have a small peak superimposed on the larger peak. The smaller peak is denoted as C' in the figure. It can be observed that the shapes of the peaks are asymmetric, skewing to the left for A, B, and D peaks. Such line shapes are characteristic of the amplitude-frequency relationship of a damped resonator with large damping coefficient [162], suggesting energy loss is quick due to the characterisation environment.

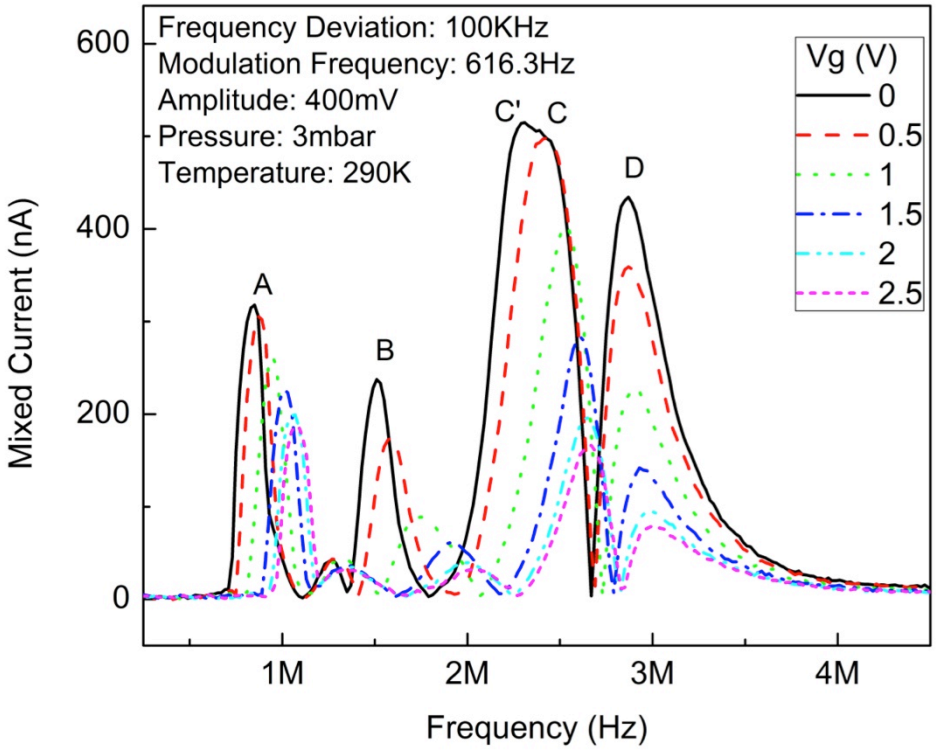

Figure 6.2: Mixed current against FM frequency with different gate voltage, measured with the setup discussed in section 3.4.6

The frequency and amplitude of the bands shown in Figure 6.2 can be extracted out. The frequency of each band against the gate voltage has been plotted onto right axis of Figure 6.3(a). The left axis of (a) plots the frequency shifts with respect to frequency at zero gate voltage. The frequency of band B is most susceptible to the gate voltage, and its frequency shift nearly doubles that of band A. Band C and band D change less than 10%. Since in the graphene resonator, components that contribute to measured peaks include not only the graphene bridge, but also the undercut metal electrodes at both ends that form cantilever resonators, those peaks can be distinguished by comparing the gate tuning effects. The peaks from the metal electrodes should be less responsive to the DC-induced stress due to their large thickness in contrast to graphene bridge, as reported in other articles [34]. Therefore, band A comes from the graphene bridge. B should be also assigned to graphene bridge instead of only band A, as will be discussed later.

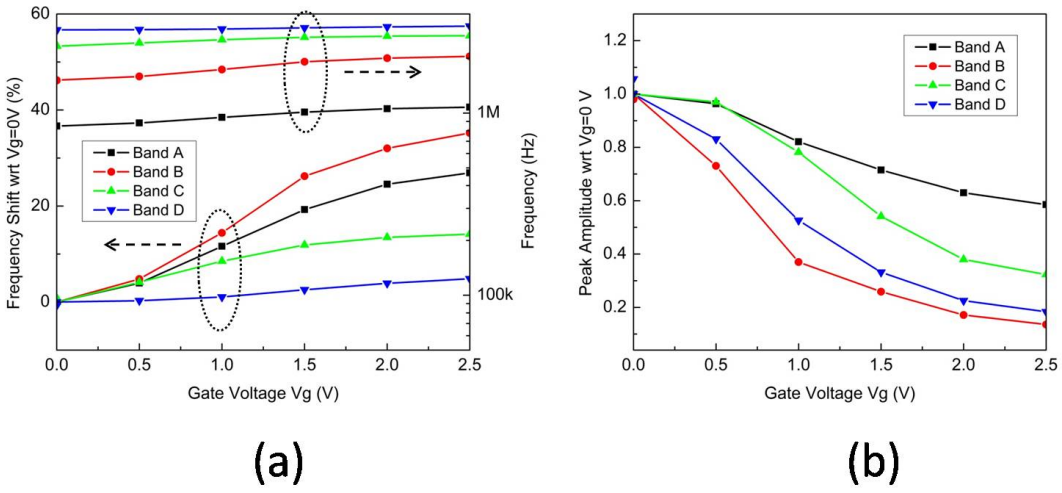

Figure 6.3: Extracted frequency shift and peak amplitude for different gate voltage

The fundamental frequency shift of graphene resonator under tuning is indeed proportional to the square root of the electrostatic force-induced tension $\sigma(V_g)$ by $f_0 = \sqrt{\sigma_0 + \sigma(V_g)/\rho}\,/2L$ [36], as seen from the black curve in Figure 6.3(a). Figure 6.3(b) plots the amplitude of the bands at different gate voltage V_g normalized to $V_g = 0$V. Band B drops most rapidly with increasing gate voltage, or equivalently, with the electrostatic force-induced stress. Moreover, as discussed in chapter 5, the graphene bridge is p-doped after the final fabrication step, which is the

de-fluorination process, so that increasing the gate voltage would decrease the charge carrier concentration in graphene, thus reducing the conductivity of the graphene bridge. Therefore, the gate effect also contributes to amplitude attenuation. However, the maximum conductivity loss at 2.5V gate voltage is only 1% compared with zero gate voltage. Therefore, the amplitude decrease mainly comes from the increased stress in graphene.

6.3.3 Actuation voltage sweep with FM actuation

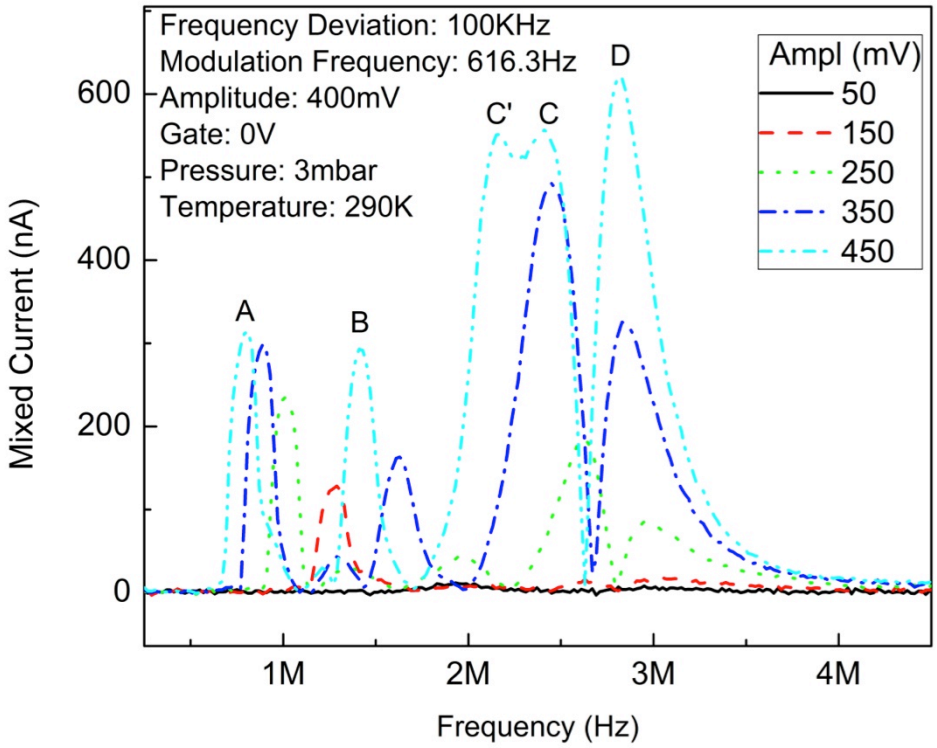

Figure 6.4: Mixed current against frequency with different FM actuation voltage

Figure 6.4 shows the measured mixed current with different actuation voltage, and the gate voltage is fixed at zero. At lower actuation voltage (50mV), only band A is observed. At the largest actuation voltage been applied (450mV), four bands are observed and the C' peak emerges again and becomes even more prominent than in the 400mV curve in Figure 6.2. The peak amplitude and frequency of the bands are extracted out and plotted in Figure 6.5(a). The right hand side axis is the frequency, and the left hand side axis is the frequency shift with respect to the peak frequencies of 450mV actuation voltage since at lower voltages (<150mV), the signals from

bands B, C, and D are too small to be identified. Obviously, band C and D shift less than 10%, while band A and band B are much more responsive to the actuation voltage. Figure 6.5(b) plots the measured peak current against the actuation voltage. The resonance amplitude of band A increases linearly at the beginning and then starts to cross over at 250mV actuation voltage due to nonlinearity [91]. The increase rate of amplitude from band B at 250mV-450mV resembles that of band A at 50mV-250mV, however, band B does not enter the nonlinear regime even at the largest actuation voltage being applied, which makes it possible for the amplitude of band B to catch up with band A.

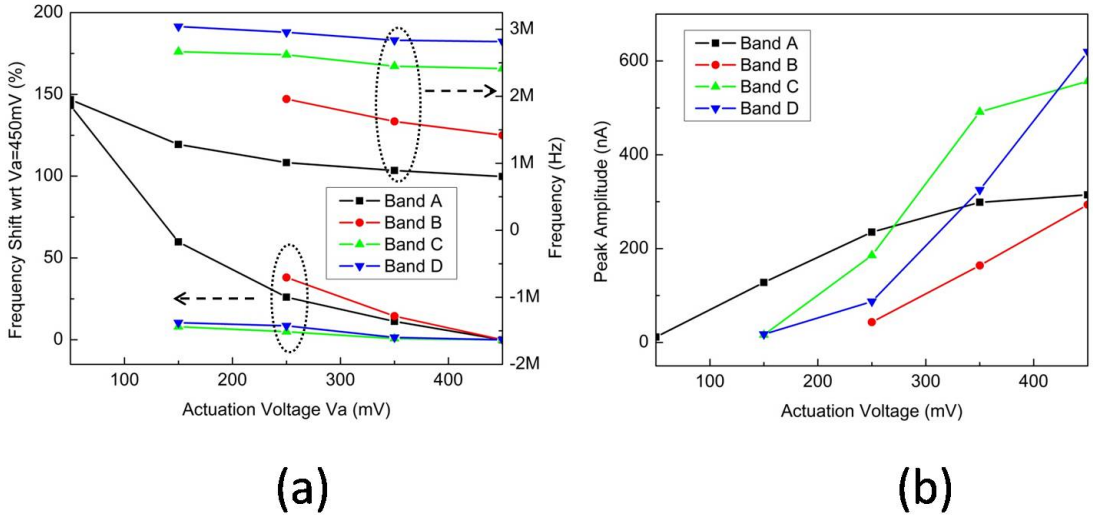

Figure 6.5: Extracted frequency shift and peak amplitude for different actuation voltage

Table 6.1 Frequency and quality factor of observed bands at 450mV actuation voltage

	Band A	Band B	Band C'	Band C	Band D
Frequency (MHz)	0.792	1.42	2.15	2.42	2.83
Quality factor	5.02	8.07	--	--	8.22

Table 6.1 lists the frequency and quality factor of the visible peaks at 450mV actuation voltage. The frequencies of band A, B, and C' have a relationship of $f_A \approx f_B/2 \approx f_{C'}/3$. As mentioned in the above discussion, the frequency shift of band B nearly doubles that of A upon gate tuning. The strong coupling of band A and band B prove that band A and B correspond to the fundamental frequency and second harmonics of graphene resonator respectively, while band C' could be the

third order harmonics according to its frequency location. Since the actuation voltage affects frequency of the resonance, the frequency at 50mV has been taken as the best evaluation of the fundamental frequency, which is about 1.94MHz. The fundamental frequency is lower than other resonators because of its larger dimension. The fundamental frequency can be simply modelled as $f_0 = \sqrt{\sigma_0/\rho}\,/2L$ at zero gate voltage, assuming the density of graphene can take the value of graphite 2200kg/m^3, the build-in stress in graphene is estimated to be 4.8MPa. The quality factor of a peak can be estimated by the ratio of its frequency f_{center} and its width f_{width} as $Q = f_{center}/f_{width}$. Because the peaks in the measurements have long tails on the right slope that obscure the evaluation of width, the full-width-at-half-maximum (FWHM) of a band f_{FWHM} has been used as the width of the band. Both the fundamental peak and the second order peak have quality factors below 10.

6.3.4 AM signal actuation

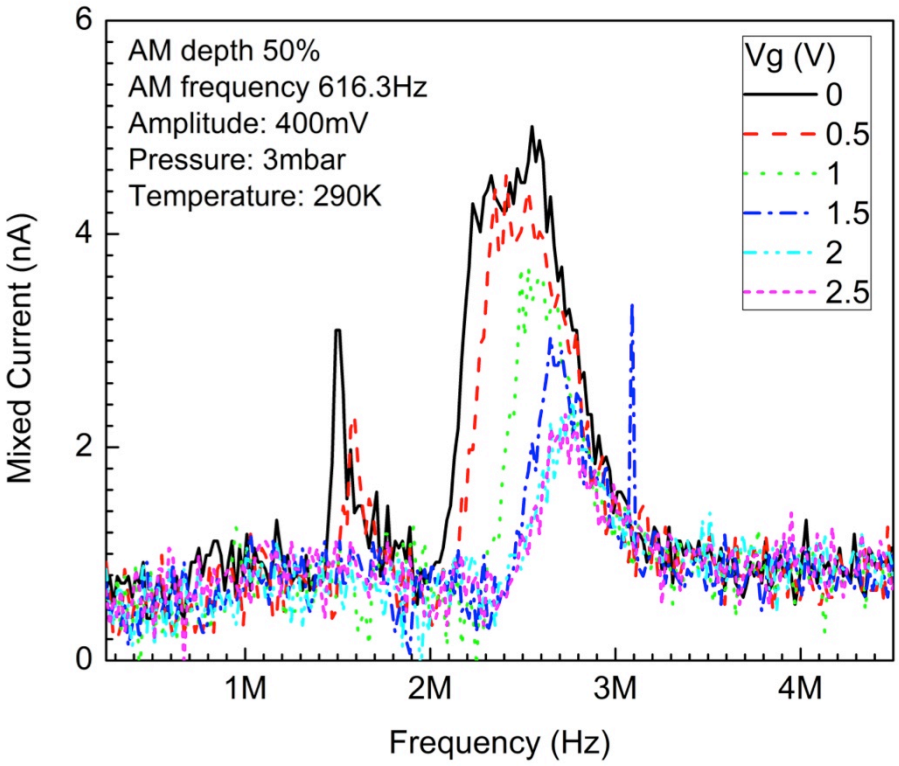

Figure 6.6: Mixed current against AM frequency with different gate voltage

For comparison, the AM signal has also been used to actuate the graphene resonator. Figure 6.6 plots the mixed current against frequency of the AM carrier wave with

different gate voltage. One obvious observation is that, the measured current is much noisier than that shown in Figure 6.2 since the AM signal is more susceptible to interference. Only two bands can be distinguished. The lower frequency band might correspond to band A in Figure 6.2, which is the fundamental frequency of the graphene resonator. The higher frequency band should correspond to band C and D in Figure 6.2. The resonance amplitude of the AM signal actuated graphene resonator is significantly smaller than that of the FM signal actuation. However, the reason behind this remains unknown. Since the AM actuation results are hard to interpret, it is rarely used in the electrical measurement of resonance.

6.4 Actuation of higher harmonics

For a doubly clamped beam subjected to uniform actuation force, the amplitude of fundamental mode is much larger than higher harmonics. With some sophisticated design, a MEMS resonator could operate at higher resonance mode [163][164][165][166][167]. The higher modes often double or triple the frequency of fundamental mode, thus pushing the operating range of resonator to even higher frequency without reducing the dimension of device, which could lead to deteriorated performance in terms of quality factor.

As observed from the measured results, the amplitude of band B, which is the higher order harmonics, is almost comparable to the amplitude of the fundamental frequency band A at large actuation voltage (400mV). This phenomenon indicates that the graphene resonator could selectively operate at two modes. Certain applications based on graphene resonator could take advantage of it. In this section, a theoretic model will be developed to understand why the second order harmonics can be boosted. The resonance mode of graphene bridge depend on the actuation force configuration, rather like actuation of the overtone of a guitar string.

6.4.1 Modal analysis

For simplicity's sake, the bending stiffness and the deflection-induced stress of equation 6.10 have been ignored, then

$$\sigma_0 t_g W w_{xx} - \alpha w_x = F_a + \rho t_g W w_{tt} \tag{6.14}$$

This equation is a forced motion equation for a string. The motions of every point of the beam are simultaneous with the same frequency but different amplitude. Their amplitude is a distributed function along the whole beam, and the shape of amplitude distribution is called a resonance mode. Different modes are mutually independent on each other. The motion of each point of the beam is a superposition of different modes. Mathematically, the solution to equation 6.14 has the form of

$$w(x,t) = \sum_i \boldsymbol{\psi}_i(x) y_i(t) \tag{6.15}$$

Here, $\boldsymbol{\psi}_i(x)$ represents the spatial modal shape of resonance mode i. $y_i(t)$ is time-dependent periodical function. For double-clamped beam, the spatial mode can be expressed as

$$\boldsymbol{\psi}_i(x) = \sin\left(\frac{i\pi x}{L}\right) \tag{6.16}$$

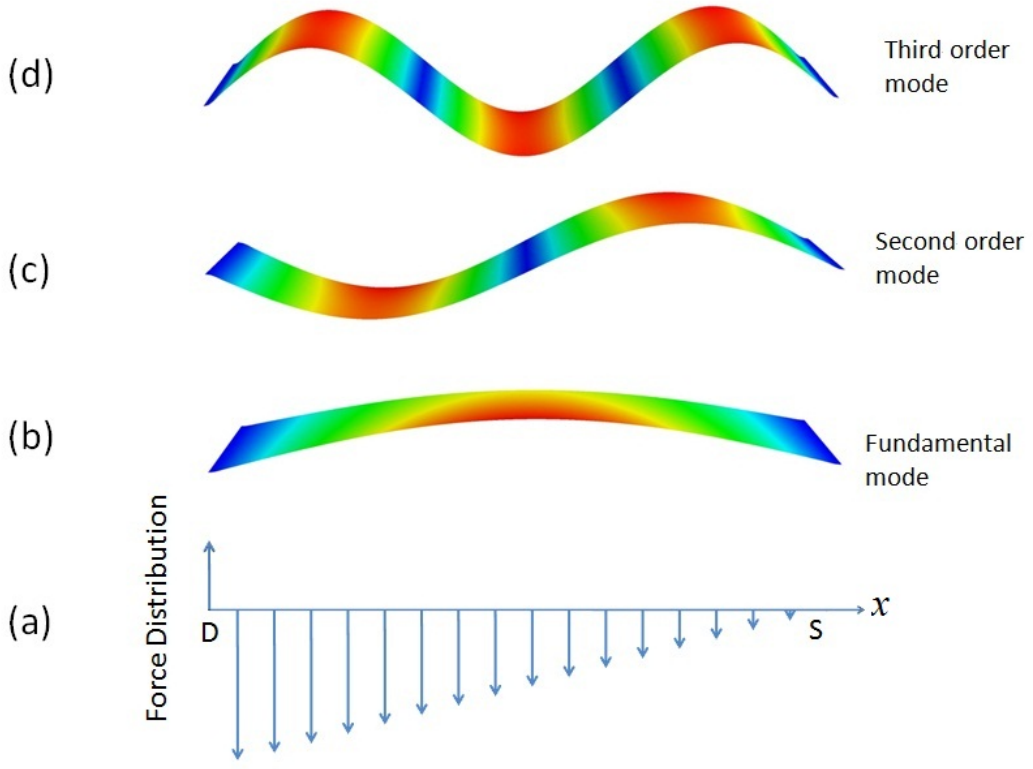

Figure 6.7: Electrostatic force distribution in single source measurement setup and the first three flexural resonance modes

The shapes of the first three flexural modes have been shown in Figure 6.7(b), (c), and (d). These modal shapes are exported from finite-element-analysis (FEA)

simulation (CoventorWare 2010). It is trivial to verify that the spatial modes are mutually orthogonal, which means

$$\int_0^L \boldsymbol{\psi}_i(x)\psi_j(x)dx = \delta_{ij}, \quad \delta_{ij} = \begin{Bmatrix} 1 & (i=j) \\ 0 & (i \neq j) \end{Bmatrix} \tag{6.17}$$

Now, the expanded expression of displacement (equation 6.14) can be used to replace $w(x,t)$ in equation 6.13. The differentiation of modal shape with respect to x has been calculated explicitly as the modal shapes have determined expression.

$$\begin{aligned} \sum_i \left(-\sigma_0 t_g W \left(\frac{i\pi}{L}\right)^2 \boldsymbol{\psi}_i(x) y_i(t) - \alpha \boldsymbol{\psi}_i(x) \big(y_i(t)\big)_t \right) \\ = F_a + \sum_i \rho t_g W \boldsymbol{\psi}_i(x) \big(y_i(t)\big)_{tt} \end{aligned} \tag{6.18}$$

Using the orthogonality of the spatial mode functions, multiplying the above equation with $\boldsymbol{\psi}_i(x)$ and integrating over the beam length, we get

$$\begin{aligned} \big(y_i(t)\big)_{tt} + \frac{\alpha}{\rho t_g W} \big(y_i(t)\big)_t + \frac{\sigma_0}{\rho} \left(\frac{i\pi}{L}\right)^2 y_i(t) \\ = -\frac{1}{\rho t_g W} \int_0^L F_a \boldsymbol{\psi}_i(x)\, dx \end{aligned} \tag{6.19}$$

Let

$$\omega_i = \sqrt{\frac{\sigma_0}{\rho}\left(\frac{i\pi}{L}\right)^2} = \frac{i\pi}{L}\sqrt{\frac{\sigma_0}{\rho}} \tag{6.20}$$

and

$$2n = \frac{\alpha}{\rho t_g W} \tag{6.21}$$

Then the equation 6.18 transforms to

$$\begin{aligned} \big(y_i(t)\big)_{tt} + 2n\big(y_i(t)\big)_t + {\omega_i}^2 y_i(t) \\ = -\frac{1}{\rho t_g W} \int_0^L F_a \boldsymbol{\psi}_i(x)\, dx \end{aligned} \tag{6.22}$$

So far, the string motion equation has been discretized into separate equations of typical damped harmonic resonators. ω_i represents the frequency of the ith mode, and n is the damping coefficient. The right side term can be viewed as the

projection of the actuation force on to the ith mode. Taking the Laplace transform on the above equation and rearranging the terms, we get

$$Y_i(s) = \frac{-\frac{1}{\rho t_g W}\mathcal{L}(\int_0^L F_a \boldsymbol{\psi}_i(x)\,dx)}{s^2 + 2ns + {\omega_i}^2} \tag{6.23}$$

where $\mathcal{L}()$ represents Laplace transform, and $Y_i(s) = \mathcal{L}(y_i(t))$. Now it can be seen that the actuation of certain mode depends upon the integration of the spatial mode function times the actuation force along the beam. The actuation force can also be written as the product of spatial part and a time-dependent function, $F_a = F_{as}(x)F_{at}(t)$. So

$$Y_i(s) = \frac{-\frac{1}{\rho t_g W}F_{at}(s)(\int_0^L F_{ax}(x)\boldsymbol{\psi}_i(x)\,dx)}{s^2 + 2ns + {\omega_i}^2} \tag{6.24}$$

Here $F_{at}(s) = \mathcal{L}(F_{at}(t))$. The amplitude peak of the ith mode is located at $\omega_{imax} = \sqrt{{\omega_i}^2 - 2n^2}$, where the amplitude reach a maximum of

$$Y_{imax} = \frac{\frac{1}{\rho t_g W}(\int_0^L f_{ax}(x)\boldsymbol{\psi}_i(x)\,dx)}{2n\sqrt{{\omega_i}^2 - n^2}} \tag{6.25}$$

In case of single source measurement, the voltage difference between graphene and the substrate is dropping from the drain electrode to the source electrode due to the resistance of the graphene bridge. Thus the actuation force amplitude can be written as $F_{ax}(x) = K_s x + C$, here K_s is the slope of the voltage and C is a constant, as illustrated in Figure 6.7(a). Thus, for the second order harmonics

$$\int_0^L F_{ax}(x)\boldsymbol{\psi}_2(x) = \int_0^L (K_s x + C)sin\left(\frac{2\pi x}{L}\right) = -\frac{K_s L^2}{2\pi} \tag{6.26}$$

And for the fundamental frequency, we have

$$\int_0^L F_{ax}(x)\boldsymbol{\psi}_1(x) = \int_0^L (K_s x + C)sin\left(\frac{\pi x}{L}\right) = \frac{K_s L^2}{\pi} + \frac{2CL}{\pi} \tag{6.27}$$

Comparing the above two equation, it can be seen that, for uniform actuation when the electrostatic actuation voltage is applied on the back gate, K_s=0. So the integral of second order harmonics is zero, thus the second mode will not be driven into resonance. However, in case the voltage is a ramp function, which is the case in single source measurement setup, the projection of the actuation force onto the

second order harmonic is not zero any more, therefore the second order mode is activated.

The intrinsic frequency of graphene bridge resonator can be expressed as $\omega_i = i\pi\sqrt{\sigma_0 + \sigma(V_{DC})/\rho}\,/L$ for the ith mode. Thus, when the gate voltage-induced stress $\sigma(V_{DC})$ increases in the graphene bridge, the frequency shift of second harmonics is larger than that of the fundamental mode by a factor of 2, as shown in Figure 6.3(a). Because of the coefficient 2 for the second mode, it is speculated that the sensitivity of force sensor based on higher harmonics of graphene resonator will improve by a factor 2 to 0.45fN/Hz$^{1/2}$ if graphene resonator works under the same condition as in [19]. The peak frequency of a resonance mode is related to its intrinsic frequency by $\omega = \sqrt{{\omega_i}^2 - 2n^2}$, where n is the damping coefficient. n increases with larger resonance amplitude due to the nonlinear damping effect [126], hence, with larger actuation voltage, the resonance peaks shift to lower frequency, which is consistent with the experiment observation in Figure 6.5(a). The amplitude of each mode Y_i is expressed as

$$Y_i = \frac{\frac{1}{\rho t_g W}\left(\int_0^L F_{ax}(x)\boldsymbol{\psi}_i(x)\,dx\right)}{2n\sqrt{{\omega_i}^2 - n^2}} \tag{6.28}$$

Because the peak frequency ω_i changes faster for higher modes with gate voltage than fundamental mode, the amplitude of the second order mode responds more to the tuning gate voltages as shown in Figure 6.5(b).

6.4.2 Simulation

In order to investigate the influence of a non-uniform electrostatic actuation force on the dynamics of the graphene resonator, finite element analysis has been conducted with Matlab code (see appendix A.3) to look at the transient response of the graphene resonator to the electrostatic force actuation. First, the graphene bridge has been discretized to N elements of the same length, so the length of each element is $h = L/N$. The following equations have been used to calculation the differentiation of the element deflection at each simulation time step $w(ph, q\tau)$.

$$w_x(ph, q\tau) = \frac{w((p+1)h, q\tau) - w(ph, q\tau)}{h} \tag{6.29}$$

$$w_{xx}(ph, q\tau) = \frac{w((p+1)h, q\tau) - 2w(ph, q\tau) + w((p-1)h, q\tau)}{h^2} \tag{6.30}$$

$$w_{tt}(ph, q\tau) = \frac{w(ph, (q+1)\tau) - 2w(ph, q\tau) + w(ph, (q-1)\tau)}{\tau^2} \tag{6.31}$$

where p refers to the element number, and q represents the time step. Replacing the above equations into equation 6.13, it can be obtained that

$$\begin{aligned} w(ph, (q+1)\tau) = {} & \tau^2\sigma\frac{w\big((p+1)h, q\tau\big) - w(ph, q\tau)}{\rho h^2} + 2w(ph, q\tau) \\ & - 2w(ph, (q-1)\tau) - \frac{\tau^2 f_a(ph, q\tau)}{t_{Gr}\rho W h} \\ & - \frac{\tau\alpha\big(w(ph, q\tau) - w(ph, (q-1)\tau)\big)}{\rho t_g W} \end{aligned} \tag{6.32}$$

The equation 6.32 is the iteration formula for the deflection of elements at each time step. The damping coefficient α has been estimated from the measured quality factor.

$$\alpha = \rho t_g W 2n = \frac{\rho t_g W}{Q} \tag{6.33}$$

where Q is the measured quality factor. The time step τ is fixed as $1/(512f)$, f is the actuation frequency that will be simulated. There are two dielectric layers between the graphene and the substrate, so the capacitance per element can be expressed as

$$C_{Gr} = 1/\left(\frac{1}{\frac{\varepsilon_{air} W h}{t_{poly}}} + \frac{1}{\frac{\varepsilon_{oxide} W h}{t_{oxide}}}\right) \tag{6.34}$$

ε_{air} and ε_{oxide} are the permittivity of air and oxide, while t_{poly} and t_{poly} represent the thickness of poly-Si and oxide respectively. And the differentiation of C_{Gr} with respect to the deflection can be expressed as

$$C'_{Gr} = -\frac{W h \varepsilon_{oxide}}{2(t_{poly}\varepsilon_{oxide} + t_{oxide}\varepsilon_{air})^2} \tag{6.35}$$

In the single source measurement setup, the DC voltage is applied through the back gate, so the DC part of the electrostatic voltage is uniform along the whole graphene bridge. The actuation AC voltage is applied to the drain electrode, and the source electrode is connected to ground through a small resistor whose voltage drop can be neglected, so

$$V_a(x,t) = \frac{(L-x)V_{AC}sin(\omega t)}{L} \tag{6.36}$$

According to equation 3.1 in chapter 3

$$F_a(ph, q\tau) = \frac{C'_{Gr}}{2}V_{DC}^2 + C'_{Gr}V_{DC}\frac{(L-ph)V_{AC}sin(2\pi fqh)}{L} \tag{6.37}$$

The equations 6.38 and 6.39 come from the assumption that the initial velocity of the elements is zero. Since the bridge is fixed at both ends, the deflection at the ends is always zero. That is why the equation 6.40 and 6.41 are true.

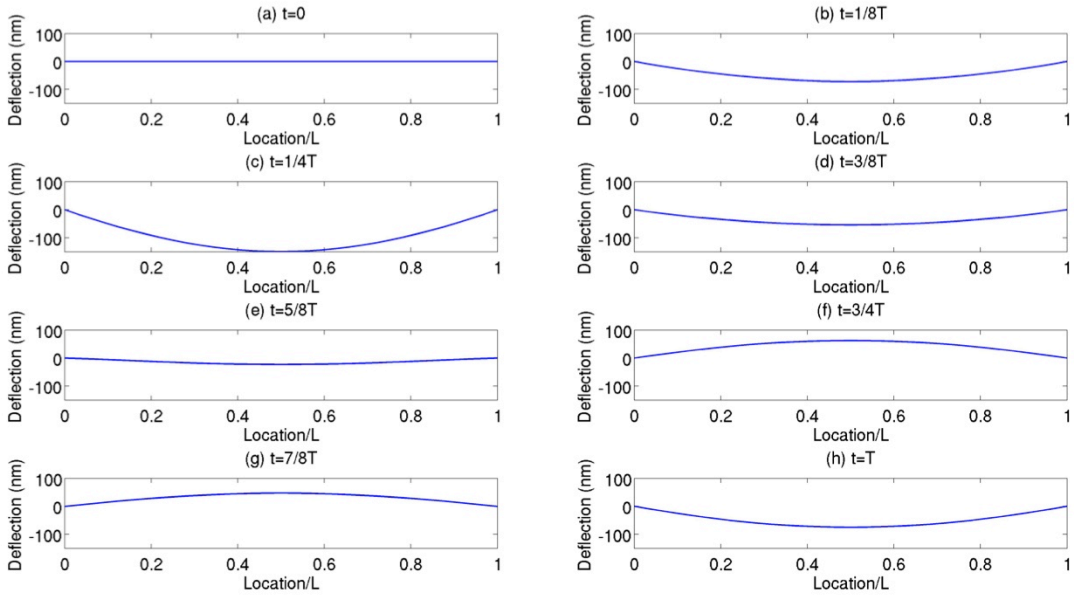

Figure 6.8: Bridge deflection in one period driven by *f=1/T*=0.75MHz actuation. The length of the bridge is 12μm

The initial and boundary conditions are

$$w(ph, 0) = 0 \tag{6.38}$$

$$w(ph, 1) = 0 \tag{6.39}$$

$$w(1, q\tau) = 0 \tag{6.40}$$

$$w(N, q\tau) = 0 \tag{6.41}$$

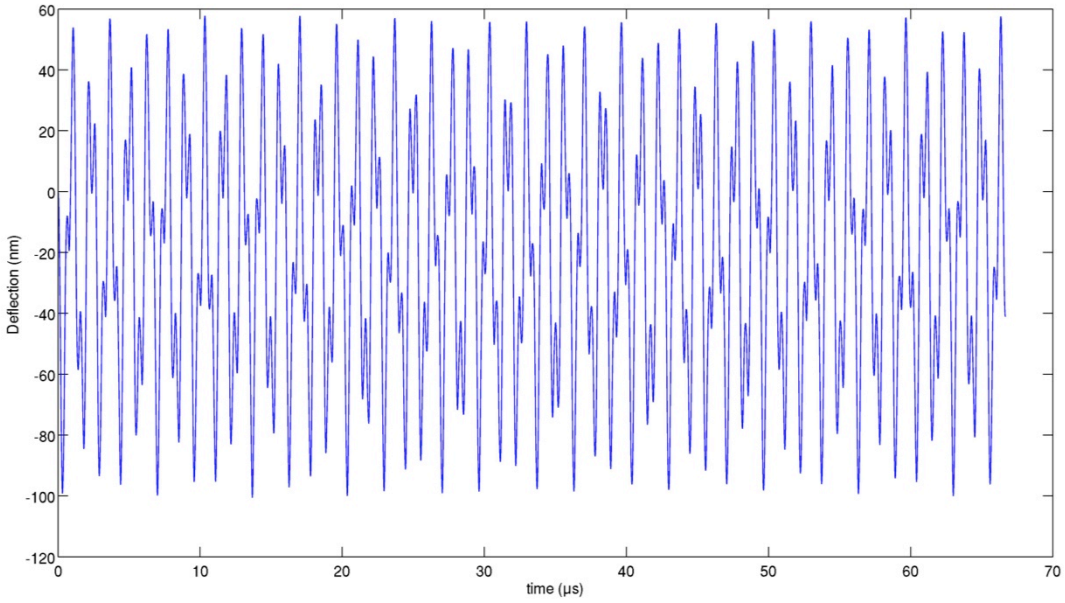

Figure 6.9: Transient response of the element located at *p=N/4* under 0.75MHz actuation

Figure 6.8 plots the transient response of a 12μm long bridge to 0.75MHz uniform actuation, which is the case for two-source measurement setup where the actuation voltage is applied on the gate. The DC voltage is 0.1V, and the amplitude of the AC signal is 0.1V as well. From the simulation, it can be observed that every point in the bridge moves simultaneously, that is to say, the phase of each point is nearly the same. Figure 6.9 plots the deflection of the element located at $p = N/4$ against time. The shape of transient response contains more than one frequency component. Applying Fast Fourier Transform (FFT), the frequency domain response of the bridge can be obtained, as shown in Figure 6.10(a). There are two peaks shown in the frequency domain plot. The first one is located at 0.75MHz, which is the forced response. There is also a peak located at around 1.95MHz, which is fundamental frequency of the graphene bridge. The simulated fundamental frequency is consistent with the measured fundamental frequency very well. No higher mode peaks can be observed. However, if the AC voltage is set to be a distributed function described by equation 6.36, which is the case for one-source measurement, the FFT clearly shows

(Figure 6.10(b)) another peak at 3.95MHz, which is the second order mode. The amplitude of the fundamental mode is more than an order of magnitude higher than the second order mode. The emergence of the higher order mode suggests that the non-uniform actuation does drive the second order mode into resonance.

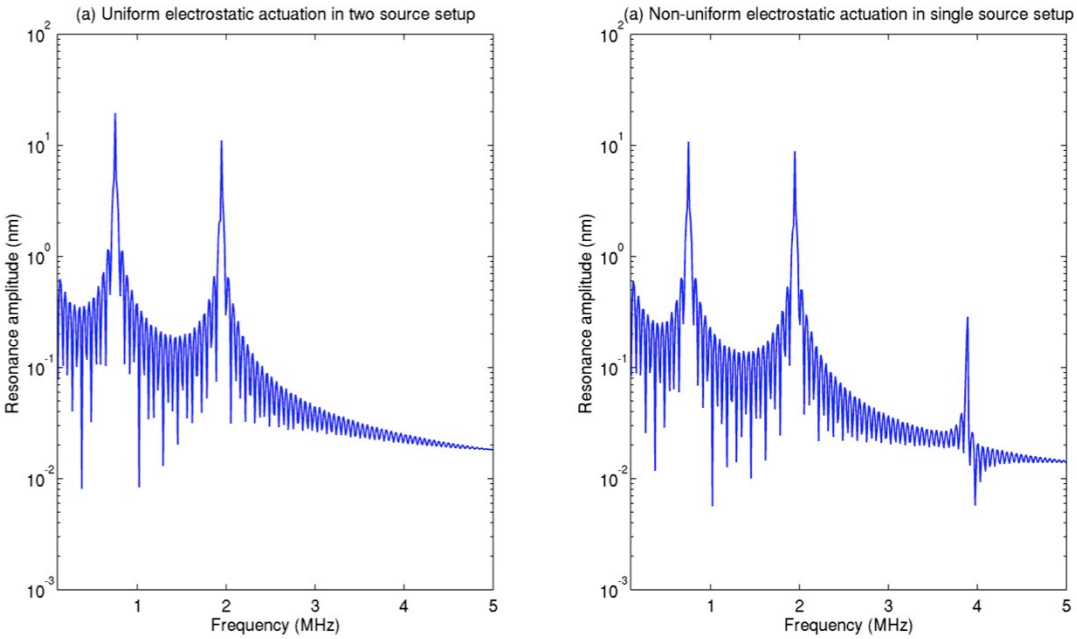

Figure 6.10: FFT results of transient response of the element at *p=N/4* under 0.75MHz actuation in two-source measurement (a), and single-source measurement (b)

Next, a frequency sweep has been conducted from 1MHz to 5MHz for both type of electrostatic force configurations. The amplitude at the actuation frequency is extracted from the FFT results and plotted against the frequency. Figure 6.11(a) shows the amplitude-frequency relationship of uniform actuation, which is the case in two-source measurement setup, while (b) shows the relationship of non-uniform actuation. Again, the higher mode resonance can be observed in (b) for non-uniform actuation force distribution. The line shape of Figure 6.11(b) resembles the shape of measured frequency sweep curve in Figure 6.4 very much. The evolvement of the bridge shape is better illustrated by looking at the time domain, as plotted in Figure 6.12. The actuation frequency is 4MHz. After a quarter of the period, the portion of the bridge close to the drain side ($x \approx 0.2L$) is pulled downward more than the portion of bridge close to the source side (b), because the electrostatic force on the drain side is larger. Approaching one period, the second mode tends to zero, and the

line shape is almost that of the fundamental mode as can be seen in (d). This shows clearly how the second order is actuated.

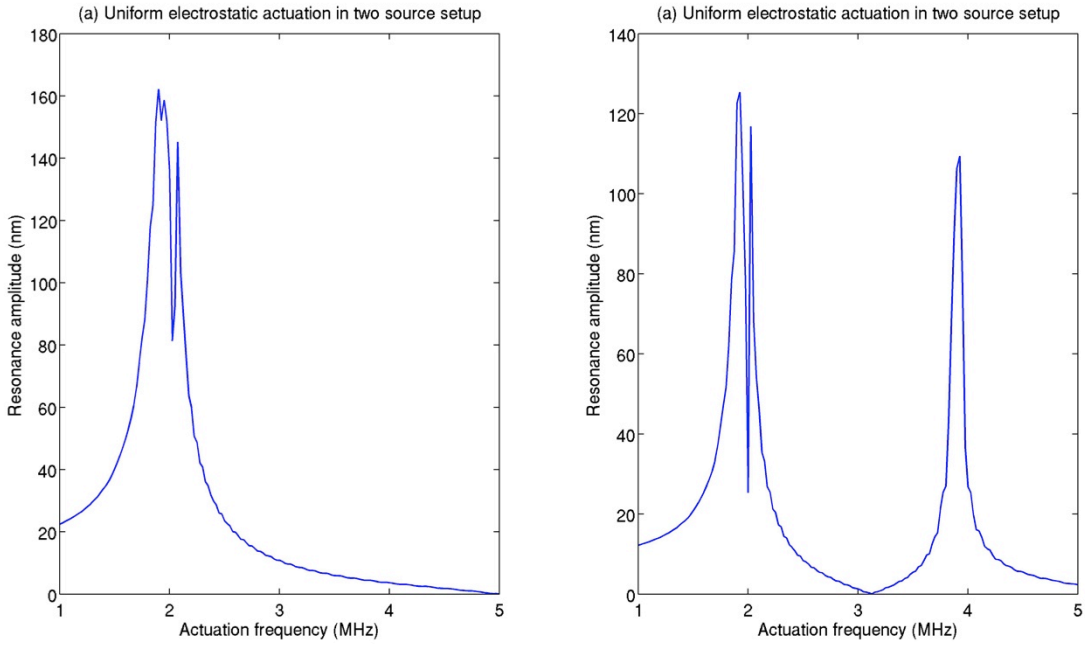

Figure 6.11: The resonance amplitude of the element at $p=M/4$ under different actuation frequency

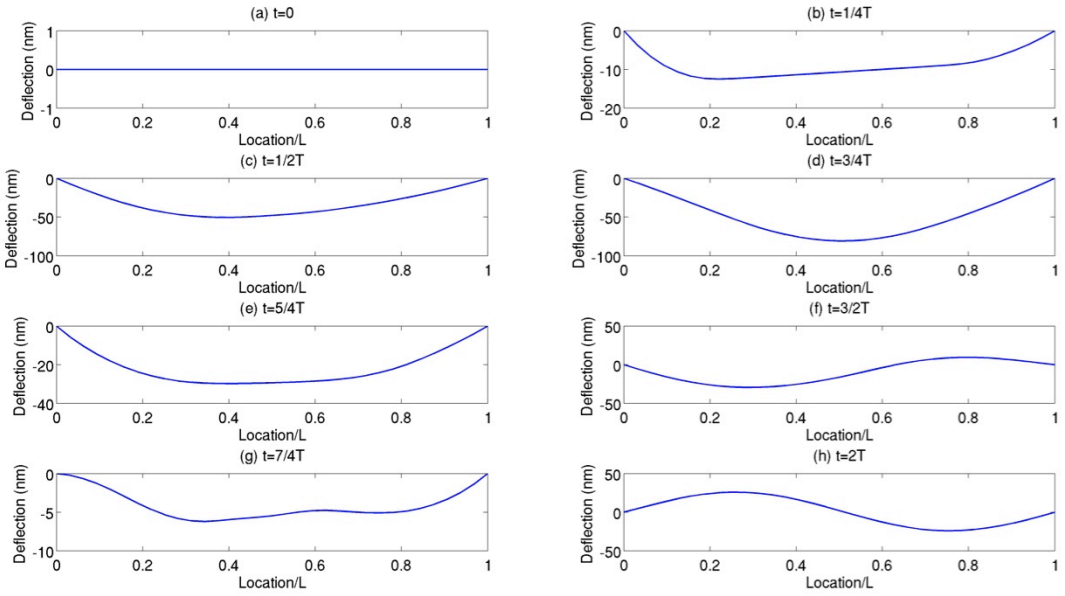

Figure 6.12: Bridge deflection in one period driven by $f=1/T$=3.95MHz actuation.

6.5 Quality factor

6.5.1 Comparison with other resonators

The quality factors of graphene resonators for all bands measured are below 10, which is relatively low compared to most MEMS resonators. Table 6.2 lists the quality factor of a few resonators made of different materials and their characterisation environment for comparison. Generally speaking, the graphene resonators and carbon nanotube resonator have lower quality factors at room temperature. At low temperature, the quality factor of graphene surges dramatically to around 10,000.

Table 6.2: List of quality factors of graphene resonators and resonators made of other materials

Author	Q	Material	Structure	Pressure	Temperature
C. Chen [36]	10,000	Graphene	Beam	unknown	5K
J. S. Bunch [19]	20-850	Graphene	Beam	$<10^{-6}$torr	RT*
	1,800				50K
A. M. van der Zande [37]	9,000	Graphene	-	$<5x10^{-5}$torr	10K
V. Sazonova [158]	40-200	CNT	Beam	<10torr	RT
J. Wang [168]	6,225	Diamond	Beam	$<5x10^{-2}$torr	RT
T. S. Biswas [169]	$>1.6x10^5$	Si_3N_4	Nano-string	$\sim 2x10^{-6}$torr	RT

*Room temperature

As observed from other MEMS resonators [170], the temperature largely affects the quality factor of graphene resonator. When temperature decreases towards absolute zero, the quality factor increases. The quality factor of graphene resonator is found to be proportional to $1/T^{\gamma}$ [37][36][37]. γ is around 0.35 ± 0.05 when temperature is between 9 K to 40 K, and approximately 2.3 ± 0.1 from 40K to room temperature. A similar phenomenon has also been reported in [36] and the quality factor is independent on the size and shape of the graphene sheet, which indicates that such a segmental dependence of quality factor on temperature is not an isolated case and might be an intrinsic property of graphene. The scaling as $1/\mathcal{T}^{0.36}$ has been observed in CNT resonator at low temperature as well [171].

6.5.2 Dissipation mechanism

Molecular dynamics (MD) simulation predicts the energy dissipation of carbon nanotube resonators follow the $1/\mathcal{T}^{0.36}$ power law from absolute zero to room temperature [172], matching the experimental observations at low temperature perfectly well. The simulation reveals that the external vibration energy is continuously converted to internal energy, which causes the increase of temperature. The coincidence of a 0.36 power in both calculation and experiment results at low temperature may suggest that thermalelastic dissipation dominates at low temperature for both CNT and graphene resonators. However, similar MD simulation performed on graphene resonator shows the quality factor scales as $1/\mathcal{T}$ [173]. The reason behind the discrepancy remains unknown.

A full understanding of the energy dissipation in graphene resonators is still lacking, since energy dissipation in resonators is very complicated and associated with various energy loss mechanisms. The common mechanisms include clamp loss[174], Ohmic loss [174] [175], surface loss [176][177] and thermoelastic loss etc [178][179][180]. Seoanez and Guinea attempted to categorize the possible dissipation mechanisms in graphene and nanotube resonators [181]. They have analysed six possible dissipation approaches and the scaling of the energy loss mechanisms as temperature. However, the analysis of the energy loss only provides a qualitatively understanding. Since the losses are related to material, dimension, characterizing method and environment. The theoretical prediction of quality factor turns out to be a tough task.

Of all the loss mechanisms, the surface loss may play an important role in graphene resonators. Surface loss is caused by the surface defects including the defects of the lattice structure or absorbates [182]. The defects introduce stress or charge gradients thus increase the entropy of the resonator, so the energy decreases. Reports have shown that the quality factor drops as the dimension scales down, when the surface to volume ratio scales up[182]. Therefore, as the surface to volume ratio of graphene is the highest of all materials due to its 2D nature, the surface loss greatly limits graphene resonators' quality factor. MD simulation of CVD-grown graphene shows the quality factor is reversely proportional the defects density [173]. The defects

induce spurious vibration modes that drain energy of the fundamental vibration. The simulation predicts that a tensile strain could possibly greatly enhance the quality factor by flattening out the buckles and suppressing the spurious modes. Previous study in graphene resonator also supports this hypothesis [183].

6.6 Conclusion

The resonance of the graphene resonator has been characterized with the one-source current mixing technique. For a 12μm long graphene resonator, the fundamental frequency is found to be around 1.94MHz. With high actuation voltage (>400mV), second mode peak can also be detected with prominent amplitude. The second order mode frequency nearly doubles that of the fundamental mode, and so does the frequency shift under tuning. Both frequencies can be tuned by the DC voltage applied on the back gate, which offers flexibility to adjust the operating frequency of the resonator. The frequencies increase with the square root of applied gate voltage, which is consistent with theoretical deduction. Generally speaking, the frequency response of second order mode changes two times faster than the fundamental mode not only to the applied gate voltage, but also the mass density and stress change, which means mass or force sensors based on the graphene resonator working at second order mode can be increased by a factor of two. For RF applications, the second mode can also reach a higher frequency without decreasing the dimension of the resonator which puts more difficulties on fabrication and may lead to performance deterioration due to size effect.

The measured quality factor of the graphene resonator is below 10 at room temperature, which is consistent with the reported strong dependence of quality factor on temperature. Similar observations have been made on carbon nanotube resonator before in other report . Both types of carbon based resonators show lower quality factor than their counterparts of other materials. The major contributor to the energy loss at higher than 40K could be surface defects, which couples energy of the working resonance mode to spurious modes.

The origin of the prominent higher mode has been analysed by decomposing the resonance of the graphene resonator into individual modes, and the projected force onto the first two modes has been calculated for different actuation voltage

distribution. It has been found that the projected force onto each mode has to do with the integration of the product of spatial modal shapes and the actuation force distribution. When the actuation force is uniform along the beam, the projected force on second mode is zero, so the second mode will not be driven into resonance, however, in the one-source current mixing measurement setup, the actuation force is a distributed function, thus the projected force is no longer zero, so that the second order mode is activated. To investigate the evolution of the bridge shape under actuation, the transient response of the resonator to different distribution of electrostatic voltage has been simulated by FEA method. It has been found that, when the actuation force is not uniform, the part of graphene subjected to large electrostatic force moves faster than the rest part, which generates the second resonance mode.

Chapter 7

Optical alignment technique for graphene and other 2D materials

7.1 Introduction

In this chapter, an optical alignment technique for photolithography will be introduced, which can be used to fabricate MEMS devices from flakes of 2D materials whose dimension is of just a few microns. The fabrication of MEMS device comprises successive steps of material deposition, followed by photolithography and etching to form desired patterns on a layer of certain material. Usually, a MEMS device involves a few layers of patterned materials. The patterns on different layers need to be placed at the desired location. Therefore, the photomask for each photolithography step relies on alignment tools and sophisticatedly designed alignment marks to align to previous layer of photomask and define their relative position. Figure 7.1(a) illustrates a basic set of alignment marks for a fabrication process comprising three lithography steps. The two squares (pink) are drawn on the first mask, while the blue cross and purple cross are drawn on second (blue) and third mask (purple) respectively which can be used to align to the squares. Conventionally, all the following marks are to be aligned with the marks patterned by the first step of photolithography to avoid error accumulation. Therefore, for simplicity, the alignment marks on first photo mask is named as master alignment marks, just like the two squares in Figure 7.1(a).

For commonly used mask aligner equipped with optical microscope, it is capable of aligning to the master alignment marks with roughly one-micron accuracy, which is the resolution limit of optical microscope. And the alignment marks should be placed in a limited area confined by the moving range of the microscopes and wafer chuck, as shown by the two dashed rectangles in Figure 7.1(b). In the alignment technique, the core is a sophisticatedly designed set of alignment marks for consecutive layers of photo masks. The first layer of the alignment marks (master alignment marks) can

be patterned around a small flake of 2D material, and the following layer of photo masks can be aligned to master marks. With this technique, one can fabricate prototype MEMS/NEMS devices from small pieces of 2D material with the ordinary mask aligner and photoresists. The alignment precision is defined by the microscope of the mask aligner. With the mask aligner, one-micron accuracy can be achieved. The only pre-requisite for this technique is that the 2D material should have certain amount of contrast compared to the substrate. The application of this technique has been demonstrated by a successful fabrication of back-gated graphene transistor.

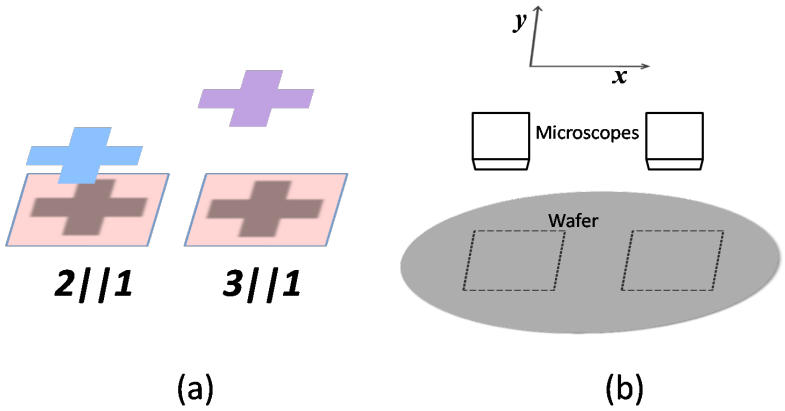

Figure 7.1: Basic alignment marks (a) and the their location (b) on a wafer

7.2 Motivation

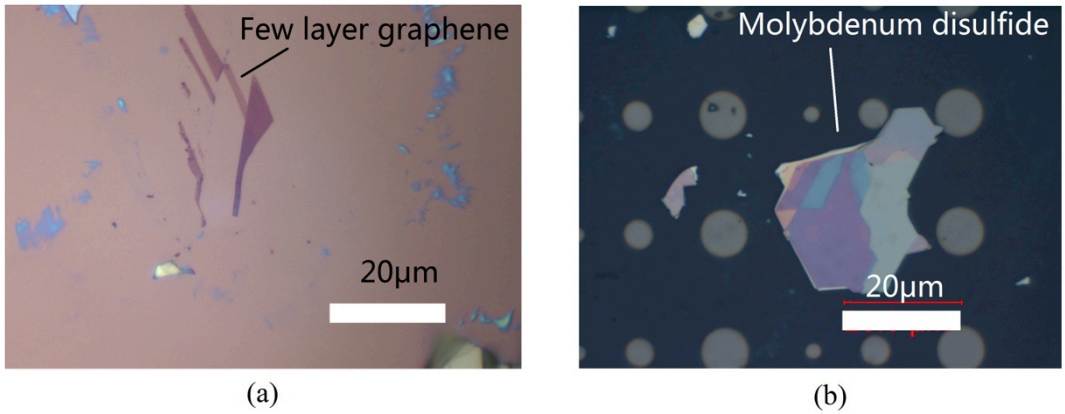

Figure 7.2: Exfoliated graphene flakes and molybdenum disulfide flakes, scale bars are 20μm

The discovery of monolayer graphene shattered the decades-long belief that 2D material does not exist in this world due to their thermal instability and inspired the graphene rush in the past few years [14][22][184]. The excellent properties of

graphene not only draw attention to the research and development of commercial products based on graphene, but also encouraged the search for other 2D materials. There have been various 2D materials emerged after the graphene such as boron nitride (BN) [185][21], molybdenum disulphide (MoS_2) and so on [20][15]. It is bound to draw more research efforts in the 2D materials and see more commercialized products based on them in the future.

However, the development of devices based on 2D materials is still on its way and facing challenges. Taking graphene as example, there are three ways to prepare graphene, including sublimation of SiC [40][145], chemical vapour deposition (CVD)[186], and mechanical exfoliation. The most widely used graphene for academic research is mechanically exfoliated from kish graphite or highly ordered paralytic graphite (HOPG), although the mechanical exfoliation technique can not produce large area graphene nor scale up for mass production. That is because both kish graphite and HOPG have very few lattice defects, the quality of exfoliated graphene is the best in terms of lattice integrity and carrier mobility. The much lower cost to exfoliate graphene is another advantage. The exfoliated graphene flakes are micron-sized, distributed randomly on the substrates, and the shape of desired monolayer graphene or multilayer graphene is irregular as shown in Figure 7.2(a). Such morphology is common for other mechanically exfoliated 2D materials such as MoS_2 flakes (Figure 7.2(b)). To makes devices from these micron-sized flakes of all kinds of randomness and irregularity appears to be beyond the capability of ordinary micro-fabrication technique.

Electron beam lithography (EBL) has been the dominant patterning technique in prototyping graphene devices from exfoliated graphene sheets [36][187][188]. The EBL technique uses electrons to expose photoresist. Since the scanning of electrons can be easily realized and precisely controlled, thus EBL is capable of exposing ultra-narrow line width and offers great flexibility of pattern writing. However, EBL has some drawbacks. The electron beam irradiation can possibly induce defects in the graphene sheet, as indicated by the appearance of a strong D peak in Raman spectrum after electron irradiation [189]. The defects will greatly degrade the carrier mobility in graphene sheet [190]. Moreover, the EBL normally uses PMMA as the photoresist, which will leave residuals on top of graphene [150], as shown in Figure

5.4(c) in chapter 5. The ordinary measures to remove the residue, such as oxygen plasma bombardment or piranha solution rinse, are not compatible with graphene. It has been reported that annealing could substantially remove the PMMA, however it cannot be removed completely [150]. The surface absorbents and contaminations is the major scattering source that limits the carrier mobilities in graphene as discussed in section 2.3.2 in chapter 2. In order to align to randomly located graphene flakes and overcome the drawbacks of EBL, an optical alignment technique have been developed, which can be incorporated into the fabrication process of devices from 2D flakes to avoid the use of EBL.

7.3 Principle of alignment

The focus of the processing technique is the alignment of different mask layers. In this section, It will be discussed that how the alignment marks are designed and to be defined around graphene flakes. For convenient, the discussion will be based on grapheen flakes, but should also be applicable to other 2D materials.

7.3.1 Substrate design

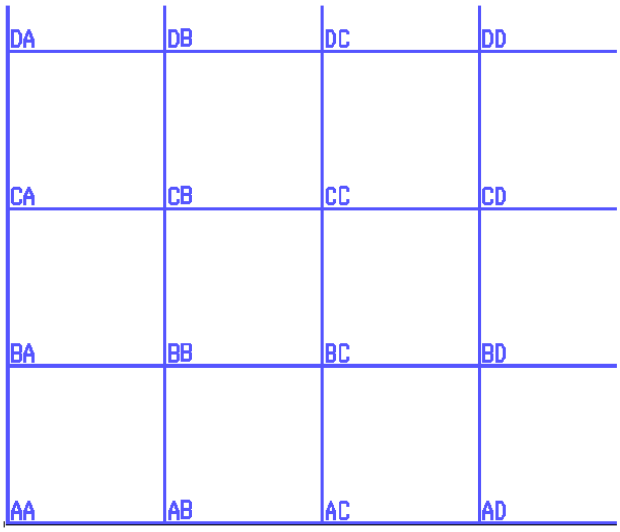

Figure 7.3: Grid for dividing substrate into small labelled square areas

Usually, graphene is exfoliated and put down onto 300nm SiO_2/Si substrate [14][134]. On this substrate, optical microscope can be used to identify monolayer graphene or multilayer graphene, and then process them with other tools. Therefore,

there is a possibility of losing track of the desired graphene flake when it is moved away out of the focus of microscope. To speed up seeking for a specific as-identified graphene flake after the sample has been transferred to other tools like the optical mask aligner, the substrate can be divided into small areas by patterning a grid of squares on the substrate (Figure 7.3(a)). In our case, the size of squares in the grid is $320\mu m \times 320\mu m$. All of the squares are labelled to serve as coordinates of the graphene flakes. The grid lines and label letters are patterned through etching the SiO_2 layer for 30nm. When a desired graphene flake is found under optical microscope, the label of the square that the graphene belongs to can be recorded. Once the sample is mounted to the aligner, it is easy to move substrate, thus the recorded square, to the view field of microscope and pinpoint the same graphene flake again.

7.3.2 Alignment mark design

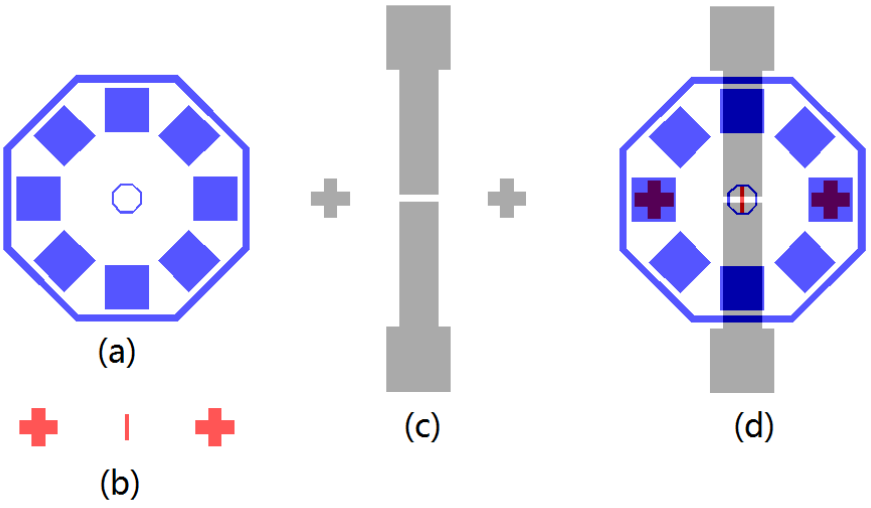

Figure 7.4: Mask design for fabricating graphene transistors

The design of the alignment mark has three features, namely, to solve the issues of random location, random orientation, and random shape of the exfoliated graphene flake. The alignment marks are a set of marks for three layers as shown in Figure 7.4. The most crucial pattern is the octagonal alignment mark on the first mask that has been shown in Figure 7.4(a), while the crosses in second (b) and third layer (c) can then be aligned to it during the fabrication once the octagonal alignment mark is

patterned around graphene flakes. Therefore, the octagonal mark in Figure 7.4(a) is the master alignment mark. The master alignment mark contains 4 pairs of squares arranged in octagonal shape so that the most proper and convenient pair can be chosen for a certain flake according to the flake's orientation. The total number of mask layers only depends on device design and its fabrication processes but not limited to three. The structural relationship of the three layers of mask is shown in Figure 7.4(d). Between the crosses of the second and third mask are the patterns for graphene and electrodes patterning, as will be discussed in the following section. Those patterns are placed at exactly the centre of the pair of crosses.

Now that the structural relationship between the alignment marks are defined, the only thing left is to pattern the first layer octagonal mark into the SiO_2 layer and make sure that graphene flake is at the centre of the auxiliary octagon. In order to align the octagonal alignment mark to the graphene flake as accurately as possible, a small auxiliary octagon is placed in the middle of the alignment mark design. All the photo masks should be light field to facilitate observing the graphene through the mask under the microscope. Subsequently, the design of the device can be aligned to the octagonal marker by pairs of crosses. In this work, the design of the graphene device is a rectangle in order to pattern the channel of field effect transistor (Figure 7.4(b)) and two long pads to define the electrode (Figure 7.4(c)). The alignment technique can be incorporated into different fabrication processes for fabricating diversified devices from exfoliated 2D flakes.

7.4 Integration of alignment mark for device fabrication

To apply the alignment technique depicted in the previous section, additional fabrication process steps can be developed and integrated with the alignment marks. In this section, the detailed fabrication of a graphene field effect transistor (GFET) incorporating the alignment technique to align to graphene flakes of a few microns in size will be presented.

7.4.1 Preparation of the graphene

The initial step of the fabrication is to prepare a proper substrate. Following the convention, the 285nm SiO_2 has been used which provides good contrast of graphene

against the substrate and enables the octagonal alignment mark to be aligned to the graphene flake. The oxide layer has been grown on top of a 4" silicon wafer by wet oxidation. The substrate is then diced into 1cm×1cm squares. The next step is the division of the surface of the substrates into grids. This is done by etching 30nm deep trenches into the SiO_2 layer using the mask shown in Figure 7.3 as described in previous section. The samples are then cleaned by sonication in IPA for 5min, in Acetone for 5min, and in Oxygen plasma for 10min to remove all the residuals. The samples are kept in oven at 200°C to keep the surface clean and dry. Graphene has been exfoliated by the generic exfoliation practice. To avoid leaving much tape residual, water soluble tape (3M water soluble wave solder tape 5414, ½ inch) have been used to exfoliate graphene from kish graphite(Grade 300, Graphene Supermarket). After a few times of exfoliation, the tape surface with graphene flakes has been put against the prepared SiO_2 substrate and pressed gently to let the graphene flakes stick to oxide surface. The substrate, together with flakes been put down, has been soaked in 60℃ de-ionized water and softly agitated for 5min to remove the tape residual. Possible monolayer graphene flakes of about 4μm has been found under optical microscope, and the grid label it belongs to has been recorded.

7.4.2 Master alignment marks transferring

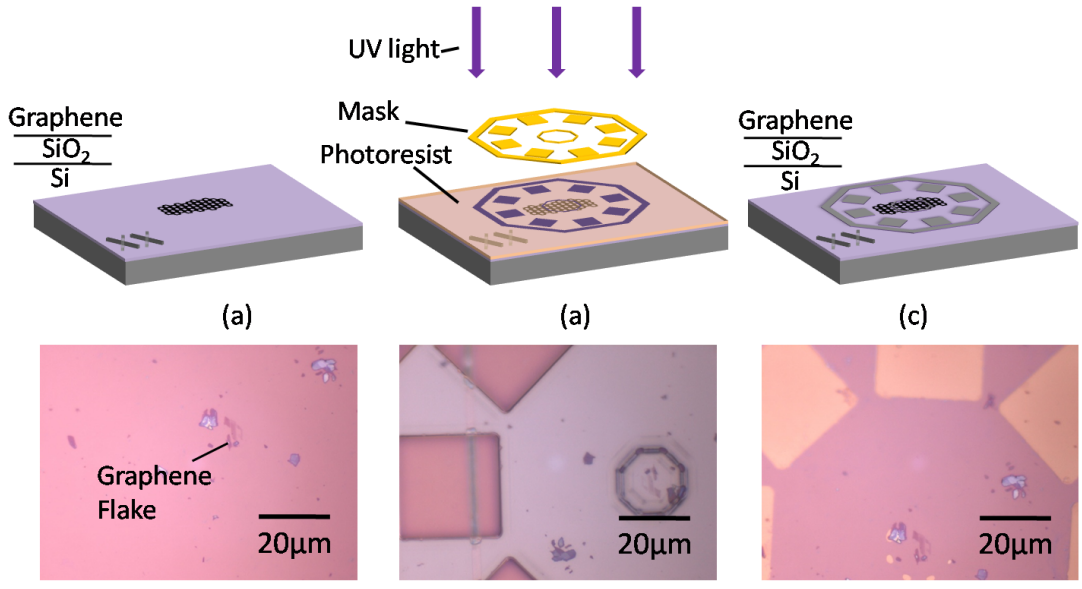

Figure 7.5: Patterning of master octagonal alignment marks around a graphene mask

Once a proper graphene flake is identified, the first alignment mark can be patterned around it. Figure 7.5 illustrates the process of transferring the octagonal alignment mark around graphene. The upper parts of the figure are schematic views of process steps, and the lower part contains optical images taken during the fabrication. Once a graphene flake has been identified on top of a substrate (Figure 7.5 (a)), about 1.4μm thick image reversal photoresist, AZ5214E has been spin coated on the substrate. The reason for using image reversal resist is because the masks have to be light field to allow the graphene flake to be observed through the mask. Under the microscope of mask aligner, the desired graphene flake can be easily re-found with the help of recorded label. The relative position of the graphene flake with respect to the master octagonal masks is adjusted manually until the graphene is centred to the middle of the small auxiliary octagon (Figure 7.5(b)). After the exposure and development of the photoresist, SiO_2 under the octagonal alignment marks is exposed and etched again by reactive ion etching for two minutes to a depth of about 30nm to transfer the octagonal alignment mark into SiO_2, while keeping the insulation of the oxide layer (Figure 7.5(c)). The photoresist is then removed with acetone.

7.4.3 Fabrication of the transistor

Figure 7.6 illustrates the fabrication process developed for a graphene transistor, integrated with the optical alignment marks. In the left column are the photo masks (all being light field) that have been used for each photolithography step, and the optical images taken after each step are on the right part. After a piece of graphene is identified (Figure 7.6(a)) and a octagonal alignment mark is patterned around it (Figure 7.6(b)) as described in the previous section, another layer of 1.2μm thick positive resist SPR350 has been spin coated for graphene patterning, and exposed with the mask illustrated in Figure 7.3(c) (also see Figure B.2(a)). On the mask plate, there are four replicas of the second layer mask oriented in four directions just like the pairs of squares in the octagonal alignment marks, which offers flexibility of choosing a proper mask according to the orientation of the exfoliated graphene flake. By aligning to the pre-patterned master octagonal alignment mark, a photoresist strip can be patterned exactly above the graphene flake and used as a mask in graphene etching process (Figure 7.6(c), also see Figure B.2(b)). The unprotected part of the

graphene flake has been etched away by O_2 plasma using the same process described in section 5.3 in chapter 5. Then the resist is removed again by acetone. Another layer of AZ5214E has been patterned with the mask shown in Figure 7.4(d) for metal lift-off (also see Figure B.2(c)). 90nm titanium, followed by 200nm aluminium, has been sputtered on top of the photoresist layer. After lift-off in acetone for 30min, the metal on photoresist will break from substrate. The sample is first rinsed by IPA and then de-ionized water to clean the metal pieces. The two electrodes are used as source and drain respectively (Figure 7.6(d)). 100nm Ti has been sputtered on the backside of the substrate immediately after removal of the oxide at the bottom, to serve as a back gate to control the conductivity of graphene.

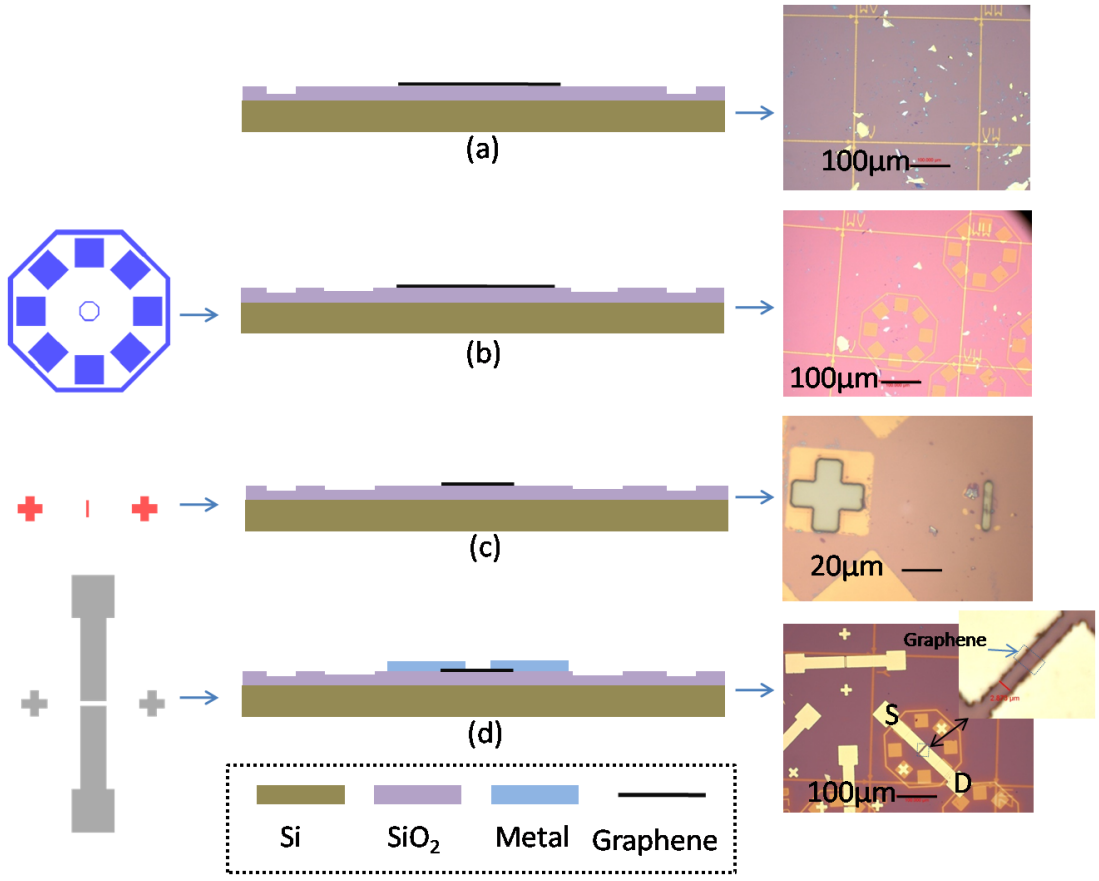

Figure 7.6: Fabrication steps of graphene field effect transistor

7.5 Results and discussion

7.5.1 Raman characterisation

Raman spectrum has been taken on the graphene channel after the fabrication process has finished. The laser wavelength is 514nm. The G band and 2D band have been observed as expected, located at 1580 and 2700 cm^{-1} respectively (Figure 7.7(a)). A static peak scan at 2D band reveals that the peak is symmetric and can be fitted very well with single Lorentz peak (Figure 7.7(b)), which proves that the graphene channel is indeed single layer graphene [125]. There is also a D band observed at around 1350 cm^{-1} with a much smaller intensity compared to G band. The D band is related to defects in graphene. However, the D band in the graphene is more likely to be caused by the edge effect if the laser spot in the Raman system covers the edge of graphene sheet [102], because the intensity of the D band is much smaller in comparison with the intensity of G band.

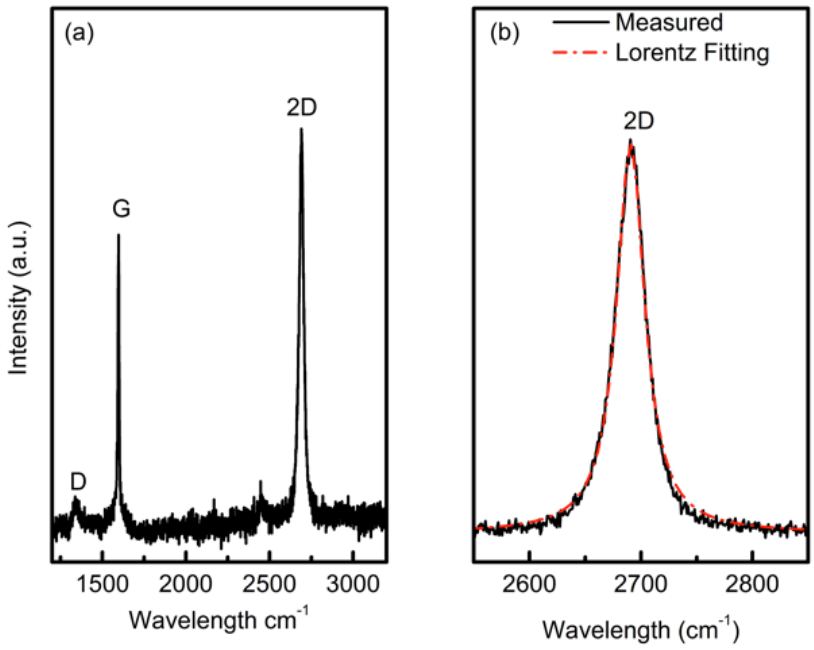

Figure 7.7: Raman spectrum of the graphene channel

7.5.2 Electrical characterisation

Figure 7.8(a) plots the drain current I_{ds} against drain voltage V_{ds} with different gate bias V_{gs} ranging from -25 to +25V, and V_{ds} has been swept from -100mV to 100mV.

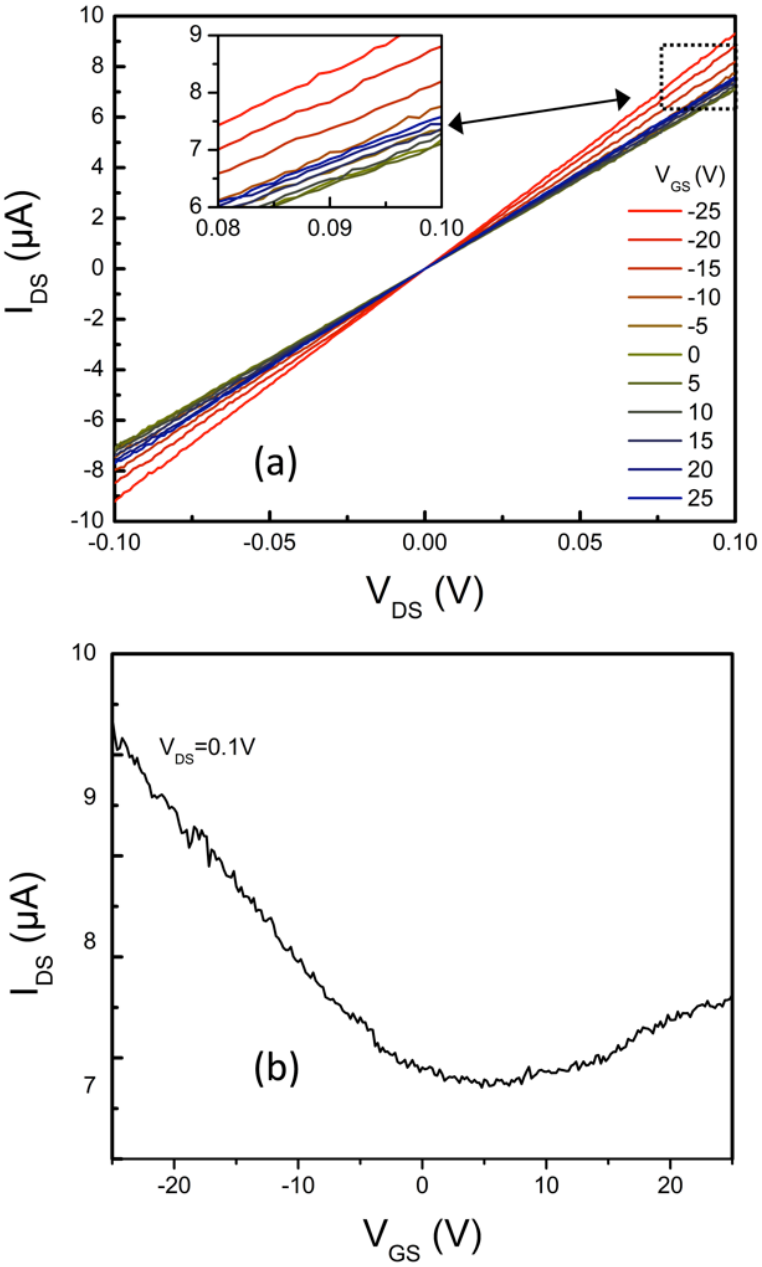

Figure 7.8: I-V measurement of graphene transistor

The slope of the curve equals to the conductance of graphene. Again, as have been observed in Figure 5.7 chapter 5, the curves are straight lines, even near the zero voltage, suggesting that the contacts between graphene is indeed Ohmic and the conductance is obviously tuneable by the back gate voltage. Figure 7.8(b) shows the influence of V_{gs} on I_{ds} curve with V_{ds} fixed at 100mV. I_{ds} decreases as the gate voltage increases from -25V to 5V, and starts to increase when the gate voltage surpasses 5V. The Dirac point, where the conductance is at its minimum and carriers

are depleted most, occurs at around 5V, which indicates graphene is p-doped. The as-fabricated graphene sheet are usually doped with holes by the ambient oxygen or water absorbed to it as mentioned in chapter 6.

Unlike the conductance measured on annealed graphene transistors which drops sharply to its minimum [191], the conductance changes more slowly near the Dirac point in Figure 7.8. The shape of the curve compares well to those measured on un-annealed graphene transistor [192], which suggests that the residuals and contaminations on top of graphene is limiting the carrier mobility, and upon annealing, the mobility can be further improved. Moreover, the contaminations causes inhomogeneous pitches of holes and electrons in the graphene sheet so that the conductance does not show a deep drop around the Dirac point [62]. Using the diffusive transport model proposed by S. Kim [193], the hole and electron mobilities have been extracted to be around 1010 cm^2/Vs and 3550cm^2/Vs respectively. The carrier mobilities of holes and electrons compare well to reported values of other graphene transistor [194].

7.6 Conclusion

Fabrication of MEMS devices requires successive photolithography steps to transfer designed patterns to each material layer. Each layer of photo mask has to be aligned with the aid of sophisticatedly designed alignment marks. Conventional mask aligners are designed for aligning wafers, which is not suitable for fabricating devices from mechanically exfoliated 2D material sheets. Therefore, the unique alignment technique has been developed for such purpose, which offers an option to researchers who do not want to employ the commonly used EBL technology for various reasons.

The core of this alignment technique is a master alignment mark of octagonal shape comprising 4 pairs of squares that can be patterned around the 2D flakes. Then the following layers of photo masks can be aligned to each pair of squares according to the orientation of the flakes. The octagon-shaped alignment mark is the enabling factor in this process. The alignment mark design solves the issues of random location to within 1μm accuracy, random orientation and the random shape of the exfoliated 2D flakes.

The application of the alignment technique has been demonstrated by successfully fabricating a graphene transistor whose channel length is only 2μm. The transistor shows comparable performance to those devices under similar condition fabricated with EBL technique. With optimization, the performance can be improved further. The alignment technique has the potential to be incorporated to the fabrication of other devices as well.

Chapter 8

Conclusion and future work

This thesis has presented the design, fabrication, and characterisation of graphene resonators, as well as an enabling alignment technique for prototyping devices from 2D flakes. In this chapter, the conclusions of the fabrication of graphene resonators will be summarized, including the substrate design in chapter 4 and the device fabrication in chapter 5, in a coherent sequence. The main findings in chapter 6 will also be reviewed, which is about characterisation results acquired by the current mixing technique presented in chapter 3, as well as the optical alignment technique in chapter 7. Based on the fabrication in chapter 5, further work to be done to improve the overall yield of the process will be suggested. The findings in chapter 6 could lead to breakthrough in graphene resonator's application in sensor and RF components, which will be an important research topic for the future.

8.1 Fabrication of suspended graphene structure

8.1.1 Initiatives and goals

In this PhD project, suspended monolayer graphene bridges have been successfully fabricated. Obtaining suspended graphene bridges is key to make graphene resonators, as well as for other applications. There have been much efforts devoted to achieve this goal with various approaches. Mechanical exfoliation has been the first technique used to fabricate graphene resonators and to isolate graphene from substrate for characterizing its intrinsic physical properties. Although this technique is of great academic value, it is not scalable for mass production of graphene devices. There are two techniques that are promising for mass production, both stemming from the large area growth of graphene. One is to release graphene grown on silicon carbide (SiC), and the other one is to release CVD-grown graphene transferred to SiO_2 substrate. The former methods lacks flexibility in choosing substrate material since the graphene layers are firmly settled on the SiC surface, the higher cost of growing graphene by sublimation of SiC is another drawback, while the later one normally employs wet

etchant to dissolve the SiO_2 layer. The wet etchant for SiO_2 etching contains HF that is highly corrosive to metal. SiO_2 is also the standard insulator in complementary metal-oxide-semiconductor (CMOS) technology, if the graphene resonator is going to be integrated with circuits to achieve a micro/nano-electromechanical system (MEMS/NEMS) device, the HF-based SiO_2 release will not be compatible with the rest of the fabrication process. That is why we are motivated to develop a new technique for graphene resonators. There are three fundamental goals to achieve in this project. First of all, it is desired that the graphene resonators can be massively fabricated. Mass production is the key to lower the average cost per device. Second, the graphene resonator should have metal contacts which enables electrical characterisation of its resonance and also enables the integration of graphene resonator into MEMS/NEMS devices. And last, the fabrication process should be compatible with commonly used materials and processing techniques, otherwise, the integration with circuit will be prohibited.

8.1.2 Substrate design

Aimed at these goals, it is proposed to utilize the poly-Si film as sacrificial layer. Poly-Si has been widely used as sacrificial material in MEMS technology. It is easy to deposit and can be etched away in vapour phase by XeF_2. It is worth pointing out that poly-Si is not the only material that can be etched in vapour phase. SiO_2 can also be etched in vapour phase by a combination of HF and water vapour. Although under very well calibrated conditions, that the HF vapour will not degrade metal much, it still etches those SiO_2 serving as dielectric material or passivation layer.

Up to now, SiO_2 is the mostly used sacrificial layer for graphene resonator fabrication, only because graphene on SiO_2 layer can be made visible under optical microscope for certain thicknesses of SiO_2. Graphene's visibility under optical microscope is not a must, nevertheless, the visibility allows quick inspection of the samples during the fabrication and makes the experimental operations much easier. As guidance, to make an atomically thin graphene sheet to be visible on a substrate, the reflection of the substrate must be sensitive to subtle changes of its surface condition, which is the case for an anti-reflective substrate. The anti-reflective substrate is realized by adjusting light beams reflected from different interfaces to meet the destructive interference condition.

Then, even a thin layer graphene is put onto the substrate, the destructive interference condition can be destructed and the reflection will change substantially and lead to high contrast. Since poly-Si/Si interface does not reflect light due to their equal refractive index, a SiO_2 layer has been inserted between, thus forming a multilayer optical system. a integral contrast defined over 400nm-740nm wavelength range have been used as target function and performed parametric study by sweeping the thicknesses of poly-Si film and SiO_2. The reflective rate calculation, as well as the contrast, has been based on the transfer matrix theory. The parametric calculation results reveal that 75nm poly-Si/100nm SiO_2/Si substrate could produce a high contrast beyond 10% in a band near 600nm wavelength. The contrast of monolayer graphene, as confirmed by 2D Raman peak, has increased from near zero under ordinary halogen lamp illumination to about 6.5% when a 600nm optical filter is inserted to the light path. In contrast, graphene on SiO_2 does not change, but remains about 8% under both illumination conditions, consistent with previously reported calculation results and experimental results. Simulation has been conducted to investigate how the doping in poly-Si layer can affect the conductivity of graphene through the modulation doping mechanism. It have been found the electron concentration in graphene is two orders of magnitude lower the donor concentration in poly-Si when the donor concentration is below 10^{15}ions/cm^3, suggesting that poly-Si will induce little change to graphene's conductivity even poly-Si is lightly doped un-intentionally.

8.1.3 Graphene resonator fabrication

Based on the 75nm poly-Si/100nm SiO_2/Si substrate, suspended graphene bridges have been fabricated. The graphene sheet has been transferred from CVD-grown graphene on copper foil with the PMMA-assisted transfer process. The graphene bridges have been arranged in four-point-probe structure with various inter-spacing intended for transmission line measurements. Metal pads have been deposited by the lift-off process to make electrical contact for graphene resonator characterisation. An issue with the metallization step is that the yield of conductive graphene channels is quite low after the metal electrodes are deposited. For 1nm Cr/80nm Au, the percentage of conductive graphene channel is 21.88% for those on SiO_2 and 5.4% on poly-Si. It has been found that the devices fabricated on SiO_2 have larger chance of being conductive than on

poly-Si substrate. Moreover, thicker metal deposition leads to a decreased percentage of conducting channels, consistent with widely reported observation that the kinetic energy of metal atoms would degrade the graphene and worsen the contact resistance. The low rate of conductive channels on poly-Si may suggest that the rough poly-Si could possibly leave nano-scopically suspended graphene sheet more vulnerable.

The conductive graphene bridges have been released by XeF_2 in vapour phase. It has been found that under a base pressure of 2torr, and 50sccm flow rate at room temperate, the 2μm wide graphene can be completely released in 55s. However, the fluorine atoms dissociated from XeF_2 molecular are highly reactive that they could bond the graphene basal plane, namely the fluorination process. *Ab initio* calculation shows that fluorination of graphene leads to opening of band gap in graphene as large as 2.7eV. Consequently, the graphene bridge after release is almost completely invisible, indicating that the light absorption rate decrease to much lower than 2.3%. And also, the resistivity of graphene bridges surges by about 15GΩ/square due to the band opening. Such high resistivity would impede the electrical measurement of graphene resonator's performance, therefore, reduction of the fluorinated graphene have been conducted by hydrazine vapour at 160°C for 24 hours. The hydrazine reduction has been proved to be an effective approach to remove the fluorine atoms while keep the hexagonal lattice of graphene intact, as suggested by considerable recovery of conductance as well as the re-emergence of Raman 2D band. Although the conductivity of graphene cannot be fully restored, its Young's modulus is not degraded by the fluorination, which is a key factor for anticipating non-degraded performance of the graphene resonators. There has been no observation of graphene bridge breakage after the XeF_2 etching, proving that the vapour phase release process is a superior process over wet etching. The overall yield of making graphene resonator is determined by the metallization process. It is believed that with better control of the metallization condition, as recent research on graphene/metal contact has achieved, the overall yield of conductive graphene channels can be increased substantially.

8.2 Characterisation of graphene resonators

8.2.1 Frequency measurement

The resonance of the de-fluorinated suspended graphene bridges has been tested electrically in vacuum at room temperature. The pressure in the vacuum chamber is around 3mbar. The metal pads connected to two ends of a graphene strip are used as source and drain electrodes, and the Si substrate has been used as gate. By applying a AC voltage (actuation signal) between the gate and graphene bridge, the bridge has been driven into resonance by the pulling electrostatic force. Because of the large frequency of graphene resonators, the low pass filter formed by the parasitic capacitance between metal electrodes and the substrate (gate) and the graphene's own resistance attenuates the resonance signal to an undetectable level. Therefore, the current mixing technique has been adopted. An AC signal that deviates from the actuation frequency by a small constant frequency difference (mixing signal) has been applied to the drain electrode. Upon resonance, the graphene bridge acts as a mixer that synthesizes the actuation signal and the mixing signal to result in a signal with frequency equal to their frequency difference, which passes the low-pass filter with no problem. The signal for actuation and for mixing can both be applied to the drain electrode at the same time by feeding the drain electrode with amplitude modulation or frequency modulation signal that both contain the two frequency components needed, which is called the one-source setup as introduced in chapter 3. The current flowing along the graphene bridge has been detected by a lock-in amplifier.

For a resonator of 12μm long and 2μm wide, the fundamental frequency is found to be around 1.9MHz, and the build-in stress is about 4.8MPa. The most intriguing phenomenon observed is that, among four resonant bands observed, there are higher order harmonics of graphene resonator. All the bands are tuneable by a DC voltage applied on the back gate. The different sensitivity of response to the tuning can be used to distinguish the resonance peaks from graphene bridge or metal electrodes. The frequency of graphene bridges should be more responsive to the tuning voltage than the metal electrode. The second order harmonic is confirmed by its tight coupling with the fundamental frequency, namely, the frequency of the second order harmonic (1.42MHz) is about twice that of the fundamental frequency (0.792MHz) at 450mV actuation

voltage, and the frequency shift under electrostatic tuning also doubles that of the fundamental peak. A third harmonic is also probably observed according to its peak location (2.14MHz) which nearly triples the fundamental frequency. When the actuation voltage increases, the response of the second order harmonics increases faster than the fundamental mode, and their amplitude eventually become comparable. This phenomenon could be of great value for graphene resonators' applications. First, the second order mode frequency is twice the fundamental frequency thus the working frequency can be further increased without shrinking the dimension, which could deteriorate the resonator's performance. And moreover, the peak frequency shift is more responsive to the physical quality change, such as mass density or stress in graphene. This property could lead to substantial improvement of graphene resonator's sensitivity.

The quality factors of all bands are quite low, even below 10. The low quality factor has been found for graphene as well as carbon nano-tube resonators at room temperature in literature [37]. It has been reported that the graphene resonator's quality factor is proportional to $1/\mathcal{T}^{2.3}$ when the temperature is between 40K up to 300K. Although the actual loss mechanism behind this remains unknown, the quality factor could improve by orders of magnitude at low temperature.

8.2.2 Second order harmonic

It has been hypothesized that the controllable and prominent second order harmonic is induced by the non-uniform electrostatic force applied on the graphene bridge. Although there have been a few MEMS cantilever resonators capable of working at higher modes, the second mode of doubly clamped bridge resonator is achieved intentionally for the first time. By decomposing the Euler-Bernoulli equation into separated independent equations describing each mode, it is found that the amplitude of each mode is determined by the projected actuation force onto that mode. The spatial mode function of the second mode is a sine function with a length period equal to the bridge length, so that a uniform electrostatic force distribution along the graphene bridges will project none to the second mode. While in the one-source characterisation setup, the actuation force is fed to the drain electrode, and the source electrode is grounded by a small resistor. Therefore, the voltage difference between the graphene and substrate will drop from the drain side to the source side, namely a ramp function.

And the projected force onto the second mode will no longer be zero, therefore, the second mode is driven into resonance. The theoretic analysis also shows that the response of the second mode frequency to mass change will double that of the fundamental mode frequency.

Finite element analysis has been performed on graphene resonators actuated by uniform and non-uniform electrostatic force of 0.75MHz respectively. The displacement of the beam at a quarter of its length has been recorded along with simulation time step. Fourier transform reveals that the displacement contains the forced response frequency component (0.75MHz) and also the fundamental frequency component (1.94MHz) for uniform actuation. For non-uniform actuation, a second order harmonic at 3.95MHz will emerge besides the other two peaks, proving that the non-uniform actuation force configuration is essential to the activation of second mode. A frequency sweep has also been performed on these two different actuation configurations, and the displacement at the actuation frequency has been extracted and plotted against different frequency. The resulted plot from non-uniform actuation shows two bands, one near the fundamental frequency while the other one is near the second mode frequency, which agrees very well with the observed peaks in measurement results.

8.3 Alignment technique for devices from exfoliated 2D materials

8.3.1 Alignment mark design

Motivated by the intention to avoid using electron beam lithography technique for fabricating devices from mechanical exfoliated 2D materials flakes, a set of alignment marks have been designed, which can be integrated into the mask design of ordinary optical mask aligner for device patterning.

The common features of the mechanically exfoliated 2D materials include random location, random orientation, and irregular shape. The size of these exfoliated flakes are often of a few microns. Therefore, it has been a huge challenge to process these flakes with the conventional mask aligner. To solve the issue of random location, a master alignment mark has been designed, which can be defined with specific location relationship to the randomly located exfoliated flakes. The master alignment marks comprises pairs of squares that are commonly used in the first layer of photo masks and

to be aligned to by following mask layers. There are totally four pairs of such squares arranged in the hexagonal shape. The most convenient pair can be chosen according to the orientation of the 2D material flake. On the following layer of masks for 2D material or metal patterning (device patterns), a pair of crosses are placed aside the device patterns. Therefore, when the crosses are aligned to the octagonal shape master alignment mark, the devices patterns are placed exactly on top of the 2D material flakes. The alignment technique can be incorporated to various fabrication processes for various device structures as long as master alignment marks are not screened by opaque materials.

8.3.2 Application of the optical alignment technique

The application of the technique has been demonstrated by the successful fabrication of a back-gated graphene field effect transistor, which contains two more layers of photo masks besides the master alignment mark. The device pattern on the second layer is a strip for patterning the graphene channel, and the pattern on the third layer are large area pads for source and drain electrodes. Raman spectroscopy has confirmed that the graphene channel is indeed monolayer. The conductivity of the graphene channel can be controlled by the gate voltage. The minimum conductivity point is found to be around 5V (Dirac point), indicating that the as-fabricated graphene sheet is p-doped. However, the conductivity does not drop sharply to near zero at Dirac point, and the shape is consistent with those measured on un-annealed graphene transistor under the similar temperature condition. The extracted electron and hole conductivity are about 1010 cm^2/Vs and 3550cm^2/Vs respectively. Such mobility is much lower than those measured in annealed graphene transistors. The main function of annealing is to remove polymer residues left on the graphene sheet. Otherwise, the residuals can induce conductive puddles of electrons and holes so that the conductivity at Dirac point does not go to zero. Moreover, the residuals may act as scattering source for the electron transportation, degrading the charge carrier velocity in graphene.

8.4 Future work

Although It has been managed to fabricate the graphene resonators in the way proposed and measure the performance. There are still works to be done in the future either to

improve the fabrication process or to demonstrate the potential application of the resonators. Moreover, the findings in this work also inspire research topics of great academic value worth exploring further.

8.4.1 Device processing

There is still an issue with the fabrication process, which is the low overall yield of conductive graphene bridges. As mentioned in chapter 5, the low percentage originates from the graphene damage caused by the metal atoms bombardment during the deposition step. Generally speaking, metal atoms evaporated by electron beam have smaller kinetic energy than those sputtered by plasma. The damage is not limited to the first few layer of metal atoms that have direct contact with the graphene sheet, but will accumulate as if the kinetic energy can be transferred to the bottom layer metal atoms. Therefore, the metal thickness should be minimized. The metal deposition rate also affects the contact resistance between graphene and metal. Lower deposition rate could lead to lower contact resistance. In summary, the metallization condition should be optimised in the future to increase the overall yield.

The other problem worth studying is the influence of fluorination on the recoverability of the conductivity. In this thesis, the vapour phase release technique of the graphene bridges have been developed, and it has been found that for graphene resonator etched for 55s by XeF_2 with 50sccm flow rate and 2torr base pressure at room temperature, its conductivity can still be recovered to a reasonable range that allows the electrical measurement of the resonance of the graphene resonators. However, this has been achieved in a heuristic manner. The resonators have also been released for 150s under the same condition and the conductivity is not recovered at all. Therefore, it is required to study under what condition will the XeF_2 cause permanent damage to graphene's lattice structure. Equipped with better understanding of the fluorination and de-fluorination's influence on the graphene resonators, we can proceed to process graphene resonator with various dimensions and scale down to explore the limit of this fabrication technique. Moreover, we could also envisage the integration of graphene resonators with CMOS technology to form a fully functional MEMS/NEMS device based on graphene.

8.4.2 Graphene sensor for mass detection

It has been theoretically proven that by measuring the second mode frequency, the mass sensitivity could improve by a factor of two. However, sound experimental results still lack. Therefore, the detection of ultra-light mass is of great importance. Yet, obtaining a high sensitivity also relies on the characterisation environment. Under our present conditions, the quality factor is so low that the sensitivity is substantially limited. To increase the quality factor, it is necessary to cool the temperature of graphene resonators down and further pump down the pressure in the vacuum chamber. Another job needs to be accomplished is a mass source that is able to emit particles or molecular that will absorb to the surface of the graphene bridge so as to change the effective mass of the graphene resonator and thus change the frequency. With better characterisation environment, a comparison of the responses of the first and second modes can be performed.

Appendix A

Matlab codes

A.1 Contrast calculation of graphene on poly-Si/SiO_2/Si substrate

```
%This program is for calculating the contrast of monolayer graphene on
%poly-Si/SiO2/Si substrate
%Author: Tao Chen, SMC, IMNS, The University of Edinburgh
%Date: From 27/10/2011

clear;
load RefractiveIndice.mat;    %Load the refractive indice table for silicon and oxide
load CMFXYZ.mat; %Load color matching function tables
N0=1; %Air refractive index
Nc=2.6-1.3i; %Graphene refractive index

Dc=0.34*1; %Graphene thickness
Dso=20:2:350; %Oxide thickness
Dsi=20:2:150; %Poly-Si thickness
Lamda=400:1:740; %Wavelength
x=size(Dso);
m=x(2)
x=size(Dsi);
n=x(2)
x=size(Lamda);
k=x(2)

for mi=1:1:m
    for ni=1:1:n
        Req1int=0;
        Req2int=0;
        for ki=1:1:k
            Nsi=interp1(WLsi,nsi,Lamda(ki))-interp1(WLsi,ksi,Lamda(ki))*j;
            Nso=interp1(WLso,nso,Lamda(ki));
            Mc=FilmMatCal(Nc,Dc,Lamda(ki));
            Mso=FilmMatCal(Nso,Dso(mi),Lamda(ki));
```

```
            Msi=FilmMatCal(Nsi,Dsi(ni),Lamda(ki));
            EM1=Mc*Msi*Mso*[1;Nsi];
            Neq1=EM1(2)/EM1(1);
            Req1=(N0-Neq1)/(N0+Neq1);
            EM2=Msi*Mso*[1;Nsi];
            Neq2=EM2(2)/EM2(1);
            Req2=(N0-Neq2)/(N0+Neq2);
            Nsivec(ki)=Nsi;
            Req2vec(ki)=abs(Req2);
            Req1vec(ki)=abs(Req1);
            Ctra=abs((abs(Req1)*abs(Req1)-abs(Req2)*abs(Req2))/(abs(Req1)*abs(Req1)));
            Ctravec(ki)=Ctra;
            Req1int=Req1int+Req1vec(ki)*(Lamda(2)-Lamda(1));
            Req2int=Req2int+Req2vec(ki)*(Lamda(2)-Lamda(1));
        end
        Req1int;
        Req2int;
        Reqdef=abs(Req1int-Req2int);
        Ctraint(mi,ni)=Reqdef/abs(Req2int);
    end
end

save CtraIntPeakSearch.mat Ctraint Lamda Dsi Dso

%ColorReq1=CMFXYZ(Lamda,Req1vec);
%ColorReq2=CMFXYZ(Lamda,Req2vec);

figure(1)
contour(Ctraint)

%figure(1)
%plot(Lamda,Ctravec)
%figure(2)
%hold off
%plot(Lamda,Req2vec,'-')
%hold on
%plot(Lamda,Req1vec,'o')
```

```
%plot3(Dsi,Lamda,Ctravec);
%xlabel('wavelength/nm (one layer graphene)');
%ylabel('Contrast')
%figure(2)
%plot3(Dsi,Lamda,abs(Req2vec));
%xlabel('wavelength/nm (without graphene)');
%ylabel('Reflectivity')

%The following is to convert the spectrum to RGB value.
function C=CMFXYZ(Lamda,Spectrum)
load CMFXYZ.mat
X=0;
Y=0;
Z=0;
LamdaSize=size(Lamda)
for k=1:1:(LamdaSize(2)-1)
    X=X+(Lamda(k+1)-Lamda(k))*Spectrum(k)*interp1(CMFWL,CMFR,Lamda(k));
    Y=Y+(Lamda(k+1)-Lamda(k))*Spectrum(k)*interp1(CMFWL,CMFG,Lamda(k));
    Z=Z+(Lamda(k+1)-Lamda(k))*Spectrum(k)*interp1(CMFWL,CMFB,Lamda(k));
end

SUM=X+Y+Z;
x=X/SUM
y=Y/SUM
z=Z/SUM
Mrgb2xyz=(1/0.17697)*[0.49,0.31,0.20;0.17697,0.81240,0.01063;0,0.01,0.99];
C=(Mrgb2xyz^-1)*[x;y;z];
%%%%%%%%%%%%%%%%%%%%%%%%%%%%%%%%%%%%%%%%%%%%%%%%%%%%%%%%
```

A.2 Modulation doped carrier concentration in graphene by poly-Si

```
%This is the main program to solve  graphene carrier
%density and the depletion depth in poly-Si, for modulation doping
%structure graphene/poly-Si or graphene/Si shottkey junction.

%Author: Tao Chen, SMC, IMNS, The University of Edinburgh
```

```
%Date: From 09/03/2012

%The iteration starts from trying to narrow the distance between the Fermi
%level in graphene (EFG) and poly-Si (EFS), the increase step of EFS will be one hundredth of the distance
%between EFG and EFS

%%%%%%%%%% Parameter initialization %%%%%%%%%%%%%%%%%%%
%ee, electron charge;
%Nd, donor concentration in poly-Si;
%EpsS, electric permittivity of poly-Si;
%PhiS, band lowering in poly-Si;
%PhiN, distance between bottom of poly-Si conduction band (ECS) and Fermi level
%ED, Dirac point energy;
%Xd, depletion depth in poly-Si
clc
clear
e=1;                    %Unit for energy
ee=1.602176e-19;    %Electron charge
hb=6.5811928e-16      %h bar, Plank's constant,    unit eV.S
VF=1e8                  %Graphene electron velocity
EpsS=11.8*8.85e-10;
ECS=-4.6+1.12/2;       % Bottom of conduction band of silicon
ED=-4.6;                  %Dirac point energy
EFIS=-4.6;                 %Intrinsic fermi level of silicon
Kb=8.617e-5; %Boltzmann constant
T=300;
%%%%%%%%%%%%%%%%%%%%%%%%%%%%%%%%%%%%%%%%%%%%%%%%%%%%%%%%
Ni=9.38e19*(T/300)^2*exp(-6884/T)              %Intrinsic electron concentration in silicon
for num=1:9 % main loop for different donor concentration in poly-Si
      Nd=10^(num+11);
EFS=EFIS+Kb*T*log(Nd/Ni);
PhiN=(ECS-EFS)/e;
s=1;   %Iteration step index
%%%%%%%%%%%%%%%%%%    Initialization    %%%%%%%%%%%%%%%%%%%%%%%%%
PhiS=0;
EFG(s)= -4.6;
```

```
eta=(EFG(s)-ED)/(Kb*T);
[y, N, err]=FD_int_num(eta,1,10e-6,1000); %Fermi Dirac integration
NPG(s)= (2/pi)*(Kb*T/(hb*VF))^2*y;
Xd(s)= NPG(s)/Nd;
PhiS(s)= ee*Nd*Xd(s)^2/(2*EpsS);

%%%%%%%%Sub loop for each donor concentration%%%%%%%%%%%%%%%%%%
while(1)
    s=s+1;
    if s==1000
        x=1:1:s-1;
        figure(1)
        plot(x, EFG)
        figure(2)
        plot(x, Xd)
        error('Exceed maximum iteration steps');
        break;
    end

    EFG(s)= EFG(s-1)+(ECS-e*PhiS(s-1)-e*PhiN-EFG(s-1))*0.01;
    eta=(EFG(s)-ED)/(Kb*T);
    [y, N, err]=FD_int_num(eta,1,10e-6,1000);
    NPG(s)= (2/pi)*((Kb*T)/(hb*VF))^2*y;
    Xd(s)= NPG(s)/Nd;
    PhiS(s)= ee*Nd*Xd(s)^2/(2*EpsS);

    if ECS-EFG(s)-e*PhiS(s)-e*PhiN <= 10e-5 %Convergence judgement
        NPGV(num)=NPG(s);
        break;
    end
end
end % Then end of the program

% The Fermi-Dirac integration program, downloaded from internet%%%%%%%%
function [ y N err ] = FD_int_num( eta, j, tol, Nmax )

% Numerical integration of Fermi-Dirac integrals for order j > -1.
```

```
% Author: Raseong Kim
% Date: September 29, 208
% Extended (composite) trapezoidal quadrature rule with variable
% transformation, x = exp( t - exp( t ) )
% Valid for eta ~< 15 with precision ~eps with 60~500 evaluations.
%
% Inputs
% eta: eta_F
% j: FD integral order
% tol: tolerance
% Nmax: number of iterations limit
%
% Note: When "eta" is an array, this function should be executed
% repeatedly for each component.
%
% Outputs
% y: value of FD integral (the "script F" defined by Blakemore (1982))
% N: number of iterations
% err: error
%
% For more information in Fermi-Dirac integrals, see:
% "Notes on Fermi-Dirac Integrals (3rd Edition)" by Raseong Kim and Mark
% Lundstrom at http://nanohub.org/resources/5475
%
% Reference
% [1] W. H. Press, S. A. Teukolsky, W. T. Vetterling, and B. P. Flannery,
% Numerical recipies: The art of scientific computing, 3rd Ed., Cambridge
% University Press, 2007.

for N = 1 : Nmax
    a = -4.5;                           % limits for t
    b = 5.0;
    t = linspace( a, b, N + 1 );        % generate intervals
    x = exp( t - exp( -t ) );
    f = x .* ( 1 + exp( -t ) ) .* x .^ j ./ ( 1+ exp( x - eta ) );
    y = trapz( t, f );
    if N > 1                            % test for convergence
```

```
            err = abs( y - y_old );
            if err < tol
                  break;
            end
      end
      y_old = y;
end
if N == Nmax
      error( 'Increase the maximum number of iterations.')
end
y = y ./ gamma( j + 1 );
```

A.3 Finite element simulation of graphene resonator

```
%This program is for calculating the transient response of graphene
%resonator to the electrostatic actuation
%Author: Tao Chen, SMC, IMNS, The University of Edinburgh
%Date: From 05/01/2014

clear
epsio=2*8.85e-12; % Permitivity of oxide
epair=8.85e-12; % Permitivity of air
beta=0.1; % Damping coefficient
E=1e12; % Graphene Young's modulus
Tg=0.34e-9; %Graphene thickness
Tp=75e-9; %Thickness of poly-Si layer, which is also the air gap distance
To=100e-9 %Thickness of oxide layer
rou=2200; %Graphene density
L=12e-6; %Length of Graphene bridge
Nmesh=32; %Number of Meshes
h=L/Nmesh;
x=0:(L/Nmesh):L;
dCgrPw=epsio^2*epair/(Tp*epsio+To*epair)^2; % differentiation of unit capacitance wrt gate voltage
Vdc=0.1; % Gate voltage
Vac=0.1; % Actuation voltage

f=1e6:25e3:5e6; %Frequency sweep
```

```
for o=1:length(f)
    Tend=50/f(o);
    tao=1/(f(o)*1024);
    for m=1:1:Nmesh+1 %Initialization
        w(m,1)=0;
        w(m,2)=0;
    end
    % for n=1:1:Tend/tao
    %   fa(n)=1/2*epsio/(Tc^2*Tg)*(0.1+A*sin(2*pi*f(o)*(n*tao)))/rou;
    % end
    for n=2:1:Tend/tao
        sum=0;
        for m=1:1:Nmesh
            sum=sum+(1/2*((w(m+1,n)-w(m,n))/h)^2)*h;
        end
        Sts=E*sum;
        %(dCgrPw*Vdc^2/2+dCgrPw*Vdc*Vac*sin(2*pi*f(o)*(n*tao)))*tao^2/(Tg*rou)
        for m=2:1:Nmesh
w(m,n+1)=(tao^2*(4.8e6+Sts)*(w(m+1,n)-2*w(m,n)+w(m-1,n)))/(rou*h^2)+2*w(m,n)-w(m,n-1) ...,
        -(dCgrPw*Vdc^2/2+dCgrPw*Vdc*Vac*(1)*sin(2*pi*f(o)*(n*tao)))*tao^2/(Tg*rou) ...,
        -beta*(w(m,n)-w(m,n-1))*tao; % Iteration equation
        end
        w(1,n)=0;
        w(Nmesh+1,n)=0;
    end
    y=w(Nmesh/4,:); % Get the displacement at a quater of the bridge length
    Nfft=2^nextpow2(length(y)-1);
    Freq=fft(y,Nfft);
    Ampl(o)=abs(Freq(65)); % Extract the amplitude at the actuation frequency

end
plot(f,Ampl);
save dataset2
% fh=plot(w(:,n));
% for n=1:1:Tend/tao
%       y=w(:,n);
%       set(fh,'y',y);
```

```
%       drawnow
%       pause(0.01)
% end
```

Appendix B

Mask designs

B.1 Graphene resonator mask

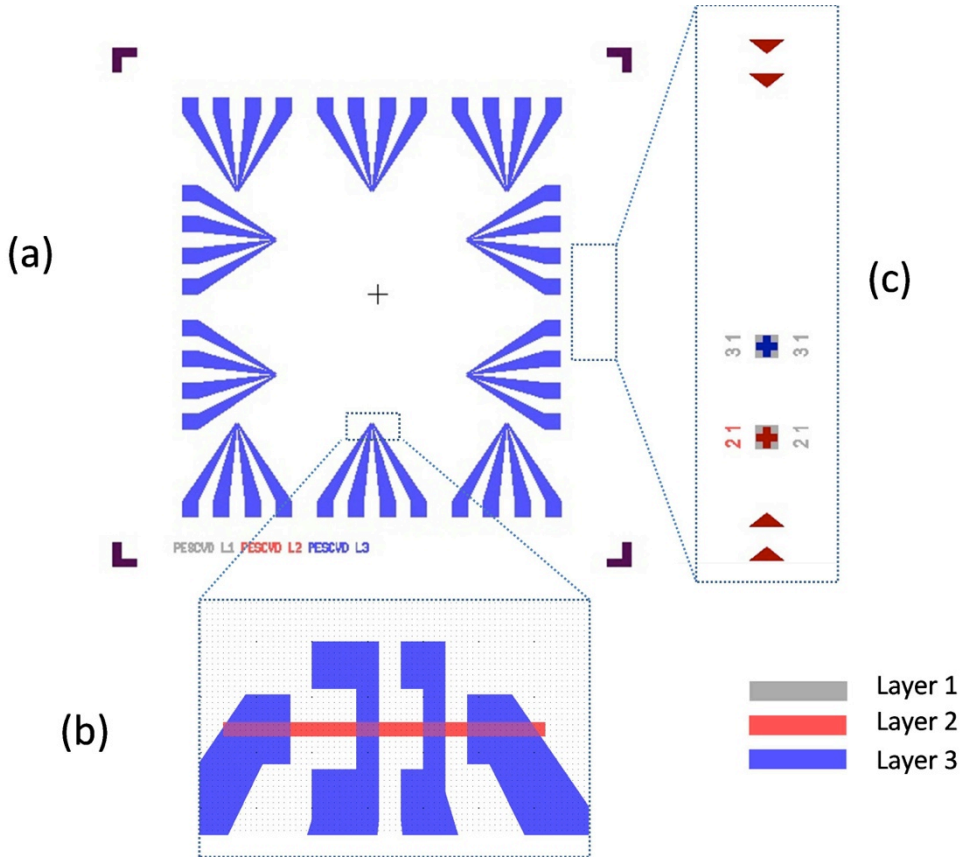

Figure B.1: Mask design for graphene resonator

B.2 Mask design for graphene transistor

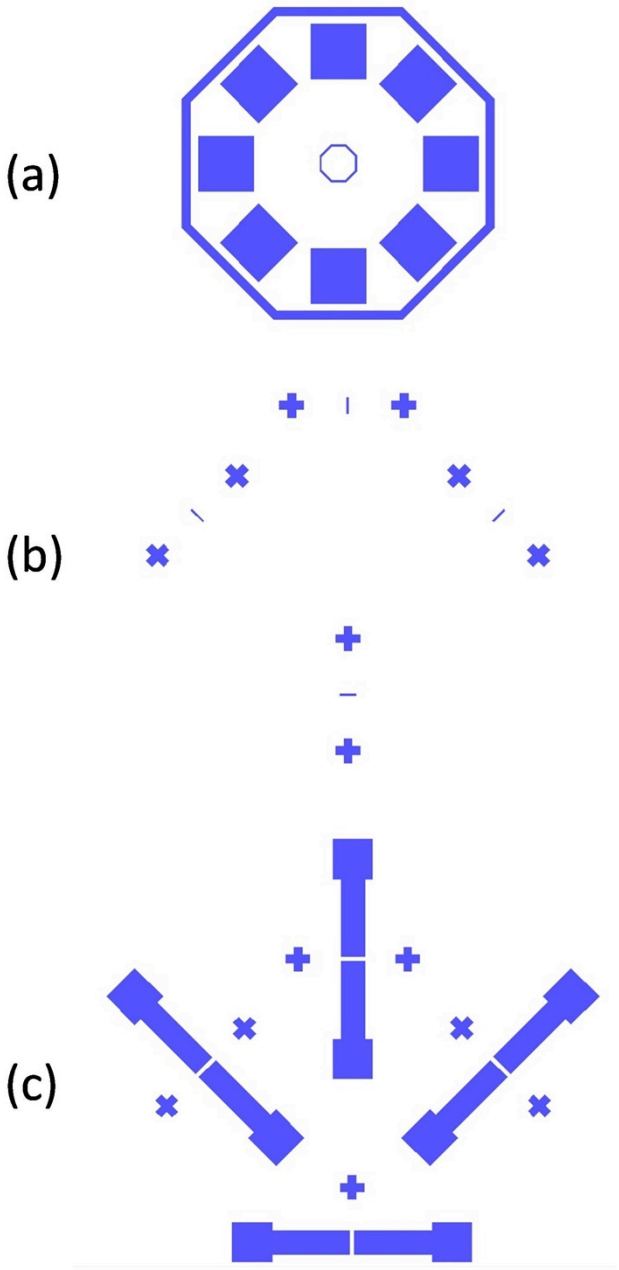

Figure B.2: Mask design for graphene field effect transistor, not to scale

Appendix C

Publications

Tao Chen, Enrico Mastropaolo, Andrew Bunting, Rebecca Cheung, Inhomogeneous actuation force activated second flexural mode in graphene electromechanical resonators, submitted to Nanoscale

Tao Chen, Enrico Mastropaolo, Andrew Bunting, Rebecca Cheung, Batch fabrication of graphene electromechanical resonator using poly-Si as sacrificial layer, to be submitted

Tao Chen, Rebecca Cheung, Mechanical properties of graphene, Contributed to chapter 43 of forthcoming Handbook of Graphene Science, CRC press, 2013

Eldad Grady, Enrico Mastropaolo, Tao Chen, Andrew Bunting, Rebecca Cheung, Low frequency graphene resonators for acoustic sensing, Microelectronics Engineering 119 (2014), pp105-108

Tao Chen, Enrico Mastropaolo, Andrew Bunting, Rebecca Cheung, Optical alignment technique for graphene transistor fabrication, presented at MNE 2012, Toulouse, paper submitted to Micro and Nano Letter

Tao Chen, Enrico Mastropaolo, Andrew Bunting, Tom Stevenson, Rebecca Cheung, Optimization of the visibility of graphene on poly-Si film by thin-film optics engineering, J. Vac. Sci. Technol. B 30, 06FJ01 (2012)

Boris Svilicic, Enrico Mastropaolo, Tao Chen, Rebecca Cheung, Piezoelectrically transduced silicon carbide MEMS double-clamped beam resonators, J. Vac. Sci. Technol. B 30, 06FD05 (2012)

Enrico Mastropaolo, Boris Svilicic, Tao Chen, Brian Flynn, Rebecca Cheung, Piezoelectrically actuated and sensed silicon carbide ring MEMS resonators, Microelectronic Engineering, Vol 97, 2012, pp220-222

Raden Dewanto, Tao Chen, Rebecca Cheung, Zhongxu Hu, Barry Gallacher, John Hedley, Reliability prediction of 3C-SiC cantilever beams using dynamic Raman spectroscopy, presented at IEEE NEMS, March 2012, Kyoto

References

[1] J. Harvey C. Nathanson, William E. Newell, Robert A. Wickstrom, John Ransford Davis, "The Resonant Gate Transistor," *IEEE Trans. Electron Devices*, vol. 14, no. 3, pp. 117–133, 1967.

[2] E. Verpoorte and N. F. De Rooij, "Microfluidics meets MEMS," *Proc. IEEE*, vol. 91, no. 6, pp. 930–953, Jun. 2003.

[3] S. S. Lee and R. M. White, "Self-excited piezoelectric cantilever oscillators," *Sensors Actuators A Phys.*, vol. 52, no. 1–3, pp. 41–45, Mar. 1996.

[4] J. Lu, T. Ikehara, Y. Zhang, T. Mihara, T. Itoh, and R. Maeda, "High quality factor silicon cantilever driven by piezoelectric thin film actuator for resonant based mass detection," *Microsyst. Technol.*, vol. 15, no. 8, pp. 1163–1169, Oct. 2008.

[5] P. R. Scheeper, W. Olthuis, and P. Bergveld, "The design, fabrication, and testing of corrugated silicon nitride diaphragms," *J. Microelectromechanical Syst.*, vol. 3, no. 1, pp. 36–42, Mar. 1994.

[6] R. A. Wolf, K. K. Deng, R. J. Davis, and S. Trolier-McKinstry, "Design, fabrication, and measurement of high-sensitivity piezoelectric microelectromechanical systems accelerometers," *J. Microelectromechanical Syst.*, vol. 12, no. 4, pp. 433–439, Aug. 2003.

[7] "Yole Développement Press - 2013 Press Releases." [Online]. Available: http://www.yole.fr/2013_press_releases.aspx.

[8] S. . Moe, K. Schjølberg-Henriksen, D. . Wang, E. Lund, J. Nysæther, L. Furuberg, M. Visser, T. Fallet, and R. . Bernstein, "Capacitive differential pressure sensor for harsh environments," *Sensors Actuators A Phys.*, vol. 83, no. 1, pp. 30–33, 2000.

[9] C. Tao, Z. Zhaohua, R. Tianling, M. Gujin, Z. Changjian, L. Huiwang, and L. Litian, "A novel dual-functional MEMS sensor integrating both pressure and temperature units," *J. Semicond.*, vol. 31, no. 7, p. 074013, Jul. 2010.

[10] A. A. Seshia, R. T. Howe, and S. Montague, "An integrated microelectromechanical resonant output gyroscope," in *Technical Digest. MEMS 2002 IEEE International Conference. Fifteenth IEEE International Conference on Micro Electro Mechanical Systems (Cat. No.02CH37266)*, 2002, pp. 722–726.

[11] A. Plecis and Y. Chen, “Fabrication of microfluidic devices based on glass–PDMS–glass technology,” *Microelectron. Eng.*, vol. 84, no. 5–8, pp. 1265–1269, May 2007.

[12] M. W. Ashraf, S. Tayyaba, and N. Afzulpurkar, “Micro Electromechanical Systems (MEMS) Based Microfluidic Devices for Biomedical Applications.,” *Int. J. Mol. Sci.*, vol. 12, no. 6, pp. 3648–704, Jan. 2011.

[13] B. Partoens and F. Peeters, “From graphene to graphite: Electronic structure around the K point,” *Phys. Rev. B*, vol. 74, no. 7, p. 075404, Aug. 2006.

[14] K. S. Novoselov, A. K. Geim, S. V Morozov, D. Jiang, Y. Zhang, S. V Dubonos, I. V Grigorieva, and a a Firsov, “Electric field effect in atomically thin carbon films.,” *Science*, vol. 306, no. 5696, pp. 666–9, Oct. 2004.

[15] A. Castellanos-Gomez, M. Poot, G. a Steele, H. S. J. van der Zant, N. Agraït, and G. Rubio-Bollinger, “Elastic properties of freely suspended MoS2 nanosheets.,” *Adv. Mater.*, vol. 24, no. 6, pp. 772–5, Feb. 2012.

[16] X. Du, I. Skachko, A. Barker, and E. Y. Andrei, “Approaching ballistic transport in suspended graphene.,” *Nat. Nanotechnol.*, vol. 3, no. 8, pp. 491–5, Aug. 2008.

[17] J. C. Meyer, a K. Geim, M. I. Katsnelson, K. S. Novoselov, T. J. Booth, and S. Roth, “The structure of suspended graphene sheets.,” *Nature*, vol. 446, no. 7131, pp. 60–3, Mar. 2007.

[18] Y. Zhang, Y.-W. Tan, H. L. Stormer, and P. Kim, “Experimental observation of the quantum Hall effect and Berry’s phase in graphene.,” *Nature*, vol. 438, no. 7065, pp. 201–4, Nov. 2005.

[19] J. S. Bunch, A. M. van der Zande, S. S. Verbridge, I. W. Frank, D. M. Tanenbaum, J. M. Parpia, H. G. Craighead, and P. L. McEuen, “Electromechanical resonators from graphene sheets.,” *Science*, vol. 315, no. 5811, pp. 490–3, Jan. 2007.

[20] H. Wang, L. Yu, Y.-H. Lee, Y. Shi, A. Hsu, M. L. Chin, L.-J. Li, M. Dubey, J. Kong, and T. Palacios, “Integrated circuits based on bilayer MoS_2 transistors.,” *Nano Lett.*, vol. 12, no. 9, pp. 4674–80, Sep. 2012.

[21] C. R. Dean, A. F. Young, I. Meric, C. Lee, L. Wang, S. Sorgenfrei, K. Watanabe, T. Taniguchi, P. Kim, K. L. Shepard, and J. Hone, “Boron nitride substrates for high-quality graphene electronics.,” *Nat. Nanotechnol.*, vol. 5, no. 10, pp. 722–6, Oct. 2010.

[22] K. S. Novoselov, D. Jiang, F. Schedin, T. J. Booth, V. V Khotkevich, S. V Morozov, and a K. Geim, “Two-dimensional atomic crystals.,” *Proc. Natl. Acad. Sci. U. S. A.*, vol. 102, no. 30, pp. 10451–3, Jul. 2005.

[23] V. Y. Aristov, G. Urbanik, K. Kummer, D. V Vyalikh, O. V Molodtsova, A. B. Preobrajenski, A. A. Zakharov, C. Hess, T. Hänke, B. Büchner, I. Vobornik, J. Fujii, G. Panaccione, Y. A. Ossipyan, and M. Knupfer, "Graphene synthesis on cubic SiC/Si wafers. perspectives for mass production of graphene-based electronic devices.," *Nano Lett.*, vol. 10, no. 3, pp. 992–5, Mar. 2010.

[24] S.-H. Ji, J. B. Hannon, R. M. Tromp, V. Perebeinos, J. Tersoff, and F. M. Ross, "Atomic-scale transport in epitaxial graphene.," *Nat. Mater.*, vol. 11, no. 2, pp. 114–9, Feb. 2012.

[25] S. Bae, H. Kim, Y. Lee, X. Xu, J.-S. Park, Y. Zheng, J. Balakrishnan, T. Lei, H. R. Kim, Y. Il Song, Y.-J. Kim, K. S. Kim, B. Ozyilmaz, J.-H. Ahn, B. H. Hong, and S. Iijima, "Roll-to-roll production of 30-inch graphene films for transparent electrodes.," *Nat. Nanotechnol.*, vol. 5, no. 8, pp. 574–8, Aug. 2010.

[26] Y. Hernandez, V. Nicolosi, M. Lotya, F. M. Blighe, Z. Sun, S. De, I. T. McGovern, B. Holland, M. Byrne, Y. K. Gun'Ko, J. J. Boland, P. Niraj, G. Duesberg, S. Krishnamurthy, R. Goodhue, J. Hutchison, V. Scardaci, A. C. Ferrari, and J. N. Coleman, "High-yield production of graphene by liquid-phase exfoliation of graphite.," *Nat. Nanotechnol.*, vol. 3, no. 9, pp. 563–8, Sep. 2008.

[27] J. T. Robinson, M. Zalalutdinov, J. W. Baldwin, E. S. Snow, Z. Wei, P. Sheehan, and B. H. Houston, "Wafer-scale Reduced Graphene Oxide Films for Nanomechanical Devices," 2008.

[28] P. Wallace, "The Band Theory of Graphite," *Phys. Rev.*, vol. 71, no. 9, pp. 622–634, May 1947.

[29] K. I. Bolotin, K. J. Sikes, Z. Jiang, M. Klima, G. Fudenberg, J. Hone, P. Kim, and H. L. Stormer, "Ultrahigh electron mobility in suspended graphene," *Solid State Commun.*, vol. 146, no. 9–10, pp. 351–355, Jun. 2008.

[30] J. Zheng, L. Wang, R. Quhe, Q. Liu, H. Li, D. Yu, W.-N. Mei, J. Shi, Z. Gao, and J. Lu, "Sub-10 nm gate length graphene transistors: operating at terahertz frequencies with current saturation.," *Sci. Rep.*, vol. 3, p. 1314, Jan. 2013.

[31] Y.-M. Lin, K. A. Jenkins, A. Valdes-Garcia, J. P. Small, D. B. Farmer, and P. Avouris, "Operation of graphene transistors at gigahertz frequencies.," *Nano Lett.*, vol. 9, no. 1, pp. 422–6, Jan. 2009.

[32] R. R. Nair, P. Blake, a N. Grigorenko, K. S. Novoselov, T. J. Booth, T. Stauber, N. M. R. Peres, and a K. Geim, "Fine structure constant defines visual transparency of graphene.," *Science*, vol. 320, no. 5881, p. 1308, Jun. 2008.

[33] S. Pang, Y. Hernandez, X. Feng, and K. Müllen, “Graphene as transparent electrode material for organic electronics.,” *Adv. Mater.*, vol. 23, no. 25, pp. 2779–95, Jul. 2011.

[34] K. S. Kim, Y. Zhao, H. Jang, S. Y. Lee, J. M. Kim, K. S. Kim, J.-H. Ahn, P. Kim, J.-Y. Choi, and B. H. Hong, “Large-scale pattern growth of graphene films for stretchable transparent electrodes.,” *Nature*, vol. 457, no. 7230, pp. 706–10, Feb. 2009.

[35] C. Lee, X. Wei, J. W. Kysar, and J. Hone, “Measurement of the elastic properties and intrinsic strength of monolayer graphene.,” *Science*, vol. 321, no. 5887, pp. 385–8, Jul. 2008.

[36] C. Chen, S. Rosenblatt, K. I. Bolotin, W. Kalb, P. Kim, I. Kymissis, H. L. Stormer, T. F. Heinz, and J. Hone, “Performance of monolayer graphene nanomechanical resonators with electrical readout.,” *Nat. Nanotechnol.*, vol. 4, no. 12, pp. 861–7, Dec. 2009.

[37] A. M. Van Der Zande, R. a Barton, J. S. Alden, C. S. Ruiz-Vargas, W. S. Whitney, P. H. Q. Pham, J. Park, J. M. Parpia, H. G. Craighead, and P. L. McEuen, “Large-Scale Arrays of Single-Layer Graphene Resonators.,” *Nano Lett.*, pp. 4869–4873, Nov. 2010.

[38] I. W. Frank, D. M. Tanenbaum, a. M. van der Zande, and P. L. McEuen, “Mechanical properties of suspended graphene sheets,” *J. Vac. Sci. Technol. B Microelectron. Nanom. Struct.*, vol. 25, no. 6, p. 2558, 2007.

[39] X. Liang, Y.-S. Jung, S. Wu, A. Ismach, D. L. Olynick, S. Cabrini, and J. Bokor, “Formation of bandgap and subbands in graphene nanomeshes with sub-10 nm ribbon width fabricated via nanoimprint lithography.,” *Nano Lett.*, vol. 10, no. 7, pp. 2454–60, Jul. 2010.

[40] S. Tongay, M. Lemaitre, J. Fridmann, a. F. Hebard, B. P. Gila, and B. R. Appleton, “Drawing graphene nanoribbons on SiC by ion implantation,” *Appl. Phys. Lett.*, vol. 100, no. 7, p. 073501, 2012.

[41] S. M.-M. Dubois, Z. Zanolli, X. Declerck, and J.-C. Charlier, “Electronic properties and quantum transport in Graphene-based nanostructures,” *Eur. Phys. J. B*, vol. 72, no. 1, pp. 1–24, Oct. 2009.

[42] D. A. Areshkin and B. K. Nikolić, “Electron density and transport in top-gated graphene nanoribbon devices: First-principles Green function algorithms for systems containing a large number of atoms,” *Phys. Rev. B*, vol. 81, no. 15, p. 155450, Apr. 2010.

[43] J.-H. Chen, C. Jang, S. Xiao, M. Ishigami, and M. S. Fuhrer, “Intrinsic and extrinsic performance limits of graphene devices on SiO2.,” *Nat. Nanotechnol.*, vol. 3, no. 4, pp. 206–9, Apr. 2008.

[44] M. Kim, N. S. Safron, C. Huang, M. S. Arnold, and P. Gopalan, “Light-driven reversible modulation of doping in graphene.,” *Nano Lett.*, vol. 12, no. 1, pp. 182–7, Jan. 2012.

[45] Q. X. Pei, Y. W. Zhang, and V. B. Shenoy, “A molecular dynamics study of the mechanical properties of hydrogen functionalized graphene,” *Carbon N. Y.*, vol. 48, no. 3, pp. 898–904, Mar. 2010.

[46] Y. Zhu, S. Murali, W. Cai, X. Li, J. W. Suk, J. R. Potts, and R. S. Ruoff, “Graphene and graphene oxide: synthesis, properties, and applications.,” *Adv. Mater.*, vol. 22, no. 35, pp. 3906–24, Sep. 2010.

[47] R. R. Nair, W. Ren, R. Jalil, I. Riaz, V. G. Kravets, L. Britnell, P. Blake, F. Schedin, A. S. Mayorov, S. Yuan, M. I. Katsnelson, H.-M. Cheng, W. Strupinski, L. G. Bulusheva, A. V Okotrub, I. V Grigorieva, A. N. Grigorenko, K. S. Novoselov, and A. K. Geim, “Fluorographene: a two-dimensional counterpart of Teflon.,” *Small*, vol. 6, no. 24, pp. 2877–84, Dec. 2010.

[48] Z. Wang, Q. Li, H. Zheng, H. Ren, H. Su, Q. Shi, and J. Chen, “Tuning the electronic structure of graphene nanoribbons through chemical edge modification: A theoretical study,” *Phys. Rev. B*, vol. 75, no. 11, p. 113406, Mar. 2007.

[49] A. Chuvilin, U. Kaiser, E. Bichoutskaia, N. A. Besley, and A. N. Khlobystov, “Direct transformation of graphene to fullerene.,” *Nat. Chem.*, vol. 2, no. 6, pp. 450–3, Jun. 2010.

[50] J. McClure, “Band Structure of Graphite and de Haas-van Alphen Effect,” *Phys. Rev.*, vol. 108, no. 3, pp. 612–618, Nov. 1957.

[51] S. Das Sarma, S. Adam, E. H. Hwang, and E. Rossi, “Electronic transport in two-dimensional graphene,” *Rev. Mod. Phys.*, vol. 83, no. 2, pp. 407–470, May 2011.

[52] J. Kohanoff, N. I. Gidopoulos, and S. Wilson, *Density Functional Theory : Basics , New Trends and Applications Chapter 26 Density Functional Theory : Basics , New Trends and Applications*, vol. 2. 2003, pp. 532–568.

[53] S. J. Clark, M. D. Segall, C. J. Pickard, P. J. Hasnip, M. I. J. Probert, K. Refson, and M. C. Payne, “First principles methods using CASTEP,” *Zeitschrift für Krist.*, vol. 220, no. 5/6/2005, pp. 567–570, May 2005.

[54] J. D. Head and M. C. Zerner, “A Broyden—Fletcher—Goldfarb—Shanno optimization procedure for molecular geometries,” *Chem. Phys. Lett.*, vol. 122, no. 3, pp. 264–270, Dec. 1985.

[55] J.-C. Charlier and S. Roche, “Electronic and transport properties of nanotubes,” *Rev. Mod. Phys.*, vol. 79, no. 2, pp. 677–732, May 2007.

[56] S. Reich, J. Maultzsch, C. Thomsen, and P. Ordejón, "Tight-binding description of graphene," *Phys. Rev. B*, vol. 66, no. 3, p. 035412, Jul. 2002.

[57] Y. Zhang, T.-T. Tang, C. Girit, Z. Hao, M. C. Martin, A. Zettl, M. F. Crommie, Y. R. Shen, and F. Wang, "Direct observation of a widely tunable bandgap in bilayer graphene.," *Nature*, vol. 459, no. 7248, pp. 820–3, Jun. 2009.

[58] S.-G. Nam, D.-K. Ki, J. W. Park, Y. Kim, J. S. Kim, and H.-J. Lee, "Ballistic transport of graphene pnp junctions with embedded local gates.," *Nanotechnology*, vol. 22, no. 41, p. 415203, Oct. 2011.

[59] G. M. Rutter, J. N. Crain, N. P. Guisinger, T. Li, P. N. First, and J. a Stroscio, "Scattering and interference in epitaxial graphene.," *Science*, vol. 317, no. 5835, pp. 219–22, Jul. 2007.

[60] J.-H. Chen, C. Jang, S. Xiao, M. Ishigami, and M. S. Fuhrer, "Intrinsic and extrinsic performance limits of graphene devices on SiO2.," *Nat. Nanotechnol.*, vol. 3, no. 4, pp. 206–9, Apr. 2008.

[61] Y. Wu, Y. Lin, A. a Bol, K. a Jenkins, F. Xia, D. B. Farmer, Y. Zhu, and P. Avouris, "High-frequency, scaled graphene transistors on diamond-like carbon.," *Nature*, vol. 472, no. 7341, pp. 74–8, Apr. 2011.

[62] E. Hwang, S. Adam, and S. Sarma, "Carrier Transport in Two-Dimensional Graphene Layers," *Phys. Rev. Lett.*, vol. 98, no. 18, p. 186806, May 2007.

[63] J.-H. Chen, W. Cullen, C. Jang, M. Fuhrer, and E. Williams, "Defect Scattering in Graphene," *Phys. Rev. Lett.*, vol. 102, no. 23, p. 236805, Jun. 2009.

[64] E. V. Castro, H. Ochoa, M. I. Katsnelson, R. V. Gorbachev, D. C. Elias, K. S. Novoselov, a. K. Geim, and F. Guinea, "Limits on Charge Carrier Mobility in Suspended Graphene due to Flexural Phonons," *Phys. Rev. Lett.*, vol. 105, no. 26, p. 266601, Dec. 2010.

[65] H. S. Song, S. L. Li, H. Miyazaki, S. Sato, K. Hayashi, A. Yamada, N. Yokoyama, and K. Tsukagoshi, "Origin of the relatively low transport mobility of graphene grown through chemical vapor deposition.," *Sci. Rep.*, vol. 2, p. 337, Jan. 2012.

[66] S. Bae, H. Kim, Y. Lee, X. Xu, and J. Park, "30 inch roll-based production of high-quality graphene films for flexible transparent electrodes," *arXiv Prepr. arXiv ...*, 2009.

[67] C. Lobo and J. L. Martins, "Valence force field model for graphene and fullerenes," *Zeitschrift fur Phys. D Atoms, Mol. Clust.*, vol. 39, no. 2, pp. 159–164, Feb. 1997.

[68] P. Keating, “Effect of Invariance Requirements on the Elastic Strain Energy of Crystals with Application to the Diamond Structure,” *Phys. Rev.*, vol. 145, no. 2, pp. 637–645, May 1966.

[69] J. Atalaya, A. Isacsson, and J. M. Kinaret, “Continuum elastic modeling of graphene resonators.,” *Nano Lett.*, vol. 8, no. 12, pp. 4196–200, Dec. 2008.

[70] K. Kudin, G. Scuseria, and B. Yakobson, “C2F, BN, and C nanoshell elasticity from ab initio computations,” *Phys. Rev. B*, vol. 64, no. 23, p. 235406, Nov. 2001.

[71] D. Clatterbuck, C. Krenn, M. Cohen, and J. Morris, “Phonon Instabilities and the Ideal Strength of Aluminum,” *Phys. Rev. Lett.*, vol. 91, no. 13, p. 135501, Sep. 2003.

[72] A. Kelly and N. H. Macmillan, *Strong solids*. Clarendon Press, 1986, p. 423.

[73] X. Wei, B. Fragneaud, C. Marianetti, and J. Kysar, “Nonlinear elastic behavior of graphene: Ab initio calculations to continuum description,” *Phys. Rev. B*, vol. 80, no. 20, p. 205407, Nov. 2009.

[74] F. Liu, P. Ming, and J. Li, “Ab initio calculation of ideal strength and phonon instability of graphene under tension,” *Phys. Rev. B*, vol. 76, no. 6, p. 064120, Aug. 2007.

[75] E. Cadelano, P. Palla, S. Giordano, and L. Colombo, “Nonlinear Elasticity of Monolayer Graphene,” *Phys. Rev. Lett.*, vol. 102, no. 23, p. 235502, Jun. 2009.

[76] W. F. van Gunsteren and H. J. C. Berendsen, “Computer Simulation of Molecular Dynamics: Methodology, Applications, and Perspectives in Chemistry,” *Angew. Chemie Int. Ed. English*, vol. 29, no. 9, pp. 992–1023, Sep. 1990.

[77] S. J. Stuart, A. B. Tutein, and J. A. Harrison, “A reactive potential for hydrocarbons with intermolecular interactions,” *J. Chem. Phys.*, vol. 112, no. 14, p. 6472, Apr. 2000.

[78] G. Kalosakas, N. N. Lathiotakis, C. Galiotis, and K. Papagelis, “In-plane force fields and elastic properties of graphene,” *J. Appl. Phys.*, vol. 113, no. 13, p. 134307, Apr. 2013.

[79] Q. X. Pei, Y. W. Zhang, and V. B. Shenoy, “A molecular dynamics study of the mechanical properties of hydrogen functionalized graphene,” *Carbon N. Y.*, vol. 48, no. 3, pp. 898–904, Mar. 2010.

[80] R. S. Ruoff and D. C. Lorents, “Mechanical and thermal properties of carbon nanotubes,” *Carbon N. Y.*, vol. 33, no. 7, pp. 925–930, Jan. 1995.

[81] J. N. Coleman, U. Khan, W. J. Blau, and Y. K. Gun'ko, "Small but strong: A review of the mechanical properties of carbon nanotube–polymer composites," *Carbon N. Y.*, vol. 44, no. 9, pp. 1624–1652, Aug. 2006.

[82] C. SCHUH, "Nanoindentation studies of materials," *Mater. Today*, vol. 9, no. 5, pp. 32–40, May 2006.

[83] R. Ferencz, J. Sanchez, B. Blümich, and W. Herrmann, "AFM nanoindentation to determine Young's modulus for different EPDM elastomers," *Polym. Test.*, vol. 31, no. 3, pp. 425–432, May 2012.

[84] D. Passeri, A. Bettucci, A. Biagioni, M. Rossi, A. Alippi, E. Tamburri, M. Lucci, I. Davoli, and S. Berezina, "Indentation modulus and hardness of viscoelastic thin films by atomic force microscopy: A case study.," *Ultramicroscopy*, vol. 109, no. 12, pp. 1417–27, Nov. 2009.

[85] W. Weaver, Jr., S. P. Timoshenko, and D. H. Young, *Vibration Problems in Engineering*. John Wiley & Sons, 1974, pp. 425–427.

[86] B. Ho Eom, P. K. Day, H. G. LeDuc, and J. Zmuidzinas, "A wideband, low-noise superconducting amplifier with high dynamic range," *Nat. Phys.*, vol. 8, no. 8, pp. 623–627, Jul. 2012.

[87] H. W. C. Postma, I. Kozinsky, a. Husain, and M. L. Roukes, "Dynamic range of nanotube- and nanowire-based electromechanical systems," *Appl. Phys. Lett.*, vol. 86, no. 22, p. 223105, 2005.

[88] R. Legtenberg, H. A. C. Tilmans, J. H. J. Fluitman, and M. Elwenspoek, "Nonlinearity and hysteresis of resonant strain gauges," *J. Microelectromechanical Syst.*, vol. 7, no. 1, pp. 122–127, Mar. 1998.

[89] M. V. Andres, K. W. H. Foulds, and M. J. Tudor, "Nonlinear vibrations and hysteresis of micromachined silicon resonators designed as frequency-out sensors," *Electron. Lett.*, vol. 23, no. 18, p. 952, 1987.

[90] R. Lifshitz and M. Cross, "Nonlinear dynamics of nanomechanical and micromechanical resonators," in *Review of nonlinear dynamics and complexity*, Weinheim: WILEY-VCH Verlag GmbH & Co. KGaA, 2008.

[91] K. L. Ekinci and M. L. Roukes, "Nanoelectromechanical systems," *Rev. Sci. Instrum.*, vol. 76, no. 6, p. 061101, 2005.

[92] J. Chaste, A. Eichler, J. Moser, G. Ceballos, R. Rurali, and A. Bachtold, "A nanomechanical mass sensor with yoctogram resolution.," *Nat. Nanotechnol.*, vol. 7, no. 5, pp. 301–4, May 2012.

[93] Y. T. Yang, C. Callegari, X. L. Feng, K. L. Ekinci, and M. L. Roukes, "Zeptogram-scale nanomechanical mass sensing.," *Nano Lett.*, vol. 6, no. 4, pp. 583–6, Apr. 2006.

[94] K. S. Novoselov, a K. Geim, S. V Morozov, D. Jiang, Y. Zhang, S. V Dubonos, I. V Grigorieva, and a a Firsov, "Electric field effect in atomically thin carbon films.," *Science*, vol. 306, no. 5696, pp. 666–9, Oct. 2004.

[95] Y. Wu, B. Wang, Y. Ma, Y. Huang, N. Li, F. Zhang, and Y. Chen, "Efficient and large-scale synthesis of few-layered graphene using an arc-discharge method and conductivity studies of the resulting films," *Nano Res.*, vol. 3, no. 9, pp. 661–669, Sep. 2010.

[96] M. S. R. Ban F. Y, "Graphene Oxide and Its Electrochemical Performance," *Int. J. Electrochem. Sci.*, vol. 7, no. 5, pp. 4345 – 4351, 2012.

[97] P. E. J. Flewitt and R. K. Wild, *Physical Methods for Materials Characterisation, Second Edition*. CRC Press, 2003, pp. 89–98.

[98] U. Stöberl, U. Wurstbauer, W. Wegscheider, D. Weiss, and J. Eroms, "Morphology and flexibility of graphene and few-layer graphene on various substrates," *Appl. Phys. Lett.*, vol. 93, no. 5, p. 051906, Aug. 2008.

[99] J. T. Robinson, J. S. Burgess, C. E. Junkermeier, S. C. Badescu, T. L. Reinecke, F. K. Perkins, M. K. Zalalutdniov, J. W. Baldwin, J. C. Culbertson, P. E. Sheehan, and E. S. Snow, "Properties of fluorinated graphene films.," *Nano Lett.*, vol. 10, no. 8, pp. 3001–5, Aug. 2010.

[100] C. D. Zangmeister, "Preparation and Evaluation of Graphite Oxide Reduced at 220 °C," *Chem. Mater.*, vol. 22, no. 19, pp. 5625–5629, Oct. 2010.

[101] A. C. Ferrari, "Raman spectroscopy of graphene and graphite: Disorder, electron–phonon coupling, doping and nonadiabatic effects," *Solid State Commun.*, vol. 143, no. 1–2, pp. 47–57, Jul. 2007.

[102] L. M. Malard, M. a. Pimenta, G. Dresselhaus, and M. S. Dresselhaus, "Raman spectroscopy in graphene," *Phys. Rep.*, vol. 473, no. 5–6, pp. 51–87, Apr. 2009.

[103] R. L. McCreery, *Raman Spectroscopy for Chemical Analysis*. John Wiley & Sons, 2005, pp. 1–5.

[104] M. S. Amer, *Raman Spectroscopy, Fullerenes and Nanotechnology*. Royal Society of Chemistry, 2010, pp. 47–49.

[105] A. A. Balandin, "Thermal properties of graphene and nanostructured carbon materials.," *Nat. Mater.*, vol. 10, no. 8, pp. 569–81, Aug. 2011.

[106] D. L. Nika and A. A. Balandin, “Two-dimensional phonon transport in graphene.,” *J. Phys. Condens. Matter*, vol. 24, no. 23, p. 233203, Jun. 2012.

[107] S. V. Dmitriev, J. A. Baimova, A. V. Savin, and Y. S. Kivshar, “Ultimate strength, ripples, sound velocities, and density of phonon states of strained graphene,” *Comput. Mater. Sci.*, vol. 53, no. 1, pp. 194–203, Feb. 2012.

[108] L. Wirtz and A. Rubio, “The phonon dispersion of graphite revisited,” *Solid State Commun.*, vol. 131, no. 3–4, pp. 141–152, 2004.

[109] J. Maultzsch, S. Reich, C. Thomsen, H. Requardt, and P. Ordejón, “Phonon Dispersion in Graphite,” *Phys. Rev. Lett.*, vol. 92, no. 7, p. 075501, Feb. 2004.

[110] R. Nicklow, N. Wakabayashi, and H. Smith, “Lattice Dynamics of Pyrolytic Graphite,” *Phys. Rev. B*, vol. 5, no. 12, pp. 4951–4962, Jun. 1972.

[111] M. . Dresselhaus, G. Dresselhaus, P. . Eklund, and D. D. . Chung, “Lattice vibrations in graphite and intercalation compounds of graphite,” *Mater. Sci. Eng.*, vol. 31, pp. 141–152, Dec. 1977.

[112] A. Grüneis, R. Saito, T. Kimura, L. Cançado, M. Pimenta, A. Jorio, A. Souza Filho, G. Dresselhaus, and M. Dresselhaus, “Determination of two-dimensional phonon dispersion relation of graphite by Raman spectroscopy,” *Phys. Rev. B*, vol. 65, no. 15, p. 155405, Mar. 2002.

[113] S. Siebentritt, R. Pues, K.-H. Rieder, and A. M. Shikin, “Surface phonon dispersion in graphite and in a lanthanum graphite intercalation compound,” *Phys. Rev. B*, vol. 55, no. 12, pp. 7927–7934, Mar. 1997.

[114] H. Yanagisawa, T. Tanaka, Y. Ishida, M. Matsue, E. Rokuta, S. Otani, and C. Oshima, “Analysis of phonons in graphene sheets by means of HREELS measurement andab initio calculation,” *Surf. Interface Anal.*, vol. 37, no. 2, pp. 133–136, Feb. 2005.

[115] a. C. Ferrari, J. C. Meyer, V. Scardaci, C. Casiraghi, M. Lazzeri, F. Mauri, S. Piscanec, D. Jiang, K. S. Novoselov, S. Roth, and a. K. Geim, “Raman Spectrum of Graphene and Graphene Layers,” *Phys. Rev. Lett.*, vol. 97, no. 18, p. 187401, Oct. 2006.

[116] F. Tuinstra and J. L. Koening, “Raman Spectrum of Graphite,” *J. Chem. Phys.*, vol. 53, no. 3, p. 1126, Sep. 1970.

[117] A. Ferrari and J. Robertson, “Interpretation of Raman spectra of disordered and amorphous carbon,” *Phys. Rev. B*, vol. 61, no. 20, pp. 14095–14107, May 2000.

[118] C. Castiglioni, M. Tommasini, and G. Zerbi, “Raman spectroscopy of polyconjugated molecules and materials: confinement effect in one and two

dimensions.," *Philos. Trans. A. Math. Phys. Eng. Sci.*, vol. 362, no. 1824, pp. 2425–59, Nov. 2004.

[119] C. Thomsen and S. Reich, "Double resonant raman scattering in graphite," *Phys. Rev. Lett.*, vol. 85, no. 24, pp. 5214–7, Dec. 2000.

[120] J. Kürti, V. Zólyomi, a. Grüneis, and H. Kuzmany, "Double resonant Raman phenomena enhanced by van Hove singularities in single-wall carbon nanotubes," *Phys. Rev. B*, vol. 65, no. 16, p. 165433, Apr. 2002.

[121] J. Maultzsch, S. Reich, and C. Thomsen, "Double-resonant Raman scattering in graphite: Interference effects, selection rules, and phonon dispersion," *Phys. Rev. B*, vol. 70, no. 15, p. 155403, Oct. 2004.

[122] M. Ramsteiner and J. Wagner, "Resonant Raman scattering of hydrogenated amorphous carbon: Evidence for π-bonded carbon clusters," *Appl. Phys. Lett.*, vol. 51, no. 17, p. 1355, Oct. 1987.

[123] M. Matthews, M. Pimenta, G. Dresselhaus, M. Dresselhaus, and M. Endo, "Origin of dispersive effects of the Raman D band in carbon materials," *Phys. Rev. B*, vol. 59, no. 10, pp. R6585–R6588, Mar. 1999.

[124] L. G. Cançado, K. Takai, T. Enoki, M. Endo, Y. A. Kim, H. Mizusaki, A. Jorio, L. N. Coelho, R. Magalhães-Paniago, and M. A. Pimenta, "General equation for the determination of the crystallite size L[sub a] of nanographite by Raman spectroscopy," *Appl. Phys. Lett.*, vol. 88, no. 16, p. 163106, Apr. 2006.

[125] A. N. Sidorov, M. M. Yazdanpanah, R. Jalilian, P. J. Ouseph, R. W. Cohn, and G. U. Sumanasekera, "Electrostatic deposition of graphene.," *Nanotechnology*, vol. 18, no. 13, p. 135301, Apr. 2007.

[126] A. Eichler, J. Moser, J. Chaste, M. Zdrojek, I. Wilson-Rae, and A. Bachtold, "Nonlinear damping in mechanical resonators made from carbon nanotubes and graphene.," *Nat. Nanotechnol.*, vol. 6, no. 6, pp. 339–42, Jun. 2011.

[127] "Model SR830 DSP lock-in amplifier manuals," *Stanford Research Systems, Inc.*, 2011. [Online]. Available: http://www.thinksrs.com/downloads/PDFs/Manuals/SR830m.pdf. [Accessed: 01-Apr-2014].

[128] K. S. Kim, Y. Zhao, H. Jang, S. Y. Lee, J. M. Kim, K. S. Kim, J.-H. Ahn, P. Kim, J.-Y. Choi, and B. H. Hong, "Large-scale pattern growth of graphene films for stretchable transparent electrodes.," *Nature*, vol. 457, no. 7230, pp. 706–10, Feb. 2009.

[129] H. Stahl, A. Hoechst, F. Fischer, L. Metzger, R. Reichenbach, F. Laermer, S. Kronmueller, K. Breitschwerdt, R. Gunn, S. Watcham, C. Rusu, and A.

Witvrouw, “Thin film encapsulation of acceleration sensors using polysilicon sacrificial layers,” in *TRANSDUCERS ’03. 12th International Conference on Solid-State Sensors, Actuators and Microsystems. Digest of Technical Papers (Cat. No.03TH8664)*, 2003, vol. 2, pp. 1899–1902.

[130] G. Gu and Z. Xie, “Modulation doping of graphene: An approach toward manufacturable devices,” *Appl. Phys. Lett.*, vol. 98, no. 8, p. 083502, 2011.

[131] J. H. Seol, I. Jo, A. L. Moore, L. Lindsay, Z. H. Aitken, M. T. Pettes, X. Li, Z. Yao, R. Huang, D. Broido, N. Mingo, R. S. Ruoff, and L. Shi, “Two-dimensional phonon transport in supported graphene.,” *Science*, vol. 328, no. 5975, pp. 213–6, Apr. 2010.

[132] C. Casiraghi, a Hartschuh, E. Lidorikis, H. Qian, H. Harutyunyan, T. Gokus, K. S. Novoselov, and a C. Ferrari, “Rayleigh imaging of graphene and graphene layers.,” *Nano Lett.*, vol. 7, no. 9, pp. 2711–7, Sep. 2007.

[133] M. Friedemann, K. Pierz, R. Stosch, and F. J. Ahlers, “Graphene on gallium arsenide: Engineering the visibility,” *Appl. Phys. Lett.*, vol. 95, no. 10, p. 102103, 2009.

[134] P. Blake, E. W. Hill, a. H. Castro Neto, K. S. Novoselov, D. Jiang, R. Yang, T. J. Booth, and a. K. Geim, “Making graphene visible,” *Appl. Phys. Lett.*, vol. 91, no. 6, p. 063124, 2007.

[135] S. Roddaro, P. Pingue, V. Piazza, V. Pellegrini, and F. Beltram, “The optical visibility of graphene: interference colors of ultrathin graphite on SiO(2).,” *Nano Lett.*, vol. 7, no. 9, pp. 2707–10, Sep. 2007.

[136] L. YOUNG, “Synthesis of Multiple Antireflection Films over a Prescribed Frequency Band,” *J. Opt. Soc. Am.*, vol. 51, no. 9, p. 967, Sep. 1961.

[137] A. Thelen, *Design of Optical Interference Coatings*. McGraw-Hill, 1989, pp. 9–10.

[138] M. J. Weber, *Handbook of Optical Materials*. CRC Press, 2002, p. 536.

[139] P. Blake and E. Hill, “Making graphene visible,” *Appl. Phys. ...*, pp. 13–15, 2007.

[140] “Commission Internationale de l’E.” [Online]. Available: http://www.research.ed.ac.uk/portal/files/8140464/JVB06FJ01.pdf. [Accessed: 21-Feb-2014].

[141] T. Takahashi, H. Tokailin, and T. Sagawa, “Angle-resolved ultraviolet photoelectron spectroscopy of the unoccupied band structure of graphite,” *Phys. Rev. B*, vol. 32, no. 12, pp. 8317–8324, Dec. 1985.

[142] Y.-J. Yu, Y. Zhao, S. Ryu, L. E. Brus, K. S. Kim, and P. Kim, "Tuning the graphene work function by electric field effect.," *Nano Lett.*, vol. 9, no. 10, pp. 3430–4, Oct. 2009.

[143] G. Gu and Z. Xie, "Modulation doping of graphene: An approach toward manufacturable devices," *Appl. Phys. Lett.*, vol. 98, no. 8, p. 083502, Feb. 2011.

[144] M. Liu, X. Yin, E. Ulin-Avila, B. Geng, T. Zentgraf, L. Ju, F. Wang, and X. Zhang, "A graphene-based broadband optical modulator.," *Nature*, vol. 474, no. 7349, pp. 64–7, Jun. 2011.

[145] S. Shivaraman, R. a Barton, X. Yu, J. Alden, L. Herman, M. Chandrashekhar, J. Park, P. L. McEuen, J. M. Parpia, H. G. Craighead, and M. G. Spencer, "Free-standing epitaxial graphene.," *Nano Lett.*, vol. 9, no. 9, pp. 3100–5, Sep. 2009.

[146] R. A. Barton, C. S. Ruiz-vargas, J. S. Alden, and H. G. Craighead, "Fabricating Arrays of Graphene Mechanical Resonators with High , Size-Dependent Quality Factors," vol. 490, no. 2007, pp. 3–4, 2010.

[147] A. Castellanos-Gomez, M. Poot, G. a Steele, H. S. J. van der Zant, N. Agraït, and G. Rubio-Bollinger, "Elastic properties of freely suspended MoS2 nanosheets.," *Adv. Mater.*, vol. 24, no. 6, pp. 772–5, Feb. 2012.

[148] E. Watanabe, A. Conwill, D. Tsuya, and Y. Koide, "Low contact resistance metals for graphene based devices," *Diam. Relat. Mater.*, vol. 24, pp. 171–174, Apr. 2012.

[149] Y. Lee, S. Bae, H. Jang, S. Jang, S.-E. Zhu, S. H. Sim, Y. Il Song, B. H. Hong, and J.-H. Ahn, "Wafer-scale synthesis and transfer of graphene films.," *Nano Lett.*, vol. 10, no. 2, pp. 490–3, Feb. 2010.

[150] Y.-C. Lin, C.-C. Lu, C.-H. Yeh, C. Jin, K. Suenaga, and P.-W. Chiu, "Graphene annealing: how clean can it be?," *Nano Lett.*, vol. 12, no. 1, pp. 414–9, Jan. 2012.

[151] W. Liu, J. Wei, X. Sun, and H. Yu, "A Study on Graphene—Metal Contact," *Crystals*, vol. 3, no. 1, pp. 257–274, Mar. 2013.

[152] K. R. Williams, K. Gupta, and M. Wasilik, "Etch rates for micromachining processing-part II," *J. Microelectromechanical Syst.*, vol. 12, no. 6, pp. 761–778, Dec. 2003.

[153] E. T. Mickelson, C. B. Huffman, A. G. Rinzler, R. E. Smalley, R. H. Hauge, and J. L. Margrave, "Fluorination of single-wall carbon nanotubes," *Chem. Phys. Lett.*, vol. 296, no. 1–2, pp. 188–194, Oct. 1998.

[154] D. E. Palin and K. D. Wadsworth, “Structure of carbon monofluoride,” *Nature*, vol. 162, p. 926, 1948.

[155] S.-H. Cheng, K. Zou, F. Okino, H. R. Gutierrez, a. Gupta, N. Shen, P. C. Eklund, J. O. Sofo, and J. Zhu, “Reversible fluorination of graphene: Evidence of a two-dimensional wide bandgap semiconductor,” *Phys. Rev. B*, vol. 81, no. 20, p. 205435, May 2010.

[156] F. Withers, S. Russo, M. Dubois, and M. F. Craciun, “Tuning the electronic transport properties of grapheme through functionalisation with fluorine.,” *Nanoscale Res. Lett.*, vol. 6, p. 526, Jan. 2011.

[157] Y. Liang and L. Yang, “Electronic Structure and Optical Absorption of Fluorographene,” *MRS Proc.*, vol. 1370, pp. mrss11–1370–yy04–02, Jun. 2011.

[158] V. Sazonova, Y. Yaish, H. Ustünel, D. Roundy, T. A. Arias, and P. L. McEuen, “A tunable carbon nanotube electromechanical oscillator.,” *Nature*, vol. 431, no. 7006, pp. 284–7, Sep. 2004.

[159] V. Gouttenoire, T. Barois, S. Perisanu, J.-L. Leclercq, S. T. Purcell, P. Vincent, and A. Ayari, “Digital and FM demodulation of a doubly clamped single-walled carbon-nanotube oscillator: towards a nanotube cell phone.,” *Small*, vol. 6, no. 9, pp. 1060–5, May 2010.

[160] P. Hagedorn and A. DasGupta, *Vibrations and Waves in Continuous Mechanical Systems*. John Wiley & Sons, 2007, pp. 116–120.

[161] H. J. R. Westra, M. Poot, H. S. J. van der Zant, and W. J. Venstra, “Nonlinear Modal Interactions in Clamped-Clamped Mechanical Resonators,” *Phys. Rev. Lett.*, vol. 105, no. 11, p. 117205, Sep. 2010.

[162] W. Thomson, *Theory of Vibration with Applications*. CRC Press, 1996, p. 80.

[163] S. Dohn, R. Sandberg, W. Svendsen, and A. Boisen, “Enhanced functionality of cantilever based mass sensors using higher modes and functionalized particles,” in *The 13th International Conference on Solid-State Sensors, Actuators and Microsystems, 2005. Digest of Technical Papers. TRANSDUCERS ’05.*, 2005, vol. 1, pp. 636–639.

[164] M. K. Ghatkesar, V. Barwich, T. Braun, J.-P. Ramseyer, C. Gerber, M. Hegner, H. P. Lang, U. Drechsler, and M. Despont, “Higher modes of vibration increase mass sensitivity in nanomechanical microcantilevers,” *Nanotechnology*, vol. 18, no. 44, p. 445502, Nov. 2007.

[165] X. Xia and X. Li, “Resonance-mode effect on microcantilever mass-sensing performance in air.,” *Rev. Sci. Instrum.*, vol. 79, no. 7, p. 074301, Jul. 2008.

[166] A. M. Ionescu, Y. Leblebici, G. Piazza, P. J. Stephanou, and A. P. Pisano, "One and two port piezoelectric higher order contour-mode MEMS resonators for mechanical signal processing," *Solid. State. Electron.*, vol. 51, no. 11, pp. 1596–1608, 2007.

[167] H. Chandrahalim, S. A. Bhave, R. G. Polcawich, J. S. Pulskamp, and R. Kaul, "PZT transduced high-overtone width-extensional resonators above 1 GHz," in *2009 IEEE International Ultrasonics Symposium*, 2009, pp. 2145–2148.

[168] J. E. Butler, D. S. Y. Hsu, and T.-C. Nguyen, "CVD polycrystalline diamond high-Q micromechanical resonators," *Tech. Dig. MEMS 2002 IEEE Int. Conf. Fifteenth IEEE Int. Conf. Micro Electro Mech. Syst. (Cat. No.02CH37266)*, vol. 3, no. 2, pp. 657–660, 2002.

[169] T. S. Biswas, A. Suhel, B. D. Hauer, A. Palomino, K. S. D. Beach, and J. P. Davis, "High-Q gold and silicon nitride bilayer nanostrings," *Appl. Phys. Lett.*, vol. 101, no. 9, p. 093105, Aug. 2012.

[170] B. Kim, M. A. Hopcroft, R. N. Candler, C. M. Jha, M. Agarwal, R. Melamud, S. A. Chandorkar, G. Yama, and T. W. Kenny, "Temperature Dependence of Quality Factor in MEMS Resonators," *J. Microelectromechanical Syst.*, vol. 17, no. 3, pp. 755–766, Jun. 2008.

[171] A. K. Hüttel, G. A. Steele, B. Witkamp, M. Poot, L. P. Kouwenhoven, and H. S. J. van der Zant, "Carbon nanotubes as ultrahigh quality factor mechanical resonators.," *Nano Lett.*, vol. 9, no. 7, pp. 2547–52, Jul. 2009.

[172] H. Jiang, M.-F. Yu, B. Liu, and Y. Huang, "Intrinsic Energy Loss Mechanisms in a Cantilevered Carbon Nanotube Beam Oscillator," *Phys. Rev. Lett.*, vol. 93, no. 18, p. 185501, Oct. 2004.

[173] Z. Qi and H. S. Park, "Intrinsic energy dissipation in CVD-grown graphene nanoresonators.," *Nanoscale*, vol. 4, no. 11, pp. 3460–5, Jun. 2012.

[174] D. S. Bindel, E. Quevy, T. Koyama, S. Govindjee, J. W. Demmel, and R. T. Howe, "Anchor loss simulation in resonators," in *18th IEEE International Conference on Micro Electro Mechanical Systems, 2005. MEMS 2005.*, 2005, pp. 133–136.

[175] F. Ayazi, "Support loss in micromechanical disk resonators," in *18th IEEE International Conference on Micro Electro Mechanical Systems, 2005. MEMS 2005.*, 2005, pp. 137–141.

[176] Z. Hao, A. Erbil, and F. Ayazi, "An analytical model for support loss in micromachined beam resonators with in-plane flexural vibrations," *Sensors Actuators A Phys.*, vol. 109, no. 1–2, pp. 156–164, Dec. 2003.

[177] Y.-H. Park and K. C. Park, “High-Fidelity Modeling of MEMS Resonators—Part I: Anchor Loss Mechanisms Through Substrate,” *J. Microelectromechanical Syst.*, vol. 13, no. 2, pp. 238–247, Apr. 2004.

[178] M. A. Abdelmoneum, M. U. Demirci, and C. T.-C. Nguyen, “Stemless wine-glass-mode disk micromechanical resonators,” in *The Sixteenth Annual International Conference on Micro Electro Mechanical Systems, 2003. MEMS-03 Kyoto. IEEE*, 2003, pp. 698–701.

[179] T. Ono and M. Esashi, “Energy dissipation in submicrometer thick single-crystal silicon cantilevers,” *J. Microelectromechanical Syst.*, vol. 11, no. 6, pp. 775–783, Dec. 2002.

[180] K. Y. Yasumura, T. D. Stowe, E. M. Chow, T. Pfafman, T. W. Kenny, B. C. Stipe, and D. Rugar, “Quality factors in micron- and submicron-thick cantilevers,” *J. Microelectromechanical Syst.*, vol. 9, no. 1, pp. 117–125, Mar. 2000.

[181] C. Seoanez, F. Guinea, and A. Neto, “Dissipation in graphene and nanotube resonators,” *Phys. Rev. B*, 2007.

[182] T. Ono and M. Esashi, “Energy dissipation in submicrometer thick single-crystal silicon cantilevers,” *J. Microelectromechanical Syst.*, vol. 11, no. 6, pp. 775–783, Dec. 2002.

[183] S. Y. Kim and H. S. Park, “The importance of edge effects on the intrinsic loss mechanisms of graphene nanoresonators.,” *Nano Lett.*, vol. 9, no. 3, pp. 969–74, Mar. 2009.

[184] A. K. Geim and K. S. Novoselov, “The rise of graphene.,” *Nat. Mater.*, vol. 6, no. 3, pp. 183–91, Mar. 2007.

[185] L. Britnell, R. V Gorbachev, R. Jalil, B. D. Belle, F. Schedin, a Mishchenko, T. Georgiou, M. I. Katsnelson, L. Eaves, S. V Morozov, N. M. R. Peres, J. Leist, a K. Geim, K. S. Novoselov, and L. a Ponomarenko, “Field-effect tunneling transistor based on vertical graphene heterostructures.,” *Science*, vol. 335, no. 6071, pp. 947–50, Feb. 2012.

[186] A. Reina, X. Jia, J. Ho, D. Nezich, H. Son, V. Bulovic, M. S. Dresselhaus, and J. Kong, “Large area, few-layer graphene films on arbitrary substrates by chemical vapor deposition.,” *Nano Lett.*, vol. 9, no. 1, pp. 30–5, Jan. 2009.

[187] Z. Jiang, Y. Zhang, Y.-W. Tan, H. L. Stormer, and P. Kim, “Quantum Hall effect in graphene,” *Solid State Commun.*, vol. 143, no. 1–2, pp. 14–19, Jul. 2007.

[188] J. R. Williams, L. Dicarlo, and C. M. Marcus, “Quantum Hall effect in a gate-controlled p-n junction of graphene.,” *Science*, vol. 317, no. 5838, pp. 638–41, Aug. 2007.

[189] D. Teweldebrhan and a. a. Balandin, “Modification of graphene properties due to electron-beam irradiation,” *Appl. Phys. Lett.*, vol. 94, no. 1, p. 013101, 2009.

[190] I. Childres, L. A. Jauregui, M. Foxe, J. Tian, R. Jalilian, I. Jovanovic, and Y. P. Chen, “Effect of electron-beam irradiation on graphene field effect devices,” *Appl. Phys. Lett.*, vol. 97, no. 17, p. 173109, Oct. 2010.

[191] J. Yan and M. S. Fuhrer, “Correlated Charged Impurity Scattering in Graphene,” *Phys. Rev. Lett.*, vol. 107, no. 20, p. 206601, Nov. 2011.

[192] K. I. Bolotin, K. J. Sikes, J. Hone, H. L. Stormer, and P. Kim, “Temperature-Dependent Transport in Suspended Graphene,” *Phys. Rev. Lett.*, vol. 101, no. 9, p. 096802, Aug. 2008.

[193] S. Kim, J. Nah, I. Jo, D. Shahrjerdi, L. Colombo, Z. Yao, E. Tutuc, and S. K. Banerjee, “Realization of a high mobility dual-gated graphene field-effect transistor with Al[sub 2]O[sub 3] dielectric,” *Appl. Phys. Lett.*, vol. 94, no. 6, p. 062107, Jan. 2009.

[194] J. Lee, L. Tao, Y. Hao, R. S. Ruoff, and D. Akinwande, “Embedded-gate graphene transistors for high-mobility detachable flexible nanoelectronics,” *Appl. Phys. Lett.*, vol. 100, no. 15, p. 152104, Apr. 2012.